



**TUS**

Ollscoil Teicneolaíochta na Sionainne:  
Lár Tíre, An tIarthar Láir  
Technological University of the Shannon:  
Midlands Midwest

**A VERSATILE MONITORING TECHNIQUE FOR  
REAL-TIME PROTEIN ACTIVITY TRACKING  
WITHIN CELLULAR AND BIOMIMETIC SCAFFOLD  
ENVIRONMENTS**

A thesis submitted for the degree of

**Doctor of Philosophy**

to the

**Technological University of the Shannon: Midlands Midwest**

By

**Laura Gabriela Rodriguez Barroso**

Supervisors: Dr. Margaret Brennan-Fournet &

Dr. Declan Devine

# Declaration of Authorship

I hereby certify that this material, which I now submit for assessment on the program of study leading to the award of PhD by Research program in PRISM Research Institute, Technological University of The Shannon: Midlands Midwest is entirely my own work and has not been taken from the work of others and to the extent that such work has been cited and acknowledged within the text of my work.

I confirm that:

- This work was done wholly or mainly while in candidature for a research degree at this institute.
- Where any part of this thesis has been previously been submitted for a degree or any other qualification at this University or any other institution, this has been clearly stated.
- Where I have consulted the published work of others, this is always clearly attributed.
- Where I have quoted from the others, the source is always given.
- With the exception of such quotations, this thesis is entirely my own work.
- I have acknowledged all main sources of help.

Signed: \_\_\_\_\_ *Lavan Ruz B.* \_\_\_\_\_ Date: \_\_\_\_\_ 12/07/2023 \_\_\_\_\_

# Acknowledgements

I would like to express my sincere gratitude to my supervisors, Dr. Margaret Brennan-Fournet and Dr. Declan Devine, for their support and invaluable guidance throughout this research journey. Their expertise, patience, and dedication played an essential role in shaping this thesis. I am truly fortunate to have had such exceptional mentors who not only shared their knowledge but also inspired me to explore new horizons in my field.

Furthermore, I acknowledge the outstanding faculty members at Technological University of The Shannon, Athlone Campus, whose commitment to academic excellence has been inspiring, and their contributions have enriched my educational experience.

To my family, I owe an immeasurable debt of gratitude. My parents, Javier and Luz Angela, have been a constant source of motivation, and their sacrifices and unwavering support have made this achievement possible. My siblings, Javi and Vero, have been my cheerleaders, providing encouragement and humour during the toughest times. My husband, Luis, deserves special mention for his encouragement and understanding throughout this journey. His support has been my pillar of strength. My extended family has also played a significant role in my journey, offering their encouragement and love.

Finally, I want to express my heartfelt gratitude to my friends and colleagues, specially Diana Garza Herrera, and Eduardo Lanzagorta Garcia who is finishing this journey with me. Your friendship and shared academic struggles made this journey not only manageable but also memorable. I am thankful for all the friendships forged during this time, and I look forward to our continued growth and collaboration in the future.

To all those who have been a part of my academic and personal life, whether mentioned here or not, I extend my warmest thanks. Your contributions have made a lasting impact on my journey, and I am forever thankful.

Sincerely,

Laura

# Table of Contents

<b>Declaration of Authorship</b> .....	2
<b>Acknowledgements</b> .....	3
<b>Table of Contents</b> .....	4
<b>List of Figures</b> .....	9
<b>ABSTRACT</b> .....	14
<b>CHAPTER 1</b> .....	17
<b>INTRODUCTION</b> .....	17
<b>1.1 Research Challenge</b> .....	18
<b>1.2 Research Question</b> .....	18
<b>1.3 Proposed Solution</b> .....	19
<b>1.4 Objectives</b> .....	19
<b>CHAPTER 2</b> .....	20
<b>LITERATURE REVIEW</b> .....	20
<b>2.1 Introduction</b> .....	21
<b>2.2 Tissue Regeneration Scaffolds</b> .....	22
2.2.1 Chitosan and Hydroxyapatite Regeneration Scaffolds.....	23
2.2.2 Tissue regeneration hydrogels .....	24
<b>2.3 Extracellular Matrix and the Extracellular Matrix Protein Fibronectin (Fn)</b> .....	25
2.3.1 Protein conformational changes and disease.....	28
<b>2.4 Overview of conventional technological processes and methodologies for molecular activity monitoring and detection within biological environments.</b> .....	30
2.4.1 Raman Spectroscopy.....	30
2.4.2 Fluorescence Resonance Energy Transfer .....	33
<b>2.5 Nanotechnology properties and applications</b> .....	35
2.5.1 Shaped Silver Nanoparticles .....	37
<b>2.6 Surface Plasmon Resonance (SPR) and Local Surface Plasmon Resonance (LSPR)</b> .....	40
<b>2.7 Triangular Silver Nanoplates applications</b> .....	42
2.7.1 Solution-phase nanoparticle sensing.....	42

2.7.2	Surface-bound nanoparticle arrays.....	43
<b>2.8</b>	<b>Immunoassays .....</b>	<b>45</b>
<b>2.9</b>	<b>Coronavirus Disease 2019 (COVID-19) .....</b>	<b>47</b>
<b>CHAPTER 3.....</b>		<b>51</b>
<b>INSTRUMENTATION AND METHODOLOGY.....</b>		<b>51</b>
<b>3.1</b>	<b>Materials for TSNP production, protection and functionalisation.....</b>	<b>52</b>
3.1.1	Materials for scaffold preparation, protein monitoring and detection .....	52
<b>3.2</b>	<b>Ultraviolet-visible spectroscopy (UV-Vis).....</b>	<b>53</b>
<b>3.3</b>	<b>Surface Plasmon Resonance (SPR) .....</b>	<b>54</b>
<b>3.4</b>	<b>Local Surface Plasmon Resonance .....</b>	<b>55</b>
3.4.1	Local Surface Plasmon Resonance Challenges.....	58
<b>3.5</b>	<b>Triangular Silver Nanoplate Seeds production.....</b>	<b>60</b>
3.5.1	Optimization of Triangular Silver Nanoplates preparation.....	61
3.5.2	TSNP gold edge-coating method for protection and functionalisation.....	61
3.5.3	Stability and sensitivity test .....	62
3.5.4	Polyethylene glycol coating of AuTSNP .....	63
<b>3.6</b>	<b>Fn functionalisation of PEGAuTSNP and pH monitoring.....</b>	<b>63</b>
<b>3.7</b>	<b>Bone tissue regeneration scaffolds preparation .....</b>	<b>64</b>
<b>3.8</b>	<b>Fn functionalisation on PEGAuTSNP and pH monitoring in the presence of Cs-HAp scaffolds.....</b>	<b>64</b>
<b>3.9</b>	<b>Cell culture with C2C12 myoblast cells .....</b>	<b>64</b>
3.9.1	Cell culture with MC3T3-E1 pre-osteoblast cells.....	65
	<b>3.9.1.1 Medium Preparation.....</b>	<b>66</b>
	<b>3.9.1.2 MC3T3-E1 cells resuscitation .....</b>	<b>66</b>
3.9.2	Cell passage .....	67
3.9.3	Cell counting.....	67
3.9.4	Protein effective-denaturing time determination .....	70
<b>3.10</b>	<b>Cell incubation with Fn functionalised PEGAuTSNP for protein monitoring overtime .....</b>	<b>71</b>
3.10.1	Cell plating and incubation with Fn functionalised PEGAuTSNP and Cs-HAp scaffolds for protein monitoring overtime.....	72
3.10.2	MC3T3-E1 cells plating and incubation with Fn functionalised PEGAuTSNP and Cs-HAp scaffolds for protein monitoring overtime.....	73

<b>3.11</b>	<b>Bone tissue regeneration hydrogel scaffolds preparation</b> .....	75
3.11.1	Monitoring of on-scaffold loaded Fn in MC3T3-E1 cells .....	75
<b>3.12</b>	<b>Nanoplate-based direct immunoassay with Fibronectin and Anti-fibronectin antibody.</b>	77
3.12.1	Nanoplate-based immunoassay system testing with active and denatured Fn .....	77
3.12.2	Nanoplate-based immunoassay system testing with spun-down Fn functionalised PEGAuTSNP .....	77
3.12.3	Nanoplate-based immunoassay with changing concentration of Anti-Fn antibody .....	78
<b>3.13</b>	<b>Nanoplate-based indirect immunoassay with Fn and Anti-Fn antibody.</b> .....	78
3.13.1	Extracellular Matrix isolation protocol .....	78
3.13.2	Detection of native fibronectin with AntiFn-PEGAuTSNP .....	79
<b>3.14</b>	<b>Nanoplate-based immunoassay for COVID-19 detection</b> .....	81
3.14.1	Spike protein optimal functionalisation volume determination .....	81
3.14.2	Nanoplate-based immunoassay with changing concentration of Anti-Spike antibody .....	82
3.14.3	Spike-AntiSpike binding PEGAuTSNP-based immunoassay .....	82
3.14.4	Spike-AntiSpike binding PEGAuTSNP-based immunoassay within horse serum .....	82
3.14.5	Dynamic Light Scattering (DLS) measurements .....	83
<b>CHAPTER 4.</b> .....		85
<b>TRIANGULAR SILVER NANOPLATES PREPARATION AND FUNCTIONALIZATION</b> ..		85
<b>4.1</b>	<b>Preface</b> .....	86
<b>4.2</b>	<b>Optimization of Triangular Silver Nanoplates preparation</b> .....	86
4.2.1	Gold edge-coating of TSNP and stability test .....	88
4.2.2	LSPR sensitivity analysis .....	89
<b>4.3</b>	<b>Fn functionalisation on PEGAuTSNP and pH dependent conformation</b> .....	90
4.3.1	Fn functionalised PEGAuTSNP monitoring in presence of Cs-HAp regeneration scaffolds	92
<b>4.4</b>	<b>Summary</b> .....	94
<b>CHAPTER 5.</b> .....		95
<b>FIBRONECTIN MONITORING IN CELLULAR AND BIOMIMETIC TISSUE SCAFFOLD ENVIRONMENTS</b> .....		95
<b>5.1</b>	<b>Preface</b> .....	96
<b>5.2</b>	<b>Fn activity monitoring within C2C12 cells</b> .....	96
5.2.1	Fn activity monitoring within C2C12 cells in the presence of bone tissue regeneration scaffolds	99

<b>5.3</b>	<b>Fn activity monitoring within MC3T3-E1 cells</b> .....	101
5.3.1	Fn activity monitoring within MC3T3-E1 cells in the presence of bone tissue regeneration scaffolds .....	105
<b>5.4</b>	<b>On-scaffold loaded Fn activity monitoring within MC3T3-E1 cells</b> .....	106
<b>5.5</b>	<b>Summary</b> .....	107
<b>CHAPTER 6</b> .....		109
<b>NANOPLATE-BASED IMMUNOASSAYS WITH FIBRONECTIN AND ANTI- FIBRONECTIN ANTIBODY</b> .....		109
<b>6.1</b>	<b>Preface</b> .....	110
<b>6.2</b>	<b>Nanoplate-based immunoassay system testing with active and denatured Fn</b> .....	110
6.2.1	Nanoplate-based immunoassay system testing with spun-down Fn functionalised PEGAuTSNP .....	112
<b>6.3</b>	<b>Nanoplate-based immunoassay with changing concentration of AntiFn antibody</b> .....	114
<b>6.4</b>	<b>Detection of native Fn using Anti-Fn antibody-functionalised PEGAuTSNP</b> .....	115
<b>6.5</b>	<b>Summary</b> .....	119
<b>CHAPTER 7</b> .....		120
<b>NANOPLATE-BASED IMMUNOASSAYS FOR COVID-19 DETECTION</b> .....		120
<b>7.1</b>	<b>Preface</b> .....	121
<b>7.2</b>	<b>Spike protein optimal functionalisation volume determination</b> .....	121
<b>7.3</b>	<b>Spike-PEGAuTSNP Detection Limits determination</b> .....	122
<b>7.4</b>	<b>Specificity analysis of the Spike-AntiSpike system</b> .....	123
<b>7.5</b>	<b>Spike protein detection-platform testing within horse serum</b> .....	125
<b>7.6</b>	<b>Summary</b> .....	134
<b>CHAPTER 8</b> .....		136
<b>CONCLUSION &amp; FUTURE PERSPECTIVES</b> .....		136
<b>CHAPTER 9</b> .....		140
<b>COMPLETED TRAINING AND WORK DISSEMINATION</b> .....		140
9.1	Completed Modules .....	141
9.2	Technical and Instrumentation Training .....	141
9.3	Conferences.....	141
9.4	Publications.....	142

<b>REFERENCES</b> .....	144
<b>APPENDICES</b> .....	166
Appendix 1: EPIGEUM online course certificate of completion .....	166
Appendix 2: Abstract for Bioengineering in Ireland Conference 2019, January 2019.....	167
Appendix 3: AIT Research Day poster, May 2019.....	168
Appendix 4: Abstract for Materials Science and Smart Materials Conference 2019 (MSSM 2019) .....	169
Appendix 5: MSSM 2019 Conference paper in Advanced Materials Research .....	170
Appendix 6: MSSM 2019 Certificate of participation.....	175
Appendix 7: AIT Research Day poster, November 2019 .....	176
Appendix 8: Abstract for Bioengineering in Ireland Conference 2020, January 2020.....	177
Appendix 9: Postgraduate Research Seminar and Poster Event 2020, June 2020 .....	178
Appendix 10: Postgraduate Research Seminar and Poster Event certificate of participation.....	179
Appendix 11: Shannon Region Postgraduate Research Conference certificate of participation ....	180
Appendix 12: PosterFest 2022, Technological University of the Shannon: Midlands Midwest ....	181
Appendix 13: Nanotech France 2022 Conference, certificate of participation. Paris, France, 15-17 June 2022 .....	182
Appendix 14: Paper published in MDPI Nanomaterials (2022) .....	183
Appendix 15: Paper published in MDPI Applied Sciences (2023).....	194
Appendix 16: Paper published in MDPI International Journal of Molecular Sciences (2023).....	213



# List of Figures

Figure 1. Scaffold-based materials and strategies (Li et al., 2014).....	23
Figure 2. Representation of ECM composition indicating cellular engagement with ECM biomolecules and primary components of ECM (Aamodt & Grainger, 2017).....	26
Figure 3. Schematic diagram of the multidomain structure of Fn. Adapted from Henderson et al., 2011. ....	28
Figure 4. GFND mutants in vitro study. Mutant Y973C formed more matrix than wild-type FN upon incubation with HEK293 cells (human embryonic kidney). Adapted from Ohashi et al., 2017. ....	29
Figure 5. Illustration of a Raman spectrum. SERS spectra of Amyloid $\beta$ -protein 40 (red) and Amyloid $\beta$ -protein 42 (turquoise). Adapted from (Yu et al., 2018).....	31
Figure 6. Adapted illustration of Raman Spectroscopy mechanism (Kim, 2015). ....	32
Figure 7. Single-molecule FRET system for proliferating cell nuclear antigen (PCNA) conformational dynamics. Cy3 fluorescent dye as the donor and Cy5 fluorescent dye as the acceptor were added at the interface of PCNA. This was done to investigate structural modifications linked to the opening and closing of the PCNA ring. A) Ring closed, high FRET signal. B) Ring open, low FRET signal (Gadkari et al., 2018). ....	34
Figure 8. Applications in Nanotechnology (Jordan et al., 2014) .....	36
Figure 9. Illustration of TSNP formation. Adapted from (Etacheri et al., 2010).....	38
Figure 10. a) Silver seed solution, b) Triangular Silver Nanoplates solution, c) TEM image of TSNP from (Aherne et al., 2008).....	39
Figure 11. Heterogeneous sandwich immunoassay, (Rizzo, 2022). ....	45
Figure 12. KIMS homogeneous immunoassay example. a) Negative analysis, b) Positive analysis. (Dinis-Oliveira, 2014).....	46
Figure 13. Transmission Electron Microscopy (TEM) of novel coronavirus SARS-COV-2 (National Institutes of Health, 2020).....	48
Figure 14. Illustration of SARS-COV-2 mechanism of infection (Kumar et al., 2021). ....	49
Figure 15. Schematic diagram of Lambert-Beer Law.....	54
Figure 16. Adaptation of a schematic diagram of SP propagation (Willets & Van Duyne, 2007). ....	55
Figure 17. Local Surface Plasmon Resonance phenomenon (Hong et al., 2012). ....	56
Figure 18. Adapted scheme of DDA calculated extinction (black line), absorption (red line) and scattering (blue line) of different silver nanoparticle geometries (Wiley et al., 2006). ....	58
Figure 19. UV-Vis spectra of AuNPs (A) without D-glucose (B) AuNPs with 25 nM D-glucose concentration. Presence of D-glucose in the sample caused a colour change which resulted in a redshift of the spectrum. Adapted from (Pandya et al., 2013) .....	60

Figure 20. C2C12 culture at ~70% confluence.....	65
Figure 21. MC3T3-E1 cells at ~50% confluence.....	66
Figure 22. Haemocytometer grid.(Arnal Barbedo, 2013).....	68
Figure 23. Fn PEGAuTSNP treatments layout in a 96 well-plate for effective-denaturing time testing. .....	70
Figure 24. Fn PEGAuTSNP treatments layout in a 96 well-plate for protein monitoring overtime.....	72
Figure 25. Fn PEGAuTSNP treatments layout in a 96 well-plate for protein monitoring overtime.....	73
Figure 26. Fn PEGAuTSNP treatments layout in a 24 well-plate for protein monitoring overtime.....	74
Figure 27. Cs-HAp hydrogels .....	75
Figure 28. Fn-hydrogels and Fn-PEGAuTSNP treatments layout in a 24 well-plate for protein monitoring overtime.....	76
Figure 29. Nanoplate-based immunoassay 96-well plate layout. ....	80
Figure 30. Nanoplate-based immunoassay layout with non-ECM proteins.....	81
Figure 31. COVID-19 detection experiment layout.....	83
Figure 32. LSPR spectra of (a) original TSNP preparation method with <130 nm FWHM and (b) optimized TSNP preparation method with ~115 nm FWHM. Narrower LSPR peak of ~115 FWHM indicates homogeneity of TSNP which improves sensitivity. ....	87
Figure 33. Gold coating and stability test of Triangular Silver Nanoplates. A 20 nm redshift was recorded upon gold coating of the nanoplates, moreover, no change in the spectrum was recorded upon exposure to NaCl 20 mM indicating successful protection of AuTSNP.....	89
Figure 34. UV-Vis spectra of AuTSNP suspended in a range of water-sucrose solutions. The LSPR $\lambda_{max}$ of the spectra increases as the sucrose concentration increases.....	90
Figure 35. UV-Vis spectra of Fn functionalised PEGAuTSNP at pH 4 and pH 7. Upon pH adjustment from pH 7 to pH 4 a 12 nm redshift was recorded due to Fn extension. ....	91
Figure 36. UV-Vis spectra of (a) Fn PEGAuTSNP with and without the presence of Cs-HAp regeneration scaffold, (b) Fn PEGAuTSNP in its compact (pH 7) and extended conformations (pH 4). .....	93
Figure 37. LSPR spectra of active (red) and denatured (black) Fn functionalised PEG- AuTSNP at different denaturing times where longer shifts for active Fn can be observed. ....	97
Figure 38. (a) LSPR spectral shift measurements of active and denatured Fn functionalised PEG- AuTSNP at different denaturing times (b) LSPR spectral shift measurements of active and denatured Fn functionalised PEG- AuTSNP at the most effective denaturing time.....	98
Figure 39. (a) LSPR spectral peaks and (b) $\Delta\lambda_{max}$ shift measurements of active Fn PEGAuTSNP incubated with C2C12 myoblasts and Cs-HAp regeneration scaffolds overtime. ....	100

Figure 40. Images of C2C12 cells taken after 32 hours of incubation with (a) Fn, (b) Fn and scaffold, (c) Fn PEGAuTSNP, (d) Fn PEGAuTSNP and scaffold, (e) PEGAuTSNP, f) PEGAuTSNP and scaffold. Cells confluence and growth was maintained overtime upon incubation with all treatments. .... 101

Figure 41. (a) LSPR spectral peaks and (b) Cumulative shift measurements of active and denatured Fn PEGAuTSNP incubated with MC3T3-E1 pre-osteoblasts. Significant redshifts were observed for active Fn with shifts over 100 nm reached after 32 h. Limited shifting was observed for the denatured protein. .... 103

Figure 42. LSPR spectra of active Fn PEGAuTSNP (red) and BSA PEGAuTSNP (black) incubated with MC3T3-E1 pre-osteoblasts overtime. No spectral recordings were obtained for BSA PEGAuTSNP after 8 h due to degradation within the cellular environment. .... 103

Figure 43. Un-smoothed and un-normalised LSPR spectra of active Fn PEGAuTSNP and BSA PEGAuTSNP incubated with MC3T3-E1 cells at 8h and 32h time points showing BSA degradation. .... 104

Figure 44. Cumulative shift measurements of active and denatured Fn PEGAuTSNP incubated with MC3T3-E1 pre-osteoblasts in the presence of Cs-HAp bone tissue regeneration scaffolds. Considerable redshifts were observed for active Fn while limited shifting was observed for the denatured protein. .... 105

Figure 45. Images of MC3T3-E1 cells taken after 32h of incubation with (i) Active Fn-PEG-Np, (ii) Denatured Fn-PEG-NP, (iii) Active Fn-PEG-Np and scaffold, (iv) Denatured Fn-PEG-Np and scaffold, (v) BSA-PEG-NP. Typical morphology was observed regardless of the treatment. .... 106

Figure 46. Cumulative shift measurements of active and denatured Fn on-scaffold incubated with MC3T3-E1 pre-osteoblasts. Similar shifting behaviour was observed with longer shifts for active Fn and limited shifting for denatured Fn. .... 107

Figure 47. LSPR spectra of FnPEGAuTSNP before (left) and after (right) addition of Anti-Fn antibody. .... 110

Figure 48. LSPR spectra of denatured Fn-PEGAuTSNP before and after addition of Anti-Fn antibody. No significant change was observed in  $\lambda_{max}$  for PEGAuTSNP and denatured Fn PEGAuTSNP. A 15 nm shift was recorded upon addition of AntiFn. .... 112

Figure 49. LSPR spectra of centrifuged Fn-PEGAuTSNP s (a) before and (b) after AntiFn antibody .... 113

Figure 50. LSPR spectra of Fn-PEGAuTSNP upon addition of increasing concentrations of AntiFn. Redshifts were observed as the concentration of AntiFn increased indicating intensifying binding of the antibody to the Fn functionalised nanoplates. .... 114

Figure 51. LSPR peak shift as a function of AntiFn concentration for Fn PEGAuTSNP. There was detection of Fn-AntiFn binding with AntiFn concentrations of 0.01 mg/mL, and system saturation was observed from 0.212 mg/mL of AntiFn. ....	115
Figure 52. LSPR spectra of AntiFn-Native Fn binding experiment .....	116
Figure 53. LSPR spectra of AntiTJP1-AntiFn binding experiment.....	118
Figure 54. LSPR spectra of Spike PEGAuTSNP with increasing amounts of AntiSpike. Redshifts were observed as the concentration of AntiSpike increased indicating intensifying binding of the antibody to the Spike functionalised nanoplates.....	123
Figure 55. LSPR peak shift as a function of Anti-Spike concentration for Spike PEGAuTSNP. Spike-PEGAuTSNP detection limit was determined in a range of AntiSpike concentration between 0.01- 0.1 mg/mL.....	123
Figure 56. LSPR spectral shifts of PEGAuTSNP, Spike functionalised PEGAuTSNP, TJP1 functionalised PEGAuTSNP before and after exposure to AntiSpike.....	124
Figure 57. Illustration of protein replacement due to stronger attachment of AntiSpike to PEGAuTSNP. ....	131
Figure 58. DLS measurements for TJP1-NP + AntiSpike and TJP1-NP within 100% HS before and after addition of AntiSpike.....	132
Figure 59. DLS measurements for TJP1-NP + AntiSpike and TJP1-NP within 50% HS before and after addition of AntiSpike.....	133
Figure 60. DLS measurements for TJP1-NP + AntiSpike and TJP1-NP within 10% HS before and after addition of AntiSpike.....	134

# List of Tables

Table 1. Ag:Au ratio volumes per TSNP aliquot.....	62
Table 2. Sucrose solutions and concentrations .....	62
Table 3. $\lambda_{\max}$ of Fn-PEGAuTSNP before and after addition of Anti-Fn .....	111
Table 4. $\lambda_{\max}$ for increasing Fn volumes before and after addition of Anti-Fn for centrifuged samples .....	113
Table 5. $\lambda_{\max}$ of AntiFn-PEGAuTSNP within different concentrations of ECM .....	116
Table 6. $\lambda_{\max}$ of AntiTJP1-PEGAuTSNP within different concentrations of ECM .....	118
Table 7. $\lambda_{\max}$ recordings before and after addition of AntiSpike.....	121
Table 8. $\lambda_{\max}$ for Spike-PEGAuTSNP and TJP1-PEGAuTSNP before and after addition of AntiSpike .....	124
Table 9. $\lambda_{\max}$ for Spike-PEGAuTSNP and TJP1-PEGAuTSNP treatments within HS before and after exposure to AntiSpike.....	125
Table 10. $\lambda_{\max}$ for TJP1-PEGAuTSNP treatments within HS before and after exposure to AntiSpike. ....	126
Table 11. Size measurements of PEGAuTSNP, Spike-PEGAuTSNP and TJP1-PEGAuTSNP treatments within HS before and after exposure to AntiSpike.....	127

# ABSTRACT

High biological noise is intrinsic within biological systems, and this poses critical challenges to the in-situ detection and measurement of biomolecular and protein activities important to advancing approaches to disease and injury treatment. These challenges arise due to possible non-specific binding of other molecules in the analyte's surrounding medium. Currently the techniques available to characterize protein behaviours in living biological systems are highly elaborate and are generally greatly hindered by the high background noise. Here we present a versatile and straight forward technique for monitoring proteins and protein interactions within cells and other complex environments, based on a novel nano-bio-technology method. Highly sensitive gold edge coated triangular silver nanoplates (AuTSNP), which are highly responsive to molecular interactions on their surfaces, are used to probe protein behaviours within complex cellular and tissue regeneration environments, as well as recognize antibody-antigen (Ab-Ag) interactions within dynamic biological surroundings. The extracellular domains within tissues involve macromolecules vital for the provision of structural support to surrounding cells and signalling cues for the modulation of diverse cellular processes. Tissue scaffolds are designed to mimic the extracellular architecture and functions. In this work, monitoring of the dynamic behaviour of a critical extracellular protein, Fibronectin (Fn), within the presence of bone tissue regeneration scaffolds and living cells is reported. The optical response of Fn functionalised AuTSNP, is used to distinguish between compact and extended conformations of the protein and indicating Fn unfolding and fibril formation on incubation within cells.

Moreover, successful detection of native Fn present in isolated Extracellular Matrix (ECM) by using Anti-Fn antibody functionalised AuTSNP is performed. The excellent sensitivity and straight forward application within complex cellular environments, poses AuTSNP as powerful new tools to detect protein interactions and monitor essential protein activity. For this reason, a potential COVID-19 detection platform is explored where SARS-CoV-2 Spike protein is detected through a nanoplate-based system using its corresponding antibody, Anti-Spike. This work is conducted within the presence of horse serum (HS) as complex environment where the dynamic surroundings present a challenge for the straightforward detection of the Ab-Ag complex binding, nonetheless, the research presented is a significant step towards the development of new technologies for medical diagnosis and monitoring.

## List of Abbreviations

Fn	Fibronectin
ECM	Extracellular Matrix
TSNP	Triangular Silver Nanoplates
AuTSNP	Gold edge-coated TSNP
PEGAuTSNP	PEG coated AuTSNP
NP	Nanoplates (PEGAuTSNP)
SPR	Surface Plasmon Resonance
LSPR	Local Surface Plasmon Resonance
NMR	Nuclear Magnetic Resonance
FRET	Fluorescence Resonance Energy Transfer
EM	Electromagnetic Radiation
DLS	Dynamic Light Scattering
AgNO <sub>3</sub>	Silver Nitrate
TSC	Trisodium Citrate
PSSS	Poly (4-styrene sulfonate sodium salt)
L-AA	L-Ascorbic Acid
HAuCl <sub>4</sub>	Chloroauric Acid
NaCl	Sodium Chloride
SB	Sodium Borohydride
PEG	Polyethylene Glycol
HAp	Hydroxyapatite
TCP	Tricalcium Phosphate
Cs	Chitosan
DMEM	Dulbecco's Modified Eagle's Medium

FBS	Fetal Bovine Serum
BSA	Bovine Serum Albumin
HS	Horse Serum
$\alpha$ -MEM	Alpha Minimum Essential Medium
UV	Ultraviolet
FWHM	Full Width at Half Maximum
TJP1	Tight Junction Protein
SARS-CoV-2	Severe Acute Respiratory Syndrome Coronavirus 2
COVID-19	Coronavirus Disease 2019
Ag	Antigen
Ab	Antibody



**CHAPTER 1.**

**INTRODUCTION**

## **1.1 Research Challenge**

In the cellular environment, high noise levels, such as fluctuations in biochemical reactions, protein variability, molecular diffusion, cell-to-cell contact and pH, both mediate and interfere with cellular responses (Iwamoto et al., 2016). The crowded cell matrix modulates protein folding, conformational dynamics and trajectories, which underpin biological processes. Raman Spectroscopy and Fluorescence Resonance Energy Transfer (FRET) are common techniques to characterise these protein activities. However, these techniques are highly elaborate and are generally greatly hindered by this crowded matrix and the high background noise of the biological environment (Eberhardt et al., 2015).

The extracellular matrix (ECM) and tissue scaffolds designed to mimic the native ECM, are critical for the provision of a structural support to surrounding cells and signalling cues for the modulation of diverse processes including cell migration, proliferation and healing activation (Kular et al., 2014). ECM proteins are implicated in cancer and have active participation in tumour progression. In particular, Fibronectin (Fn), a critical ECM protein whose functions are governed by its conformational activity, is receiving increasing attention due to its participation in various phases of tumour proliferation and other complications of medical importance such as Fn Glomerulopathy (Brennan-Fournet et al., 2015; Castelletti et al., 2008; J. P. Wang & Hielscher, 2017).

Moreover, newly emerging diseases demand for their accurate and rapid detection to prevent transmission and allow rapid treatment for diseased individuals. For instance, the COVID-19 pandemic has had a significant impact in the world causing millions of lives. It has emerged as the most consequential global health since the influenza pandemic (Casella et al., 2022). Recent research has presented metallic nanoparticles as a promising tool for the detection of COVID-19 establishing new research pathways for the development of a range of techniques in assisting the prompt response to rising-disease challenges (Iravani, 2020).

## **1.2 Research Question**

Can a versatile label free system for the real-time tracking of proteins, and detection of protein-protein binding interactions within high noise cellular environments be developed using plasmonic nanostructures?

### **1.3 Proposed Solution**

Currently, there are techniques available for protein characterization which are able to detect conformation and structural variations in proteins, however, they need expensive and elaborate instrumentation, extensive data analysis and their signals are generally greatly hindered by the high background noise of cellular environments. Alternatively, noble metal nanoparticles are known to have remarkable optical, catalytic, electronic and magnetic properties, and have been intensely researched for the development of highly sensitive nanobiosensors to investigate a range of molecules and detect their interactions (Jia et al., 2006; Y. Zhang et al., 2014).

This project aims to demonstrate the gold edge-coated triangular silver nanoparticles (AuTSNP) as powerful new tools to signature protein conformational transitions in living cells and monitor essential protein activity. This versatile method has the potential to provide accurate and rapid detection of proteins and lead to better treatments for rising-infection and disease challenges.

### **1.4 Objectives**

The overall aim is to demonstrate the gold edge-coated triangular silver nanoparticles (AuTSNP) as powerful new tools to signature protein conformational transitions within living cells, monitor essential protein activity and sense Antigen-Antibody interactions above high background noise level by:

- 1) Monitoring Fn conformational transitions with plasmonic resonance responsive AuTSNP.
- 2) Validating AuTSNP as highly sensitive tools for protein conformational dynamics detection in high noise cellular environments and in the presence of biomimetic scaffolds.
- 3) Optimising on-scaffold loaded protein conformational monitoring method within the presence of different cell lines.
- 4) Analysing the ability of AuTSNP to detect binding of Antigen-Antibody complexes.
- 5) Demonstrating the sensitivity of AuTSNP to detect Antigen-Antibody interactions within dynamic environments.

**CHAPTER 2.**

**LITERATURE REVIEW**

## 2.1 Introduction

In living systems, molecular species occupy a substantial part of the intracellular medium around 40% of volume (Długosz & Trylska, 2011). This complex environment not only contains water molecules, ions and metabolites, but also other macromolecules such as proteins, nucleic acids and lipids (Ostrowska et al., 2019). In the last decades, experimental methods have been developed to study macromolecules in real time and under *in vivo* conditions (Długosz & Trylska, 2011). However, the high noise levels of the crowded biological environment, such as fluctuations in biochemical reactions, protein variability, molecular diffusion, cell-to-cell contact and pH, influence but also obstruct cellular responses and internal dynamics (Iwamoto et al., 2016). In this high complex environment, experiments that are performed under cellular conditions face significant challenges as cellular crowding increases the opportunities of weak but undesired interactions (Feig et al., 2017).

Noble metal nanoparticles and their remarkable properties have been under intense research for their use in the detection and monitoring of biomolecules. Their high sensitivity has positioned them as a promising alternative for the study of molecules and their interactions within different environments. Particularly, triangular silver nanoparticles (TSNP) possess some of the highest reported sensitivities among metals and have the potential to provide accurate and rapid detection and monitoring of critical biomolecules (Y. Zhang et al., 2014). This to lead in the future to better treatments for disease challenges as well as to enhance tissue repair by monitoring proteins or growth factors loaded onto tissue regeneration scaffolds and their consequent release to assisting the healing processes. Scaffolds provide a fibrous architecture that mimics the native extracellular matrix supporting cell attachment, viability, growth and migration (Abbasi et al., 2020). A promising approach for inducing bone formation includes the delivery of a variety of osteoinductive and vasculogenic growth factors, which success relies on the constant growth factor release (Kuttappan et al., 2018). The proposed technology aims to assist in the monitoring of these released factors to benefit current treatment practices. Moreover it intends to establish a guideline for the development of detection platforms for medically significant molecules.

## 2.2 Tissue Regeneration Scaffolds

Typically in the surgical field, the course of treatment of a damaged tissue (for wound healing, bone and nerve regeneration, among others) consists of performing a tissue transplant from one site to another in the same patient (autograft) or harvesting tissue from a donor (allograft) (Baldwin et al., 2019). However, these techniques have some limitations as they are expensive, painful and there is risk of immunogenic reaction by the patient and bacterial infection (Dhillon et al., 2022; O'Brien, 2011). Alternatively, regenerative medicine is a multidisciplinary science which aims to restore normal function to damaged tissues or organs caused by disease, trauma or injury by constructing biological substitutes that improve tissue function (Atala, 2004; Mao & Mooney, 2015). This intense field includes tissue engineering and integrates self-healing treatment techniques involving biocomposite fabrication using biomaterials which exhibit beneficial biofunctionalities (NIH, 2018). Tissue engineering can assist in the regeneration of impaired tissue integrity by the combination of cells from the body and highly porous scaffold biomaterials, which act as templates for the growth of new tissue (O'Brien, 2011).

The tissue-engineering field aims to use artificial scaffolds to mimic the native extracellular matrix (ECM), which plays a critical role as a framework of tissue. There are two key approaches in this field, first, on these scaffolds, cells can be seeded *in vitro* to adhere and proliferate for the production of tissue foundations for transplantation. Second, scaffolds can operate as vehicles for growth factors incorporation and release as well as drug delivery devices, thus accelerating the recovery process (Howard et al., 2008; Kurokawa et al., 2017). Among the most commonly used materials for tissue regeneration scaffolds fabrication, ceramics, biomaterials, hydrogels, natural polymers and synthetic polymers can be found. Poly-hydroxyl acids such as poly lactic c-co-glycolic acid (PLGA) and PLA have been widely used for tissue regeneration procedures as they are reported to degrade by hydrolysis providing well-regulated drug delivery (Howard et al., 2008). Particularly, in the bone regeneration field, ceramics such as hydroxyapatite and tri-calcium phosphate (TCP) are commonly employed, and can be used in combination with biological materials such as chitosan, a promising biomaterial (O'Brien, 2011; Sulaiman et al., 2013).

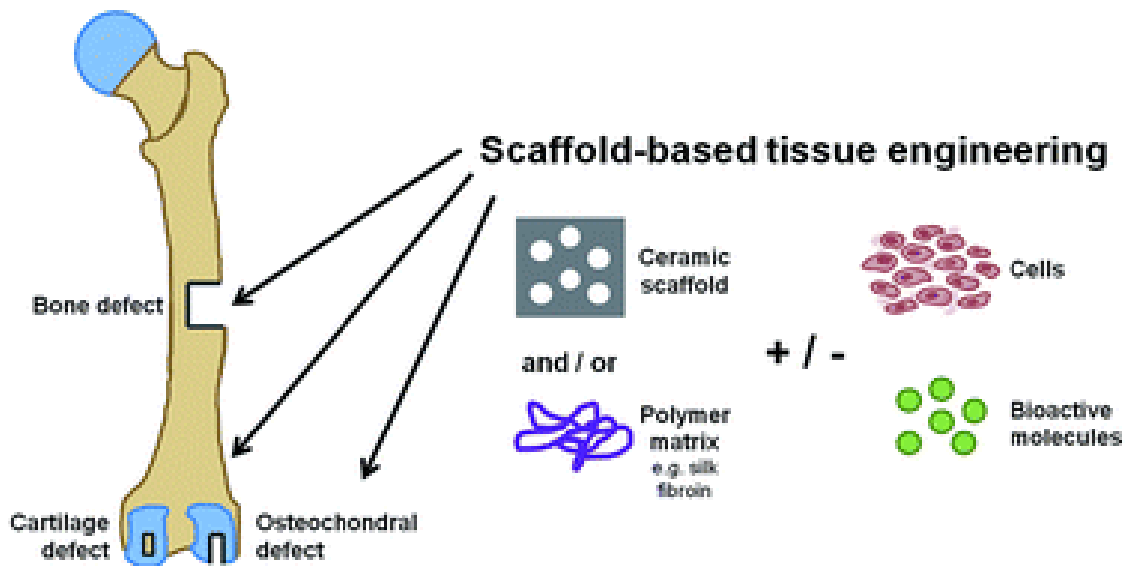


Figure 1. Scaffold-based materials and strategies (Li et al., 2014)

In general terms, the desirable scaffold properties include excellent biocompatibility, biodegradability, bioactivity, architecture (appropriate porosity) and mechanical properties (Turnbull et al., 2018). Examples of tissue engineering of scaffold-based materials to achieve desirable properties are illustrated in Figure 1. Moreover, a biomimetic scaffold that degrades and releases loaded products within a restricted time frame, is crucial for the successful uninterrupted regeneration of cellular architecture (Qasim et al., 2017).

### 2.2.1 Chitosan and Hydroxyapatite Regeneration Scaffolds

Chitosan (Cs), an aminated polysaccharide, is a promising crustacean derivative biomaterial prepared by the deacetylation of chitin and highly abundant in nature (Jiménez-Gómez et al., 2020). It is considered as one of the constituents with the highest rate of production and degradation on the planet (Lizardi-Mendoza et al., 2016). This biomaterial exhibits excellent biodegradability, biomimetic, biocompatibility and antimicrobial properties for tissue engineering applications and the simulation of self-healing matrices and mimetic tissue repair scaffolds (Abdel-Fattah et al., 2007; Adrian Martău et al., 2019). Additionally, it is a hydrophilic material, which stimulates cell adhesion and proliferation, and its degradation remains non-toxic (Levengood & Zhang, 2014). Cs can be easily managed and manufactured in diverse forms such as fibres, sponges, hydrogels, among others, which makes it attractive for regenerative medicine and tissue repair. In these fields, the manufacturing of porous structures is

highly demanded for the production of epithelial and soft tissues (Rodríguez-Vázquez et al., 2015).

Hydroxyapatite (HAp) is an inorganic mineral, a bioactive ceramic present in human bones and teeth representing around 65% to 70% of the bone (Ummul & Salisbury, 2020). This bioceramic is biocompatible, bioactive and thermodynamically stable in biofluids making it a desirable material for a range of applications in biomedicine, where calcium phosphate-based bone replacement constituents are widely used (Gomes et al., 2019; Irsen et al., 2005).

In bone tissue engineering, composites containing natural biopolymers and calcium phosphates, such as chitosan-hydroxyapatite (Cs-HAp), with highly porous microscopic structure for the penetration of cells and the transfer of nutrients and oxygen have been studied, focusing to mimic the fibrous structure of the ECM. These studies have confirmed the osteoconductivity, biodegradation, biocompatibility and the promising mechanical strength of the scaffolds for their orthopaedic use (Escobar-sierra et al., 2015; Gomes et al., 2019).

As an illustration, Qasim et al. (2017) performed in-vivo studies in chinchilla rabbits to monitor the cellular response as well as the degradation profile of porous freeze gelled Cs and Cs-HAp scaffolds after implantation in bone defects (Qasim et al., 2017). In this study, the importance of HAp addition into porous Cs scaffolds is highlighted as results showed greater cellular migration within scaffold as well as their delayed degradation. This emphasised the importance of bone regeneration scaffolds composites that include calcium phosphates, HAp in the reported case, as they improve osteoblast response and biological response to Cs scaffolds, demonstrating the potential of composite scaffolds in tissue-engineering applications in the clinical setting (Levengood & Zhang, 2014).

### **2.2.2 Tissue regeneration hydrogels**

In the last years, hydrogels have received increasing attention as outstanding options for tissue engineering as a result of their similarity to the natural extracellular matrix's structure and composition. Moreover, the capacity to tune the hydrogels surface morphology, shape, size and porosity has facilitated their use for simultaneous seeding of various cells, tissue architecture and vascularization (El-Sherbiny & Yacoub, 2013).



Hydrogels can be constructed to assist in cell migration, proliferation and differentiation. Additionally, these supports allow oxygen and nutrients transport in a vastly hydrated 3D environment that simulates native tissue (Spicer, 2020). Commonly, these 3D structures are composed of hydrophilic polymers held together through covalent bonds or physical intra/inter molecular attractions. They absorb significant amounts of water swelling without dissolving, which results in soft and rubbery consistencies mimicking living tissue (El-Sherbiny & Yacoub, 2013). The primary structural component of hydrogels is based on two parameters including the method of binding the polymer chains within the gel network, and the amount of water expected to be absorbed by the hydrogel (Mantha et al., 2019). A range of natural and synthetic polymers have been used for the development of hydrogels for tissue engineering applications such as development of connective tissue, skin, bone, cartilage, among others (El-Sherbiny & Yacoub, 2013). Hydrogels from natural origins can be classified in protein-based materials (ie. collagen, elastin, fibrin), polysaccharide-based materials (ie. alginate, chitosan, glycosaminoglycans) and those derived from decellularized tissue (Catoira et al., 2019). They are usually formed of ECM components, which presents an advantage since it makes them intrinsically biocompatible, among other advantages such as biodegradability and safety, all of which provide a favourable environment for cell growth, adhesion, regeneration and proliferation (G. Tang et al., 2020). Depending on the desired application, hydrogels can be fabricated through several cross-linking methods including physical, chemical, enzymatic and radiation cross-linking (Z. Ahmad et al., 2022).

### **2.3 Extracellular Matrix and the Extracellular Matrix Protein Fibronectin (Fn)**

The extracellular matrix is a non-cellular element present in all tissues and organs composed of around 300 proteins responsible for the provision of structural support to cells as well as the control of critical cellular functions such as cell differentiation, migration and proliferation (Kular et al., 2014; Yue, 2014). The principal elements of the extracellular matrix include collagen, proteoglycans, laminins and fibronectin (Figure 2). These have subtypes that play different roles in the ECM structure and properties which dictate their functions in the body (Walker & Mojares, 2018).

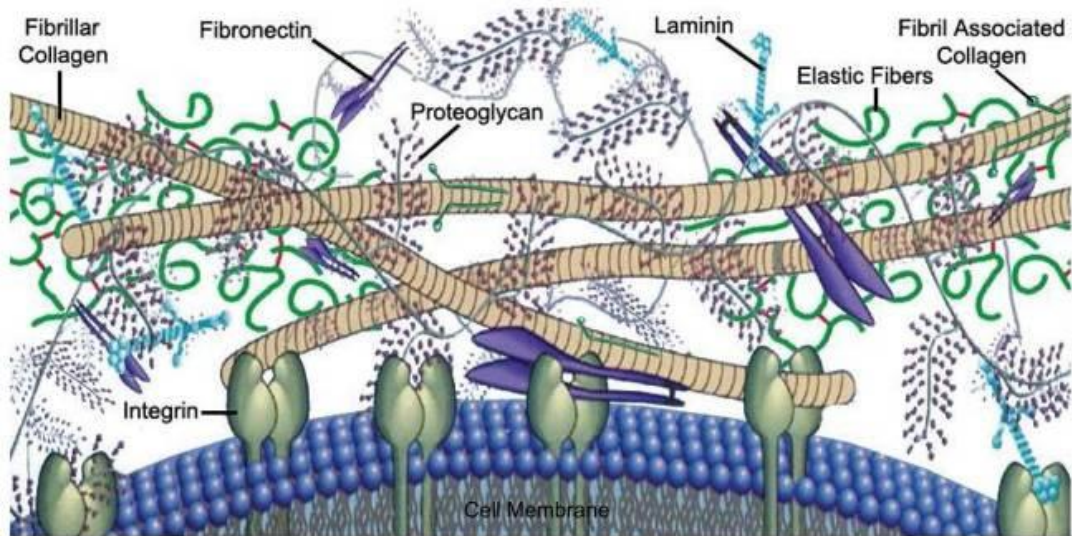


*Figure 2. Representation of ECM composition indicating cellular engagement with ECM biomolecules and primary components of ECM (Aamodt & Grainger, 2017).*

Collagen is the principal component of the ECM and the most abundant structural protein in the human body (Walker & Mojares, 2018), it provides stability and strength for body tissues building nets along cellular structures (Avila Rodríguez et al., 2017). Proteoglycans are glycosylated proteins present in all ECM of connective tissues with the function of providing hydration and swelling pressure of the tissue allowing it to resist compressional forces (Yanagishita, 1993). Other key constituents of the extracellular matrix are laminins, structural components of basement membranes that separate parenchymal cells from the connective tissue. These proteins carry out critical cellular functions by regulating tissue architecture, cell migration, cell adhesion and matrix-mediated signalling (Hamill et al., 2009). Finally, Fibronectin (Fn), which is another critical protein of the extracellular matrix whose functions are controlled by its conformational activity.

Fn is a high molecular weight multidomain glycoprotein of around 250 kDa encoded by FN1 gene that can be found in a fibrous or insoluble form usually in the pericellular space of fibroblasts, and can be synthesized by other cell types such as macrophages and endothelial cells (Conde-Agudelo et al., 2014; National Institutes of Health, 2020a). Fn also exists in a plasmatic or soluble form circulating in the blood stream which is mainly secreted by hepatocytes in the liver (Feist & Hiepe, 2013; Hörmann, 1995; Proctor, 1987).

This protein is a heterodimer consisting of two protein chains of around 230-270 kDa linked by disulphide bonds at the C-terminal end (Henderson et al., 2011) (Figure 3). Fn monomers are composed by subunits called domains or modules; there are 12 FN type I domains, 2 FN type II domains and 15-18 FN type III domains, each of which control different cellular processes (Ohashi et al., 2017). These processes take place in the embryonic development, wound repair, blood clotting and maintenance of normal tissue architecture during adult life (Gee et al., 2008). Fn production is known to increase with age with no associated pathologies, and when in homeostasis, it plays important roles in cell adhesion, growth, migration and differentiation. However, if this ubiquitous protein is under altered conditions, it can promote the activation of signalling pathways that control tumorigenesis, metastasis, fibrosis, among other diseases (Feist & Hiepe, 2013; J. P. Wang & Hielscher, 2017).

As an illustration, it has been reported that Fn has a role in human infective diseases, as it is a target for a variety of microorganisms, mainly bacteria. These microorganisms have binding receptors to Fn, which stimulate attachment to, and infection to host cells (Speziale et al., 2019). Moreover, this glycoprotein plays important roles in the mesangial matrix expansion, associated with diabetic nephropathy and deterioration of renal function (Klemis et al., 2017).

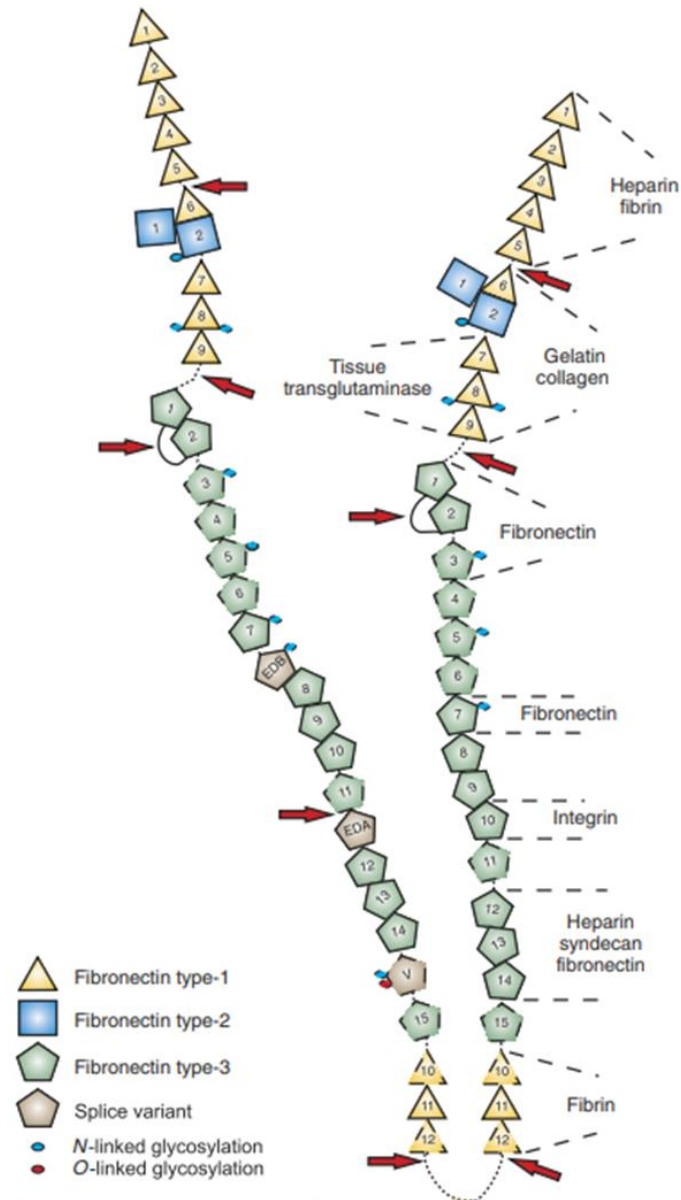


Figure 3. Schematic diagram of the multidomain structure of Fn. Adapted from Henderson et al., 2011.

### 2.3.1 Protein conformational changes and disease

Proteins consist of a specific amino acid sequence which results in the protein being assembled in a certain three-dimensional conformation. This structure possesses moving parts whose mechanical actions are correlated with chemical reactions (Alberts et al., 2002). This correlation between protein conformation and function has been widely analysed for the understanding of biological processes. As proteins are dynamic molecules, they are capable of changing their structure modifying their function and modulating other molecules functions (Moree et al., 2015). Numerous clinical

diagnoses rely on the accurate detection and quantification of proteins or peptides (Bennienn & Daggett, 2002). Variations in protein folding and structure play a critical role in the control of regulatory mechanisms in cells (Brennan-Fournet et al., 2015). When proteins fail to fold into their native 3D structure, several human disorders could develop posing significant challenges to human health (Peng & Alexov, 2017). Some of these diseases have been grouped together under the term Protein Conformational Disorders (PCDs) which include Alzheimer's, transmissible spongiform encephalopathies, type 2 Diabetes mellitus, Huntington disease, Parkinson, among others (Ashraf et al., 2014; Soto, 2001).

Furthermore, among studied pathologies associated with Fn, Glomerulopathy with Fn Deposits (GFND) or Fn glomerulopathy, can be found. This hereditary kidney disease, which usually begins in adulthood, is related to mutations in the FN1 gene causing kidney failure (National Institutes of Health, 2020). These studies have reported an alteration in protein folding caused by the mutation Y973C (replacement of amino acid tyrosine for cysteine in position 973 of FN1 gene). This mutation interposes an additional cysteine in FN domain III<sub>4</sub> altering protein folding due to an abnormal Cys-Cys bond formation, enhancing nonfibrillar aggregation in the renal mesangium and subendothelial space as shown in Figure 4 (Castelletti et al., 2008; Ohashi et al., 2017).

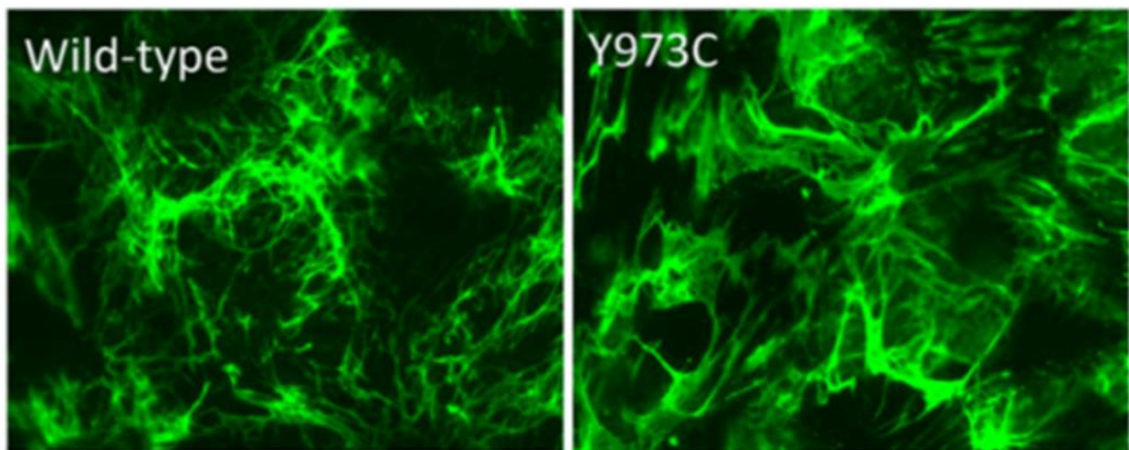


*Figure 4. GFND mutants in vitro study. Mutant Y973C formed more matrix than wild-type FN upon incubation with HEK293 cells (human embryonic kidney). Adapted from Ohashi et al., 2017.*

There are existing techniques for protein characterization able to detect conformations and structural variations in proteins. These techniques include spectroscopic methods such as Raman Spectroscopy, Nuclear Magnetic Resonance, and fluorescent methods

such as Fluorescence Resonance Energy Transfer (FRET) (Brennan-Fournet et al., 2015).

## **2.4 Overview of conventional technological processes and methodologies for molecular activity monitoring and detection within biological environments.**

Spectroscopy is known as the study of the interaction between matter and electromagnetic radiation. Spectroscopic methods are commonly used for the characterization of samples and their qualitative and quantitative analysis (Bumrah & Sharma, 2016). As mentioned before these methods include Raman Spectroscopy, Fluorescence Resonance Energy Transfer (FRET) and Nuclear Magnetic Radiation (NMR), among others.

### **2.4.1 Raman Spectroscopy**

Raman Spectroscopy has become a useful tool for the qualitative and quantitative analysis and characterization of proteins and their secondary structures, as well as the analysis of other complex structures like enzymes, bacteria and viruses, among others (Bunaciu et al., 2015). It uses variations in the frequencies of scattered monochromatic radiations to obtain the information concerning molecular vibrations for elucidating molecule compositions and structures (Ram et al., 2013).

In the past decades, Raman Spectroscopy has been a useful tool in molecular diagnostics due to its ability to characterize a unique signature of a sample at a biochemical level, which can lead to improved treatments and diagnosis of several diseases caused by biochemical changes in tissues and cells (Kong et al., 2015; Martins Ramos et al., 2015). As an example, Liberal de Almeida et al (2016), developed a model by use of Raman spectroscopy to approximate urea and creatinine concentration in human serum (biomarkers of renal function) (de Almeida et al., 2016). Studies where Raman spectroscopy is applied for the differentiation between LDL and HDL cholesterol are also reported, as well as for the differentiation between healthy patients serum and serum of hepatitis C virus infected patients (Rohleder et al., 2004; Saade et al., 2008). A variant of Raman called “Surface-Enhanced Raman spectroscopy” (SERS) technique has also been described where hexagonal silver nanoparticles are used in the sera of patients in a study for the rapid monitoring of gastrointestinal cancer and other benign diseases (Ito et al., 2014).

Moreover, in the last couple of years Raman Spectroscopy was reported as a useful tool in the differentiation of Amyloid  $\beta$ -protein isoforms and conformations. These proteins are known to be involved in the development of Alzheimer's disease. In the study of Yu et al. (2018), they develop a system using SERS coupled with principal component analysis (PCA) which readily distinguishes A $\beta$ 40 and A $\beta$ 42 (Figure 5). Their results showed that the method is able to reveal assembly dependent changes in protein conformation and self-binding. This can assist in the discovery of target sites for drug development and for testing its effects on protein assembly processes (Yu et al., 2018).

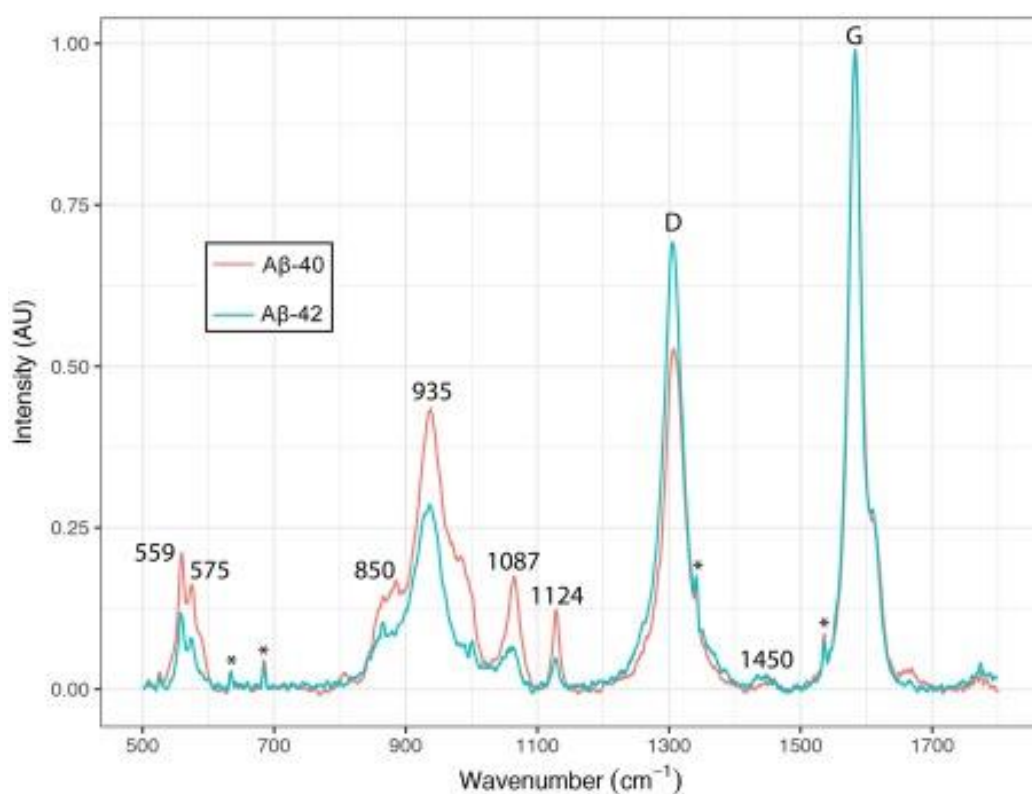


Figure 5. Illustration of a Raman spectrum. SERS spectra of Amyloid  $\beta$ -protein 40 (red) and Amyloid  $\beta$ -protein 42 (turquoise). Adapted from (Yu et al., 2018).

Modifications in molecular conformation and geometry of a sample can produce significant changes in Raman band positions, usually called frequency shifts, which can then be compared to a molecular vibrational frequencies table where sample molecules can be identified as each molecule has a unique frequency (Benevides et al., 2003). Raman Spectroscopy is based on the Raman effect, which is produced through the exchange of energy between incident photons and the vibrational energy levels of the molecule. Raman scattering involves the scattering of laser light onto a sample, with

energy exchanged between the incoming light and the sample. The light scattered by the molecules contains frequencies distinct from the original monochromatic light, representing the molecular vibrational frequencies. When a molecule absorbs radiation, its energy increases proportionally to the photons. This increased energy can manifest in various forms, such as electronic, vibrational, or rotational energy within the molecule. The Raman spectrum is then generated based on the vibrational movements resulting from the change in the molecular dipole moment induced by the light source (Goh et al., 2017) (Figure 6).

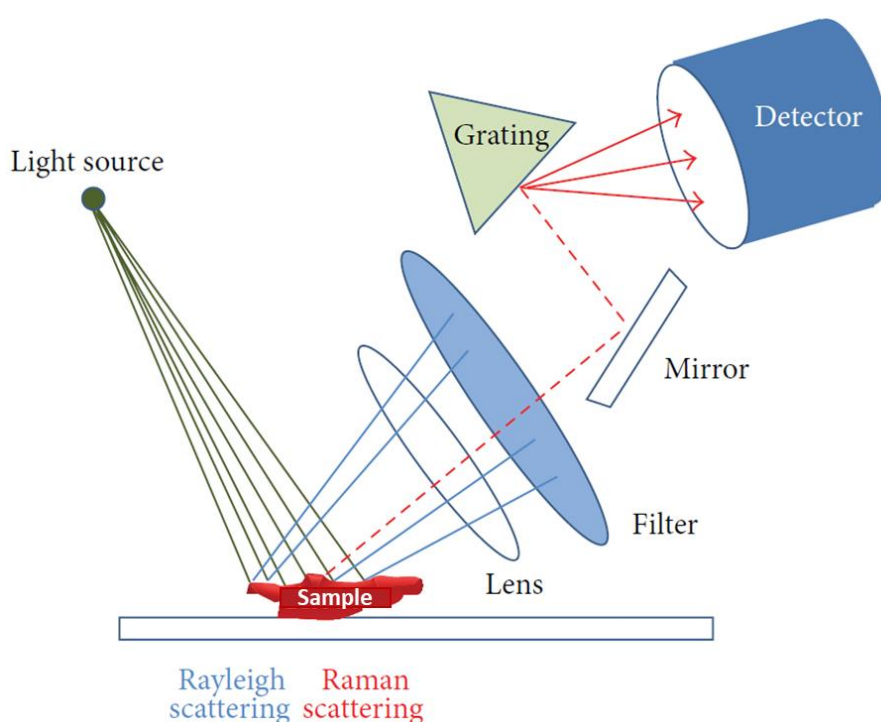


Figure 6. Adapted illustration of Raman Spectroscopy mechanism (Kim, 2015).

Raman is a promising technique for protein characterization, however, there are some limitations in its use including the need of expensive instrumentation and sophisticated data analysis (Eberhardt et al., 2015; Segtnan et al., 2009). Moreover, analyzing samples in complex environments represents a challenge as biomolecules are ubiquitously in all biological systems in different concentrations (Kuhar et al., 2018).



## 2.4.2 Fluorescence Resonance Energy Transfer

Fluorescence Resonance Energy Transfer (FRET) is a fluorescent method for studying molecular interactions inside of cells (Sekar & Periasamy, 2003). This technique allows the calculation of the distance between two fluorochromes (donor and acceptor) when they are between 10-100 Å when FRET occurs after the overlapping of the donor's emission spectrum over the excitation spectrum of the acceptor (Held, 2012; Sekar & Periasamy, 2003; T. Heyduk, 2002).

FRET is usually used to study interactions between molecules (intermolecular) and single molecule FRET (smFRET) technique is used for intramolecular studies. The latter can be used for the study of folding and unfolding of macromolecules as well as their fluctuations and stability (Ha et al., 1999; T. Heyduk, 2002).

FRET has been reported as a clinically relevant tool for diagnostic assays such as immunoassays for the detection of protein cancer biomarkers (i.e. alpha-fetoprotein in testicular cancer, prostate specific antigen, estrogen receptor in breast cancer, etc), protein-protein interactions (i.e. methicillin resistant *S. aureus*, vancomycin resistant *Enterococci*), DNA dynamics among others. It has also been integrated with real-time PCR and other molecular diagnostics techniques for prenatal screening and infectious disease diagnostics (Qiu & Hildebrandt, 2019).

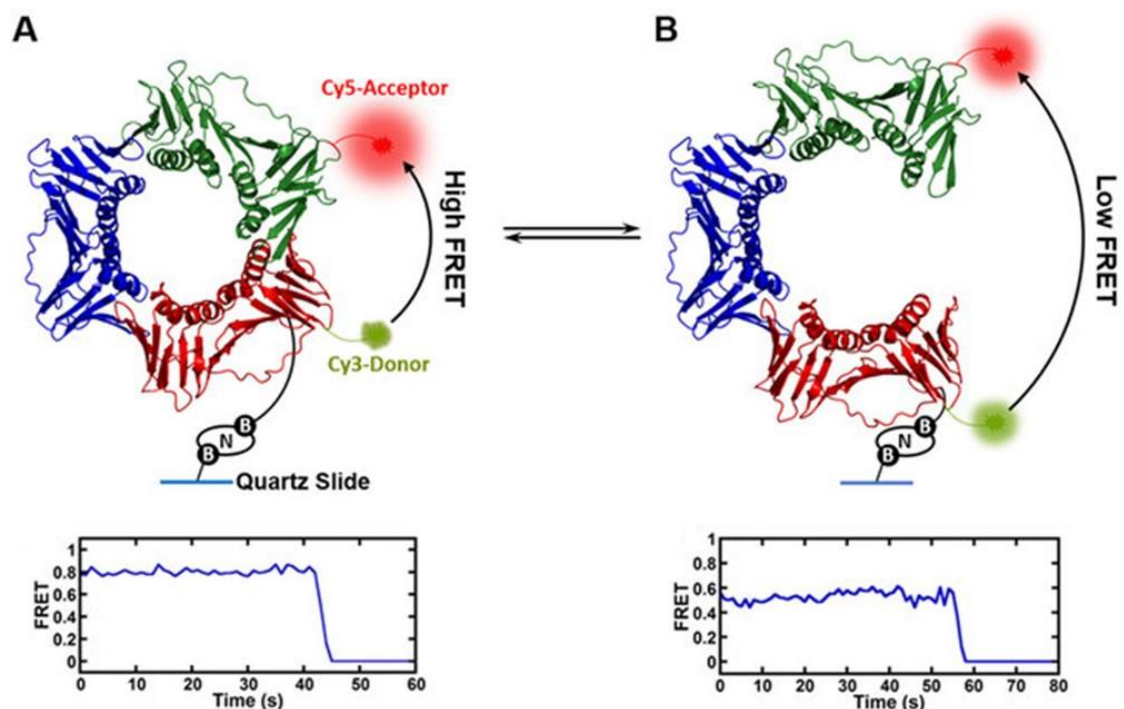


*Figure 7. Single-molecule FRET system for proliferating cell nuclear antigen (PCNA) conformational dynamics. Cy3 fluorescent dye as the donor and Cy5 fluorescent dye as the acceptor were added at the interface of PCNA. This was done to investigate structural modifications linked to the opening and closing of the PCNA ring. A) Ring closed, high FRET signal. B) Ring open, low FRET signal (Gadkari et al., 2018).*

As an illustration, Gadkari et al. (2018) studied the dynamics of a sliding DNA clamp (proliferating cell nuclear antigen, PCNA) by single-molecule FRET as it is involved in DNA replication and repair (crucial mechanisms for cell functioning and proliferation). The results showed high FRET signals when PCNA ring was closed and low signal when the ring opened due to conformational changes as shown in Figure 7. This research presents FRET as a promising technique for studying protein dynamics and DNA interactions (Gadkari et al., 2018).

FRET has also been employed for the study of molecular conformational changes of extracellular matrix proteins which are known to be involved in critical cellular processes. Antia et al. (2009) developed a model using FRET where aging of the extracellular matrix was detected over 72 hours through the formation and stretching of Fn fibrils (Antia et al., 2009).

Moreover, Mizutani et al. (2010) developed a FRET based biosensor to measure BCR-ABL (gene associated with chronic myeloid leukaemia) activity and its reaction to drugs within living cells. This was carried out to develop an efficient method for the assessment of Imatinib drug efficiency in chronic myeloid leukaemia (CML). The technique was carried out by analysing the increased FRET efficiency upon intramolecular binding of CrkL (Crk-like proto-oncogene, adaptor protein), which is a typical substrate of BCR-ABL, to phosphorylated tyrosine. Phosphorylation levels of CrkL have been used as markers of BCR-ABL activity and drug responses This was accomplished by designing a protein in which CrkL was sandwiched between two fluorochromes, Venus (a variant of the yellow fluorescent protein) and enhanced cyan fluorescent protein. In this study, it was necessary to modify the designed protein several times in order to avoid false positives and enhance the FRET signals (Mizutani et al., 2010).

Fluorescent methods for the detection and study of a range of molecules have been widely used over the years. In the last decade they were considered standard for biological assays in both industry and academia. However, when studies are carried out

in the presence of cells and other biological environments, the preparation of samples is extensive in order to minimise non-specific binding of undesired molecules. Nanoparticle-based methods such as local refractive index changes, nanoparticle aggregation, charge transfer interactions, among others, were introduced as promising alternative methods for the sensitive analysis of biomolecules (Stuart et al., 2004).

## **2.5 Nanotechnology properties and applications**

Nanotechnology is an extensive field, which refers to the synthesis and utilization of particles of up to 100 nm in size (Kammakakam, 2021). It is considered to “improve and even revolutionize” technology and industry sectors where progress in the creation of innovative materials with unique properties have been reported (Mobasser & Firoozi, 2016). Nano-research is globally active and the use of the technology has been in increasing demand as it is being used in a variety of products such as cosmetics, sunscreen, fabrics, among other applications as illustrated in Figure 8 (Jordan et al., 2014; Lyddy, 2009). The physical and chemical properties of nanoparticles differ considerably in comparison to their bulk counterparts, as properties are highly dependent on size. For example, magnetization per atom and magnetic anisotropy of nanoparticles could be higher than those of bulk species (Gubin et al., 2005). The surface area of a nanosized material is higher in comparison to the bulk material since their surface-to-volume ratio is higher when the size is smaller (Biener et al., 2009).



silver offer high stability, easy chemical synthesis and tuneable surface functionalisation (Vinci & Rapa, 2019).

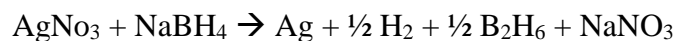
### 2.5.1 Shaped Silver Nanoparticles

Metal nanoparticles are in rising demand due to their remarkable optical, catalytic, electronic and magnetic properties and possible applications (Jia et al., 2006; Kammakakam, 2021). Silver has been widely used throughout history in numerous applications including metalcraft, photography and medicine and is now considered a focal point in nanotechnology (Raza et al., 2016). In modern times, nano-sized silver structures have captured most of the attention due to their properties for the development of novel antimicrobial agents, platforms for detection and diagnosis, coating of medical devices, among others (Burduşel et al., 2018). Numerous aqueous and non-aqueous methods have been reported in the past years for the production of silver nanoparticles with tuneable shape and size (Etacheri et al., 2010). These methods include electron irradiation, laser ablation, biological artificial methods, photochemical methods and microwave processing (Güzel & Gülbahar, 2016). These techniques can be time consuming and they need strict and accurate preparation conditions in order to have homogeneous silver nanoparticles (Z. Zhang et al., 2018).

However, straightforward chemical methods for production of silver nanoparticles have also been reported. Within these methods for synthesis, chemical reduction (as proposed in this thesis) with organic and inorganic agents is the most common approach. Some of the agents used for the reduction of silver ions ( $\text{Ag}^+$ ) are sodium citrate, ascorbate, sodium borohydride, hydrogen, Tollens reagent, N, N-dimethylformamide (DMF), and poly (ethylene glycol)-block copolymers, among others. This reduction results in the formation of metallic silver ( $\text{Ag}^0$ ), which agglomerates and then forms metallic colloidal silver particles, which need to be stabilized with polymeric compounds (poly (vinyl alcohol), poly (vinylpyrrolidone), poly (ethylene glycol), etc) to prevent nanoparticle coalescence (Iravani et al., 2014; Kelly et al., 2012). In this work, triangular silver nanoparticles (TSNP) are synthesized through a seed mediated approach. In the seed silver nanoparticle synthesis, silver nitrate ( $\text{AgNO}_3$ ) is reduced by sodium borohydride ( $\text{NaBH}_4$ ) in the presence of poly (sodium styrenesulphonate) salt as stabilizer. Moreover, the latter has a critical role in the formation of the triangular nanostructures as previous studies reported that its

absence in the process caused inhomogeneous samples with varying shapes and sizes (Aherne et al., 2008).

The reduction of silver in the seed production can be illustrated with the following chemical reaction (Solomon et al., 2007):



It has also been reported that citrate ( $\text{C}_6\text{H}_5\text{Na}_3\text{O}_7$ ) and ascorbic acid ( $\text{C}_6\text{H}_8\text{O}_6$ ) have some influence in the formation of triangular silver nanoparticles as they react with unreacted  $\text{Ag}^+$  ions from the spherical seeds (Etacheri et al., 2010) (Figure 9). After the formation of seed silver nanoparticles, these are then used to mediate the reduction of unreacted silver by ascorbic acid and finally citrate is added to the reaction to stabilize the sample (Figure 10) (Etacheri et al., 2010; Kelly et al., 2012).

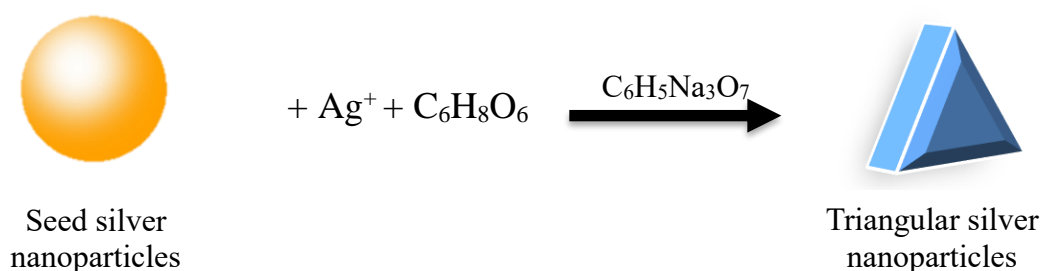


Figure 9. Illustration of TSNP formation. Adapted from (Etacheri et al., 2010).

In biosensing applications, the local surface plasmon resonance (LSPR) of the nanoparticles is used where changes in the position of the LSPR bands are observed. This position depends on the nanoparticles shape, size, uniformity and composition, hence the importance in the homogeneity of nanoparticles in biosensing studies (Loiseau et al., 2019). A varied range of nanostructures with high refractive index sensitivities have been reported to date such as triangular silver nanoplates (TSNP),

edge gold coated silver nanoprisms, nanorice, nanobipyramids, and nanorings (Y. Zhang et al., 2014).

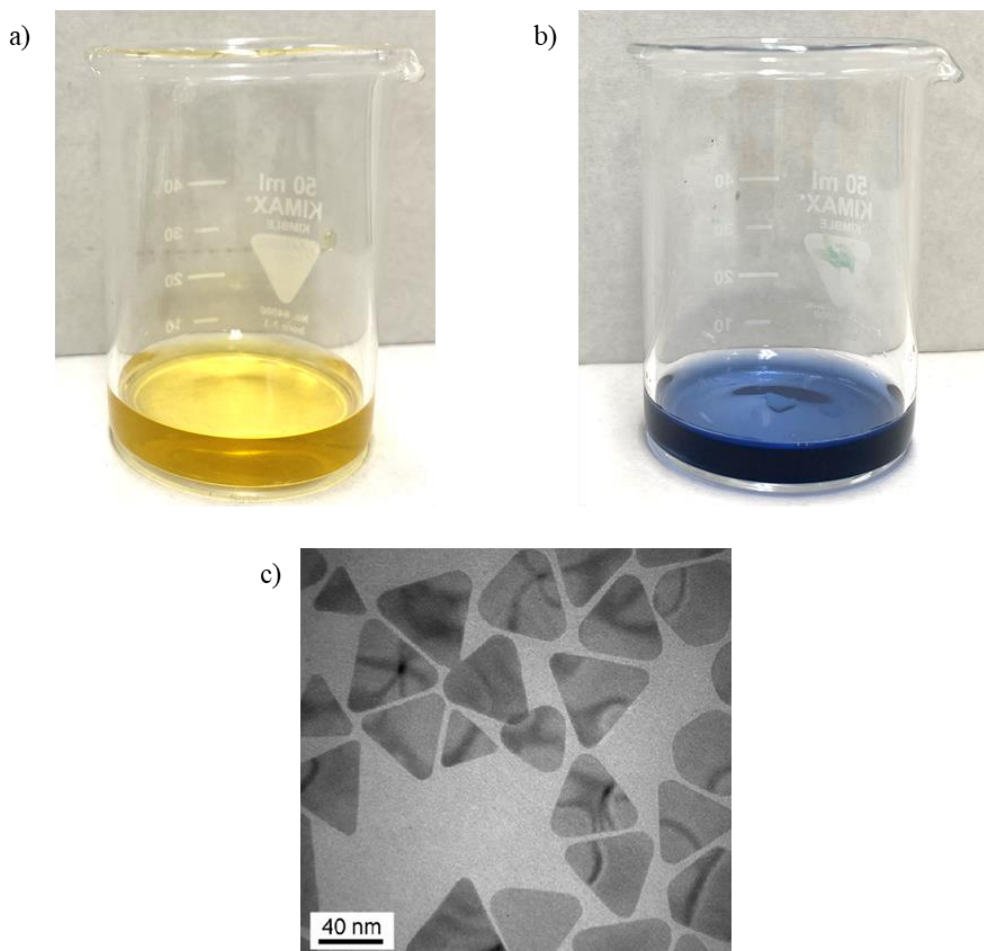


Figure 10. a) Silver seed solution, b) Triangular Silver Nanoplates solution, c) TEM image of TSNP from (Aherne et al., 2008).

Among these diverse nanostructures, TSNP exhibit attractive tunable plasmonic properties due to their sharp corners (J. Ahmad et al., 2019). Their optical profile displays the strongest and sharpest bands among all metals (Petryayeva & Krull, 2011). However, they have been found to be highly unstable in physiological environments (Munehika et al., 2007; Wijaya et al., 2017). Generally, silver nanostructures have been observed to be unstable under physiological conditions due to chloride ions and other anions causing catalytic oxidation (etching) of the surface of the nanoplates. Etching of TSNP can result in corroding of the triangular structure to disc shaped or small spherical nanoparticles, thereby compromising their plasmonic resonance properties (Aherne et al., 2009; Y. Zhang et al., 2014). One approach by Aherne et al. (2009) that has proven to be effective in protecting the silver nanoplates from etching is the presence of a thin gold coating at silver nanostructure edges which also enhances

their LSPR sensitivity (Aherne et al., 2009). In this study, the epitaxial deposition of a thin layer of gold in the triangular nanoplates edges was accomplished demonstrating that at low Ag:Au ratios the nanoplates are successfully edge-coated without any structural damage associated with galvanic replacement and with no major changes in the nanoplates optical properties. This approach not only provides protection against etching by chloride ions but also demonstrates that etching is face-selective and it does not affect the flat {111} faces of the nanoplates. The study also reported the enhanced sensitivity of the gold-edge coated triangular silver nanoplates to changes in the local refractive index which makes them promising tools for the development of refractive-index based biosensors.

## **2.6 Surface Plasmon Resonance (SPR) and Local Surface Plasmon Resonance (LSPR)**

Surface plasmons are electromagnetic waves confined on the surface between a metal-dielectric medium. The excitation of these plasmons by electromagnetic radiation (EM) is known as Surface Plasmon Resonance (SPR). Moreover, Local Surface Plasmon Resonance (LSPR) is an optical phenomenon, which has emerged as a sensitive label-free biosensing technique, which makes use of the sensitivity of these plasmons frequency to changes in local index of refraction at the nanoparticle surface (Unser et al., 2015).

Refractive index is known as the ratio of the speed of light of a specified wavelength in air to its speed in the studied environment medium (Silla et al., 2014). Thus, changes in the environment can be sensed through LSPR wavelength shift measurements as LSPR is sensitive to local dielectric environment variations, hence, LSPR bands exhibit redshifts as the medium refractive index increases (Long & Jing, 2014; Willets & Van Duyne, 2007). This is a powerful tool for optical biosensing applications in a range of areas including biology, biochemistry and medical sciences (Y. Tang et al., 2010). SPR and LSPR based techniques have the potential to be used as portable devices for diagnosis, easy to use point-of-care (POC) device platforms (Mauriz et al., 2019).

For instance, in a study of Vu Nu et al., (2018), tau and phosphorylated tau proteins (neuronal proteins) are detected through an immunoassay in human blood sera by use of a SPR fibre sensor for the early diagnosis of Alzheimer's disease (AD). The study consisted in the immobilization of Tau antibody onto a thiol Self-assembled Monolayer (SAM) followed by the detection of total Tau proteins. The results showed a higher



concentration of phosphorylated tau protein in the blood of AD patients in comparison to the control group patient-samples. Truong and co-workers demonstrated with this study the potential application of SPR devices for POC testing of tau proteins present in human blood (Vu Nu et al., 2018).

Another study by Liyanage et al. (2017) achieved the biosensing of attomolar ( $10^{-18}$  moles per litre) concentrations of a cardiac biomarker, Troponin T (cTnT), in human plasma, serum and urine. This biomarker is of clinical importance as it is involved in the diagnosis of myocardial infarction. In this study they measured the LSPR wavelength shift of anti-cTnT functionalised gold triangular nanoplates (AuTNPs) which is caused by the change in the local refractive index upon cTnT binding. This study demonstrated the potential of LSPR-based nanobiosensors with excellent limit of detection (LOD) for attomolar concentrations (Liyanage et al., 2017).

Furthermore, in a study of K. Wang et al. (2017), an LSPR biosensor that combines Rayleigh scattering spectroscopy with Dark-field Microscopy (DFM) is described for the *in situ* detection and monitoring of telomerase activity in the presence of cancer cells (positive for telomerase) and normal cells. In this study single chain DNA was functionalised on gold nanoparticles and gold satellites which were assembled through DNA specific hybridization. Telomerase activity triggered the coupled nanoparticles disassembly which was observed as an LSPR spectral blueshift along with colour changes in the scattering colour from green (in cancer cells) to orange (in normal cells). Results showed higher activity of telomerase in cancer cells than in normal cells which proposes this method for its application in the monitoring of intracellular telomerase activity and distinction between cancer cells and healthy cells (K. Wang et al., 2017).

LSPR-based nanosensors were also employed in a comprehensive study by Endo et al. (2006) where they developed a multiarray optical nanochip constructed by a core-shell structured nanoparticle layer for screening biomolecular interactions between immunoglobulins (IgA, IgD, IgG, IgM) by antigen-antibody reaction. In this study, antibodies were immobilized onto a multiarray LSPR-based nanochip, and after that, different concentrations of antigen solutions were added to the array. Optical evaluation was carried out by UV-Vis spectroscopy measurements where results showed that the absorbance strength was proportional to the concentration of the applied antigen on the array spot. This highlights the possibility of this method for its application in point-of-

care diagnosis in a label-free, low cost and convenient manner as well as its applications in biomarker research, cancer diagnosis and detection of infectious microorganisms (Endo et al., 2006).

## **2.7 Triangular Silver Nanoplates applications**

As previously mentioned, noble metal nanoparticles have been significantly studied due to their remarkable properties and potential applications based on the LSPR of the nanoparticles. Earlier studies have shown that plasmon frequency is particularly sensitive to nanoparticle properties such as shape, size and dielectric environment. Among the diverse nanostructures with high refractive index sensitivities, TSNP exhibit attractive tunable plasmonic properties due to their sharp corners. These nanoparticle sensors have been employed in two main detection modalities, solution-phase nanoparticle sensing and surface-bound nanoparticle arrays.

### **2.7.1 Solution-phase nanoparticle sensing**

Solution-phase nanoparticle sensing is a straight forward and powerful modality that can efficiently detect molecules of interest. Particularly, it is a useful tool to study biological molecules in aqueous phase as they are homogeneously in phase with the sensitive nanoparticles where their total surface area is exposed to the target molecule. This decreases the need for further sample preparation (Haes et al., 2004; Y. Zhang et al., 2014).

As an illustration, in a previous comprehensive study by Y. Zhang et al. (2014), TSNP were used for the highly sensitive detection of C-reactive protein (hs-CRP). This is an acute phase indicator for infection and inflammation that has been investigated as a diagnostic accessory (Clyne & Olshaker, 1999). In Zhang's studies, TSNP and AuTSNP were functionalised with cytidine 5'-diphosphocholine (PC), which has high affinity for CRP (PC-CRP binding was facilitated by using  $\text{CaCl}_2$  as it is  $\text{Ca}^{2+}$  dependent), and it was used as a receptor agent in a one-step rapid detection of this protein. Human CRP in different concentrations was incubated with TSNP and AuTSNP and UV-Vis measurements were taken after 3 minutes at each concentration. Results showed blue shifts for PC-TSNP due to etching by the chloride ions from  $\text{CaCl}_2$  in comparison to increasing red shifts for AuTSNP for increasing concentrations of CRP. This research presents nanostructure biosensors that are not attached to a substrate

as advantageous tools, as they are homogeneously in phase with the analyte and their total surface area is exposed to the target molecule. It also highlights the potential of the gold edge-coating procedure which not only serves as nanoplates protection but enhances the limit of detection of these TSNP biosensors (Y. Zhang et al., 2014).

Another study by Brennan-Fournet et al. (2015) also used TSNP in a straightforward assay for the detection of CTSB (cathepsin B) in serum, as it is an important disease biomarker which increased levels are known to be involved in cancer. In this study, protein conformational changes of Fn, which was functionalised on TSNP, were analysed to understand its folding/unfolding behaviour when exposed to different pH solutions. This protein was observed to change from compact (at pH 7) to extended formats when exposed to a buffer solution at pH 4. For CTSB studies, cleavage of Fn protein functionalised on TSNP was used as indicator of CTSB presence in human serum. Fn functionalised nanoplates were incubated overnight in serum at pH 4 to guarantee a spectral response to serum proteins, non-specific binding and protein corona formation. Results showed a clear blue shift in the spectra, which indicated the reduced extension of Fn and no significant non-specific binding which showed Fn as a strong inhibitor to non-specific binding and allowing the detection of CTSB activity (Brennan-Fournet et al., 2015).

Moreover, in a study of Q. Cai et al (2022) the development of a colorimetric assay for the detection of chemotherapeutic drug 6-mercaptopurine (6-MP) based on the LSPR of triangular silver nanoplates (TSNP) is reported. TSNP are etched in the presence of chloride ions (Cl<sup>-</sup>) resulting in a change of shape, which is observed as a blueshift on the LSPR spectrum. In the presence of 6-MP there is a protective effect on the nanoplates, hence, there is a reversed shift of the spectrum. In this study there is a linear relationship between the concentration of the drug and the LSPR wavelength shifts, establishing a fast and selective detection method (Q. Cai et al., 2022).

### **2.7.2 Surface-bound nanoparticle arrays**

In contrast to solution-phase nanoparticle biosensing, nanostructuring techniques such as nanoparticle arrays are attractive options due to their low cost and straightforward tunability. The nanoarray behavior can be considerably controlled by varying

nanoparticle size, matrix material and distance between particles (Aliofkhazraei, 2015; Brady et al., 2018).

For instance, the Van Duyne group developed an LSPR biosensor by using nanoparticle-antibody conjugates in a silver nanoprism array (Hall et al., 2011). The method consisted in the enhancement of the LSPR wavelength shift for sensitive detection of low concentration analytes by using gold nanoparticle-labeled antibodies. The Van Duyne group used the biotin-antibiotin pair and demonstrated a nearly 400% enhancement shift of the antibody-analyte binding. The biotin-specific antibodies were incubated with a gold colloidal solution for functionalization and UV-Vis measurements were carried out before and after incubation to verify correct attachment of the anti-biotin to the particles. Silver nanoprism arrays (nanosphere lithography, NSL) functionalized with biotin-terminated ligands were fabricated to facilitate amine-conjugated biotin to attach. Extinction spectrum measurements were carried out prior and after incubation with either nanoparticle-anti-biotin and native anti-biotin to observe the shift difference when nanoparticle plasmonic coupling (silver nanoprisms-gold colloids) occurred. Results showed a 400% enhanced shift of the anti-biotin-nanoparticle conjugate in comparison to the native anti-biotin. This indicates the coupling of the local surface plasmons of the nanoparticle label with the nanoparticle substrate plasmons, which results in LSPR spectrum shifts that add to the refractive index induced shifts. This study demonstrates LSPR sensors as powerful tools for antibody-antigen studies and the versatility of the method to be enhanced when taking advantage of the nanoparticles coupling properties.

LSPR properties of noble metal nanoparticles have been extensively used over the past decades in biological and chemical sensing areas. Selective biosensing of molecules using labeled nanoparticles has been under intense research where outstanding tunable and unique plasmonic properties of silver and gold nanoparticles have been demonstrated (Loiseau et al., 2019). Moreover, LSPR-based techniques can be used together with other methods (dual plasmonic sensing) to enhance optical signals, which makes them an attractive tool for molecule biosensing studies.

## 2.8 Immunoassays

Immunoassays are bioanalytical methods that play important roles in areas such as clinical diagnostics, biopharmaceutical analysis, food testing, and environmental monitoring, among others (Vashist & Luong, 2018). They are based on the quantitation of an analyte through the reaction of an antigen (analyte) and an antibody which is specific to the analyte (Darwish, 2006). The assay reagent antibodies capture the antigen selectively or emit a detection signal. The assays can employ electrochemiluminescent, colorimetric and fluorescent detection methods, among others (Marian & Seghezzi, 2013). The high selectivity of antibodies towards their matching antigens facilitates the recognition of the antigen-antibody system even in complex environments (Rizzo, 2022).

Immunoassays can be classified as homogeneous or heterogeneous depending on the experimental technique followed to perform the assay. Heterogeneous immunoassays (ie. Enzyme-linked Immunosorbent Assay, ELISA), which are most commonly known as sandwich immunoassays or immunometric immunoassays consist in an immobilized antibody onto a solid support which binds to the sample analyte, then a second labelled antibody which recognises another part of the analyte generates the signal (Figure 11) (Rizzo, 2022). An important feature of heterogeneous assays is the need of a washing step before the final analysis; the labelled antibody must be detached from the free label prior to measuring the signal (Dinis-Oliveira, 2014).

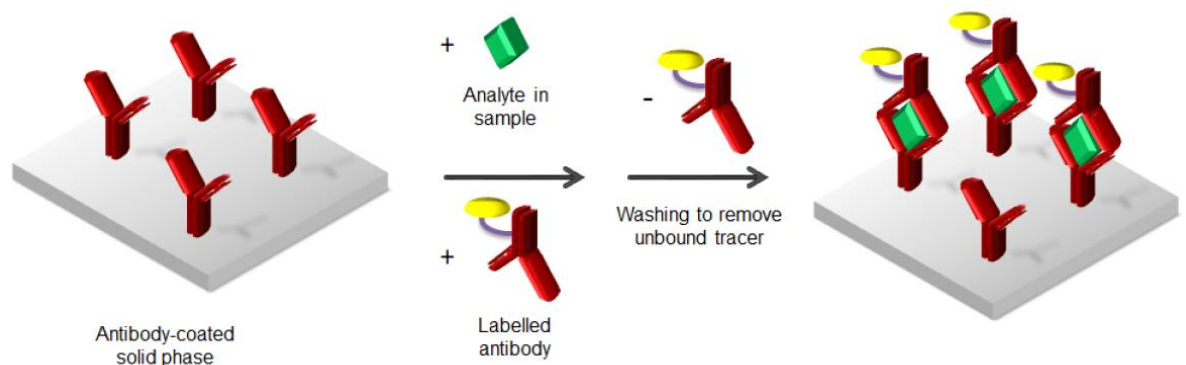


Figure 11. Heterogeneous sandwich immunoassay, (Rizzo, 2022).

In the case of homogeneous immunoassays (ie. Kinetic Interaction of Microparticulates in Solution, KIMS) (Figure 12), the process is simplified when the detection signals are generated without the need of a separation step of the antibody-bound label, however, the use of solvents for extraction of the analytes before the immunoassay is convenient to increase selectivity (Dinis-Oliveira, 2014; Liu et al., 2016).

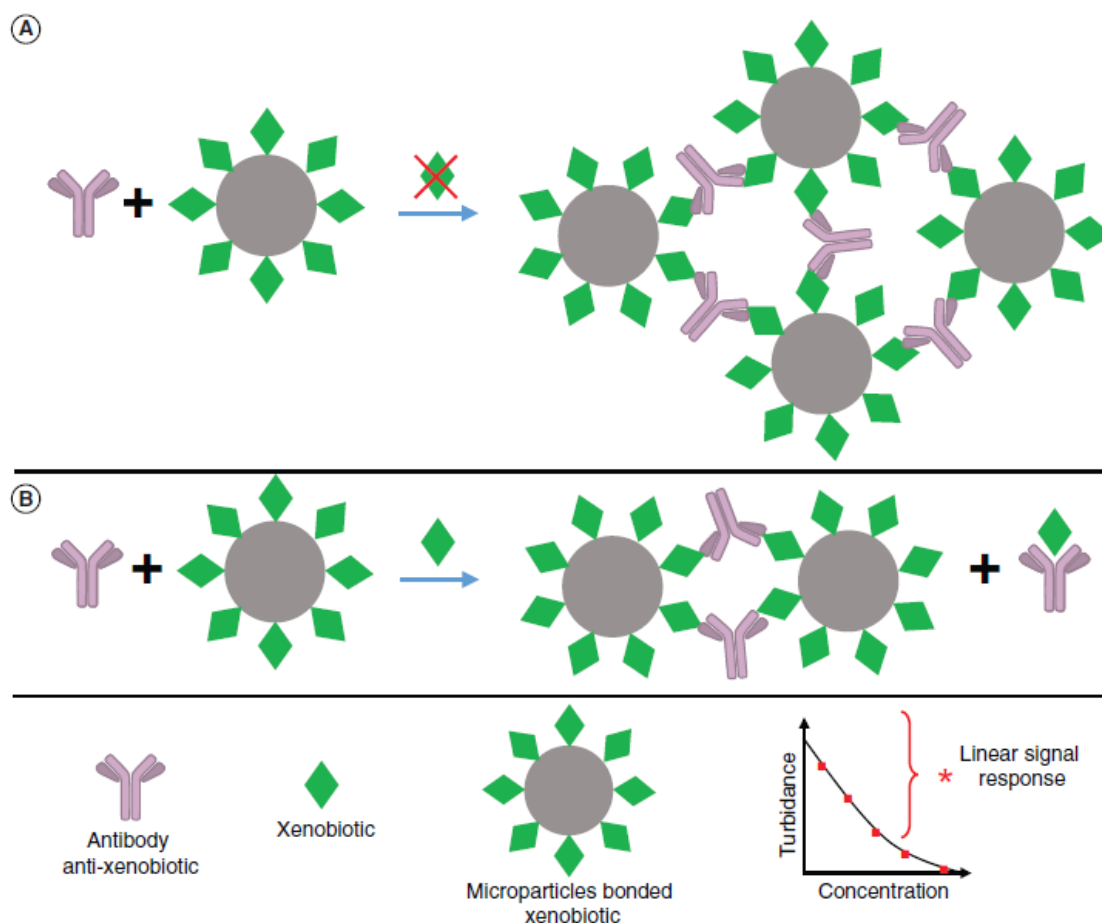


Figure 12. KIMS homogeneous immunoassay example. a) Negative analysis, b) Positive analysis. (Dinis-Oliveira, 2014).

A recent example of the application of immunoassays is in the recent pandemic named by the World Health Organization (WHO) as “COVID-19” which is caused by the severe acute respiratory syndrome coronavirus 2 (SARS-CoV-2)(Cascella et al., 2022; Rizzo, 2022). Its rapid and accurate detection is extremely important to prevent the spread of the infection. The gold standard for the detection of the virus has been the reverse transcription polymerase chain reaction (RT-PCR) which consists in the analysis of the virus RNA present in patient samples (Carter et al., 2020). This has

motivated researchers to find other alternatives for the detection, diagnosis and treatment of this viral threat. Currently, chemiluminescence immunoassays and traditional ELISAs have been approved by the United States Food and Drug Administration (FDA), but some other methods have shown promising results for the detection of COVID-19 and are currently under research (Rizzo, 2022).

Immunoassays are selective and sensitive, however, labelling agents are commonly used to increase sensitivity and catalyse the reaction (Ahmed et al., 2020). Moreover, these methods involve laborious protocols and, in some cases, several days to complete a reaction (Cox et al., 2019). Other limitations could include poor signal stability, and the need for large sample volumes since tests are usually carried out in 96-well format, which requires between 100  $\mu$ L and 200  $\mu$ L of sample, limiting ability to add replicates (PerkinElmer & Inc, n.d.).

## 2.9 Coronavirus Disease 2019 (COVID-19)

Since the influenza pandemic of 1918, **coronavirus disease 2019** (COVID-19) has emerged as the most consequential global health crisis taking more than 6 million lives worldwide (Cascella et al., 2022). It is transmitted through viral particles encapsulated in droplets from saliva or mucus from an infected individual to a healthy individual (Jayaweera et al., 2020). SARS-Cov-2 belongs to the *Coronaviridae* family (subdivided in two subfamilies *Coronavirinae* and *Torovirinae*) and *Nidovirales* order. Within the *Coronavirinae* subfamily there are 4 main subgenera: Alphacoronavirus, Betacoronavirus, Gammacoronavirus and Deltacoronavirus (Harapan et al., 2020). SARS-Cov-2 is a member of the Betacoronavirus genera with two highly infectious viruses, SARS-Cov and MERS-Cov (Middle Eastern respiratory syndrome coronavirus) (Burrell et al., 2017; Harapan et al., 2020).

The positive-stranded RNA (+ssRNA) coronaviruses have a crown-like aspect as shown by electron microscopes (Figure 13). This is due to the spike glycoproteins present in the virus envelope.

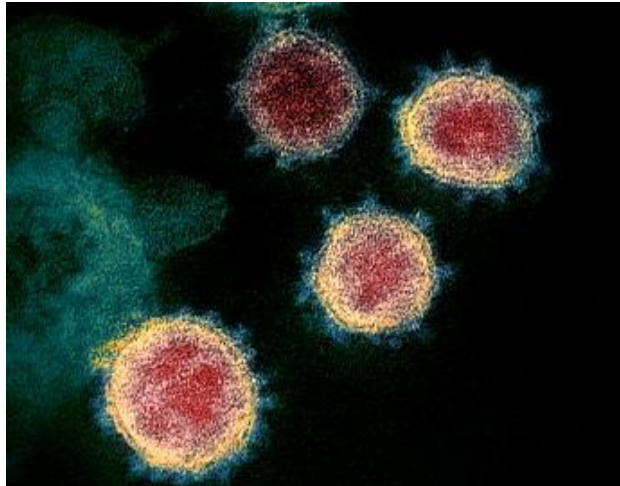


*Figure 13. Transmission Electron Microscopy (TEM) of novel coronavirus SARS-CoV-2 (National Institutes of Health, 2020).*

The coronavirus encodes four proteins in its structure, Nucleocapsid (N) protein (covers viral RNA critical for replication and transcription), Membrane (M) protein (vital role in the coronavirus assembly), Spike (S) protein with S1/S2 subunits (mediates virus-host cell attachment), Envelope (E) protein (virus-host cell interactions) and other several non-structural proteins (nsp) (Boopathi et al., 2020). The mechanism of infection of SARS-Cov-2 consists in the interaction between a cell surface receptor ACE-2 (angiotensin-converting enzyme-2) and the receptor binding domain (RBD) of the S protein. The virus entry into the host human cell takes place after the fusion of the S protein to the cell membrane mediated by its cleavage by host cell proteases (serine proteases, transmembrane serine protease 2, cathepsin B or L), and furin present in the cell membrane (Figure 14) (Kumar et al., 2021).



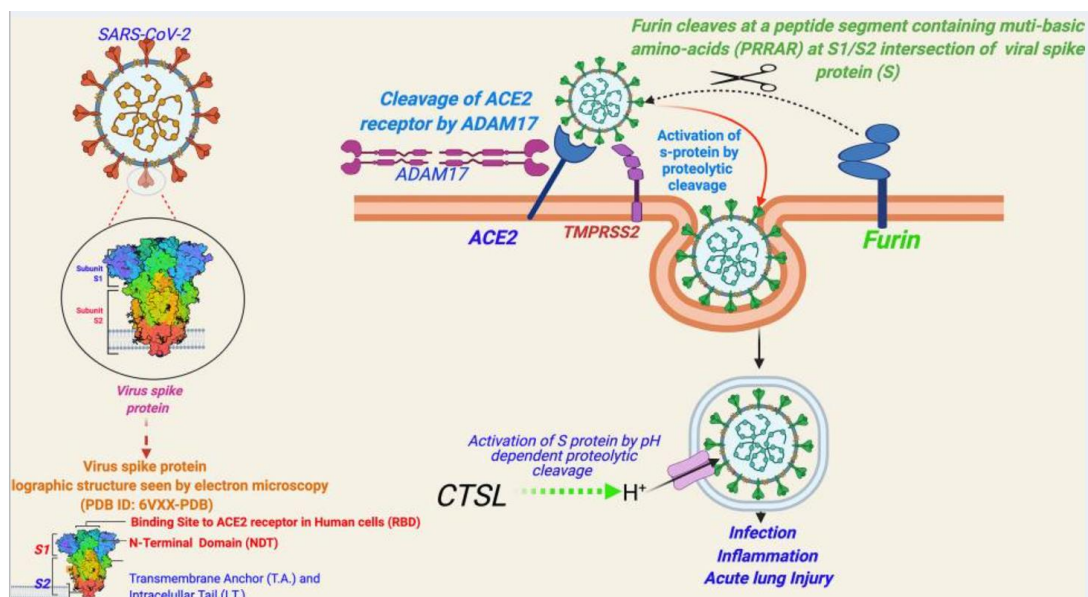


Figure 14. Illustration of SARS-CoV-2 mechanism of infection (Kumar et al., 2021).

To date, the gold standard for the detection of the virus has been the reverse transcription polymerase chain reaction (RT-PCR) which consists in the analysis of the virus RNA present in patient samples (Carter et al., 2020). Nonetheless, this technique is complex, time-consuming and labour intensive, thus, improved techniques for faster and easier detection must be sought after (Iravani, 2020; Teymouri et al., 2021). In recent research, the potential of metallic nanoparticles for the detection of COVID-19 has been presented, for instance, colourimetric assays with gold nanoparticles and LSPR based techniques with gold nanospikes for the detection of nucleic acids and antibodies, respectively (Iravani, 2020).

In a study developed by Moitra et al. (2020), naked-eye detection of SARS-CoV-2 is achieved through a colorimetric assay using gold nanoparticles (AuNPs) functionalised with thiol-modified antisense oligonucleotides (ASOs), which are specific for the N-gene, the nucleocapsid phosphoprotein of SARS-CoV-2. Upon collection of a COVID positive sample, the thiolated ASO-functionalised AuNPs agglomerate as a consequence of the target RNA sequence present in the sample. This causes an alteration in its SPR which is further enhanced by the addition of Ribonuclease H (RNaseH) responsible for RNA cleavage, leading to visible precipitation of AuNPs (Moitra et al., 2020).

Moreover, metallic nanoparticles have also been used for the detection of COVID-19 through an optofluidic platform with gold nanospikes constructed by electrodeposition. Funari et al. (2020) detected the presence of SARS-CoV-2 antibodies specific to the spike protein in human plasma. Results are interpreted through changes in the LSPR of the gold nanospikes upon antigen-antibody (Ag-Ab) binding. In this study low LOD was achieved which falls under the clinical relevant concentration range (Funari et al., 2020) .

In recent years, several other nanoparticle-based biosensors for the detection of coronavirus have been developed such as gold NPs, Lanthanide doped polystyrene NPs, graphene, quantum dots, among others. These biosensors use LSPR principles and plasmonic effect-based colorimetry. This presents the nanobiosensors as advantageous options for the detection of viral infections in contrast to conventional testing methods. (Naikoo et al., 2022).

**CHAPTER 3.**  
**INSTRUMENTATION**  
**AND METHODOLOGY**

### **3.1 Materials for TSNP production, protection and functionalisation**

Silver nitrate  $\geq 99.9\%$  (204390-1G), trisodium citrate  $\geq 99.0\%$  (S4641-25G), poly (4-styrene sulfonate sodium salt) (434574-5G), L-Ascorbic acid  $\geq 99.0\%$  (A92902-100G), chloroauric acid  $\geq 99.9\%$  (520918-1G), sodium borohydride  $\geq 99.0\%$  (213462-25G), disodium phosphate buffer (30414-500G)  $\geq 99.9-101\%$ , sodium phosphate monobasic monohydrate (71507-1KG), fibronectin bovine plasma (F4759-1G), polyethylene glycol 20000 (8.17018), sucrose (84097-1KG) were obtained from Sigma Aldrich. The pump used in the nanoplates' synthesis was Syrris FRX pump, and the UV plate reader used was Biotek Synergy HT Microplate Reader from Biotek Instruments.

#### **3.1.1 Materials for scaffold preparation, protein monitoring and detection**

Chitosan high MW (419419-50G), hydroxyapatite (04238-1KG), water for HPLC (270733-2.5L), C2C12 myoblast cell line (91031101-1VL), Dulbecco's Modified Eagle's Medium (D1145-500ML), trypsin-EDTA Solution 1X (59428C-500ML), Fetal Bovine Serum (F7524-500ML), Horse Serum donor herd (H1270-500ML), penicillin-streptomycin (P4333-20ML) and L-glutamine solution (G7513-20ML), Anti-FN antibody (AV41490-100UL), were obtained from Sigma Aldrich. MC3T3-E1 pre-osteoblast cell line (CRL-2593) was obtained from ATCC, Gibco Alpha Minimum Essential Medium (41061029), Invitrogen SARS-CoV-2 Spike Protein (RBD) Polyclonal Antibody (PA5-114451, 0.5-1 mg/mL) and Invitrogen SARS-CoV-2 Nucleocapsid/Spike Protein (RBD) Recombinant Protein (RP87706) were obtained from ThermoFisher. Sodium bicarbonate 99.5% was obtained from Acros Organics (Fisher Scientific UK Ltd., Loughborough, United Kingdom), poly(ethylene glycol) 600 dimethacrylate (02364-100) was obtained from Polysciences Inc, benzophenone, 99% (A10739.30) was obtained from Alfa Aesar. Human TJP1 recombinant protein (APrEST83050, 0.5-1 mg/mL) and human-specific AntiTJP1 antibody (HPA001636, 0.5-1 mg/mL) were obtained from AtlasAntibodies. The UV curing system used was Dr. Gröbel UV-Electronic GmbH; cellular images were captured with an inverted light-microscope Olympus CKX41 from Olympus Life Science with a 3.0 MP camera attachment. Pulsed UV equipment used for scaffold sterilization was Samtech Pulsed UV system (Samtech Model PUV-01). Zetasizer Pro was obtained from Malvern Panalytical Ltd.

### 3.2 Ultraviolet-visible spectroscopy (UV-Vis)

The main tool used for the study of noble metal nanoparticles and their optical properties is the ultraviolet-visible spectroscopy. These nanoparticles both absorb and scatter light, which results in an extinction spectrum, known as the sum of absorption and scattering. In this project, the spectrometer used for the study of TSNP is Biotek Synergy HT Microplate Reader from Biotek Instruments. This equipment offers different detection technologies such as absorbance measurement, fluorescence and luminescence. For the purpose of this study, absorbance will be described.

UV-Vis spectroscopy is based on absorption spectroscopy where UV visible light is absorbed by a sample as it passes through the well (Pentassuglia et al., 2018). The molecule of interest will have an influence in the quantity of light absorbed (Jones et al., 2004). Absorbance ( $A$ ) or optical density (OD) follows the Lambert-Beer Law (Rafferty, 2019),

$$A = \varepsilon cl$$

Where,

$\varepsilon$ : Molar extinction coefficient (constant for a given chemical under particular conditions)

$c$ : Concentration of the solution

$l$ : Path length in cm

This establishes that the optical density of a sample is proportional to the constant path length and the concentration of the absorbing species (Ball, 2006) (Figure 15).

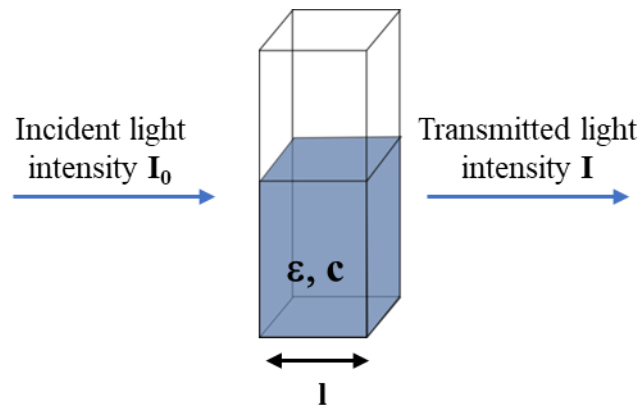


Figure 15. Schematic diagram of Lambert-Beer Law

### 3.3 Surface Plasmon Resonance (SPR)

Surface plasmons are electromagnetic waves confined on the surface between a metal-dielectric medium. The excitation of these plasmons by electromagnetic radiation (EM) is known as Surface Plasmon Resonance (SPR). These plasmons propagate on  $x$  and  $y$  directions between the metal and the dielectric medium for distances on the order of tens to hundreds of microns with decay lengths in the  $z$  direction on the order of 200 nm (Willems & Van Duyne, 2007; Zamarreño et al., 2014) (Figure 16). Commonly, plasmon-resonance condition shifts can be detected through three approaches: SPR imaging, SPR wavelength shift and SPR angle shift. The first method involves light at constant wavelength and constant incident angle mapping the reflectivity of the studied surface as a function of position, the second and third approaches analyse the reflectivity of light as a function of either wavelength/angle of incidence at constant angle of incidence/wavelength respectively (Brockman et al., 2000; Willems & Van Duyne, 2007).

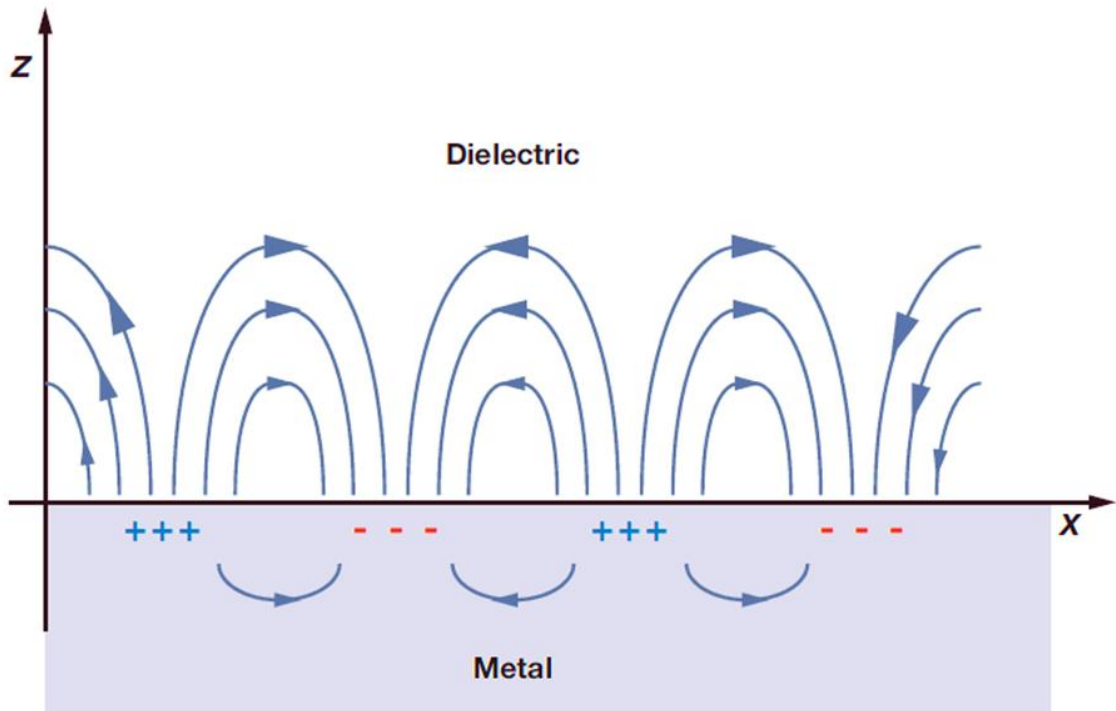


Figure 16. Adaptation of a schematic diagram of SP propagation (Willets & Van Duyne, 2007).

### 3.4 Local Surface Plasmon Resonance

Optical properties of noble metal nanostructures are ruled by their unique Local Surface Plasmon Resonance (LSPR), which refers to the collective oscillation of electrons around nanoparticles and their interaction with incident light of a certain wavelength (Ding & Chen, 2016; Kelly et al., 2012). These nanoparticles are much smaller than the incident light (Willets & Van Duyne, 2007). The plasmon resonance takes place when the oscillation frequency of photons and electrons is matched (Long & Jing, 2014). This collective oscillation is maximized at the resonance wavelength, which takes place at the visible light spectrum for noble metal nanoparticles (Hong et al., 2012) (Figure 17). Silver and gold are commonly used noble metals for nanoparticle production due to their energy levels of d-d transitions, which exhibit LSPR in the visible range of the spectrum (Petryayeva & Krull, 2011).

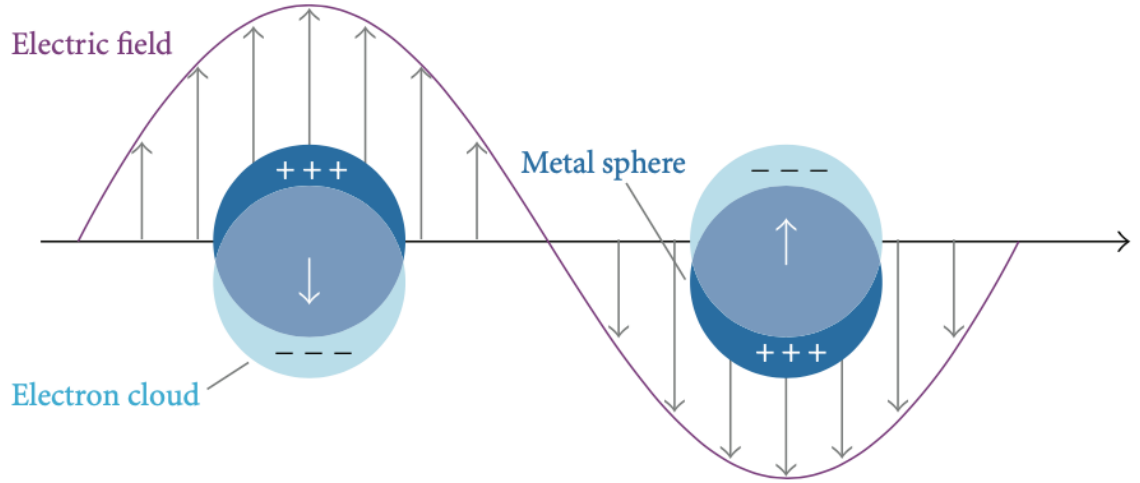


Figure 17. Local Surface Plasmon Resonance phenomenon (Hong et al., 2012).

Optical properties of nanoparticles can be illustrated through Gustav Mie's solution to Maxwell's equations (Modified Long Wavelength Approximation MLWA)(Unser et al., 2015; Willets & Van Duyne, 2007) which is used to describe the extinction spectra ( $C_{ext}$ ) of a given nanoparticle:

$$C_{ext} = \frac{24\pi^2 R^3 \varepsilon_m^{\frac{3}{2}} N}{\lambda \ln(10)} \frac{\varepsilon_i}{(\varepsilon_r + X\varepsilon_m)^2 + \varepsilon_i^2}$$

Where,

$R$ : Radius of the nanoparticle.

$\lambda$ : Wavelength of the incident light.

$\varepsilon_m$ : Dielectric constant of the surrounding environment.

$\varepsilon_r$  and  $\varepsilon_i$  : Real and imaginary dielectric constants of the bulk metal, respectively.

$N$ : Electron density (number of nanoparticles).

$X$ : Shape of the particle ( $X=2$  for the case of a sphere).

As shown above, LSPR oscillations are intensely dependent upon particle properties like shape, size, and dielectric constant as well as the dielectric constant of the surrounding environment (Kelly et al., 2012). However, Mie's theory only offers



solution for spherical and shell geometries, hence, approximation for all other shapes must be carried out. Researchers have developed supplementary methods for these calculations including discrete dipole approximation (DDA) and the finite difference time domain method (FDTD); in both of these numerical methods the analysed particle is represented as  $N$  polarizable components which can interact with the electric field delivered (Wiley et al., 2006; Willets & Van Duyne, 2007). There is a range of nanoparticles including nanodiscs, nanoprisms, nanospheres, among others, which exhibit sensitive detection of LSPR signals, nevertheless, among these variants, non-spherical low-symmetry nanoparticles offer a higher sensitivity to refractive index changes (Hong et al., 2012).

In a comprehensive study by Wiley and co-workers, DDA calculations for different silver nanostructures were carried out to illustrate how geometry is related to nanostructure optical properties. In this study, it was demonstrated that nanostructures with sharp corners show greater red-shift peaks than of spherical nanoparticles due to the accumulation of charges at the corners. The increase in the separation of charges (surface polarization) when segregated into the corners results in the reduction of the restoring force for electron oscillation, which can then be observed as a red shift of the resonance peak (Aizpurua et al., 2005). The researchers also compared different anisotropic 2D nanostructures which showed increased surface polarization along their long axis displaying more red-shifted peaks in comparison to isotropic nanostructures (Wiley et al., 2006).

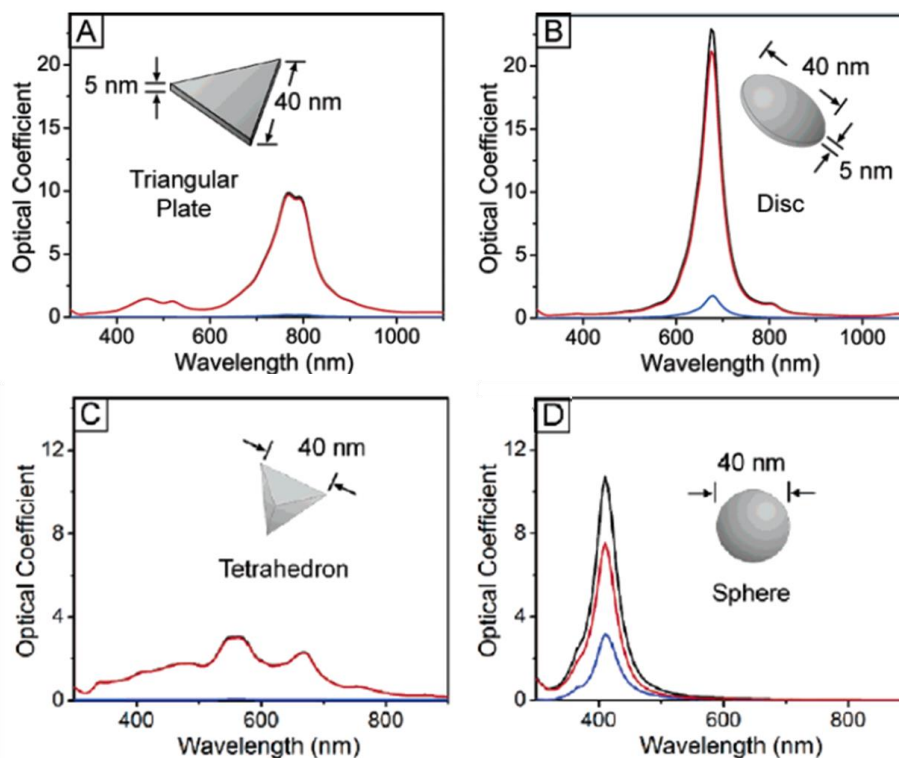


Figure 18. Adapted scheme of DDA calculated extinction (black line), absorption (red line) and scattering (blue line) of different silver nanoparticle geometries (Wiley et al., 2006).

Figure 18 illustrates the difference in the UV-Vis spectra of different anisotropic and isotropic nanostructures where it can be observed that the less symmetrical nanostructures show more red-shifted peaks than that of the mirror symmetry structures. However, in figures 18B and 18D, the resonance peaks are more intense, which is due to the increased dipole moment when the circular symmetry absorbs and scatters light more intensely (Aizpurua et al., 2005; Wiley et al., 2006)

In this project, triangular silver nanoplates were prepared and their remarkable optical properties studied and described, as less symmetrical nanostructures have shown to have increased sensitivity to changes in the local refractive index. All LSPR recordings were carried out using 96-well plates with the Biotek Synergy HT microplate reader. The microplate reader was adjusted for absorbance measurements from wavelengths 300-900 nm in 1 nm increments.

### 3.4.1 Local Surface Plasmon Resonance Challenges

As mentioned in the previous sections, Local Surface Plasmon Resonance has developed as a strong alternative for label-free biosensing applications. This technique

employs the sensitivity of metal nanoparticles' surface plasmons to the changes in the refractive index of the medium in which they are immersed. Noble metal nanoparticles have been under intense research due to their remarkable properties and their growing advantages in biosensing methods, however, several challenges have been experienced through research when using LSPR technique (Unser et al., 2015). These challenges include improving the limit of detection and selectivity in a complex solution, among others.

LSPR technique is highly sensitive, however, when it comes to the study of small molecules, large amounts of sample are required to cover the particles surface to enhance detection. The first strategy to deal with the limit of detection challenge involves the "sandwich" detection of samples consisting of primary antibody-antigen-secondary antibody conjugate. In this method the primary antibody captures the target sample while the secondary antibody increases the molecular mass of the target improving the limit of detection (Guo et al., 2015). Another strategy is by enzymatic amplification where there is an enhanced response caused by by-products of chemical reactions. This method utilizes the primary antibody-antigen-secondary antibody format where the secondary antibody has a molecule attached that reacts with the target molecule, resulting in the precipitation of a by-product that amplifies the LSPR signal (Lee et al., 2011; Unser et al., 2015).

LSPR sensing method is excellent when employed without interfering elements, however, when analyzing a sample in complex solutions (e.g. blood), results could present false significant red shifts. These due to non-specific bindings as a result of other proteins and macromolecules in the media surrounding the analyte which may bind to the nanoparticles causing inaccurate results (Chen et al., 2010; Unser et al., 2015). One of the reported approaches to improving the selectivity is through functionalization layers, in this case, the selectivity will be determined from the functionalization layer

on the surface of the nanoparticles (Unser et al., 2015).

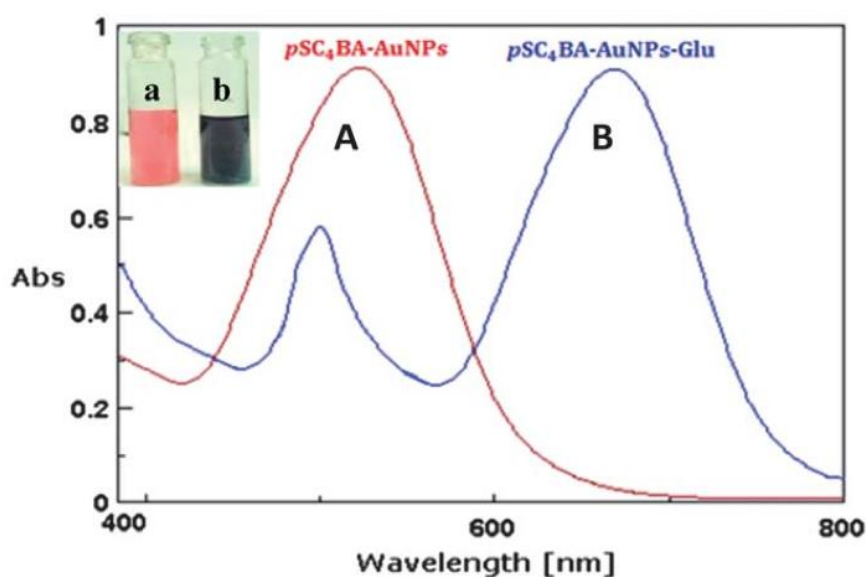


Figure 19. UV-Vis spectra of AuNPs (A) without D-glucose (B) AuNPs with 25 nM D-glucose concentration. Presence of D-glucose in the sample caused a colour change which resulted in a redshift of the spectrum. Adapted from (Pandya et al., 2013)

As an illustration, in a previous study of (Pandya et al., 2013), colorimetric detection of glucose in human blood serum is carried out through a non-enzymatic approach where receptor calix[4]arene/phenyl boronic acid (CX-PBA) functionalized AuNPs recognized glucose. This sensitive colorimetric detection assay involved the aggregation of AuNPs when there was presence of D-glucose, and a colour change from wine red to blue was reported resulting in a red shift of the LSPR spectra as illustrated in Figure 19 (Pandya et al., 2013).

### 3.5 Triangular Silver Nanoplate Seeds production

Triangular Silver Nanoplates were prepared by a seed mediated approach where silver nitrate is reduced by sodium borohydride, and a further reduction of silver ions is mediated by ascorbic acid (Aherne et al., 2009). Seeds were prepared in a beaker on a magnetic stirrer continuously at 700 rpm. 4.5 mL of ultrapure water were added to the beaker followed by the addition of 500  $\mu\text{L}$  of trisodium citrate (TSC) 25 mM as particle stabilizer, 250  $\mu\text{L}$  of poly (4-styrene sulfonate sodium salt) (PSSS) 500  $\text{mgL}^{-1}$  as a shape-directing agent and 300  $\mu\text{L}$  of sodium borohydride ( $\text{NaBH}_4$ ) 10mM (Aherne et al., 2008). Subsequently, 5 mL of silver nitrate ( $\text{AgNO}_3$ ) 0.5 mM were added with a

pump at a rate of  $2 \text{ mL min}^{-1}$  close to the centre of the vortex. Seeds were then left to grow on the bench for at least 4 h before starting with the TSNP synthesis.

### **3.5.1 Optimization of Triangular Silver Nanoplates preparation**

In first experiments Aherne's protocol was followed by adding 5 mL of ultrapure water to a beaker in continuous stirring at 700 rpm, followed by the addition of 75  $\mu\text{L}$  of ascorbic acid (L-AA) 10mM as reducing agent, 200  $\mu\text{L}$  of the seeds solution, 3 mL of  $\text{AgNO}_3$  0.5 mM at a pump rate of  $1 \text{ mL min}^{-1}$ , and finally 500  $\mu\text{L}$  of TSC 25 mM (Kelly et al., 2012). The final volume was then brought to 10 mL with ultrapure water leaving a concentration of silver of 16.692 ppm in the solution. This protocol showed results of broad localised surface plasmon resonances (LSPR).

In the modified method, 4 ml of ultrapure water were added to a beaker in continuous stirring at 700 rpm, 75  $\mu\text{L}$  of L-AA were added subsequently, followed by the addition of 350  $\mu\text{L}$  of seeds solution, 3 ml of  $\text{AgNO}_3$  at a pump rate of  $1 \text{ mL min}^{-1}$  (Syrris FRX pump) and finally 350  $\mu\text{L}$  of TSC. No further solutions were added in this method leaving a final total volume of 7.775 mL leaving a higher concentration of silver of 21.962 ppm in the solution.

The size of the TSNP can be changed by adjusting the volume of the seeds added to the reaction (D. Charles et al., 2010). A small amount of seeds results in bigger TSNP and big amount of seeds results in smaller TSNP (Y. Zhang et al., 2014).

### **3.5.2 TSNP gold edge-coating method for protection and functionalisation**

Upon TSNP preparation, the gold coating procedure was executed where different amounts of Chloroauric acid ( $\text{HAuCl}_4$ ) were added to 1 ml TSNP solution aliquots (0.4071 ml of silver in the aliquot) together with 18.9  $\mu\text{L}$  of L-AA. The respective amounts of gold, in this case, 0  $\mu\text{L}$ , 3.8  $\mu\text{L}$ , 7.6  $\mu\text{L}$ , 18.9  $\mu\text{L}$ , 20  $\mu\text{L}$ , 26.5  $\mu\text{L}$  and 37.8  $\mu\text{L}$  were slowly added dropwise with a micropipette to the TSNP aliquot following Table 1 where silver:gold ratios per aliquot are indicated. Then, stability test was carried out to verify the least amount of gold needed for a successful gold flashing of the nanoplates.

Table 1. Ag:Au ratio volumes per TSNP aliquot

<b>Ratio Ag:Au</b>	<b>Au volume (<math>\mu</math>L)</b>
1:0	0
1:0.009	3.8
1:0.019	7.6
1:0.046	18.9
1:0.049	20
1:0.060	26.5
1:0.928	37.8

### 3.5.3 Stability and sensitivity test

To test the success of the gold coating procedure, 100  $\mu$ L of AuTSNP solution were exposed to 100  $\mu$ L of 20 mM sodium chloride (NaCl) solution (1:1 ratio) in an Eppendorf tube. This was measured using the Biotek Synergy HT microplate reader to observe any changes in the LSPR spectra. The microplate reader was adjusted for absorbance measurements from wavelengths 300-900 nm in 1 nm increments.

Following the gold coating of the nanoplates, their LSPR sensitivity to variation in the refractive index was carried out by the sucrose method. AuTSNPs were suspended in a 1:1 ratio to different concentrations of sucrose solutions (10%-50% (w/v)) prepared as illustrated in Table 2, and measured using a microplate reader. The corresponding refractive index for each sucrose solution according to the Brix scale is stated in Table 2 (Featherstone, 2015).

Table 2. Sucrose solutions and concentrations

<b>Sucrose (g)</b>	<b>Water (mL)</b>	<b>Concentration</b>	<b>Refractive index Brix Scale (RIU)</b>
1	9	10%	1.3333
2	8	20%	1.3478
3	7	30%	1.3638
4	6	40%	1.3811
5	5	50%	1.4200

### **3.5.4 Polyethylene glycol coating of AuTSNP**

Before carrying out the protein monitoring assays, TSNPs were coated with polyethylene glycol (PEG) to provide a protective layer. This helped minimise the direct contact between the protein and the AuTSNPs, minimising the influence in the protein conformational behaviour.

The AuTSNP solution was centrifuged at 16000 rpm at 4°C for 40 minutes and then, the clear supernatant was discarded. The blue pellet of nanoplates was resuspended with a 0.01% solution of PEG 20,000 in a 1:1 AuTSNP-PEG ratio in an Eppendorf tube.

### **3.6 Fn functionalisation of PEGAuTSNP and pH monitoring**

Phosphate buffer  $\text{Na}_2\text{HPO}_4$ , 0.2 M was prepared by dissolving 2.84 g of  $\text{Na}_2\text{HPO}_4$  in 100 mL of NaCl 0.2 M.

Phosphate buffer  $\text{NaH}_2\text{PO}_4$ , 0.2 M at pH 4.16 was prepared by dissolving 3.12 g of  $\text{NaH}_2\text{PO}_4$  in 100 mL of NaCl 0.2 M.

To prepare the buffer at pH 7.23, 40.5 mL  $\text{Na}_2\text{HPO}_4$  0.2 M, 9.5 mL  $\text{NaH}_2\text{PO}_4$  0.2 M and 50 mL of ultrapure water were mixed. Before starting the experiments, buffers were diluted to 0.01 M.

PEGAuTSNPs were functionalised with the protein by incubating 25  $\mu\text{L}$  of Fn with 50  $\mu\text{L}$  of PEG-NP in an Eppendorf tube. After that, 37.5  $\mu\text{L}$  of the Fn functionalised PEG-NP were incubated with 200  $\mu\text{L}$  of phosphate buffer pH 7.2 and pH 4.1 respectively in two new Eppendorf tubes. A 100  $\mu\text{L}$  sample of each Eppendorf tube were placed in a 96-well plate and UV-Vis measurements were performed in a microplate reader to record the protein structural changes. The microplate reader was adjusted for absorbance measurements from wavelengths 300-900 nm in 1 nm increments.

### **3.7 Bone tissue regeneration scaffolds preparation**

Chitosan (Cs) scaffolds were prepared using a previously reported novel one-step photocrosslinking reaction under the presence of UV light (Devine et al., 2019). For the preparation, 1.5 g of high molecular weight Cs was dissolved by using 12.5 mL of 1% acetic acid and left on the bench for 1 h. Subsequently, the protonated Cs paste was neutralized by immersing it in a sodium bicarbonate solution 0.1 M for 10 minutes. Then, excess liquid was removed by absorbing it from the paste with filter papers. 100  $\mu$ L of PEG 600 DMA and 500  $\mu$ L of 0.1% (w/v) benzophenone were added to the now dried paste and mixed. Following that, 1.5 g of HAp powder was added into the paste and mixed well. Cs-HAp scaffold paste was pressed in a silicon mould to have small circular samples, subsequently, the mould was placed in the UV curing system (Dr. Gröbel UV-Elektronik GmbH, spectral range 315-400 nm, high intensity 10-13.5 mW  $\text{cm}^2$ ) for 10 minutes. All of the samples were flipped over mid-curing.

### **3.8 Fn functionalisation on PEGAuTSNP and pH monitoring in the presence of Cs-HAp scaffolds**

The Fn functionalisation of PEGAuTSNP procedure was carried out as previously described. After that, two small circular scaffolds were placed in two Eppendorf tubes followed by the addition of 200  $\mu$ L of phosphate buffer (pH 7.2 or pH 4.1) and the Fn PEGAuTSNP. The Eppendorf tubes were incubated at room temperature for approximately 30 minutes. UV-Vis measurements in a microplate reader were performed to record the protein behavioural changes. The microplate reader was adjusted for absorbance measurements from wavelengths 300-900 nm in 1 nm increments.

### **3.9 Cell culture with C2C12 myoblast cells**

C2C12 is a myoblast cell line from mice muscles which exhibits rapid growth and differentiation from myoblasts to myotubes. It has been demonstrated that there can be a shift in the differentiation pathway from myoblastic cells to osteoblast lineage if cells are treated with bone morphogenic protein 2 (BMP-2) (Katagiri et al., 1994). For this cell line, cell passages were carried out every 3-4 days when cell confluence was around



80-85% in a 1:10 split. First batch of C2C12 cells was obtained from a previously cultured flask starting in passage number 3. Typical C2C12 morphology is displayed in Figure 20.

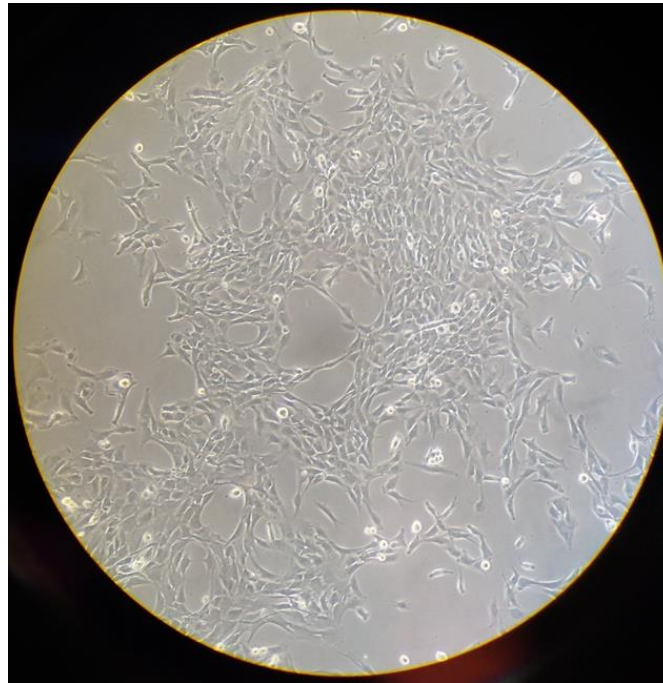


*Figure 20. C2C12 culture at ~70% confluence.*

### **3.9.1 Cell culture with MC3T3-E1 pre-osteoblast cells**

MC3T3-E1 is an immortalized murine calvarial cell line (pre-osteoblastic) widely used as model for osteoblast biology (Hwang & Horton, 2019). This subclone is reported to exhibit high levels of osteoblast differentiation when grown in the presence of ascorbic acid and inorganic phosphate (D. Wang et al., 1999). This cell line was passaged every 2-3 days when cell confluence was around 80-85% in a 1:10 split. MC3T3-E1 cells were obtained fresh from the American Type Culture Collection in passage number 17. Typical MC3T3 morphology is shown in Figure 21.

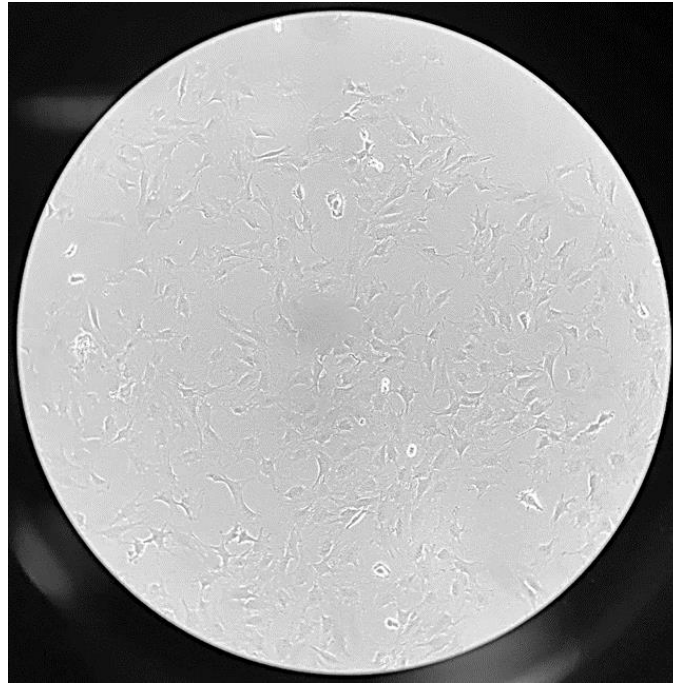


*Figure 21. MC3T3-E1 cells at ~50% confluence.*

### **3.9.1.1 Medium Preparation**

C2C12 cells were cultured in phenol red-free supplemented Dulbecco's Modified Eagle Medium (DMEM). MC3T3-E1 cells were cultured in phenol red-free supplemented Minimum Essential Medium  $\alpha$  ( $\alpha$ -MEM).

Both mediums were previously prepared with 50 mL Fetal Bovine Serum (FBS), 5 mL of L-Glutamine if needed, and 5 mL of Penicillin-Streptomycin for a 500 ml bottle of medium, this was carried out to have the desired concentrations of 10% of FBS, 1% Penicillin-Streptomycin and 1% L- Glutamine. 60 mL of the pure medium were taken out of each bottle to add the complements.

### **3.9.1.2 MC3T3-E1 cells resuscitation**

The cryovial containing 1 mL MC3T3-E1 cells was taken out of the nitrogen tank and was immediately placed in a water bath at 37°C to thaw for a couple of minutes. After that, the thawed cells were poured into a 15 mL Eppendorf tube containing 9 mL of fresh complete  $\alpha$ -MEM media. The tube was then centrifuged at 130 RCF for 5 minutes to get a pellet of cells.

Following the centrifugation, the supernatant was carefully discarded without disturbing the cell pellet. This pellet was then resuspended in 1 mL of fresh media and poured in a T-25 flask for culturing. Consequently, 4 mL of fresh media were added to the T-25 flask and closed tightly.

The flask was properly labelled with cell name, passage number (P18), date and name, and it was placed into an incubator with 5% CO<sub>2</sub> flow at 37 °C for 3 days until 80-85% confluence was reached.

### **3.9.2 Cell passage**

Before starting the passage, trypsin, culture medium (DMEM or  $\alpha$  –MEM) and sterile PBS for cell culture (pH 7.4) were thawed for at least half an hour in the incubator at 37°C. Medium contained in the previously cultured T-flask was discarded. Following that, 5 mL of sterile PBS were added to the flask to clean the remaining medium and avoid deactivation of trypsin. The PBS was discarded and 2 mL of trypsin were added to the flask in direction to the growth area. The flask was left in the incubator at 37°C for 5 minutes to help the trypsin detach the cells.

After the incubation, cells were observed in the microscope to verify if they were properly detached before continuing with the procedure. Consequently, 6 mL of medium were added to the flask to deactivate trypsin and, all the liquid contained in the T-flask was poured in a 15 mL Eppendorf tube for centrifugation at 150 rcf for 5 minutes. Immediately after centrifugation, supernatant was discarded and the pellet of cells was resuspended with 1 mL of culture medium.

For the cell passage, 100  $\mu$ L of the resuspended pellet were taken and poured in a new T-flask and 10-12 mL of cell medium were added (1:10 split). The new T-flask with the cells was incubated for 3-4 days at 37°C and 5% CO<sub>2</sub> flow for growth. This protocol was followed for both cell lines, however, for MC3T3-E1 the centrifugation step is performed at 130 rcf for 5 minutes and passages were carried out every 2-3 days.

### **3.9.3 Cell counting**

Cell counting procedure was executed to perform the monitoring experiments where an initial density of  $25 \times 10^4$  cells per mL (200  $\mu$ L per well;  $5 \times 10^4$  cells per well) were

seeded in flat bottom 96-well plates. For this, cell culture passage procedure was followed as stated in section 3.10.2, where a previously cultured T-flask was taken from the incubator and media was discarded. Then, 5 mL of sterile PBS were added to the flask to clean the remaining medium. Following that, PBS was discarded and 2 mL of trypsin were slowly added to the flask over the growth area. The flask was left in the incubator at 37°C for 5 minutes for trypsin to detach the cells.

Consequently, 6 mL of medium were added to the flask and all the liquid in the T-flask was poured in a 15 mL Eppendorf tube for centrifugation at 150 rcf for C2C12 cells or 130 rcf for MC3T3-E1 cells, for 5 minutes. Subsequently, cells were resuspended in 2 mL of culture medium and 20 µL of cells were transferred to a microcentrifuge tube. Then, 80 µL of trypan blue were added to the microcentrifuge tube (cells: trypan ratio 1:4) and cells were counted using a haemocytometer.

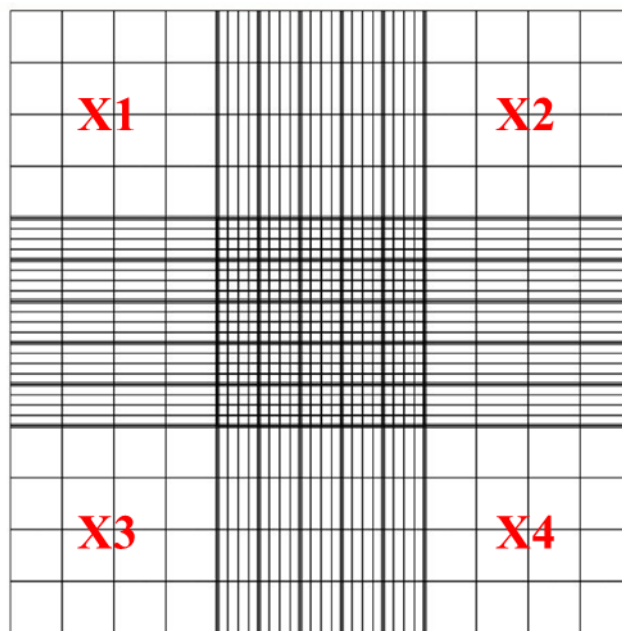


Figure 22. Haemocytometer grid.(Arnal Barbedo, 2013)

The haemocytometer was previously cleaned with 70% Isopropyl alcohol (IPA) to get rid of any remains of previously counted cells that could interfere with the current cell-count. After cleaning, a glass slide was placed on top of the haemocytometer grid and a drop of the previously trypan stained cells was placed on the edge of the slide until the drop dispersed underneath. Finally, the haemocytometer was placed under the

microscope and only the white cells (blue stained cells indicate cell death) observed on the haemocytometer quadrants (outer 4 as shown in Figure 22) were counted.

Cell density was calculated as follows:

Equation 1:

$$\frac{X1 + X2 + X3 + X4}{4} = Y \times 10^4 \text{ cells/mL}$$

$(Y \times 10^4) \times 5 \text{ trypan blue dilution factor} = Z \times 10^4 \text{ cells/mL}$  (i.e. Total cells)

Equation 2:

$$C_1 V_1 = C_2 V_2 \quad \longrightarrow \quad V_1 = \frac{(C_2 \text{ cells/mL}) \cdot (V_2 \text{ mL})}{C_1 \text{ cells/mL}}$$

Where:

$C_1$ : Total cells (i.e.  $Z \times 10^4 \text{ cells/mL}$ )

$C_2$ : Desired cell density

$V_2$ : Desired total volume of fresh media + cells (in mL) to be added to the wells (this volume is dependent on the number of wells; 200  $\mu\text{L}$  of cells is added per well)

$V_1$ : Volume of cells to be added to  $V_2$  fresh media

After determination of  $V_1$ ,

Equation 3:

$$\text{Fresh media needed} = V_2 - V_1$$

Finally, the mL of  $V_1$  calculated in equation 2 is added to the calculated  $V_2$  in equation 3, to obtain the desired cell density.

### 3.9.4 Protein effective-denaturing time determination

Prior to the cell treatments for active Fn monitoring, protein effective-denaturing time was determined in order to treat the cells with denatured Fn functionalised PEGAuTSNP to act as a negative control for protein extension overtime.

C2C12 cells were counted and then plated with an initial density of  $25 \times 10^4$  cells per mL in a flat bottom 96-well plate and incubated for 24 h until confluence was reached.

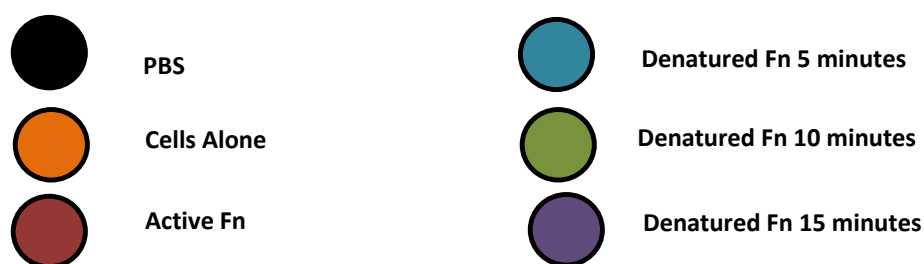
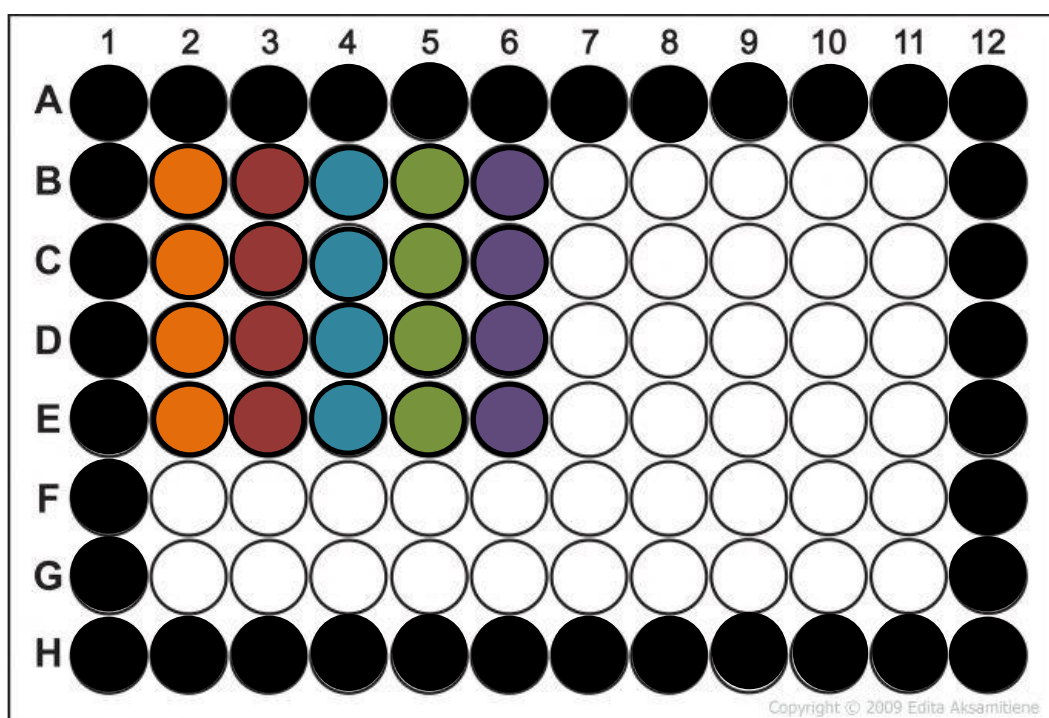


Figure 23. Fn PEGAuTSNP treatments layout in a 96 well-plate for effective-denaturing time testing.

After that, 3 Eppendorf tubes containing  $20 \mu\text{l}$  of  $1 \text{ mg mL}^{-1}$  Fn were placed in a water bath at  $95^\circ\text{C}$  for 5 minutes, 10 minutes and 15 minutes respectively. Following that,  $600\mu\text{L}$  of PEGAuTSNP were placed in 3 Eppendorf tubes and  $20 \mu\text{L}$  of the recently denatured Fn samples were added to each tube correspondingly for preincubation.

Additionally, 600  $\mu\text{L}$  of PEGAuTSNP and 20  $\mu\text{L}$  of active 1 mg mL<sup>-1</sup> Fn were also preincubated.

All Fn-functionalised nanoplates were incubated with the cells in a PEGAuTSNP: MEDIA ratio of 1:1.167, following the template in Figure 23. Prior to adding the nanoplates to the cells, culture media was changed to fresh media. UV-Vis readings were taken at 5 different time points (0 h, 3 h, 8 h, 24 h, and 32 h) in a microplate reader. The microplate reader was adjusted for absorbance measurements from wavelengths 300-900 nm in 1 nm increments. Results were plotted and compared afterwards to determine the most effective denaturing time.

### **3.10 Cell incubation with Fn functionalised PEGAuTSNP for protein monitoring overtime**

For Fn monitoring overtime, C2C12 cells were plated with an initial density of  $25 \times 10^4$  cells per mL in a flat bottom 96-well plate and incubated for 24 h until confluence was reached. After reaching confluence, PEGAuTSNP, active Fn functionalised PEGAuTSNP and denatured Fn-functionalised PEGAuTSNP were incubated with the cells in a PEGAuTSNP: MEDIA ratio of 1:1.167, following the template in Figure 24. Culture media was changed to fresh media before adding the treatments to the corresponding wells. UV-Vis readings were taken at 5 different time points (0 h, 3 h, 8 h, 24 h, and 32 h) in a microplate reader. The microplate reader was adjusted for absorbance measurements from wavelengths 300-900 nm in 1 nm increments.

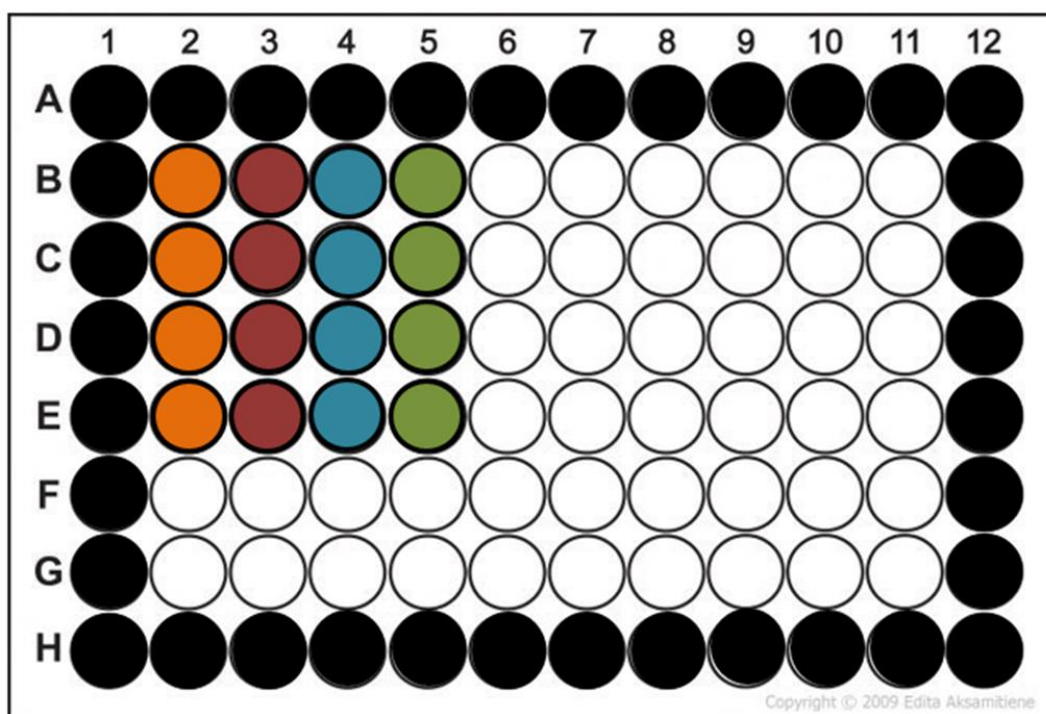


Figure 24. Fn PEGAuTSNP treatments layout in a 96 well-plate for protein monitoring overtime.

### 3.10.1 Cell plating and incubation with Fn functionalised PEGAuTSNP and Cs-HAP scaffolds for protein monitoring overtime

For Fn monitoring within cells and in the presence of Cs-HAP scaffolds, cells were plated with an initial density of  $25 \times 10^4$  cells per mL in a flat bottom 96-well plate and incubated for 24 h until confluence was reached. Bone tissue regeneration scaffolds were placed in the wells before adding the cells. Pulse UV sterilization of the scaffolds was carried out prior to incubation with cells where 90 pulses of 800 watts frequencies were administered on the scaffolds at a rate of 1 pulse per second. This was carried out to prevent any contamination in the cell culture. After reaching confluence, PEGAuTSNP and active Fn functionalised PEGAuTSNP were incubated with the cells in a PEGAuTSNP: MEDIA ratio of 1:1.167, following the template in Figure 25.



Culture media was changed to fresh culture media before adding the treatments to the corresponding wells. UV-Vis readings were taken at 5 different time points (0 h, 3 h, 8 h, 24 h, and 32 h) in a microplate reader. The experiment was repeated three times under the same conditions with three technical replicates per treatment in each experiment.

The microplate reader was adjusted for absorbance measurements from wavelengths 300-900 nm in 1 nm increments.

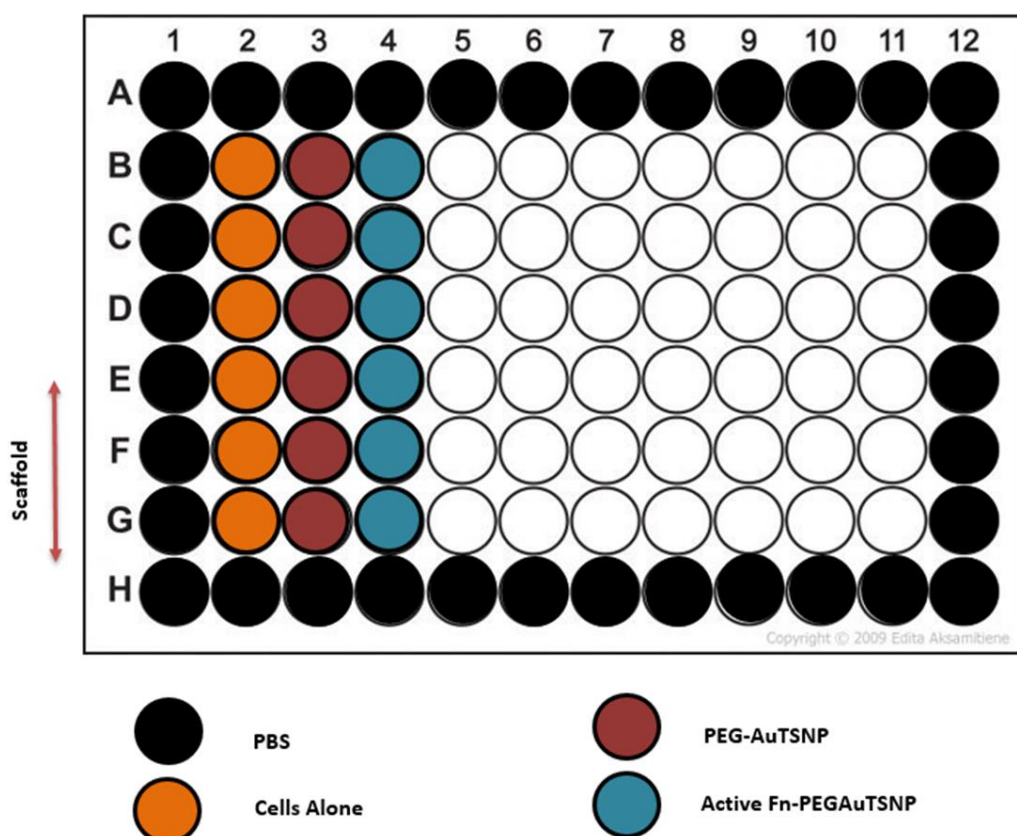


Figure 25. Fn PEGAuTSNP treatments layout in a 96 well-plate for protein monitoring overtime.

### 3.10.2 MC3T3-E1 cells plating and incubation with Fn functionalised PEGAuTSNP and Cs-HAp scaffolds for protein monitoring overtime

MC3T3-E1 cells were plated with an initial density of  $76 \times 10^4$  cells per mL in a flat bottom 24-well plate and incubated for 24 h until confluence was reached. After reaching confluence, PEGAuTSNP, active Fn functionalised PEGAuTSNP and denatured Fn-functionalised PEGAuTSNP were incubated with the cells in a

PEGAuTSNP: MEDIA ratio of 1:1.167, following the template in Figure 26. Culture media was changed to fresh media before adding the treatments to the corresponding wells.

Cs-HAp scaffolds were placed in transwell inserts and placed in the wells. UV-Vis readings were taken at 5 different time points (0 h, 3 h, 8 h, 24 h, and 32 h) in a microplate reader. Transwell inserts were taken out of the wells prior to the UV-Vis measurements. The microplate reader was adjusted for absorbance measurements from wavelengths 300-900 nm in 1 nm increments.

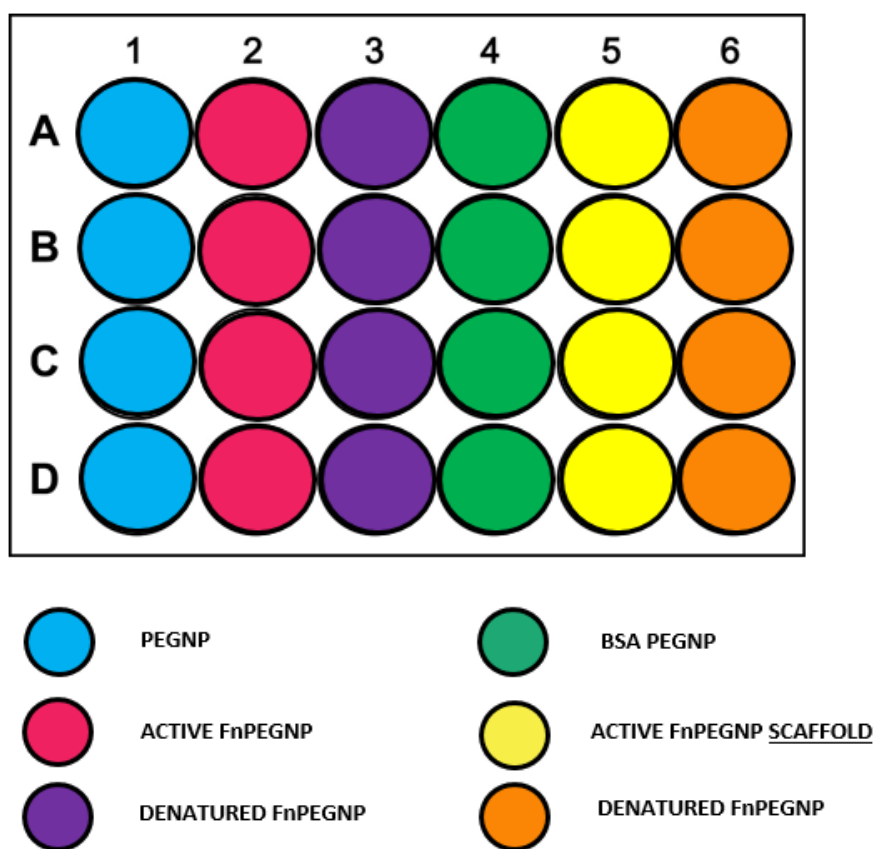


Figure 26. Fn PEGAuTSNP treatments layout in a 24 well-plate for protein monitoring overtime.

Assay was repeated three times under the same conditions with four technical replicates per treatment in each experiment.

### 3.11 Bone tissue regeneration hydrogel scaffolds preparation

Cs hydrogel scaffolds were prepared as previously described under this chapter in section 3.7 with high molecular weight Cs, PEG 600 DMA, benzophenone and HAp. The used volume of 1% acetic acid was modified to 30 mL to change the texture of the scaffold into a viscous material. Cs-HAp scaffold paste was then pressed in a silicon mould which was placed afterwards in the UV curing. All samples were flipped over mid-curing.

After curing, all samples were placed in a 24 well-plate and injected with 200  $\mu$ L of ultrapure water to make them transparent and modify its consistency into a hydrogel. Samples were left on the bench until the injected water was absorbed and consistency was as desired, resulting in an aqueous hydrogel for pipette handling (Figure 27).



Figure 27. Cs-HAp hydrogels

#### 3.11.1 Monitoring of on-scaffold loaded Fn in MC3T3-E1 cells

MC3T3-E1 cells were plated at an initial density of  $25 \times 10^4$  cells/mL in a flat bottom 96-well plate and incubated for 24 h until confluence was reached. Ten hydrogels were prepared and 5  $\mu$ L of Fn in its active and denatured forms were injected into each

hydrogel. Furthermore, 1 mL of PEGAuTSNPs were synthesized and coated with Fn in its active and denatured forms. After reaching cellular confluence, cell culture media was changed to fresh media (50  $\mu$ L), and 75  $\mu$ L of hydrogel + 75  $\mu$ L of PEGAuTSNP were added to each well following the template in Figure 28.

Active and denatured Fn-PEGAuTSNP + unloaded hydrogel were used as a positive and negative control respectively for protein extension overtime. The 96-well plate was analysed in the microplate reader adjusted for absorbance measurements from wavelengths 300-900 nm in 1 nm increments

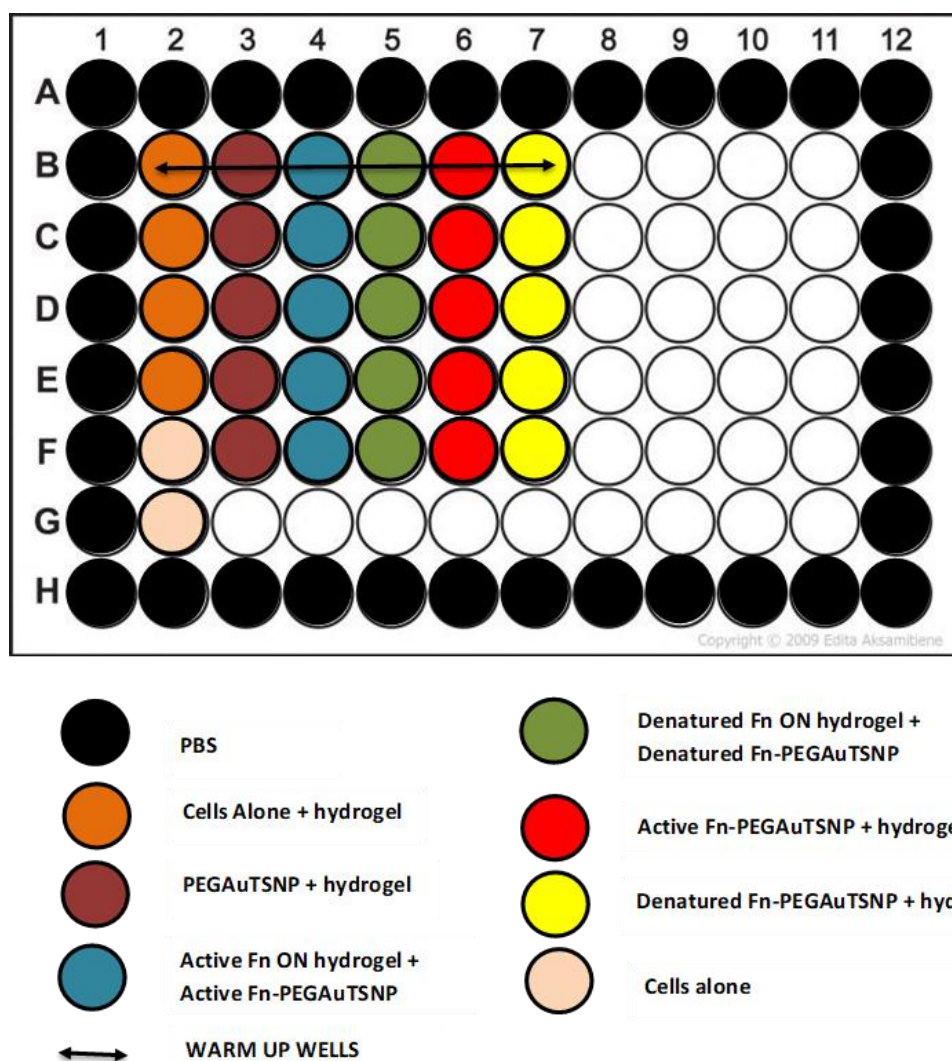


Figure 28. Fn-hydrogels and Fn-PEGAuTSNP treatments layout in a 24 well-plate for protein monitoring overtime

The experiment was repeated two times under the same conditions with four technical replicates per treatment in each experiment.

### **3.12 Nanoplate-based direct immunoassay with Fibronectin and Anti-fibronectin antibody.**

The sensitivity and suitability of the nanoplates LSPR system for antibody (Ab)-antigen (Ag) binding testing was assessed in a nanoplate-based direct immunoassay by using purified Fn and its corresponding antibody.

#### **3.12.1 Nanoplate-based immunoassay system testing with active and denatured Fn**

PEGAuTSNP were prepared as per previous sections and several concentrations of Fn were added to 1 mL of PEGAuTSNP (5 µg, 8 µg, 10 µg, 15 µg) to observe the minimum required to perceive a difference in the spectrum and use the minimum possible to successfully coat the nanoplates. Samples were placed in a 96-well plate and analysed in the microplate reader adjusted for absorbance measurements from wavelengths 300-900 nm in 1 nm increments.

Following the first reading, 1 µg of Anti-Fn was added to each of the wells and the plate was analysed in the microplate reader once more to observe shift differences upon Ab-Ag binding and determine the least amount to successfully cover the nanoplates' surface.

Denatured FnPEGAuTSNP was used as negative control for binding.

#### **3.12.2 Nanoplate-based immunoassay system testing with spun-down Fn functionalised PEGAuTSNP**

Experiment in section 3.12.1 was replicated with a different approach. Several concentrations of Fn were added to 1 mL of PEGAuTSNP (5 µg, 8 µg, 10 µg, 15 µg) and analysed before and after the addition of 1 µg of AntiFn. Samples of Fn-PEGAuTSNP were centrifuged at 16000 rpm at 4°C for 40 minutes to discard free non-attached Fn from the supernatant and observe differences in the LSPR spectra related to Anti-Fn and Fn binding in the supernatant instead of in the nanoplates surface.

Similar to the previous experiment, samples were placed in a 96-well plate and analysed in the microplate reader. Following the first reading, 1 µg of Anti-Fn was added to each of the wells. The microplate reader was adjusted for absorbance measurements from wavelengths 300-900 nm in 1 nm increments.

### **3.12.3 Nanoplate-based immunoassay with changing concentration of Anti-Fn antibody**

The limit of detection (LOD) of the Ag-Ab system was determined by using different concentrations of antibody in a sample of Fn-PEGAuTSNP. PEGAuTSNP were prepared as previously stated and 5 µg of Fn were incubated with 1 mL of PEGAuTSNP. Subsequently, 99 µL of Fn-PEGAuTSNP were placed in a well of a 96-well plate and 1 µg of Anti-Fn was added and analysed in the plate reader. Following that, 2 µg, 4 µg, 6 µg, 8 µg, 10 µg, 12 µg and 14 µg of Anti-Fn were added to the same well and readings were performed between each quantity. At the end of the experiment the sum of Anti-Fn in the well was 57 µg. All the experiment was performed in the same well to avoid variations in the readings and keep uniformity. For absorbance measurements the microplate reader was adjusted from wavelengths 300-900 nm in 1 nm increments.

### **3.13 Nanoplate-based indirect immunoassay with Fn and Anti-Fn antibody.**

The nanoplates LSPR system for Ab-Ag binding within a complex environment was assessed in a nanoplate-based indirect immunoassay by using Anti-Fn and ECM isolated from cell culture containing native Fn.

#### **3.13.1 Extracellular Matrix isolation protocol**

ECM isolation from cell culture was performed based on the protocol developed by Hellewell et al. (2017) to study the interaction between native Fn from live cells and Anti-Fn antibody. MC3T3-E1 cells were cultured and plated in a 6 well-plate at high density and placed in the incubator for 24h until 95% confluent. Ammonium Hydroxide (NH<sub>4</sub>OH, 20 mM) was prepared with de-ionized water in an extractor hood. After that, the culturing plate was removed from the incubator and culture medium was removed from each well with a micropipette. Wells were gently rinsed with 1 mL of PBS without

Ca<sup>2+</sup>/Mg<sup>2+</sup> and the liquid containing PBS and remaining media was removed from the wells. Consequently, 300 µL of Ammonium Hydroxide were added to each well with rocking for a few seconds before washing each well with 1 mL of distilled water. The ammonium hydroxide solubilized material containing water, ammonium hydroxide, and lysed cells was immediately removed with a micropipette. After that, the 6-well plate was tilted at an angle and remaining ECM was collected from the bottom of the well by using a cell scraper (Hellewell et al., 2017). The collected ECM was placed in Eppendorf tubes and analysed in a microliter UV/VIS spectrophotometer (Picodrop, model PICOPET01) to test suitability of the collected samples containing overall proteins.

### **3.13.2 Detection of native fibronectin with AntiFn-PEGAuTSNP**

Three concentrations of cell-isolated ECM (100%, 50% and 15%) were prepared with distilled water. After that, the ECM samples were exposed to a concentration of 0.21 mg/mL AntiFn-PEGAuTSNP (functionalised-NP before saturation point as per LOD curve) in a 1:1.5 ECM: AntiFn-PEGAuTSNP ratio and placed on a 96-well plate (Figure 29) to analyse interactions between native Fn and the antibody. Purified Fn samples in concentrations of 100% and 15% were used as positive controls for binding of Anti-Fn with Fn (1:1.5 Fn: AntiFn-PEGAuTSNP ratio). The 96-well plate was analysed in the microplate reader.

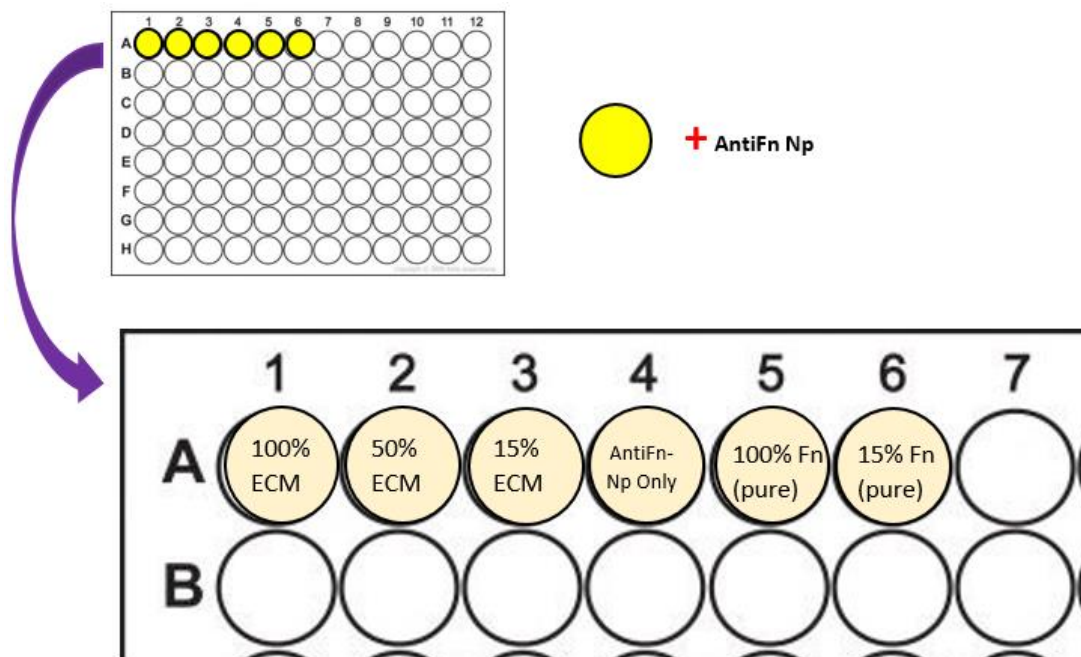


Figure 29. Nanoplate-based immunoassay 96-well plate layout.

A second experiment was carried out with Anti-TJP1 (TJP1= Tight Junction Protein 1) antibody as negative control for binding since it is human tight junction protein 1 (TJP1) targeted antibody non-specific to Fn (Figure 30). The antibodies were used in similar concentration as the previous experiment with AntiFn-PEGAuTSNP. The antibody conjugate TJP1 was used as positive control for binding (1:1.5 TJP1: AntiFn-PEGAuTSNP ratio).



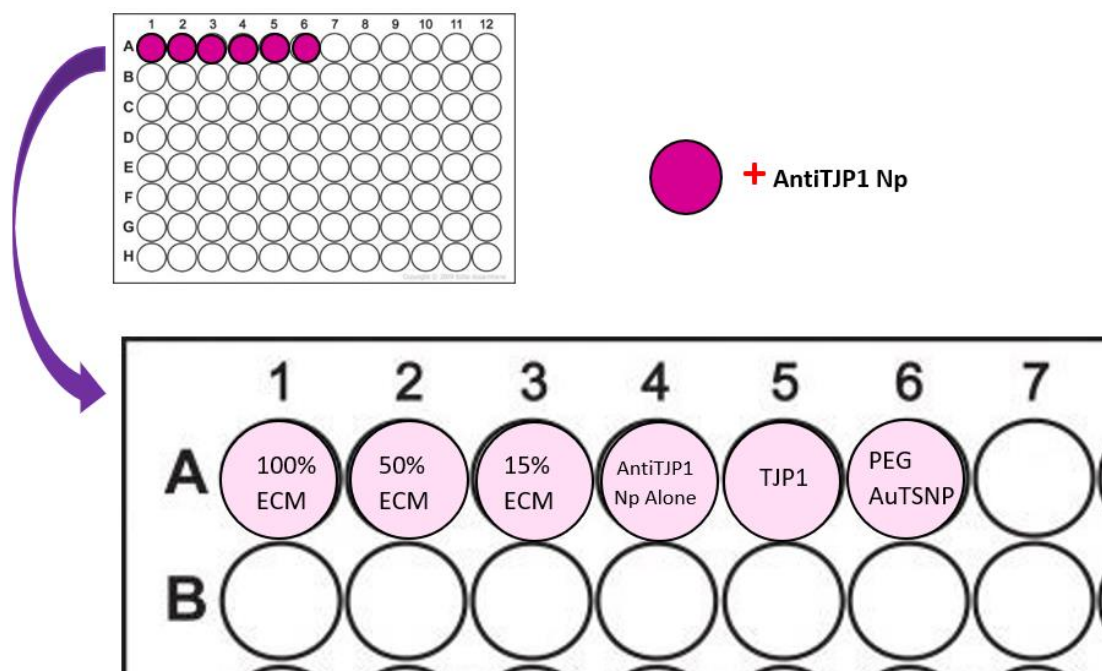


Figure 30. Nanoplate-based immunoassay layout with non-ECM proteins.

Absorbance measurements were performed in a microplate reader adjusted from wavelengths 300-900 nm in 1 nm increments. All experiments were repeated twice under the same conditions.

### 3.14 Nanoplate-based immunoassay for COVID-19 detection

#### 3.14.1 Spike protein optimal functionalisation volume determination

PEGAuTSNP were prepared as per previous protocol and different amounts of spike protein were added to the nanoplates. 1 mL of PEGAuTSNP were placed in five Eppendorf tubes (5 mL total) and 1  $\mu$ g, 3  $\mu$ g, 5  $\mu$ g, 7  $\mu$ g, and 10  $\mu$ g of Spike protein was added to each tube respectively. A sample of 100  $\mu$ L was taken from each tube and placed on a 96-well plate. The plate was analysed in the plate reader.

After the first reading, 1  $\mu$ g of Anti-Spike antibody was added to each well and the plate was analysed again to observe changes on the LSPR.

Plate reader measurements were adjusted from wavelengths 300-900 nm in 1 nm increments.

### **3.14.2 Nanoplate-based immunoassay with changing concentration of Anti-Spike antibody**

After suitable concentration of spike PEGAuTSNP was determined, 4  $\mu\text{g}$  spike/mL PEGAuTSNP were used with different amounts of Anti-Spike to determine nanoplate saturation point.

A sample of 100  $\mu\text{L}$  of Spike PEGAuTSNP was placed on a 96-well plate and analysed in the plate reader. After that 1  $\mu\text{g}$  of Anti-Spike was added to the well and the plate was analysed again in a microplate reader with adjusted wavelengths from 300-900 nm in 1 nm increments. Following that, 2  $\mu\text{g}$ , 4  $\mu\text{g}$ , 6  $\mu\text{g}$ , 8  $\mu\text{g}$  and 10  $\mu\text{g}$  were added to the same well and the plate was analysed between every addition. The final sum of Anti-Spike in the well at the end of the experiment was 31  $\mu\text{g}$ .

All the experiment was performed in the same well to avoid variations in the readings and keep uniformity.

### **3.14.3 Spike-AntiSpike binding PEGAuTSNP-based immunoassay**

Spike-PEGAuTSNP was exposed to AntiSpike to test the nanoplate-based immunoassay platform. 100  $\mu\text{L}$  Spike-PEGAuTSNP in the previously stated concentration, and 100  $\mu\text{L}$  TJP1-PEGAuTSNP (5  $\mu\text{L}$  TJP1/mL PEGAuTSNP) were placed in a 96-well plate and analysed on the plate reader. After the first reading 4  $\mu\text{g}$  Anti-Spike were added to both wells and the plate was analysed again. TJP1-PEGAuTSNP was used as negative control for binding.

The microplate reader was adjusted from wavelengths 300-900 nm in 1 nm increments for absorbance measurements.

### **3.14.4 Spike-AntiSpike binding PEGAuTSNP-based immunoassay within horse serum**

Binding of the Spike-AntiSpike complex within horse serum as a high noise environment was monitored using PEGAuTSNP. Spike-PEGAuTSNP was prepared with 4  $\mu\text{g}$  of Spike in 1 mL of PEGAuTSNP and TJP1-PEGAuTSNP was prepared in a similar concentration of 5  $\mu\text{g}$  of TJP1 in 1 mL of PEGAuTSNP. The latter was used as a negative control for binding with the Spike antibody.

Three different concentrations of horse serum (100%, 50% and 10%) were prepared with distilled water to observe differences in the LSPR as a result of the high concentration of proteins within the serum.

Samples were placed in a 96-well plate (Figure 31) in a ratio of 1:1.67 horse serum: functionalised PEGAuTSNP, similar to previous experiments within cell culture. The plate was analysed in the plate reader where measurements were adjusted from wavelengths 300-900 nm in 1 nm increments. After the first analysis, 4  $\mu$ g of Anti-Spike was added to all wells and plate was analysed again.

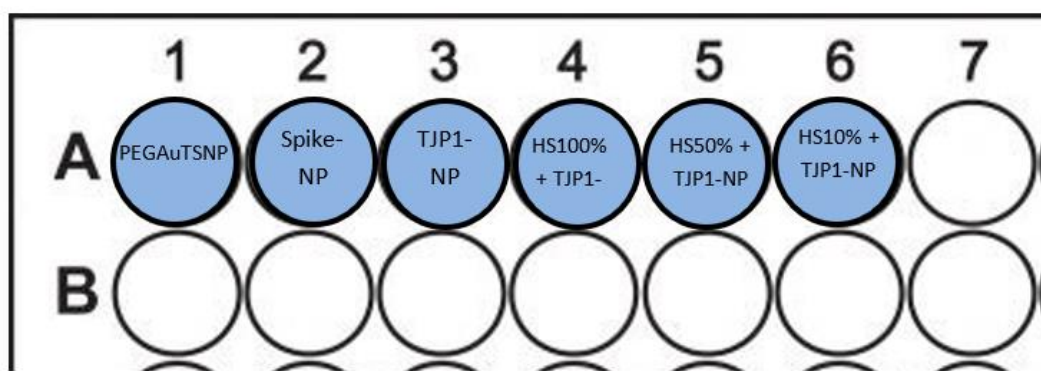


Figure 31. COVID-19 detection experiment layout

### 3.14.5 Dynamic Light Scattering (DLS) measurements

Dynamic Light Scattering (DLS) also known as photon correlation spectroscopy (PCS) is extensively used in research for the study of proteins, colloidal particles, and nanoparticles (Schintke & Frau, 2020). It studies the diffusion of molecules in solution through the diffusion coefficient and hydrodynamic radius, which are dependent on the analysed molecules size and shape (Stetefeld et al., 2016). DLS measurements consist in scattered laser light from the simultaneous Brownian motion of particles in a solution. Particles size can be obtained when their movement is monitored over a time range. When the laser light comes across the sample molecules, the incident light is scattered in all directions, and the scattering intensity is recorded by the instrument detector. The intensity fluctuations of scattered light are correlated in relation to time to define the speed of intensity fluctuations, which relates to the diffusion of molecules (Sandhu et al., 2018).

Zetasizer Pro from Malvern Panalytical Ltd was used for particle size measurements with DTS0012 polystyrene disposable cuvettes. All samples from section 3.14.4 were diluted with ultrapure water in a 1:10 dilution. One mL of the newly diluted sample was placed in the disposable cuvette and the cuvette lid was placed on top. Size measurements were repeated 3 times per sample at 25 °C and results were analysed in ZS XPLOER software.

**CHAPTER 4.**  
**TRIANGULAR SILVER**  
**NANOPLATES**  
**PREPARATION AND**  
**FUNCTIONALIZATION**

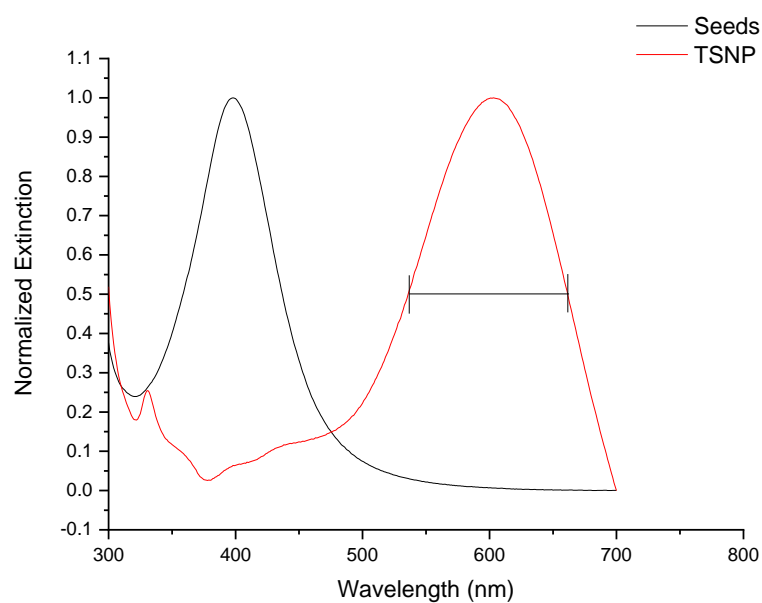
## 4.1 Preface

In this chapter, the preparation and optimization of triangular silver nanoplates (TSNP) is presented as well as their functionalization with the extracellular matrix protein Fn. A previously reported preparation method by Aherne et al. (2008) consisting on the reduction of silver nitrate by sodium borohydride and followed by further reduction of silver ions by ascorbic acid was optimised in order to enhance the nanoplates optical properties. Stability and sensitivity studies were performed to ensure these powerful TSNP properties were maintained for protein monitoring studies within different environments (Aherne et al., 2008).

## 4.2 Optimization of Triangular Silver Nanoplates preparation

The triangular silver nanoplates preparation was optimized from the Aherne et al (2008) original protocol by concentrating the silver in the TSNP solution.

a)



b)

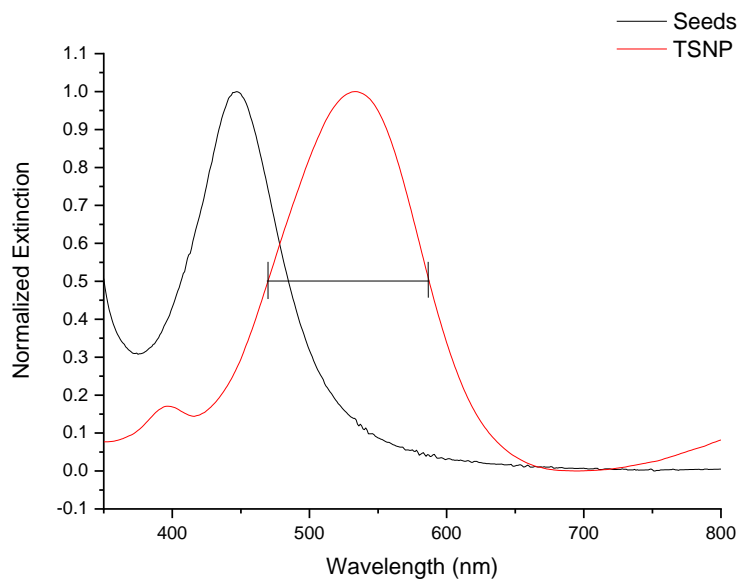


Figure 32. LSPR spectra of (a) original TSNP preparation method with  $<130$  nm FWHM and (b) optimized TSNP preparation method with  $\sim 115$  nm FWHM. Narrower LSPR peak of  $\sim 115$  nm FWHM indicates homogeneity of TSNP which improves sensitivity.

In the original protocol of (Aherne et al., 2008), after the Triangular Silver Nanoplates synthesis, the final volume of the solution was brought up to 10 mL, leaving a concentration of silver of 16.692 ppm in the solution. This protocol showed results of broad localised surface plasmon resonances (LSPR) of more than 130 nm full width at half maximum (FWHM) as shown in Figure 32a. The broad FWHM of the TSNP peak can be attributed to the inhomogeneity of sizes and nanoparticle shapes in the solution. This can diminish the nanoplates sensitivity which is a critical property in TSNP when used in nanosensing applications (D. Charles et al., 2008).

When the TSNP preparation was optimized, the concentration of silver in the nanoplates solution was brought up to 21.962 ppm, resulting in a narrower LSPR peak of  $\sim 115$  nm FWHM indicating homogeneity of TSNP with edge lengths of around 20-25 nm (Aherne et al., 2008; Y. Zhang et al., 2014) (Figure 32b). This can also be attributed to the low water volume in the solution which led to higher absorbance spectra. It has been reported that the high percentage of triangular geometries and the platelet structure of the nanoplates, is partly responsible for the high sensitivities of the TSNP LSPR. Moreover, this sensitivity is enhanced in highly structured silver nanoparticle aggregates (in solution) than in single silver nanoparticles (D. Charles et al., 2008).

According to Aherne et al. (2008), line widths of the LSPR decrease as nanoplate volume increases which results in the decrease in plasmon damping and improved sensitivity of the nanoplates (Aherne et al., 2008).

#### **4.2.1 Gold edge-coating of TSNP and stability test**

Silver nanostructures are advantageous compared to other metal nanostructures due to their strong surface plasmon resonance, however, their signals could be reduced when used in biological environments due to their low stability in detrimental conditions (i.e. physiological environments) (Murshid et al., 2013). In previous studies, it is mentioned that the addition of gold at silver nanoparticles surface provoked its dissolution due to galvanic replacement as it causes hollow gold nanoparticles (Xia & Xia, 2014). Nonetheless, an approach proven to be successful by maintaining the silver nanoplates plasmonic resonance properties, was the addition of gold to the nanoplate edges by slow addition of a gold precursor, in this work,  $\text{HAuCl}_4$  (Aherne et al., 2009; Murshid et al., 2013).

Following the TSNP synthesis, a thin coat of gold was added to the solution in order to protect the nanoplates against etching by chloride ions. Several amounts of  $\text{HAuCl}_4$  were added to the TSNP sol after growth, and stability test was performed to determine the least amount of gold needed for the nanoplates to be protected within saline solutions. LSPR  $\lambda_{\text{max}}$  of TSNP was measured at 579 nm; after gold coating, the LSPR showed a red shift measured at 599 nm. The least amount of gold to edge-coat and successfully protect the TSNP was found to be 20  $\mu\text{L}$  (1:0.049 AgAu ratio) as no blueshift in the LSPR peak is observed upon exposure to NaCl 20 mM as shown in Figure 33.



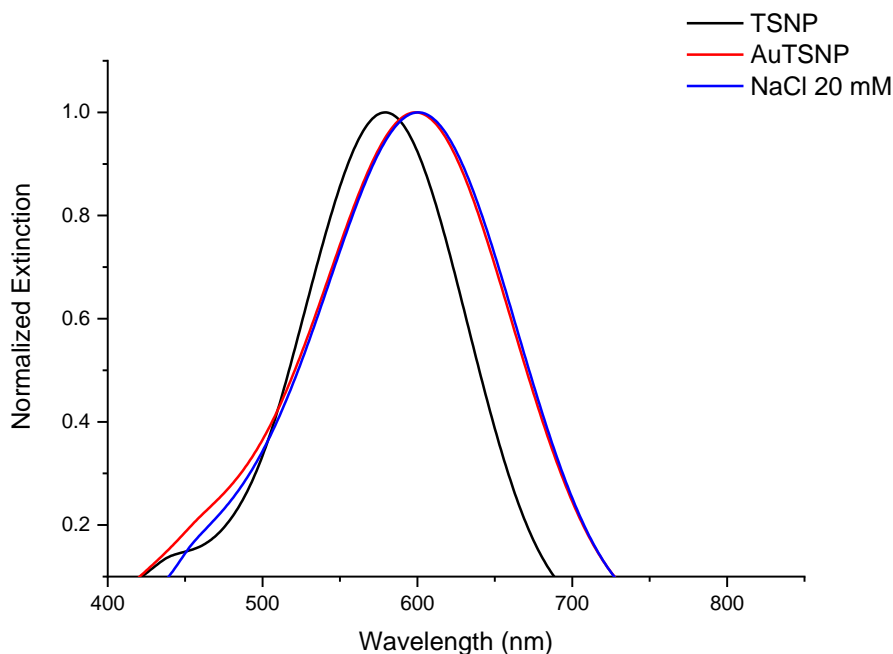


Figure 33. Gold coating and stability test of Triangular Silver Nanoplates. A 20 nm redshift was recorded upon gold coating of the nanoplates, moreover, no change in the spectrum was recorded upon exposure to NaCl 20 mM indicating successful protection of AuTSNP.

As demonstrated by Aherne et al. (2009), deposition of a thin layer of gold in the triangular nanoplates edges at low Ag:Au ratios successfully protects the nanoplates without causing any structural damages associated with galvanic replacement. Moreover, no major changes in the nanoplates optical properties occur besides enhancement of its optical sensitivity (Aherne et al., 2009).

#### 4.2.2 LSPR sensitivity analysis

Upon TSNP gold edge-coating procedure, the refractive index sensitivity of the nanoplates was analysed by the previously reported sucrose method by D. Charles et al (2010). AuTSNP were exposed to different concentrations of water-sucrose solutions (10%, 20%, 30%, 40%, 50% (w/v)) in a 1:1 ratio. This test varies the medium refractive index within which the AuTSNP are suspended, and can provide a measure of the nanoplate sensitivity without interfering with the nanoplates stability. This method is a useful approach for the assessment of AuTSNP performance as nanobiosensors.

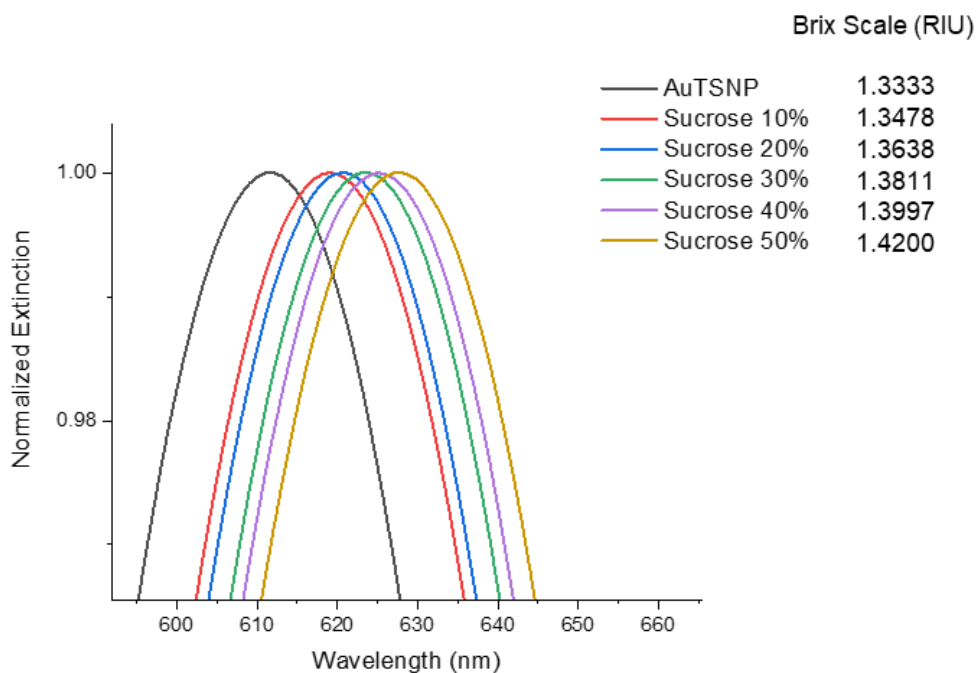


Figure 34. UV-Vis spectra of AuTSNP suspended in a range of water-sucrose solutions. The LSPR  $\lambda_{max}$  of the spectra increases as the sucrose concentration increases

There are other several approaches to test nanoparticle sensitivity by using solvents, however, they have been found to modify the structure of the nanoparticles which is not ideal for the purpose of this project as TSNP plasmonic properties could be compromised. In the sucrose method studies, TSNP solution is exposed to increasing concentrations of sucrose solutions to evaluate the potential of the nanoplates for their use in sensing applications when there is a change in the refractive index surrounding the TSNP. This method was followed and the results (Figure 34) are in agreement with the previously reported outcomes by D. Charles et al, where the LSPR  $\lambda_{max}$  of the spectra increases as the sucrose concentration increases (D. Charles et al., 2008; D. Charles et al., 2010).

### 4.3 Fn functionalisation on PEGAuTSNP and pH dependent conformation

Before the protein monitoring experiments, AuTSNP were coated with Polyethylene Glycol (PEG) to minimise contact between the particles and the Fn protein, and to offer particle extra protection against the physiological environment. The biocompatible and non-immunogenic nature of PEG makes it an attractive polymer to be bonded to other

components for its use in therapeutic methods, drug delivery and wound healing, minimising any immune responses of the cellular environment (Sikka & Midha, 2019; Zarintaj et al., 2020). PEG is also soluble in water and other organic solvents which facilitates its assembly to the nanoparticles surface (Saifullah et al., 2020). Fn conformational changes were monitored by suspending the Fn functionalised PEG coated AuTSNP in two phosphate buffers at different pH (pH 7.2 and pH 4.1) as Fn is known to change its configuration upon pH adjustment.

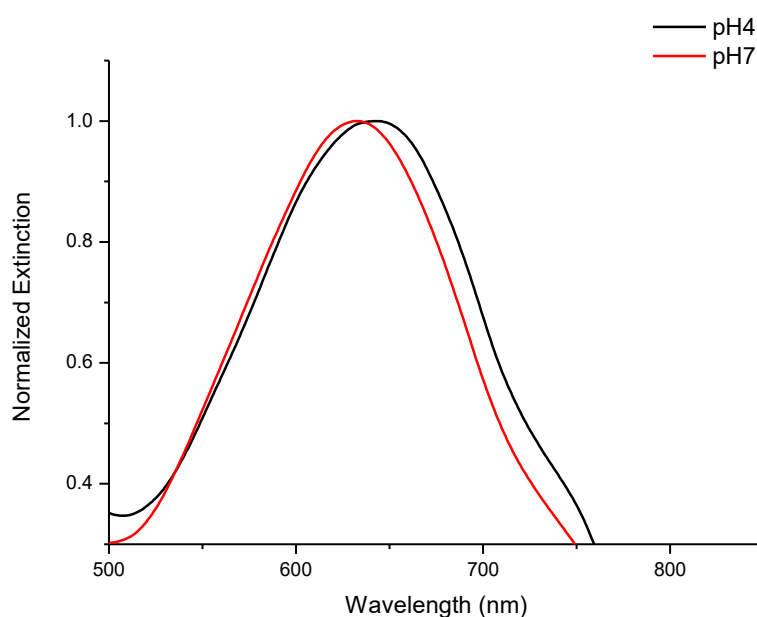


Figure 35. UV-Vis spectra of Fn functionalised PEGAuTSNP at pH 4 and pH 7. Upon pH adjustment from pH 7 to pH 4 a 12 nm redshift was recorded due to Fn extension.

It can be found in literature that Fn has an extended conformation when in acidic or high salt conditions, whereas within low salt conditions it shows a “coiled compact” conformation (Maurer et al., 2015). In previous studies where Fn conformational changes are analysed within different pH environments, Fn is reported to have a hydrodynamic radius of 23 nm when compacted, and when it extends the radius increases up to 130 nm for single Fn strands (Brennan-Fournet et al., 2015; Tooney et al., 1983). Fn can form much larger strands as networks and fibrils can develop and be mediated within the ECM (Tooney et al., 1983). The experiment was carried out by incubating the Fn functionalised PEGAuTSNP in two phosphate buffers and followed by UV-Vis measurements after pH modification. In Figure 35, LSPR  $\lambda_{\max}$  of Fn PEGAuTSNP at pH 7 was measured at 633 nm; upon pH adjustment from pH 7 to pH

4, the LSPR  $\lambda_{\max}$  was measured to be 645 nm. The LSPR spectrum at pH 4 was redshifted by 12 nm upon Fn extension due to a higher refractive index surrounding the nanoplates. The presence of the compact protein strand on top of the nanoplate surface occupies a larger surface area; however, it does not bulge from the surface than an elongated Fn strand, which can explain the shift in the spectrum. As shown in Figure 35, the LSPR peak was slightly broadened in comparison to unfunctionalised AuTSNP (AuTSNP spectrum in Figure 33), this can be attributed to the PEG layer coating the nanoplates surface (Brennan-Fournet et al., 2015).

#### **4.3.1 Fn functionalised PEGAuTSNP monitoring in presence of Cs-HAp regeneration scaffolds**

Fn functionalised PEGAuTSNP were incubated with Cs-HAp regeneration scaffolds and conformational changes of the protein were monitored upon incubation in two phosphate buffers at different pH (pH 7.2 and pH 4.1).

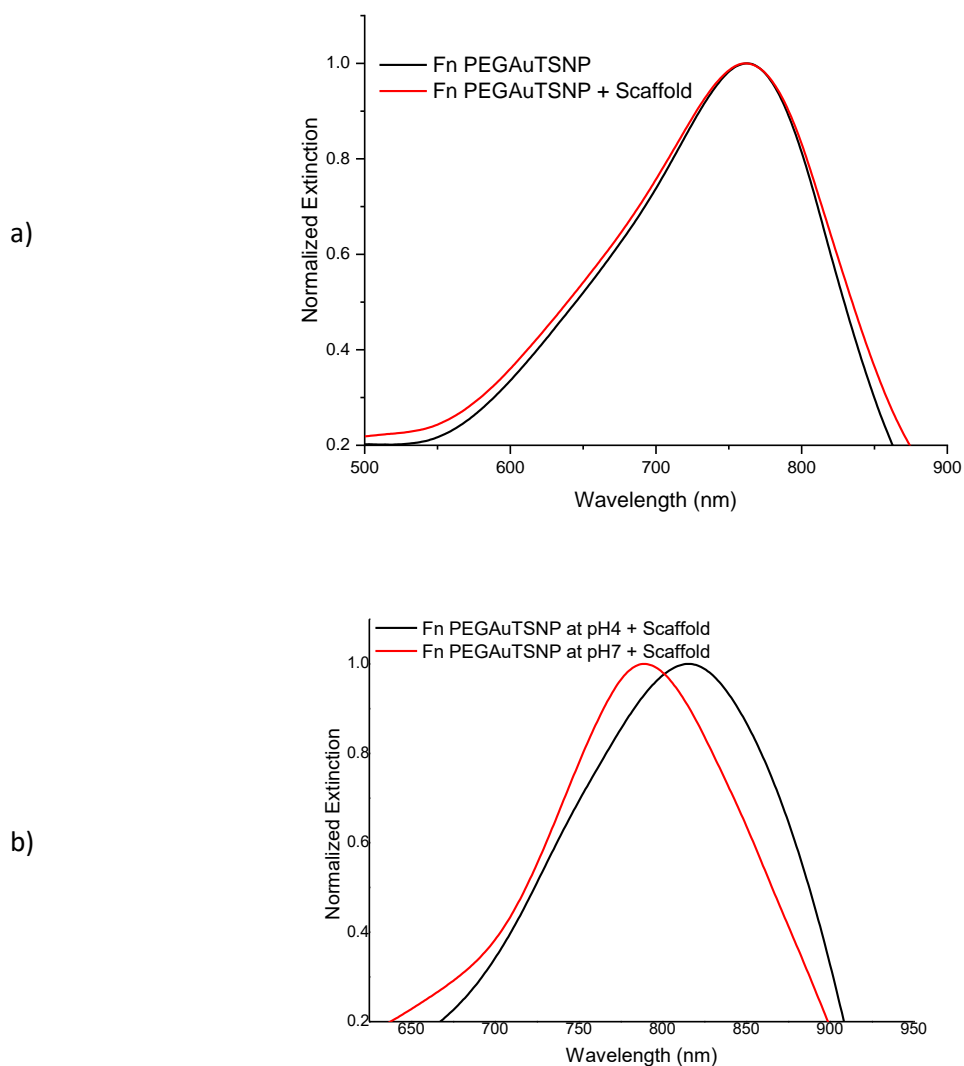


Figure 36. UV-Vis spectra of (a) Fn PEGAuTSNP with and without the presence of Cs-HAp regeneration scaffold, (b) Fn PEGAuTSNP in its compact (pH 7) and extended conformations (pH 4).

Before any pH adjustments, the Fn functionalised PEGAuTSNP were incubated with and without the presence of the scaffold to observe any interactions that could interfere with the next steps. As shown in Figure 36a, the LSPR spectrum of the Fn functionalised nanoplates with and without the presence of the Cs-HAp scaffold was highly similar when no pH adjustment was induced which can indicate strong attachment of the protein to the nanoplate. A minimal interaction can be observed with the presence of the scaffold resulting in the band broadening.

Upon Fn functionalised PEGAuTSNP incubation at different pH values in the presence of the scaffold, the behaviour of the LSPR spectra was very similar as the last experiments (Figure 35) where a red shift of around 25 nm was recorded upon Fn unfolding when adjusting the pH (Figure 36b). This experiment was carried out to demonstrate the capacity of PEGAuTSNP to readily monitor protein transitions in presence of biomimetic tissue scaffolds.

#### 4.4 Summary

The work described in this chapter details the preparation of Triangular Silver Nanoplates by a previously reported method where silver nitrate is reduced by ascorbic acid catalysed by seed silver nanoparticles. The previous method showed results of broad LSPR resonance peaks indicating inhomogeneity of the nanoplates solution which could result in decreased sensitivity. The preparation method was optimized by concentrating the silver in the solution to enhance the triangular nanoplate properties.

This chapter also described the nanoplate protection method where several amounts of gold were added to different TSNP samples and were exposed to sodium chloride solutions. Obtained results determined the least amount of gold needed to successfully coat the nanoplates to prevent the loss of their triangular shape, as well as to maintain the needed LSPR sensitivity to changes in the refractive index. The sucrose method to assess the sensitivity of the nanoplates was also described in this chapter where results are in agreement with those in literature.

The functionalization of ECM protein, Fn, on PEGAuTSNP was also outlined in this chapter where its conformational changes after pH adjustments are analysed. The protein unfolds when pH is adjusted to 4 which can be observed as redshift in the LSPR when compared to its compact format at pH 7. Same experiment was carried out in the presence of Cs-HAp bone tissue regeneration scaffolds to demonstrate the ability of AuTSNP to monitor protein dynamics in presence of biomimetic scaffolds.

After optimisation on the TSNP preparation and the enhancement of their properties, the next task is the monitoring of Fn in the presence of two different cell lines and in the presence of the scaffold. This to assess the potential of TSNP to readily sense and monitor target biomolecules when analysed in high noise cellular environments.

**CHAPTER 5.**

**FIBRONECTIN  
MONITORING IN  
CELLULAR AND  
BIOMIMETIC TISSUE  
SCAFFOLD  
ENVIRONMENTS**

## **5.1 Preface**

In this chapter, results on Fn unfolding activity monitoring are presented. These extracellular matrix (ECM) protein conformational changes were observed and analysed overtime upon incubation with gold-edge coated TSNP (AuTSNP) in the cellular environment. Two cell lines were used for these experiments to highlight the high sensitivity of AuTSNP to detect and monitor protein behaviour within different high background noise cellular environments as well as in the presence of biomimetic bone tissue regeneration scaffolds which mimic the native extracellular matrix.

## **5.2 Fn activity monitoring within C2C12 cells**

Fn unfolding activity was monitored overtime within cell culture in C2C12 myoblast cells. Active and denatured Fn functionalised PEGAuTSNP were incubated with C2C12 myoblast cells and the protein behaviour was compared over 32 hours in time points of 0 h, 3 h, 8 h, 24 h, and 32 h. This was carried out to guarantee that the LSPR redshifts overtime corresponded to active Fn extension activity and fibril formation, and discard non-specific binding of other elements present in the cell culture media such as hormones, growth factors, among others (Arora, 2013). Three different denaturing times were tested to determine the most effective time required to adequately degrade the Fn and impede its response to the ECM biological cues which mediate its formation into fibrils.



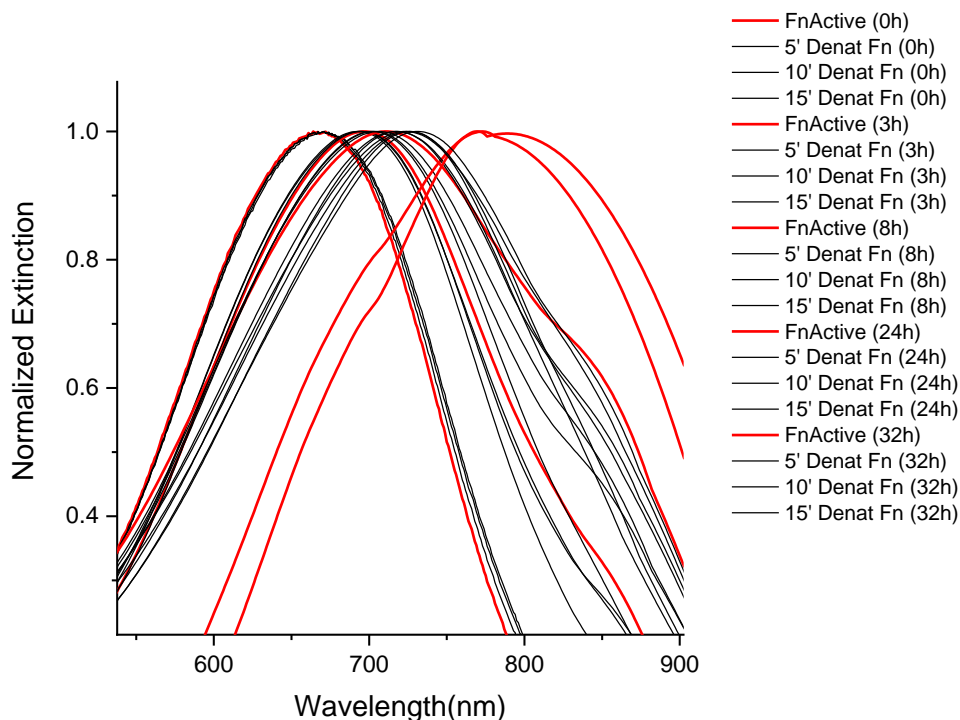


Figure 37. LSPR spectra of active (red) and denatured (black) Fn functionalised PEG- AuTSNP at different denaturing times where longer shifts for active Fn can be observed.

As shown in Figure 37, LSPR measurements showed considerable red shifts for the active protein compared to the denatured protein regardless of the denaturing time. The active protein showed shifts of approximately ~30 nm between 0 h and 8 h of incubation, while longer shifts of approximately 80 nm were measured at 24 h. The denatured Fn (15 minutes) incubated with C2C12 cells followed a similar  $LSPR_{max}$  profile up to the 24 h time point. Beyond this time point, further red shifts were shown for the active Fn (~46 nm) compared with minimal shifts for the denatured protein (~6 nm).

This can be attributed to the expected unfolding and extension activity, and progressive fibrillar organization of the active protein overtime, compared to the denatured Fn within the cellular environment (Rozario et al., 2010). These results correlate with the most recent studies by Antia et al (2009) on Fn unfolding behaviour within the extracellular matrix, where fluorescence studies were carried out to detect major changes in the conformation of this ECM protein providing evidence of increased

extension of Fn fibrils indicating matrix maturation and extracellular matrix ageing (Antia et al., 2008; Gourdon et al., 2015).

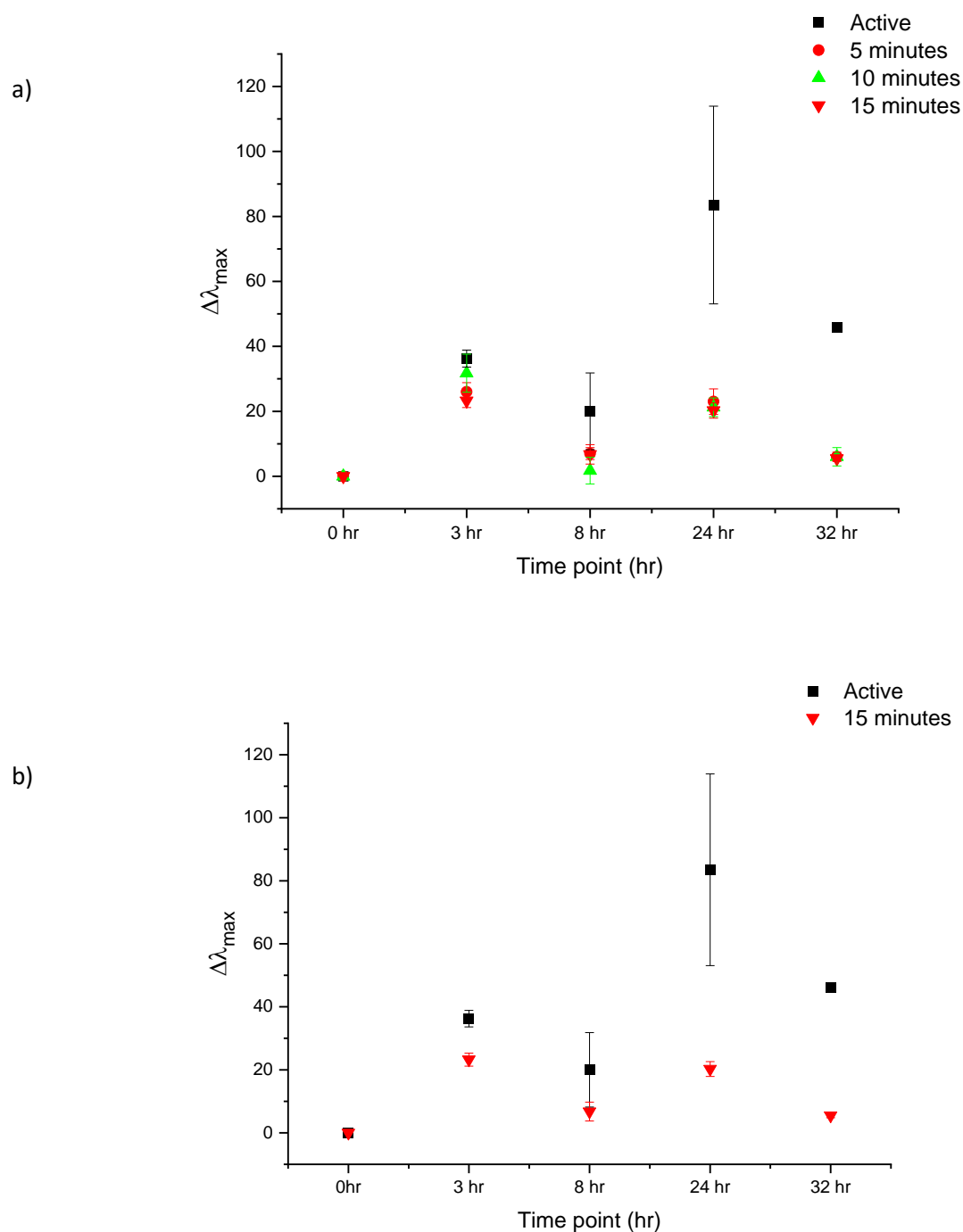


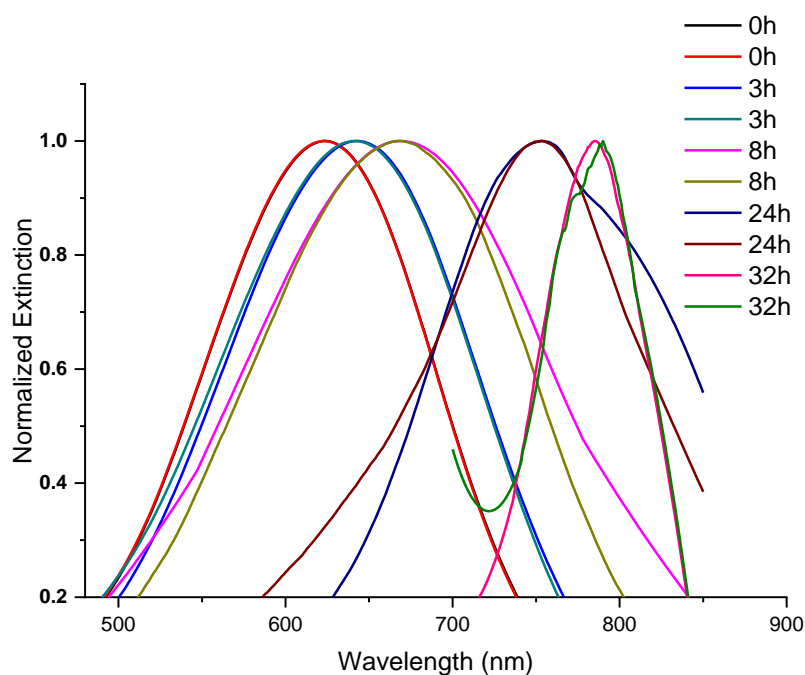
Figure 38. (a) LSPR spectral shift measurements of active and denatured Fn functionalised PEG- AuTSNP at different denaturing times (b) LSPR spectral shift measurements of active and denatured Fn functionalised PEG- AuTSNP at the most effective denaturing time.

As observed in Figure 38, the most effective protein-denaturation time was determined to be 15 minutes in a water bath at 95 °C. The clear higher shift of active Fn has been demonstrated to progressively rise as the degree of degradation of the denatured Fn increases. These results highlight the effectiveness of PEGAuTSNP to detect active protein conformational transitions over high noise cellular environments.

### 5.2.1 Fn activity monitoring within C2C12 cells in the presence of bone tissue regeneration scaffolds

Active Fn functionalised PEGAuTSNP were incubated with C2C12 myoblast cells and Cs-HAp scaffolds, and monitored over 32 hours in time points of 0 h, 3 h, 8 h, 24 h, and 32h. Fn behaviour overtime was detected using LSPR shifts to record fibril formation of the protein and interaction with the nanoplates in the presence of Cs-HAp regeneration scaffolds.

a)



b)

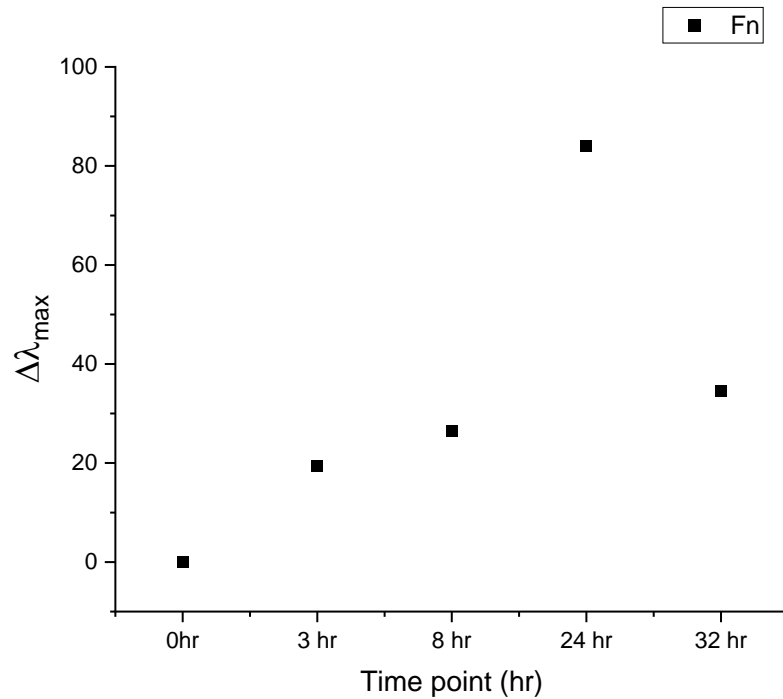
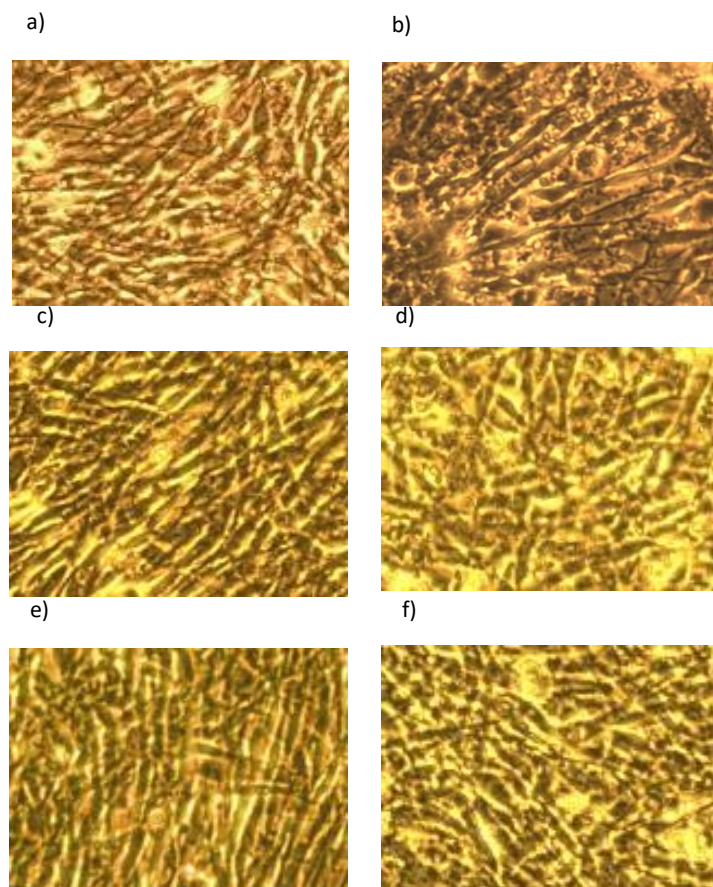


Figure 39. (a) LSPR spectral peaks and (b)  $\Delta\lambda_{\max}$  shift measurements of active Fn PEGAuTSNP incubated with C2C12 myoblasts and Cs-HAp regeneration scaffolds overtime.

Similar behaviour to active Fn without the presence of the tissue regeneration scaffolds was observed in this experiment. Redshifts of approximately ~20 nm between 0h and 8h were measured, and longer shifts were observed from the 24 h of incubation time point onwards (~80 nm). After 24 h the scaffolds showed an interaction with the nanoplates and the cells, as can be observed in Figure 39a, however, clear strong LSPR spectrum can be perceived. Nevertheless, in future experiments, PEGAuTSNP: culture media ratio could be modified in order to enhance the LSPR signal.



*Figure 40. Images of C2C12 cells taken after 32 hours of incubation with (a) Fn, (b) Fn and scaffold, (c) Fn PEGAuTSNP, (d) Fn PEGAuTSNP and scaffold, (e) PEGAuTSNP, f) PEGAuTSNP and scaffold. Cells confluence and growth was maintained overtime upon incubation with all treatments.*

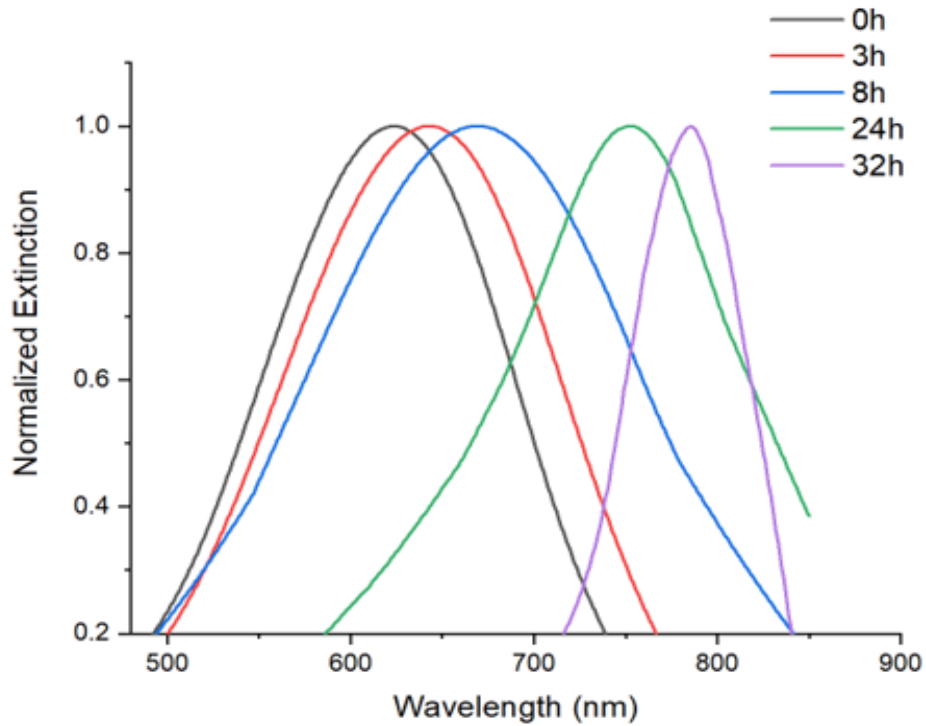
In both experiments, cells were observed under the inverted light-microscope Olympus CKX4 after 32 h and normal C2C12 myoblast cell morphology was observed in all treatments as shown in Figure 40. There was no observable detrimental effect from the nanoplates nor the scaffold on the cells as confluence and growth was maintained overtime upon incubation with Fn functionalised PEGAuTSNP, unfunctionalised PEGAuTSNP and Cs-HAp regeneration scaffolds.

### **5.3 Fn activity monitoring within MC3T3-E1 cells**

After successful results on Fn activity tracking within C2C12 myoblasts, similar experiments were carried out in the presence of MC3T3-E1 preosteoblast cells. Active Fn functionalised PEGAuTSNP, Bovine Serum Albumin (BSA) functionalised PEGAuTSNP and unfunctionalised PEGAuTSNP were incubated with MC3T3-E1 pre-

osteoblast cells, and monitored over 32 hours in time points of 0 h, 3 h, 8 h, 24 h, and 32 h. Considerable redshifts can be observed for active Fibronectin where shifts over 100 nm are reached after 32 hours, while limited shifting is observed for the denatured protein (~60 nm) as shown in Figure 41.

a)



b)

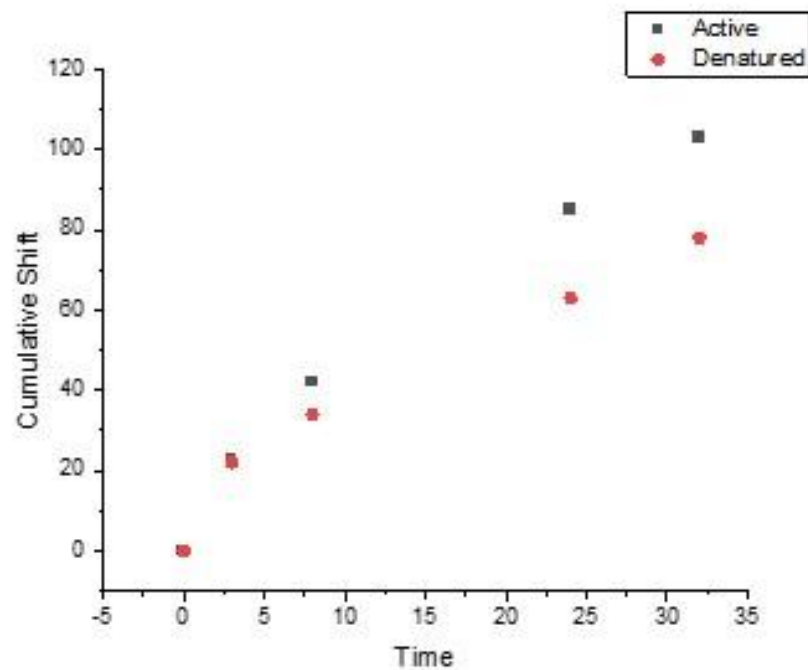


Figure 41. (a) LSPR spectral peaks and (b) Cumulative shift measurements of active and denatured Fn PEGAuTSNP incubated with MC3T3-E1 pre-osteoblasts. Significant redshifts were observed for active Fn with shifts over 100 nm reached after 32 h. Limited shifting was observed for the denatured protein.

BSA functionalised PEGAuTSNP were incubated in this experiment as a second negative control on protein extension activity. BSA has been used in similar protein monitoring experiments to provide controls to track nanoplate protein corona formation and non-specific binding (Brennan-Fournet et al., 2015). Moreover, previous studies have shown that BSA PEGAuTSNP are degraded overtime due to cellular conditions.

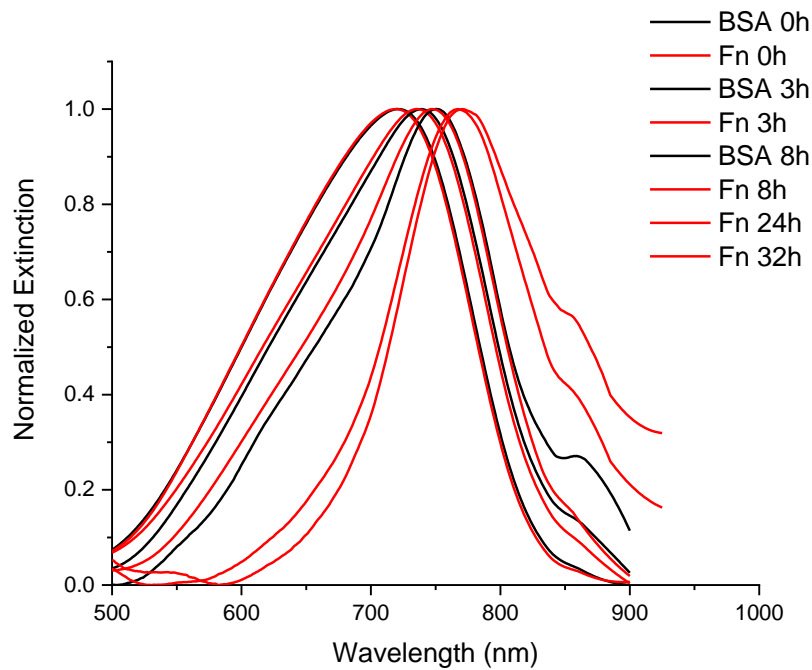


Figure 42. LSPR spectra of active Fn PEGAuTSNP (red) and BSA PEGAuTSNP (black) incubated with MC3T3-E1 pre-osteoblasts overtime. No spectral recordings were obtained for BSA PEGAuTSNP after 8 h due to degradation within the cellular environment.

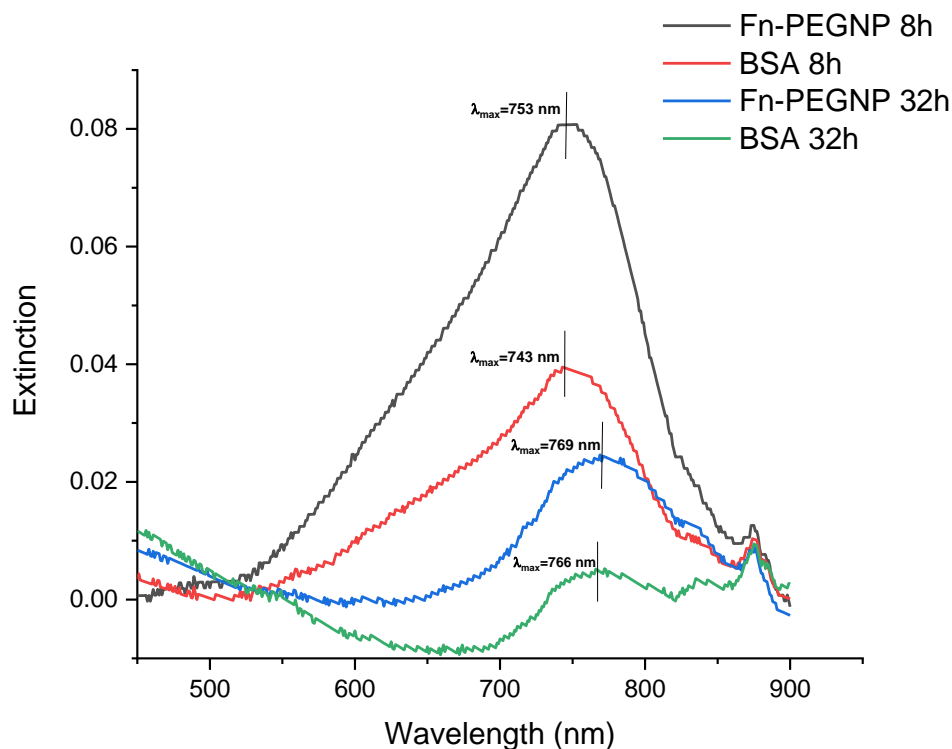


Figure 43. Un-smoothed and un-normalised LSPR spectra of active Fn PEGAuTSNP and BSA PEGAuTSNP incubated with MC3T3-E1 cells at 8h and 32h time points showing BSA degradation.

As observed in Figure 42, BSA behaviour overtime was similar than that of Fn with critical differences in the LSPR spectra which can be attributed to BSA PEGAuTSNP degradation due to cellular conditions resulting in a reduced spectral intensity in comparison to Fn PEGAuTSNP. LSPR recordings for the last time points, 24 h and 32 h, were unclear. This is illustrated in Figure 43 with un-smoothed and un-normalised LSPR spectra where evident degradation of BSA within the cellular environment can be perceived, nonetheless, spectral shifts for Fn overtime were recorded. This degradation of BSA PEGAuTSNP within the cellular environment occurred after only 8 h of incubation within MC3T3-E1 cells and spectra is weaker and nearly unreadable in the 32 h time point. Broadness of the spectrum can be observed and credited to non-specific binding of other cellular proteins and constituents (Brennan-Fournet et al., 2015).

In future experiments, both BSA and denatured Fn functionalised nanoplates will be analysed in the same assays to compare as non-specific binding is expected from the results, nonetheless, the extinction LSPR of Fn PEGAuTSNP and denatured Fn



PEGAuTSNP is expected to retain as there is strong attachment and insulating effect of the Fn on the AuTSNP from cellular degradation.

### 5.3.1 Fn activity monitoring within MC3T3-E1 cells in the presence of bone tissue regeneration scaffolds

Active and denatured Fn functionalised PEGAuTSNP were incubated with MC3T3-E1 pre-osteoblast cells and Cs-HAp scaffolds, and monitored over 32 hours in time points of 0 h, 3 h, 8 h, 24 h, and 32 h. Fn behaviour overtime was detected using LSPR shifts to record Fn extension and fibrillar organization activity, as well as interaction with the nanoplates when in presence of bone regeneration scaffolds.

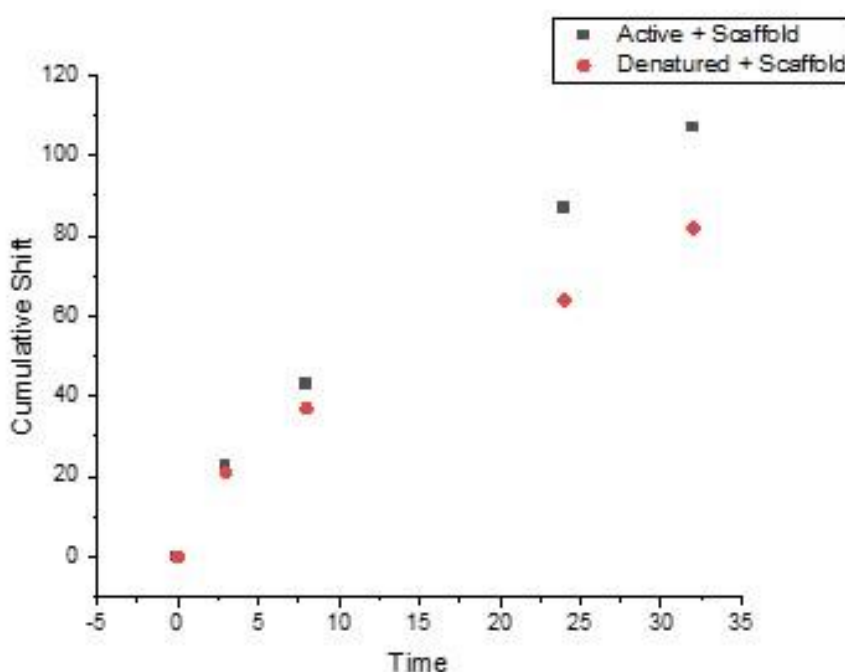
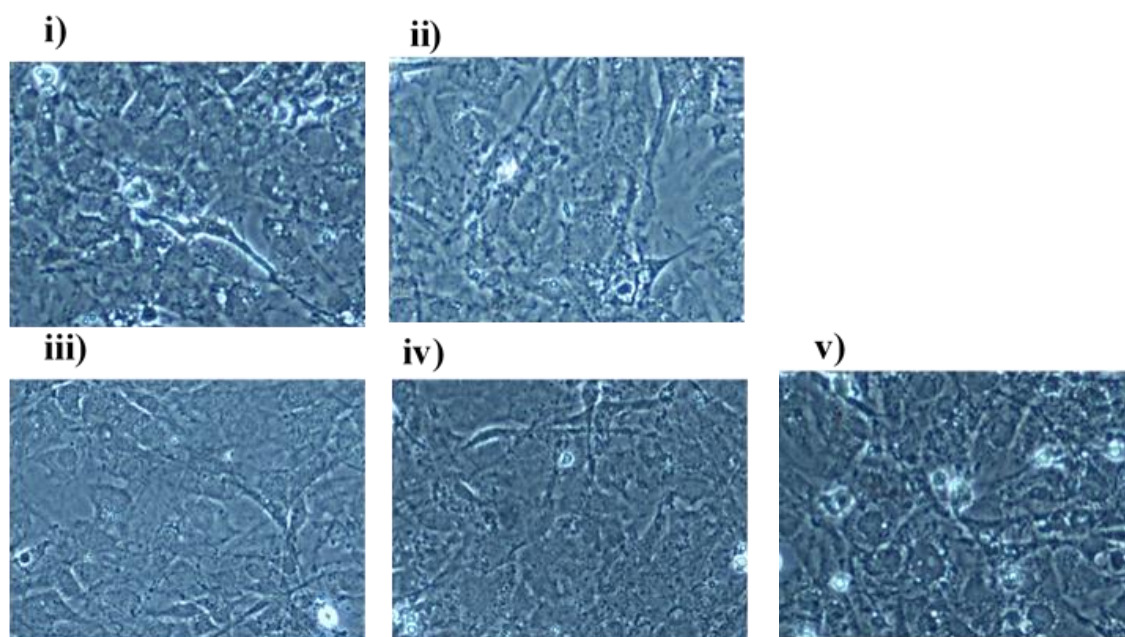


Figure 44. Cumulative shift measurements of active and denatured Fn PEGAuTSNP incubated with MC3T3-E1 pre-osteoblasts in the presence of Cs-HAp bone tissue regeneration scaffolds. Considerable redshifts were observed for active Fn while limited shifting was observed for the denatured protein.

Similar to previous experiments, longer shifts can be observed for the active protein, and limited shifting is observed for the denatured protein. Shifts as long as 44 nm are recorded for the active protein around the 24 h time point and total shifting of 103 nm is observed by the end of the experiment at 32 h. For the denatured protein, shorter shifts of 18 nm can be observed with total shifting of 78 nm by the 32h time point

(Figure 44). These results are in keeping with the expected behaviour of Fn extension activity within the ECM of the cellular environment.



*Figure 45. Images of MC3T3-E1 cells taken after 32h of incubation with (i) Active Fn-PEG-Np, (ii) Denatured Fn-PEG-NP, (iii) Active Fn-PEG-Np and scaffold, (iv) Denatured Fn-PEG-Np and scaffold, (v) BSA-PEG-NP. Typical morphology was observed regardless of the treatment.*

At the end of the experiment cells were observed under inverted light-microscope. Typical MC3T3 pre-osteoblast cell morphology was observed in all treatments as shown in Figure 45. No detrimental effect was observed from the nanoplates or the scaffold on the cells with growth and optimal confluence maintained overtime upon incubation with active and denatured Fn functionalised PEGAuTSNP, and Cs-HAP regeneration scaffolds.

#### **5.4 On-scaffold loaded Fn activity monitoring within MC3T3-E1 cells**

On-scaffold loaded Fibronectin was monitored in its active and denatured forms within the presence of MC3T3-E1 cells. The scaffolds used were in a hydrogel format in a clear transparent colour to avoid interferences with the dark blue colour of the AuTSNP. Fn was monitored over 32 hours at 5 different time points (0 h, 3 h, 8 h, 24 h, and 32 h) to observe conformational changes of the protein within the ECM of the cells over time.

Active Fn showed increasing extension activity after every time point resulting in longer shifts. Contrastingly, denatured Fn showed smaller shifts overtime, similar performance to previous experiments where the non-significant shifts correspond to non-specific binding of other media constituents but not the fibrillar formation activity of Fn.

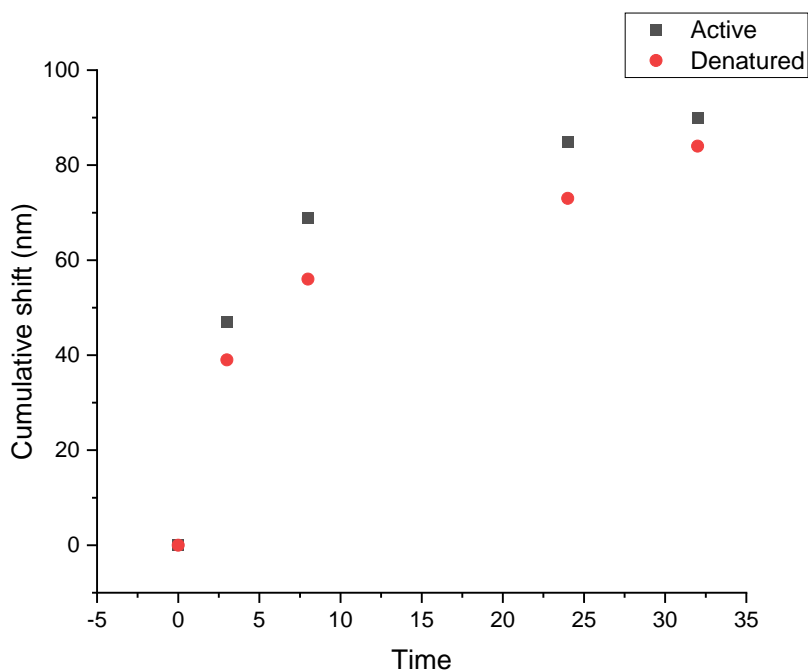


*Figure 46. Cumulative shift measurements of active and denatured Fn on-scaffold incubated with MC3T3-E1 pre-osteoblasts. Similar shifting behaviour was observed with longer shifts for active Fn and limited shifting for denatured Fn.*

Fn fibrils from the functionalised AuTSNP, and Fn-hydrogel fibrils were expected to merge together with the cells ECM, resulting in protein extension and fibrillar organization leading to longer shifts overtime. It has been reported that Fn is assembled into fibrils of the ECM and it has been studied mainly in cell culture, where the protein binds to molecules on the cells surface (including integrins and syndecans) and additionally recruits other Fn molecules to form fibrils (Maurer et al., 2015).

## 5.5 Summary

The work outlined in this chapter describes the monitoring of the ECM protein Fn activity within the cellular environment. Protein functionalised nanoplates were

incubated with C2C12 cells and monitored overtime expecting redshifts in the LSPR spectra as a result of Fn unfolding overtime and fibril formation within the extracellular matrix. Results correlated with previous studies on Fn activity. These results were validated by monitoring denatured Fn functionalised nanoplates where shorter shifts were expected as the protein's degradation impedes its fibril formation activity.

In this chapter, experiments on Fn conformational activity in the presence of bone tissue regeneration scaffolds are also described. Similar results to previous experiments without the presence of scaffolds were observed which indicates the effectiveness of the PEGAuTSNP to detect protein dynamics within complex cellular environments. After every experiment the cells were observed under the microscope to verify there was no detrimental effect of the nanoplates on the cells.

Fn monitoring experiments within a different cell line, MC3T3-E1 pre-osteoblasts, were further outlined in this chapter. LSPR recordings were expected to redshift overtime as observed with the previous cell line. The results were validated by monitoring BSA functionalised nanoplates where degradation of BSA was expected as it is known to be broken down in high salinity environments.

Additionally, on-scaffold loaded Fn was monitored overtime. Fabrication of the bone tissue regeneration scaffolds was modified to achieve a hydrogel consistency to readily monitor the loaded protein onto the scaffold over time within the presence of cells. Results were in agreement with previous experiments with the traditional scaffolds where longer shifts were observed for the active protein and limited shifting was recorded for denatured Fn.

After demonstrating the high sensitivity of the PEGAuTSNP to study protein dynamics, the next step is to test the ability of PEGAuTSNP to detect binding of an antibody-antigen complex within dynamic environments.

**CHAPTER 6.**

**NANOPLATE-BASED  
IMMUNOASSAYS WITH  
FIBRONECTIN AND  
ANTI-FIBRONECTIN  
ANTIBODY**

## 6.1 Preface

In this chapter a nanoplate-based platform for immunological testing is outlined. The sensitivity and suitability of the nanoplates LSPR system for antibody (Ab)-antigen (Ag) binding testing was assessed. Fibronectin and its corresponding antibody were used as model proteins for the Ab-Ag system testing where the protein concentrations to successfully cover the nanoplates was determined to avoid non-specific binding in future testing within high noise environments. Moreover, the limit of the detection of the antibody-antigen system was analysed by exposing Fn functionalised nanoplates to different concentrations of the antibody.

The high sensitivity of the AuTSNP as tools for immunoassays is demonstrated through Ab-Ag binding analysis within isolated extracellular matrix as a complex environment. The Anti-Fn functionalised nanoplates bind to the corresponding antigen Fn in its native environment.

## 6.2 Nanoplate-based immunoassay system testing with active and denatured Fn

Several concentrations of Fn were added to 1 mL PEGAuTSNP aliquots to determine the minimum amount of the protein to successfully cover the nanoplates and observe differences in the spectrum and a  $\mu\text{g}$  of Anti-Fn was added afterwards to analyse binding. After that, denatured Fn was used as a negative control for Fn- AntiFn binding.

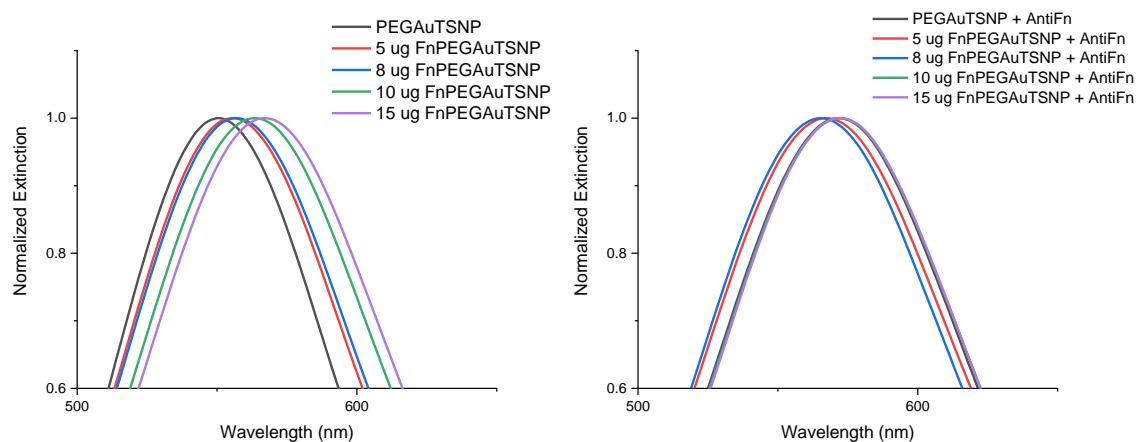


Figure 47. LSPR spectra of FnPEGAuTSNP before (left) and after (right) addition of Anti-Fn antibody.

Table 3.  $\lambda_{max}$  of Fn-PEGAuTSNP before and after addition of Anti-Fn

<i>Fn Concentration</i>	<b>0 <math>\mu\text{g}</math> (bare NP)</b>	<b>5 <math>\mu\text{g}</math></b>	<b>8 <math>\mu\text{g}</math></b>	<b>10 <math>\mu\text{g}</math></b>	<b>15 <math>\mu\text{g}</math></b>
$\lambda_{max}$ Before	550	556	557	564	567
$\lambda_{max}$ With Abs	571	567	565	572	572
$\Delta\lambda$	21	11	8	8	5

As reflected in Figure 47, changes in the spectra were observed with low concentrations of Fn. Results show that when higher concentrations of the protein were added to PEGAuTSNP, longer red shifts were recorded as expected (Figure 47 left). For all added amounts of Fn, a red shift in the  $\lambda_{max}$  was observed upon addition of Anti-Fn (Figure 47 right). In table 3, expanded results show that shorter red shifts are recorded in higher Fn concentration samples once the Anti-Fn is added. This could be attributed to the Anti-Fn binding to free-unattached Fn within the nanoplates solution which would lead to no detection from the nanoplates, and only minimal binding of AntiFn to Fn-PEGAuTSNP recorded.

To validate the binding of Fn to its antibody AntiFn, a second analysis was carried out with denatured Fn-PEGAuTSNP (1  $\mu\text{g}$  Denat Fn) followed by the addition of 1  $\mu\text{g}$  Anti Fn upon the first analysis. As shown in Figure 48, there was no significant change in the  $\lambda_{max}$  of the PEGAuTSNP (~597 nm) and the denatured Fn-PEGAuTSNP (~595 nm), nevertheless, once the Anti-Fn was added, a shift of 15 nm (610 nm) was registered.

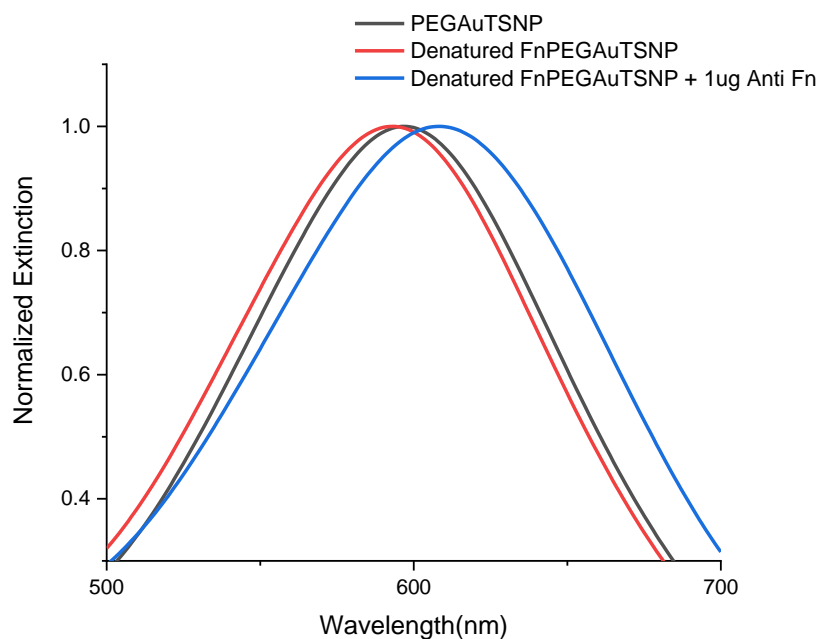


Figure 48. LSPR spectra of denatured Fn-PEGAuTSNP before and after addition of Anti-Fn antibody. No significant change was observed in  $\lambda_{max}$  for PEGAuTSNP and denatured Fn PEGAuTSNP. A 15 nm shift was recorded upon addition of AntiFn.

The 15 nm redshift observed for the denatured protein could be a result of the antibody binding directly to the PEGAuTSNP surface since fibronectin is denatured and potentially disintegrated upon high heat inactivation. According to T. Li et al. (2021), heat treatment causes changes in protein structure which could inhibit its binding capacity of the epitopes to antibodies (T. Li et al., 2021).

### 6.2.1 Nanoplate-based immunoassay system testing with spun-down Fn functionalised PEGAuTSNP

To evaluate the previously stated hypothesis about the antibody binding to free Fn at higher concentrations, a different approach was tested where the Fn-PEGAuTSNP samples were centrifuged and analysed before and after the addition of 1  $\mu$ g of Anti-Fn and compared to the previous non-centrifuged samples.



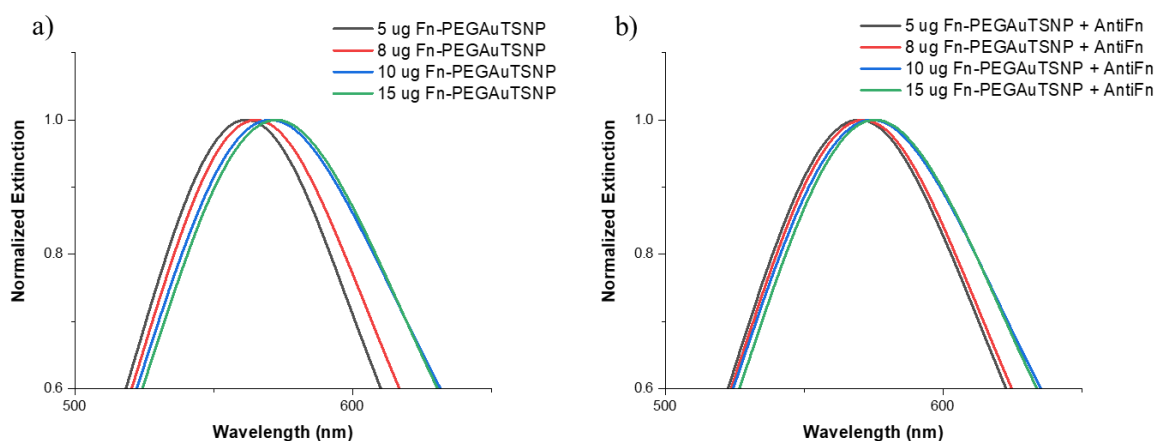


Figure 49. LSPR spectra of centrifuged Fn-PEGAuTSNP s (a) before and (b) after AntiFn antibody

Table 4.  $\lambda_{max}$  for increasing Fn volumes before and after addition of Anti-Fn for centrifuged samples

<b>Fn concentration</b>	<b>0 <math>\mu\text{g}</math> (bare NP)</b>	<b>5 <math>\mu\text{g}</math></b>	<b>8 <math>\mu\text{g}</math></b>	<b>10 <math>\mu\text{g}</math></b>	<b>15 <math>\mu\text{g}</math></b>
<b><math>\lambda_{max}</math> Before AntiFn (nm)</b>	550	562	565	570	572
<b><math>\lambda_{max}</math> After AntiFn (nm)</b>	571	570	571	574	576
<b><math>\Delta\lambda</math> (nm)</b>	21	8	6	4	4

As presented in Table 4, the  $\lambda_{max}$ es of centrifuged Fn-PEGAuTSNP before exposure to Anti-Fn compared to previous non-centrifuged nanoplates (Table 3) was between 4 nm and 8 nm more redshifted potentially due to the higher concentration of Fn coated nanoplates after centrifugation. Upon addition of AntiFn, shorter shifts are recorded for the higher concentrations of Fn in Fn-PEGAuTSNP similar to earlier experiments, suggesting minor differences between centrifuged and non-centrifuged samples.

Results from sections 6.2 and 6.2.1 have shown constant decrease in shifting after higher Fn concentration Fn-PEGAuTSNP are exposed to the antibody. It can be observed that Fn concentrations of 8  $\mu\text{g}$ , 10  $\mu\text{g}$  and 15  $\mu\text{g}$  show limited shifts upon Anti-Fn binding suggesting saturation of the nanoplates surface. In next experiments the concentration of 5  $\mu\text{g}$  Fn/mL of PEGAuTSNP will be used as the starting concentration for Ag-Ab binding testing.

### 6.3 Nanoplate-based immunoassay with changing concentration of AntiFn antibody

The limit of detection of the Ag-Ab system was determined by exposing a sample of Fn-PEGAuTSNP to increasing concentrations of Anti-Fn antibody.

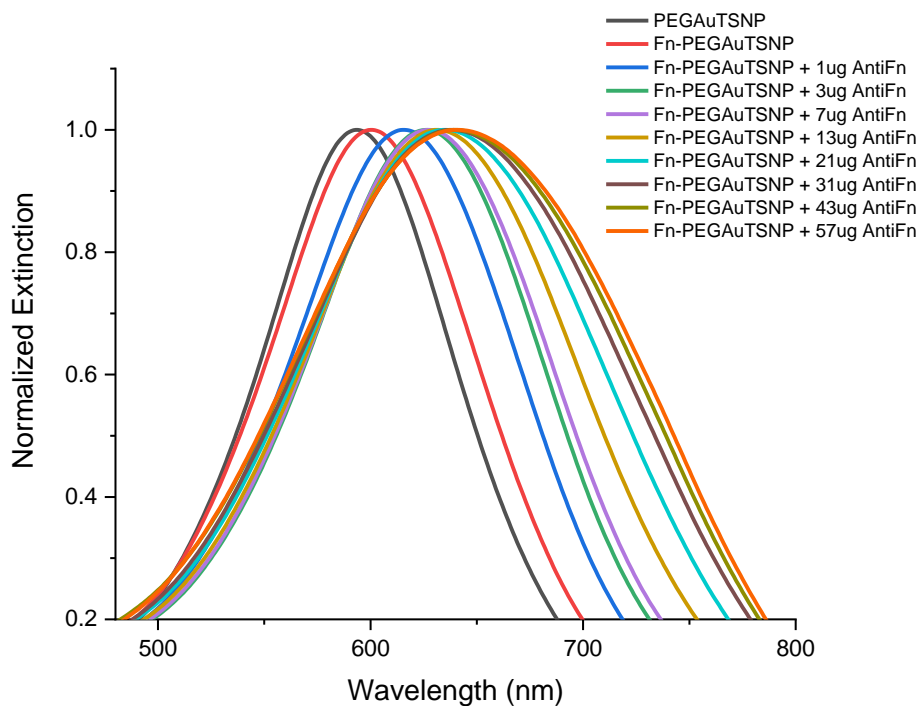


Figure 50. LSPR spectra of Fn-PEGAuTSNP upon addition of increasing concentrations of AntiFn. Redshifts were observed as the concentration of AntiFn increased indicating intensifying binding of the antibody to the Fn functionalised nanoplates.

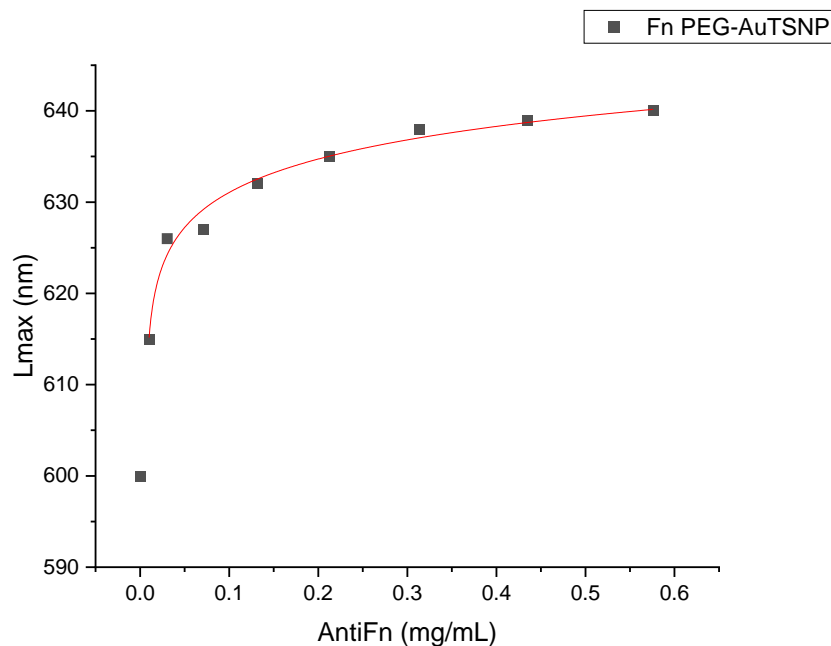


Figure 51. LSPR peak shift as a function of AntiFn concentration for Fn PEGAuTSNP. There was detection of Fn-AntiFn binding with AntiFn concentrations of 0.01 mg/mL, and system saturation was observed from 0.212 mg/mL of AntiFn.

As observed in Figure 50, there is evident redshifting as the concentration of AntiFn increases, which indicates intensifying binding of the antibody to the Fn functionalised nanoplates. There is detection of Fn-AntiFn binding with AntiFn concentrations of 0.01 mg/mL, and that shorter redshifts are recorded for the highest concentrations of antibody, indicating system saturation from 0.212 mg/mL of AntiFn (Figure 51). This correlates with the studies by Y. Zhang et al. (2014) where cytidine 50-diphosphocholine (PC)-coated AuTSNP detect C-reactive protein (CRP) in concentrations as low as 0.0000033 mg/mL showing the remarkable features of the AuTSNP and their wide-ranging limits of detection (Y. Zhang et al., 2014).

#### 6.4 Detection of native Fn using Anti-Fn antibody-functionalised PEGAuTSNP

The sensitivity of Fn antibody functionalised nanoplates to detect its corresponding antigen within its native environment was tested. AntiFn-PEGAuTSNP were exposed to different concentrations of cell-extracted ECM as a complex and native environment of Fn.

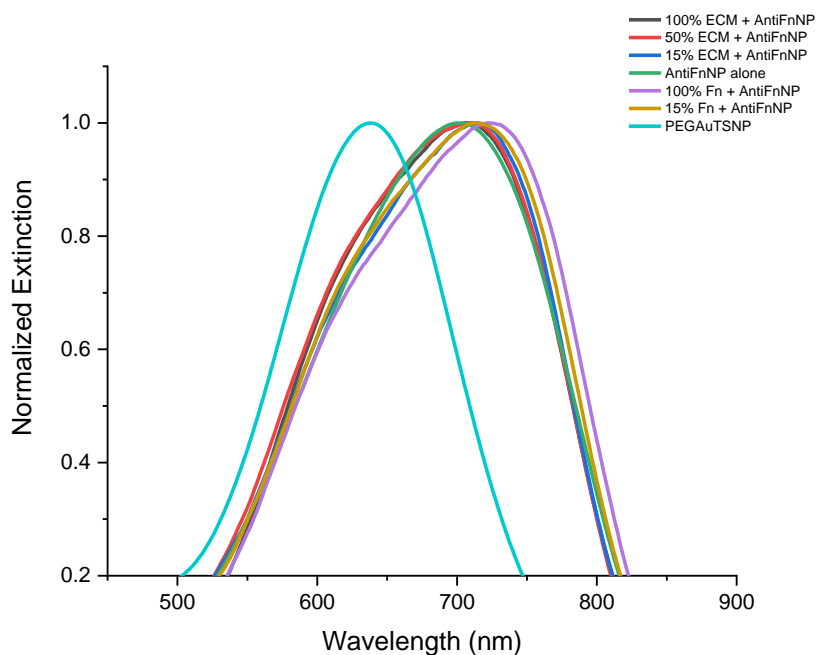


Figure 52. LSPR spectra of AntiFn-Native Fn binding experiment

Table 5.  $\lambda_{max}$  of AntiFn-PEGAuTSNP within different concentrations of ECM

<b><i>Treatment</i></b>	<b><i><math>\lambda_{max}</math></i></b>
<b><i>PEGAuTSNP</i></b>	638 nm
<b><i>AntiFn-PEGAuTSNP</i></b>	703 nm
<b><i>100% ECM + AntiFn-PEGAuTSNP</i></b>	707 nm
<b><i>50% ECM + AntiFn-PEGAuTSNP</i></b>	711 nm
<b><i>15% ECM + AntiFn-PEGAuTSNP</i></b>	715 nm
<b><i>100% Fn + AntiFn-PEGAuTSNP</i></b>	723 nm
<b><i>15% Fn + AntiFn-PEGAuTSNP</i></b>	714 nm

According to Table 5 PEGAuTSNP  $\lambda_{max}$  was recorded at 638 nm and upon functionalisation with Anti-Fn, a shift of 65 nm was observed indicating successful coating of the nanoplates with the antibody. Following this, the functionalised

nanoplates were exposed to different concentrations of cell-isolated ECM and analysed, showing a shifting profile different than expected with longer shifts recorded for the less concentrated ECM samples. One of the reasons could be attributed to the clumping of ECM proteins as a result of the cell scraping performed in the isolation protocol, impeding Fn binding sites to be sufficiently exposed to bind to its corresponding antibody; once the sample is diluted, the proteins disaggregate and Fn is exposed. According to Sediq et al. (2016), one of the reasons for protein aggregation is the induced mechanical stress during friction of two solid surfaces, in this case, the cell scraper and the flask containing the cell culture. In future testing, ECM samples can be briefly homogenised to make the proteins scatter and aid in binding site recognition for the antigen of interest (Sediq et al., 2016).

Nonetheless, for all concentrations of ECM the shift recorded is positive from 4 nm to 12 nm shifts indicating binding of AntiFn-PEGAuTSNP to native Fn. This was validated with the addition of 100% and 15% purified Fn (non-native) as positive controls, where expected redshifts of 20 nm and 11 nm, respectively, were recorded.

Further testing was carried out with the use of AntiTJP1-PEGAuTSNP as negative control for binding since it is a human -tight junction protein 1 (TJP1) targeted antibody non-specific to Fn.

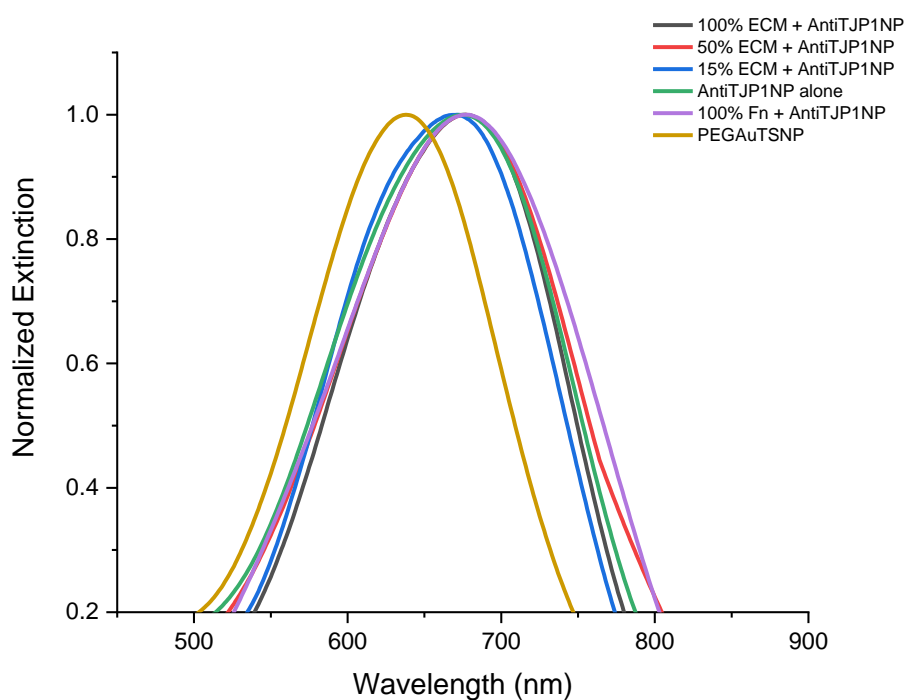


Figure 53. LSPR spectra of AntiTJP1-AntiFn binding experiment

Table 6.  $\lambda_{max}$  of AntiTJP1-PEGAuTSNP within different concentrations of ECM

<b><i>Treatment</i></b>	<b><i><math>\lambda_{max}</math></i></b>
<b><i>PEGAuTSNP</i></b>	638 nm
<b><i>AntiTJP1-PEGAuTSNP</i></b>	675 nm
<b><i>100% ECM + AntiTJP1-PEGAuTSNP</i></b>	677 nm
<b><i>50% ECM + AntiTJP1-PEGAuTSNP</i></b>	677 nm
<b><i>15% ECM + AntiTJP1-PEGAuTSNP</i></b>	671 nm
<b><i>100% Fn + AntiTJP1-PEGAuTSNP</i></b>	678 nm

As shown in Table 6 a shift of 37 nm was recorded for PEGAuTSNP upon addition of AntiTJP1, indicating functionalisation of the nanoplates with the antibody. When the nanoplates were exposed to the different concentrations of ECM extract, limited shifts

between 1-2 nm were observed. These results show the TJP1 antibody did not recognise epitopes from proteins in the MC3T3-E1 isolated ECM. Similar behaviour was observed when the TJP1 antibody-functionalised nanoplates were exposed to purified Fn with a 3 nm shift compared to ~20 nm shifts when Fn is exposed to AntiFn-PEGAuTSNP.

## **6.5 Summary**

Along this chapter, the ability of PEGAuTSNP for their use as platforms for immunoassays was successfully demonstrated. The effective protein concentrations to functionalise the nanoplates and avoid potential non-specific binding were determined. The Ab-Ag binding was detected within a complex environment where native Fn from the extracellular matrix was successfully detected by using Anti-Fn antibody-coated nanoplates.

The results were validated with the use of PEGAuTSNP functionalised with human-specific Anti-TJP1, which showed limited shifting when exposed to the isolated extracellular matrix in comparison to Anti-Fn which displayed strong redshifts as a result of their specificity to detect native Fn.

In the next chapter, a potential platform for the detection of COVID-19 will be presented by using PEGAuTSNP functionalised with SARS-CoV-2 Spike protein and its corresponding antibody.

**CHAPTER 7.**

**NANOPLATE-BASED  
IMMUNOASSAYS FOR  
COVID-19 DETECTION**



## 7.1 Preface

In this chapter, the development of a potential platform for SARS-CoV-2 Spike protein detection is presented. The adequate working-concentrations to effectively cover the nanoplates surface and act as a starting point for the optimization of the immunoassay are described. The detection platform is tested in a direct assay with Spike-PEGAuTSNP, its antibody conjugate Anti-Spike, and TJP1-PEGAuTSNP as a negative control. This is in addition to a more complex experiment performed within horse serum (HS) acting as a dynamic environment to analyse the interaction between the Spike functionalised nanoplates and Anti-Spike antibody, and determine the suitability of the proposed system as well as the sensitivity of the nanoplates for its further development and future use in clinical settings.

## 7.2 Spike protein optimal functionalisation volume determination

To determine the Spike protein concentration to successfully cover the nanoplates' surface, a range of protein quantities were added to 1 mL PEGAuTSNP ( $\lambda_{\max}$ : 576 nm) samples and analysed. One  $\mu\text{g}$  of the Spike's corresponding antibody was added afterwards to analyse changes in the LSPR recordings.

Table 7.  $\lambda_{\max}$  recordings before and after addition of AntiSpike

<i>Spike concentration</i>	<i>1 <math>\mu\text{g}</math></i>	<i>3 <math>\mu\text{g}</math></i>	<i>5 <math>\mu\text{g}</math></i>	<i>7 <math>\mu\text{g}</math></i>	<i>10 <math>\mu\text{g}</math></i>
<i><math>\lambda_{\max}</math> before AntiSpike (nm)</i>	603	647	641	632	632
<i><math>\lambda_{\max}</math> after AntiSpike (nm)</i>	615	651	647	639	638
<i><math>\Delta\lambda</math>(nm)</i>	12	4	6	7	6

As shown in table 7, the recorded  $\lambda_{\max}$  for the Spike-functionalised PEGAuTSNP was higher as the concentrations of Spike protein increased. Nonetheless, between 5  $\mu\text{g}$  and 10  $\mu\text{g}$  of Spike functionalised nanoplates, the recorded  $\lambda_{\max}$  started to decrease and stabilized around 632 nm presumably indicating saturation of the nanoplates surface. This was tested by adding one  $\mu\text{g}$  of the Anti-Spike antibody, where a short increase in the  $\lambda_{\max}$  was predicted as a result of the further coverage of uncoated sections of the nanoplates, and the binding of the Ab-Ag complex.

Upon exposure to the antibody, results demonstrated higher  $\lambda_{\max}$  recordings for all samples as expected, however, the  $\lambda_{\max}$  for the samples with higher protein-concentrations between 5-10  $\mu\text{g}$  showed decreasing values, similar to the recordings prior to Anti-Spike addition. This could indicate the binding of the antibody only to the Spike protein available on the now fully functionalised nanoplates surface. The latter can be confirmed through the analysis of the  $\Delta\lambda$ , where it can be observed that between the concentrations of 5  $\mu\text{g}$  and 10  $\mu\text{g}$  of Spike in PEGAuTSNP, the shift difference is constant between 6 nm and 7 nm indicating the maximum possible binding of the Anti-Spike to spike was reached.

The aforementioned results suggest that the protein volume that successfully covers the nanoplates surface before the saturation point is between 3  $\mu\text{g}$  and 5  $\mu\text{g}$ . Considering this, a concentration of 4  $\mu\text{g}$  per mL of PEGAuTSNP was used for further testing.

### 7.3 Spike-PEGAuTSNP Detection Limits determination

Spike functionalised PEGAuTSNP were used with different amounts of Anti-Spike as described in section 3.14.2. As shown in Figure 54, expected redshifts were recorded for increasing concentrations of Anti-Spike which suggests intensifying binding of the antibody to the Spike functionalized nanoplates.

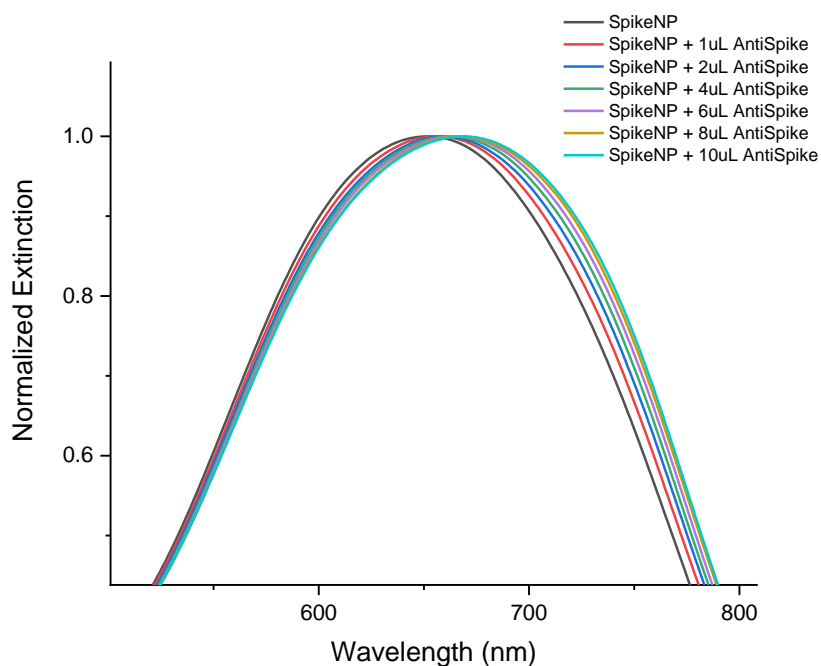


Figure 54. LSPR spectra of Spike PEGAuTSNP with increasing amounts of AntiSpike. Redshifts were observed as the concentration of AntiSpike increased indicating intensifying binding of the antibody to the Spike functionalised nanoplates.

It can be analysed from Figure 55 that binding of the Spike-AntiSpike complex can be detected with AntiSpike concentrations of 0.01 mg/mL. Moreover, shorter redshifts were observed for the highest concentrations of antibody, indicating Ab-Ag system saturation from 0.13 mg/mL of AntiFn. Hence, Spike-PEGAuTSNP detection limit was determined in a range of AntiSpike concentration between 0.01- 0.1 mg/mL. In a comparative study of (Dobrynin et al., 2022) detection limit ranges of rapid antigen tests were recorded between 0.0000098-0.0000786 mg/mL. This opens an area of opportunity to improve the proposed technique detection limits.

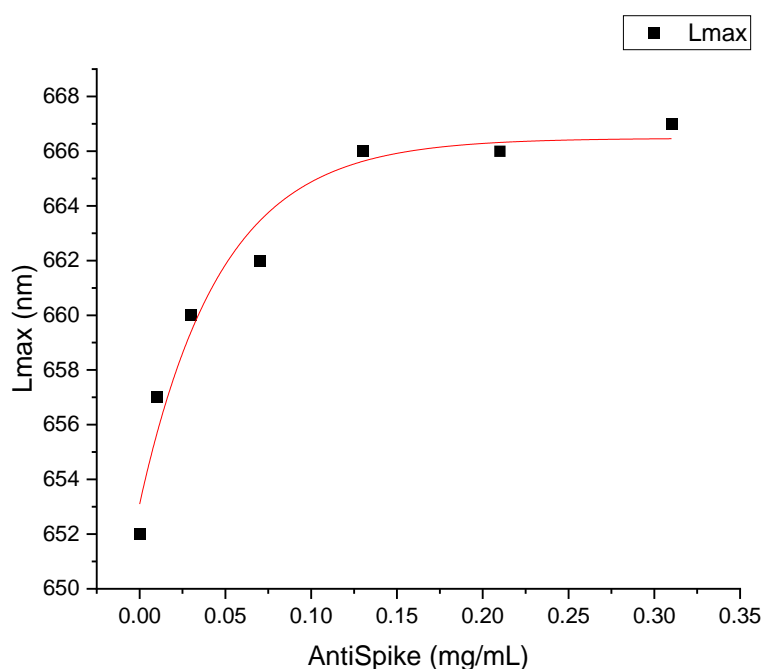


Figure 55. LSPR peak shift as a function of Anti-Spike concentration for Spike PEGAuTSNP. Spike-PEGAuTSNP detection limit was determined in a range of AntiSpike concentration between 0.01- 0.1 mg/mL.

#### 7.4 Specificity analysis of the Spike-AntiSpike system

Specificity of the Spike-AntiSpike system was tested with the previously established concentrations of Spike-PEGAuTSNP and AntiSpike as per detection limits curve (Figure 55). The TJP1 protein was used as a negative control for binding since

AntiSpike antibody is specific to Spike protein according to the manufacturer information.

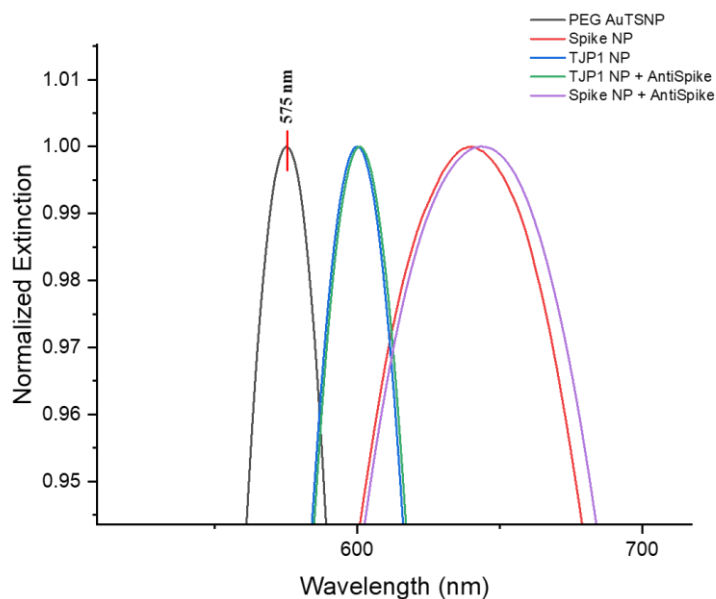


Figure 56. LSPR spectral shifts of PEGAuTSNP, Spike functionalised PEGAuTSNP, TJP1 functionalised PEGAuTSNP before and after exposure to AntiSpike

Table 8.  $\lambda_{max}$  for Spike-PEGAuTSNP and TJP1-PEGAuTSNP before and after addition of AntiSpike

	$\lambda_{max}$ Spike- PEGAuTSNP (nm)	$\lambda_{max}$ TJP1- PEGAuTSNP (nm)
<i>Before AntiSpike</i>	639	600
<i>After AntiSpike</i>	646	601
$\Delta\lambda$	7	1

As shown in Figure 56 the LSPR for bare PEGAuTSNP was recorded at 575 nm and redshifts of 65nm (to 639nm) and 25nm (to 600 nm) were observed upon functionalisation with Spike and TJP1 proteins respectively. According to Table 8, a shift of 7 nm for the Spike PEGAuTSNP was measured after exposure to its corresponding antibody, while a shift of only 1 nm was detected for the TJP1-PEGAuTSNP.

It is worth noting that the concentration of both stock proteins is  $\sim 1$ mg/mL and they are also similar in size, around 30 kDa for Spike and 33 kDa for TJP1(Maffei et al., 2021). Hence, the reduced shift of the TJP1 nanoplates (25nm) compared to the Spike nanoplates (65nm), suggesting weak attachment of the TJP1 protein to the

PEGAuTSNP surface. This can also be inferred when evident binding between the antibody and its Spike counterpart (7 nm) is observed, but there is almost no shifting (1 nm) with TJP1 and AntiSpike. This behaviour could indicate no recognition of the antibody, which would be expected, or a stronger affinity of the AntiSpike for the nanoplates causing a replacement on the nanoplates' surface.

DLS measurements will be carried out to further analyse the protein's behaviour. Additionally, Spike-AntiSpike binding interactions will be studied in the presence of horse serum (HS) as a high background noise environment to analyse the sensitivity of the nanoplates for the detection of protein interactions within complex mediums.

## 7.5 Spike protein detection-platform testing within horse serum

Binding of Spike to AntiSpike was analysed in the presence of HS as complex environment to study the nanoplates sensitivity. TJP1 was used as a control for binding.

Table 9.  $\lambda_{max}$  for Spike-PEGAuTSNP and TJP1-PEGAuTSNP treatments within HS before and after exposure to AntiSpike.

	<i>Spike NP</i>	<i>HS 100% + Spike</i>	<i>HS 50% + Spike</i>	<i>HS 10% + Spike</i>	<i>TJP1 NP</i>	<i>HS 100% + TJP1 NP</i>	<i>HS 50% + TJP1 NP</i>	<i>HS 10% + TJP1 NP</i>
<i><math>\lambda_{max}</math> before Antispike (nm)</i>	590	609	612	607	596	612	617	604
<i><math>\lambda_{max}</math> after Antispike (nm)</i>	603	617	619	609	597	620	620	606
<i><math>\Delta\lambda</math> (nm)</i>	13	8	7	2	1	8	3	2

As shown in table 9, the  $\lambda_{max}$  for the Spike functionalised PEGAuTSNP was initially recorded at 590 nm. As predicted, upon binding of the antibody to the Spike, a shift of 13 nm was detected. There was a similar behaviour in the cases where the Spike-PEGAuTSNP were in presence of HS at three different concentrations (100%, 50%, 10%), where positive shifts of 8 nm, 7 nm and 2 nm were recorded respectively. When TJP1-PEGAuTSNP (initial  $\lambda_{max}$ : 596 nm) were exposed to AntiSpike, a minimal shift

(1 nm) was recorded similar to previous experiments. Nonetheless, shifts of 8 nm, 3nm and 2 nm were recorded for TJP1-NP upon addition of the AntiSpike in the presence of HS. These unanticipated positive shifts in relation to TJP1 could be associated with non-specific binding of the HS components to the added AntiSpike. According to Riond et al. (2009), HS is a non-standardized component of blood with varying concentrations of several proteins, albumins and globulins, among other components; this could interrupt, obstruct or in this case, interfere with the predicted experiment behaviour (Riond et al., 2009).

Additional experiments were carried out only analysing TJP1 to confirm the previous results and further investigate the behaviour patterns the protein when exposed to AntiSpike within the presence of serum.

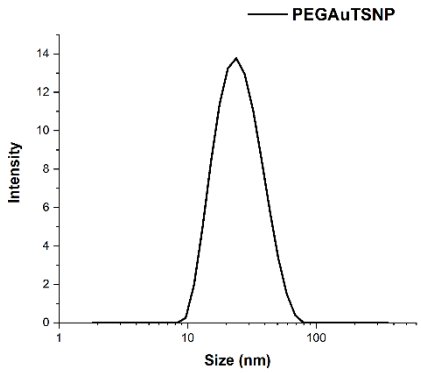
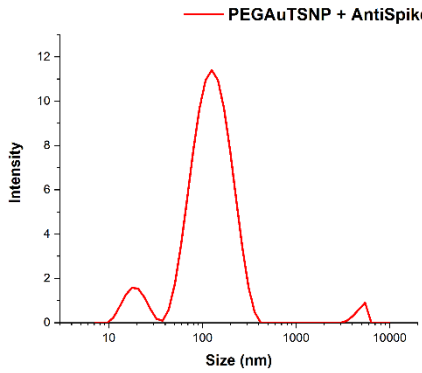
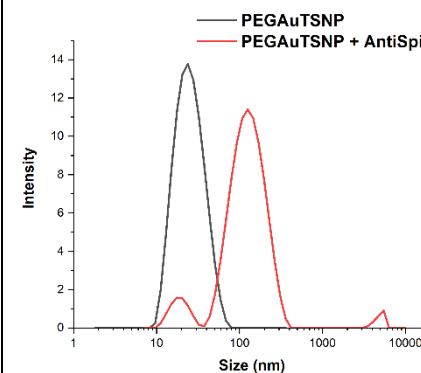
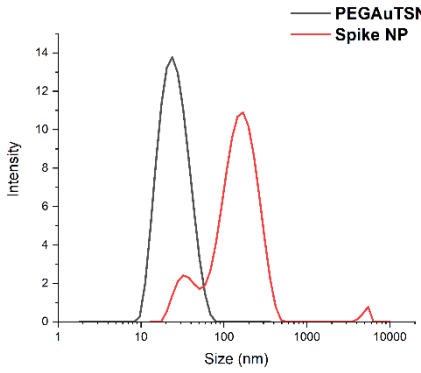
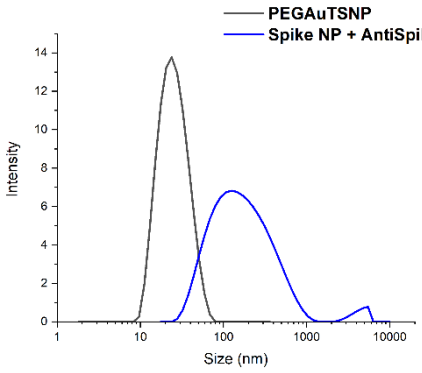
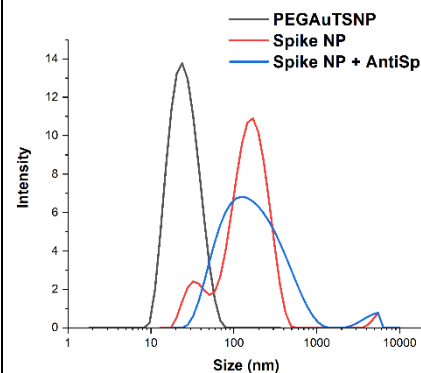
Table 10.  $\lambda_{max}$  for TJP1-PEGAuTSNP treatments within HS before and after exposure to AntiSpike.

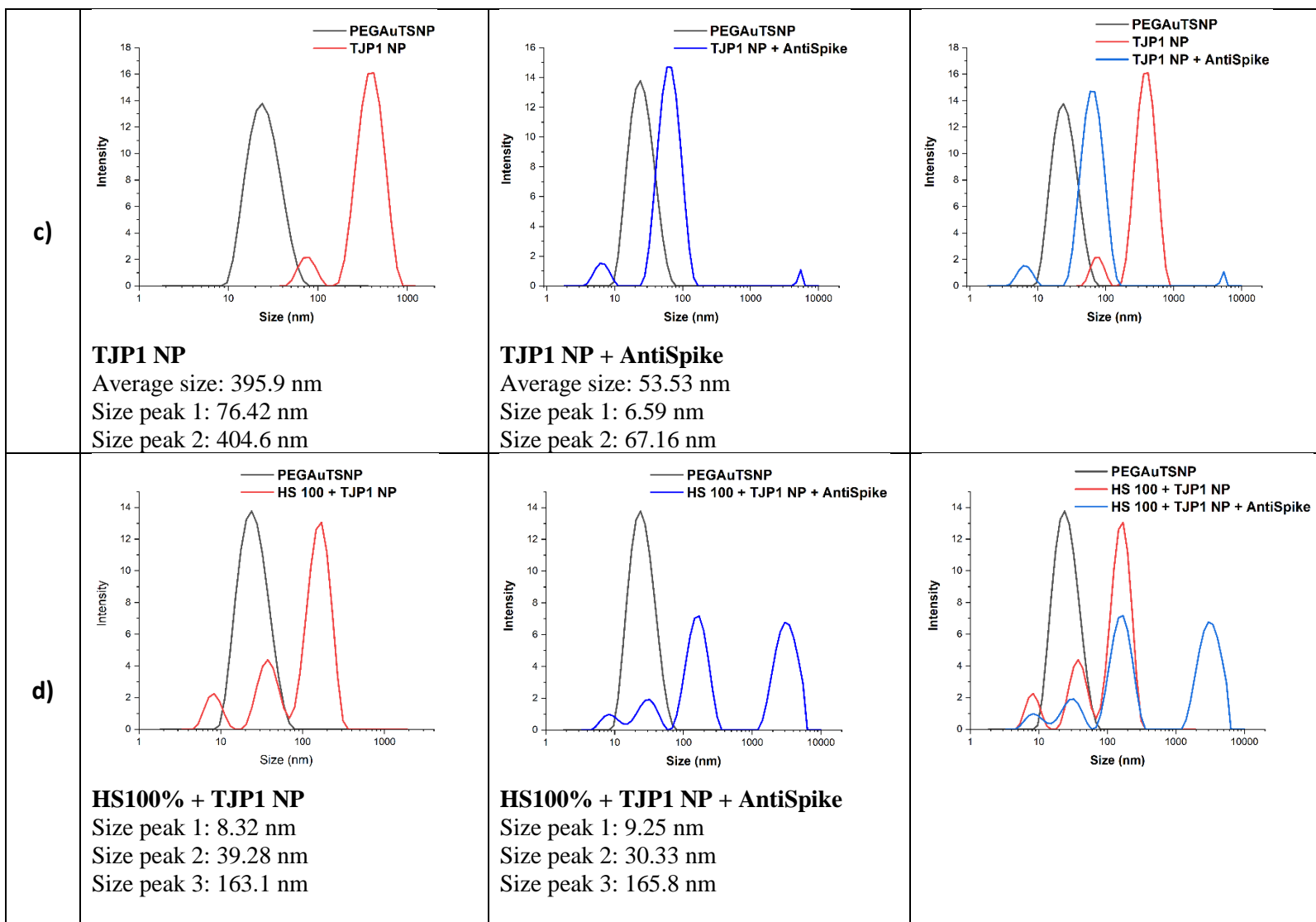
	<i>PEG AuTSNP</i>	<i>Spike NP</i>	<i>TJP1 NP</i>	<i>HS 100% +TJP1 NP</i>	<i>HS 50% +TJP1 NP</i>	<i>HS 10% +TJP1 NP</i>
<i><math>\lambda_{max}</math> before AntiSpike (nm)</i>	589	604	597	628	627	618
<i><math>\lambda_{max}</math> after AntiSpike (nm)</i>	614	619	614	633	632	620
<i><math>\Delta\lambda</math></i>	25	15	17	5	5	2

In the latest experiments, PEGAuTSNP  $\lambda_{max}$  was recorded at 589nm and shifts of 15 nm and 8 nm were recorded upon functionalisation with Spike and TJP1 respectively, where similar to previous tests, there is weaker attachment of the TJP1 onto the nanoplates. According to Table 10, registered  $\lambda_{max}$ es appear to be higher upon exposure to AntiSpike in all treatments comparable to the previous experiment.

Moreover, shifts of 5 nm and 2 nm were recorded for TJP1-NP upon addition of the AntiSpike in the presence of HS in concentrations of 100%, 50% and 10% respectively. As mentioned earlier, a binding of AntiSpike to TJP1 protein is not expected and there appears to be an interaction between the AntiSpike and the TJP1 nanoplates. For this reason, further analysis was necessary to gain a better understanding of the possible causes of binding, thus, DLS measurements were carried out for all treatments following the addition of antibody.

Table 11. Size measurements of PEGAuTSNP, Spike-PEGAuTSNP and TJP1-PEGAuTSNP treatments within HS before and after exposure to AntiSpike.

	Size measurement before AntiSpike	Size measurement after AntiSpike	Superimposed graphs
a)	 <p><b>PEGAuTSNP (NP)</b> Size: 21.77 nm</p>	 <p><b>PEGAuTSNP + AntiSpike</b> Size peak 1: 19.57 nm Size peak 2: 137.4 nm</p>	
b)	 <p><b>Spike NP</b> Size peak 1: 35.37 nm Size peak 2: 170.1 nm</p>	 <p><b>Spike NP + AntiSpike</b> Size: 119.7 nm</p>	





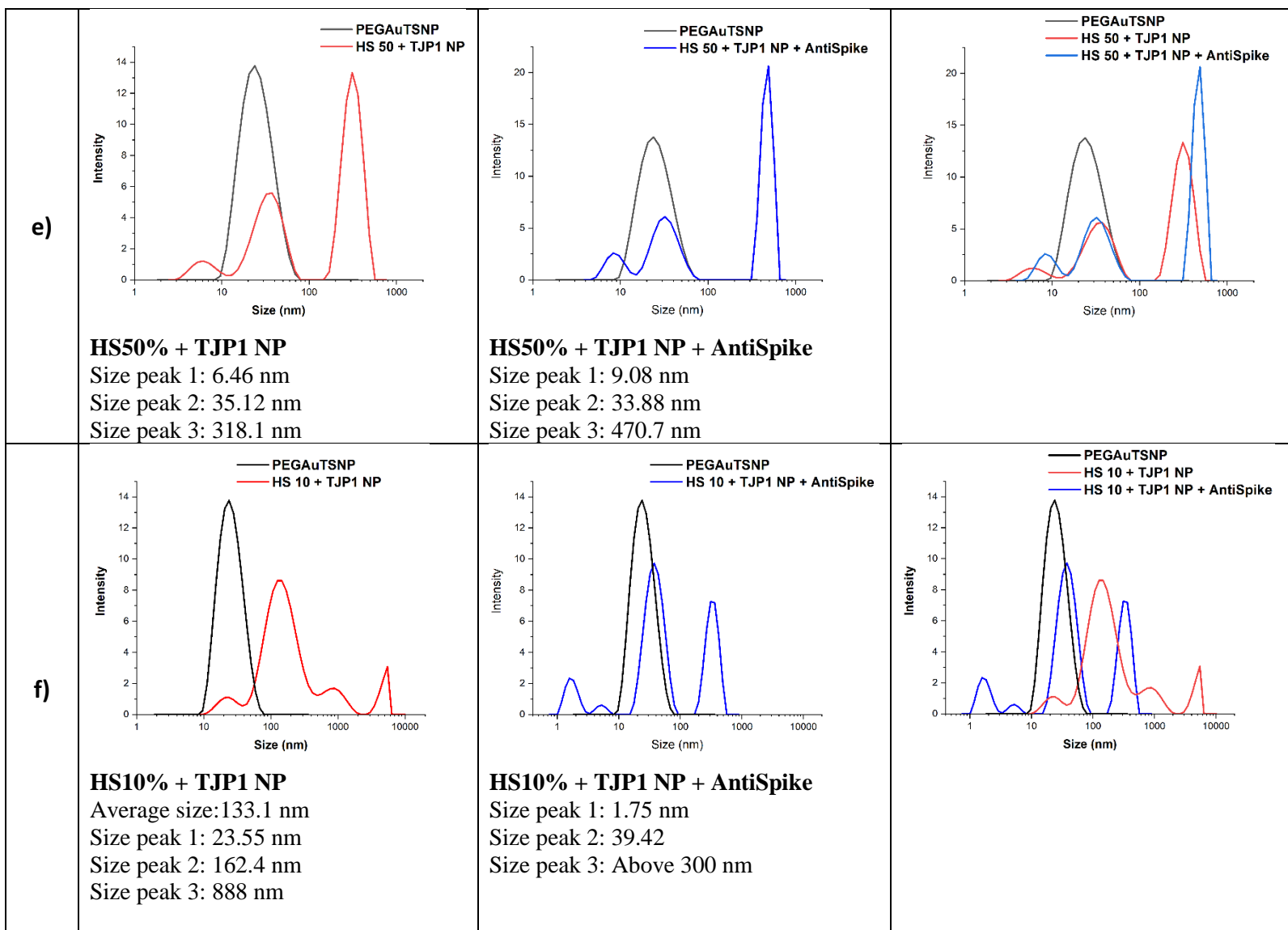


Table 11 above shows the DLS size measurements for all treatments before and after exposure of AntiSpike. In most cases it can be observed there was an increase in the size of the particles after the apparent binding of the antibody, nonetheless, three peaks can be observed in all samples containing horse serum even before exposure to AntiSpike, possibly indicating the coexistence of nanoparticles of different sizes within the same sample or agglomeration of horse serum proteins (Vasile et al., 2012). A similar phenomenon is observed in the study of Schintke and Frau (2020) where the interaction between nanoparticles and mouse serum was analysed through DLS measurements showing several peaks where results indicated poor signal stability when the serum sample was unfiltered, suggesting the presence of large agglomerates affects particle size (Schintke & Frau, 2020).

As mentioned before, AntiSpike seemed to show stronger affinity for the nanoplates causing the TJP1 to be replaced by the antibody on the nanoplates' surface (Figure 57). DLS measurements in Table 11c show a size measurement of around 395.9 nm for TJP1-PEGAuTSNP which corresponds only to an 8 nm shift in the LSPR spectrum as stated in Table 10 (from 589 nm to 597 nm), this could be attributed to TJP1 causing networking by itself. Since networking is not a close reaction to the PEGAuTSNP surface, it does not reflect in a large shift (Brennan-Fournet et al., 2015). Upon AntiSpike addition, there is a reduction in size to around 53.53 nm possibly indicating the breakage of the TJP1 network on the nanoplates, nonetheless, there still is an LSPR recording of 17 nm which could be attributed to the replacement of the TJP1 for the Antispikes.

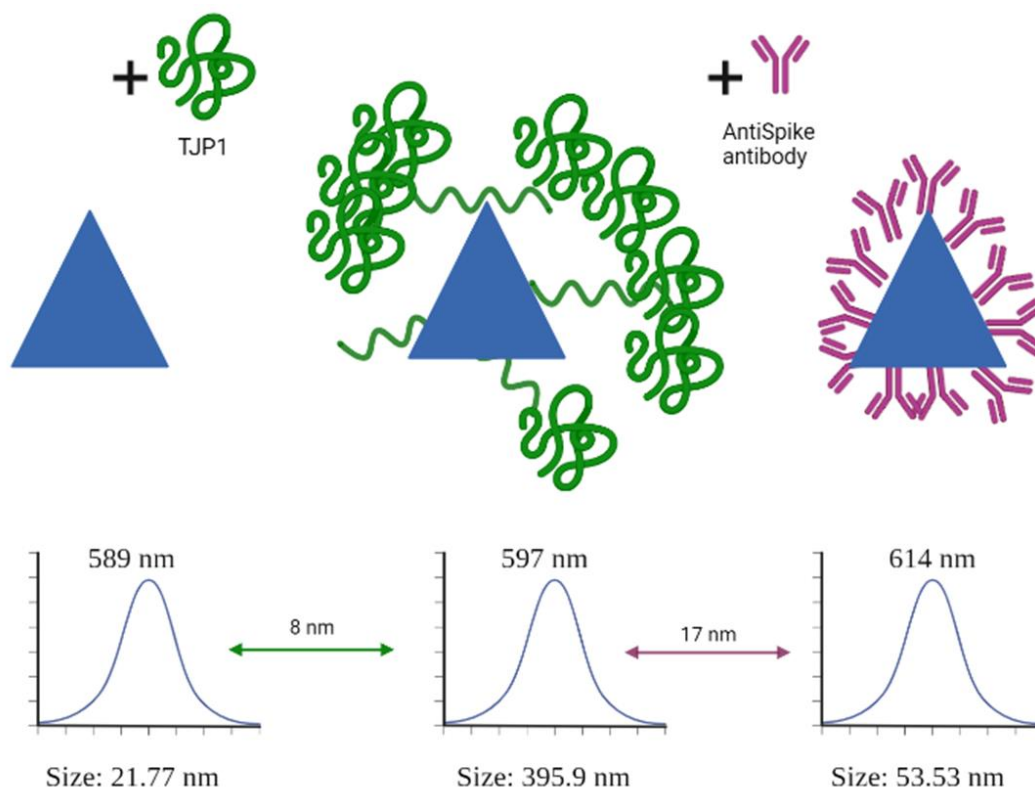


Figure 57. Illustration of protein replacement due to stronger attachment of AntiSpike to PEGAuTSNP.

For the system within horse serum, a more detailed analysis of the results revealed that upon addition of AntiSpike there was an increase in size only for a small population of particles. In the case of 100% HS with TJP1 nanoplates, a Polydispersity Index (PI) of 0.33 was recorded, after the sample interacted with the antibody there was an increase in PI to 0.78 as shown in Table 11d. The higher PI implies there is a polydisperse sample as a result of all the components already present in the horse serum, and perhaps a small population of nanoplates in the sample now bound to the added AntiSpike producing different sized particles. In Figure 58, when results are compared to TJP1 NP + AntiSpike (red plot, around 53.53 nm in size) a resemblance can be observed with the HS100 + TJP1 NP plot (blue) where a size of 39.28 nm is recorded. This could be related to the similarity in size between TJP1 NP interacting with the antibody and the HS proteins interacting with the TJP1 NP. When all the system is analysed as a whole, namely HS100 + TJP1 NP + AntiSpike, a peak of 163.1 nm (blue plot) can be related to the 165.8 nm peak from the green-coloured plot suggesting the TJP1-coated nanoplates did not bind to AntiSpike and kept their size, nonetheless, a fourth peak in

the green plot above the 1000 nm region could be attributed to the AntiSpike binding and networking with components from the HS.

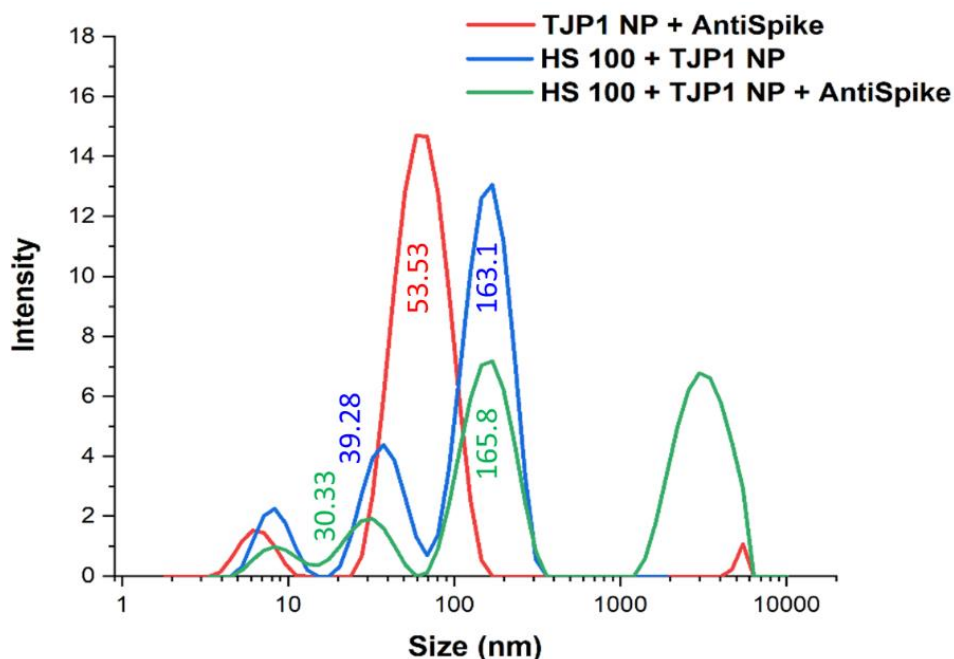


Figure 58. DLS measurements for TJP1-NP + AntiSpike and TJP1-NP within 100% HS before and after addition of AntiSpike

Fifty percent diluted horse serum behaved in a similar manner where an increase in the size was observed with the presence of AntiSpike in the sample. The 50% HS with TJP1 nanoplates sample (Table 11e) with a PI of 0.40 showed an increase to a PI of 0.69 as a consequence of higher polydispersity. In Figure 59, similar to HS100, a relation can be observed between the plots where TJP1 NP + AntiSpike (red), and HS50 + TJP1 NP (blue) can be identified within the HS50 + TJP1 NP + AntiSpike sample (green) where it can be observed that a fraction of the HS50 + TJP1 nanoplates interacted with the antibody, resulting in a higher intensity peak of 470.7 nm.

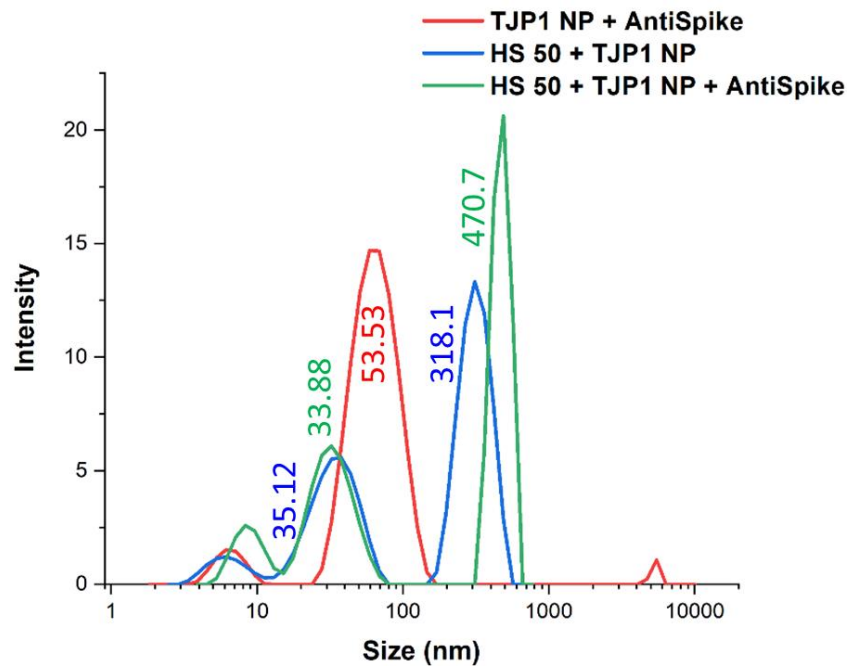


Figure 59. DLS measurements for TJP1-NP + AntiSpike and TJP1-NP within 50% HS before and after addition of AntiSpike

In line with the previous HS concentrations, TJP1 NP + AntiSpike, and HS10 + TJP1 NP can be identified within the most diluted sample (Figure 60). Similar to the other HS samples, the plot suggests the TJP1-coated nanoplates did not bind to AntiSpike, but the antibody created networks with serum contents resulting in a peak in the highest region among all samples. Moreover, it can be observed that comparable with above results, the size of HS 10 + TJP1 NP sample is 133.1 nm (blue plot), and upon AntiSpike

addition, a fraction of the sample reduces in size to 39.42 nm (green), validating the hypotheses where the antibody breaks the TJP1 network causing the size reduction.

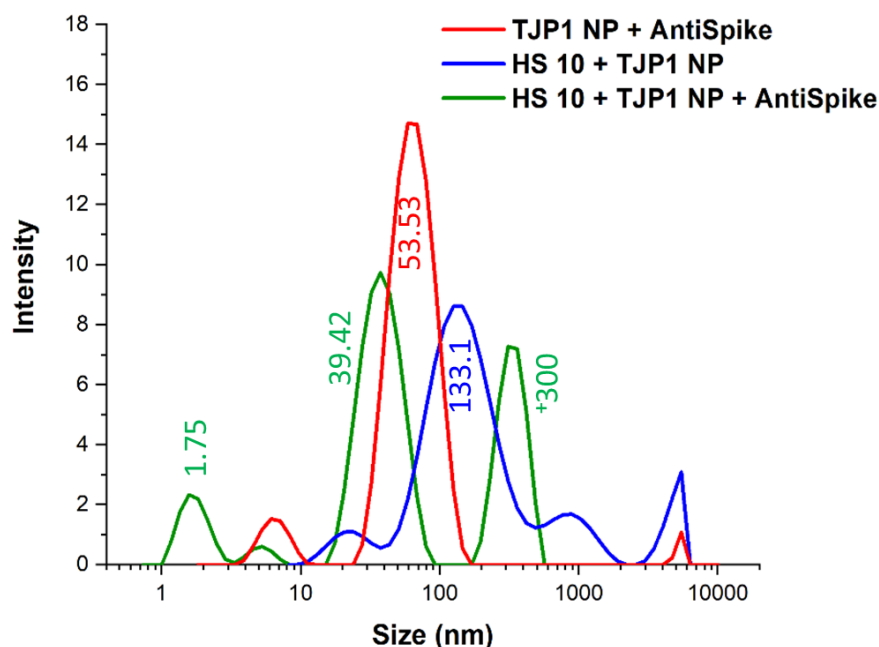


Figure 60. DLS measurements for TJP1-NP + AntiSpike and TJP1-NP within 10% HS before and after addition of AntiSpike

## 7.6 Summary

Throughout this chapter, the optimal functionalisation concentrations to successfully cover the surface of the PEGAuTSNP were determined. Experiments revealed adequate concentration of 4  $\mu\text{g}$  per mL of PEGAuTSNP for both Spike and AntiSpike proteins. Spike functionalised nanoplates were detected in an assay with the addition of AntiSpike, where the versatility and specificity of the AuTSNP to be used in the detection of the Spike-AntiSpike binding system was demonstrated. When the experiment was performed within horse serum as a complex environment, unforeseen performance was observed with LSPR redshifts for the TJP1 protein treatments upon addition of the AntiSpike antibody. These redshifts were unexpected considering that AntiSpike should not have affinity for TJP1. DLS measurements were performed to further analyse the outcomes where it was concluded that different-sized nanoparticle populations were present in the samples. Moreover, results suggested the interaction of the AntiSpike with horse serum components, explaining the size and  $\lambda_{\text{max}}$  increments

upon addition of this antibody. Additionally, it was concluded that TJP1 formed networks which were broken up upon addition of AntiSpike as a result of its stronger affinity to the PEGAuTSNP surface.

**CHAPTER 8.**  
**CONCLUSION & FUTURE**  
**PERSPECTIVES**



In this work, the successful optimization of gold edge-coated triangular silver nanoplate's preparation protocol was carried out demonstrating strong and distinctive LSPR recordings. Experiments were carried out to determine the best Ag:Au ratio (1:0.049) to successfully coat the edge of the nanoplates for protection against etching by chloride and for the increase in sensitivity for efficient protein functionalised PEGAuTSNP monitoring within high saline environments. Sensitivity of the AuTSNP was studied with the sucrose test to ensure strong LSPR results in future experiments.

Fn conformational changes were monitored with and without the presence of Cs-HAp bone tissue regeneration scaffolds upon incubation at two different pH values (pH 4.1 and pH 7.2). The results demonstrated the potential of PEGAuTSNP as powerful tools to signature protein conformational transitions from compact to extended formats, and readily monitor critical protein behaviour in presence of biomimetic tissue scaffolds.

Following that, Fn transitional behaviour was monitored in C2C12 myoblast cells environment with and without the presence of the scaffolds over 32h at five different time points to analyse the extension and fibril formation of the protein overtime. Redshifts over the 32 hours could be observed indicating the active protein unfolding activity. Denatured Fn was functionalised on the AuTSNP as a control where no redshifts were expected. Results correlate with recent experiments on Fn unfolding activity and fibril formation within the extracellular matrix. In addition, MC3T3-E1 pre-osteoblast cells were cultured to study and compare Fn conformational behaviour overtime, where similar results to the previous experiments were observed with and without the presence of the Cs-HAp bone tissue regeneration scaffolds. Furthermore, bone tissue regeneration scaffolds in the form of hydrogels were further studied to monitor the now-loaded protein onto the scaffold over time within the presence of cells. Findings were consistent to previous experiments with the stiff scaffolds with longer shifts observed for the active protein compared to those of denatured Fn. With both cell lines, cell morphology was observed after 32 h showing normal cell structure and growth with no observable adverse effects from the nanoplates or the scaffold on the cells.

After the high sensitivity of the PEGAuTSNP to study protein dynamics was demonstrated, their ability to detect binding of antibody-antigen complexes within dynamic environments was evaluated. Purified Fn was detected through direct assays with the antibody, as well as through indirect assays detecting native Fn present in cell-isolated ECM. In the direct experiments, the possibility of the antibody recognising nanoplate-unattached Fn in the samples was presented.

A centrifugation approach was used to remove unattached Fn and observe differences in the spectra for centrifuged and non-centrifuged samples. Similar behaviour was observed in both methods upon addition of the antibody suggesting minor differences when samples were centrifuged.

Optimal protein concentration of 5  $\mu\text{g}$  of Fn per mL of PEGAuTSNP to entirely coat the surface of the nanoplates was determined and further used in the AntiFn-Fn LOD determination. Detection of Fn-AntiFn binding was achieved with antibody concentrations of 0.01 mg/mL and the nanoplates saturation point was determined. Following that, native Fn was detected by using AntiFn-PEGAuTSNP within isolated ECM in different concentrations to observe differences in the shifting profile caused by the variations in the concentration of biological components in the ECM. Results were validated by comparing the shifting profile of native Fn to that of purified Fn, and with AntiTJP1-PEGAuTSNP used as a negative control for binding to ECM proteins. Results showed native Fn from the ECM can be successfully detected by using AntiFn antibody-coated nanoplates. AntiTJP1-coated nanoplates showed limited shifting when exposed to isolated ECM in comparison to AntiFn-coated nanoplates which displayed strong redshifts as a result of their specificity to detect the native Fn protein.

Considering the previous promising results, PEGAuTSNP were applied with SARS-CoV-2 Spike protein and its corresponding antibody to present their potential as a platform for the detection of COVID-19. Adequate protein-functionalisation concentrations to successfully cover the nanoplates' surface were determined, where results revealed volumes of 4  $\mu\text{g}$  per mL of PEGAuTSNP for Spike and AntiSpike were efficient volumes for further experimentation. The AbAg-complex binding was detected in a direct assay through the exposure of AntiSpike to Spike-functionalised nanoplates. Results demonstrated the versatility and specificity of the gold edge-coated triangular silver nanoplates for their use in the detection of the Spike-AntiSpike system with longer shifts recorded for Spike-PEGAuTSNP upon addition of AntiSpike in comparison to the negative control, TJP1-PEGAuTSNP.

Additional experiments were carried out in the presence of horse serum as a dynamic environment to test the sensitivity of the AuTSNP-based immunoassay within a complex environment, where interesting behaviour was observed with LSPR redshifts for the TJP1 treatments after exposure to AntiSpike antibody. These results were further analysed with DLS measurements where several nanoparticle populations of varying sizes were identified in the samples, providing insights into the outcomes of the experiments. The use of TJP1 as a control

showed interesting performance within horse serum samples where it could be concluded that protein-protein networks were formed which were then broken up by the added AntiSpike antibody due to its stronger affinity to the nanoplates surface. In future research alternative complex environments and controls to validate the results can be assessed, as well additional steps taken such as the filtering of bigger molecules within the samples to minimize non-specific binding and polydispersity of the samples under study.

Overall, this work has presented the gold edge-coated triangular silver nanoplates as powerful new tools to signature protein conformational transitions within living cells, monitor essential protein activity and detect antigen-antibody interactions above high background noise levels. Furthermore, this project has presented the possibility of AuTSNP to be used in nanoplate-based immunoassays for the detection of COVID-19 or potentially other diseases within medical settings and on field. Nonetheless, there are challenges remain and limitations associated with high noise environments suggesting further research is required for the development of AuTSNP detection-platforms with enhanced sensitivity and performance.

**CHAPTER 9.**

**COMPLETED TRAINING**

**AND WORK**

**DISSEMINATION**

## **9.1 Completed Modules**

- Health and Safety Induction
- EPIGEUM Concise Research Integrity Online Course System
- Writing Skills for Graduate Students
- Advanced Writing for Graduates
- Introduction to Research Paradigms
- Dissemination and Research Profile for Doctoral Researchers
- Research Ethics
- Postgraduate Pathways
- Advanced Polymer Chemistry
- Innovation and Research Commercialisation

## **9.2 Technical and Instrumentation Training**

- UV-Visible Spectroscopy
- Pulse-UV sterilization system
- Cell culture techniques
- Fourier-Transform Infrared Spectroscopy
- Fluorescent light microscopy
- Dynamic Light Scattering (Malvern Zetasizer)

## **9.3 Conferences**

- Podium presentation in Bioengineering in Ireland 2019 (BINI 2019). January 2019, Limerick, Ireland.
- Poster presentation in Athlone Institute of Technology Research Seminar 2019. May 2019, Athlone, Ireland.
- Podium presentation in 6<sup>th</sup> International Conference on Materials Science & Smart Materials 2019 (MSSM 2019). July 2019, Birmingham, United Kingdom.

- Poster presentation in Athlone Institute of Technology Research Seminar 2019. November 2019, Athlone, Ireland.
- Podium presentation in Bioengineering in Ireland 2020 (BINI 2020). January 2020, Carlow, Ireland.
- Online poster presentation in AIT Postgraduate Research Seminar and Poster Event 2020. June 2020.
- Online poster presentation and organization of the Shannon Region Postgraduate Research Conference. May 2021.
- Poster presentation in Technological University of The Shannon PosterFest 2022. January 2022.
- Podium presentation in Nanotech France Conference 2022. June 2022, Paris, France.

#### 9.4 Publications

- **Rodriguez Barroso L.G.**, Lanzagorta Garcia E, Mojicevic M, Alkan Tas B, Huerta M, Pogue R, Devine DM, Brennan-Fournet M. Triangular Silver Nanoplates as a Bioanalytical Tool: Potential COVID-19 Detection. *Int J Mol Sci.* 2023 Jul 26;24(15):11974. <https://doi.org/10.3390/ijms241511974>
- **Rodriguez Barroso, L.G.**, Lanzagorta Garcia, E., Mojicevic, M., Huerta, M.; Pogue, R., Devine, D.M., Brennan-Fournet, M. Triangular Silver Nanoparticles Synthesis: Investigating Potential Application in Materials and Biosensing. *Appl. Sci.* 2023, 13, 8100. <https://doi.org/10.3390/app13148100>
- **Rodriguez Barroso, L. G.**, Azaman, F. A., Pogue, R., Devine, D., & Fournet, M. B. (2022). Monitoring *In Vitro* Extracellular Matrix Protein Conformations in the Presence of Biomimetic Bone-Regeneration Scaffolds Using Functionalized Gold-Edge-Coated Triangular Silver Nanoparticles. *Nanomaterials*, 13(1), 57. MDPI AG. Retrieved from <http://dx.doi.org/10.3390/nano13010057>
- **Barroso, L.**, Garcia, L., Azaman, F. A., Devine, D. M., Lynch, M., Huerta, M., & Fournet, M. B. (2020). Monitoring of Extracellular Matrix Protein Conformations in the Presence of Biomimetic Bone Tissue Regeneration Scaffolds. *Key Engineering Materials*, 865, 43–47. <https://doi.org/10.4028/www.scientific.net/kem.865.43>

- Buckley, J., Araujo, J. A., Aribilola, I., Arshad, I., Azeem, M., Buckley, C., Fagan, A., Fitzpatrick, D. P., Garza Herrera, D. A., Hyland, T., Imtiaz, M. B., Khan, M. B., Lanzagorta Garcia, E., Moharana, B., Mohd Sufian, M. S. Z., Osterwald, K. M., Phelan, J., Platonava, A., Reid, C., **Rodriguez-Barroso, L.**,...Zainol, I. (2023). How transparent are quantitative studies in contemporary technology education research? Instrument development and analysis. *International Journal of Technology and Design Education*. <https://doi.org/10.1007/s10798-023-09827-9>
- Buckley, J., Adams, L., Aribilola, I., Arshad, I., Azeem, M., Bracken, L., Breheny, C., Buckley, C., Chimello, I., Fagan, A., Fitzpatrick, D. P., Garza Herrera, D., Gomes, G. D., Grassick, S., Halligan, E., Hirway, A., Hyland, T., Imtiaz, M. B., Khan, M. B., Lanzagorta Garcia, E., Lennon, P., Manaf, E., Meng, J., Mohd, M., Moraes A., Osterwald, K., Platonava, A., Reid, C., Renard, M., **Rodriguez-Barroso, L.**, ... Zhang, L. (2021). An assessment of the transparency of contemporary technology education research employing interview-based methodologies. *International Journal of Technology and Design Education*, 0123456789. <https://doi.org/10.1007/s10798-021-09695-1>

## REFERENCES

- Aamodt, J. M., & Grainger, D. W. (2017). Extracellular Matrix-based Biomaterial Scaffolds and the Host Response. *Biomaterials*, in 2011, 47–73.  
<https://doi.org/10.1016/j.biomaterials.2016.02.003>.
- Abbasi, N., Hamlet, S., Love, R. M., & Nguyen, N. T. (2020). Porous scaffolds for bone regeneration. In *Journal of Science: Advanced Materials and Devices* (Vol. 5, Issue 1, pp. 1–9). Elsevier B.V. <https://doi.org/10.1016/j.jsamd.2020.01.007>
- Abdel-Fattah, W. I., Jiang, T., El-Bassyouni, G. E. T., & Laurencin, C. T. (2007). Synthesis, characterization of chitosans and fabrication of sintered chitosan microsphere matrices for bone tissue engineering. *Acta Biomaterialia*, 3(4), 503–514.  
<https://doi.org/10.1016/j.actbio.2006.12.004>
- Adrian Martău, G., Mihai, M., & Cristian Vodnar, D. (2019). *polymers The Use of Chitosan, Alginate, and Pectin in the Biomedical and Food Sector-Biocompatibility, Bioadhesiveness, and Biodegradability*. <https://doi.org/10.3390/polym11111837>
- Aherne, D., Charles, D. E., Brennan-Fournet, M. E., Kelly, J. M., & Gun'ko, Y. K. (2009). Etching-resistant silver nanoprisms by epitaxial deposition of a protecting layer of gold at the edges. *Langmuir*, 25(17), 10165–10173. <https://doi.org/10.1021/la9009493>
- Aherne, D., Ledwith, D. M., Gara, M., & Kelly, J. M. (2008). Optical properties and growth aspects of silver nanoprisms produced by a highly reproducible and rapid synthesis at room temperature. *Advanced Functional Materials*, 18(14), 2005–2016.  
<https://doi.org/10.1002/adfm.200800233>
- Ahmad, J., Wen, X., Li, F., & Wang, B. (2019). Novel triangular silver nanoparticle modified membranes for enhanced antifouling performance. *RSC Advances*, 9(12), 6733–6744.  
<https://doi.org/10.1039/c8ra10540e>
- Ahmad, Z., Salman, S., Khan, S. A., Amin, A., Rahman, Z. U., Al-Ghamdi, Y. O., Akhtar, K., Bakhsh, E. M., & Khan, S. B. (2022). Versatility of Hydrogels: From Synthetic Strategies, Classification, and Properties to Biomedical Applications. *Gels*, 8(3).  
<https://doi.org/10.3390/gels8030167>



- Ahmed, S., Ning, J., Peng, D., Chen, T., Ahmad, I., Ali, A., Lei, Z., Abu bakr Shabbir, M., Cheng, G., & Yuan, Z. (2020). Current advances in immunoassays for the detection of antibiotics residues: a review. *Https://Doi.Org/10.1080/09540105.2019.1707171*, 31(1), 268–290. <https://doi.org/10.1080/09540105.2019.1707171>
- Aizpurua, J., Bryant, G. W., Richter, L. J., García De Abajo, F. J., Kelley, B. K., & Mallouk, T. (2005). Optical properties of coupled metallic nanorods for field-enhanced spectroscopy. *Physical Review B - Condensed Matter and Materials Physics*, 71(23), 1–13. <https://doi.org/10.1103/PhysRevB.71.235420>
- Alberts, B., Johnson, A., Lewis, J., Raff, M., Roberts, K., & Walter, P. (2002). *Protein Function - Molecular Biology of the Cell*. <http://www.ncbi.nlm.nih.gov/books/NBK26911/#A468>
- Aliofkhazraei, M. (2015). Handbook of nanoparticles. In M. Aliofkhazraei (Ed.), *Handbook of Nanoparticles*. Springer International Publishing. <https://doi.org/10.1007/978-3-319-15338-4>
- Antia, M., Baneyx, G., Kubow, K. E., & Abstract, V. V. (2008). Fibronectin in aging extracellular matrix fibrils is progressively unfolded by cells and elicits an enhanced rigidity response. *NIH Public Access*, 139(1), 229–420.
- Antia, M., Baneyx, G., Kubow, K. E., & Vogel, V. (2009). Fibronectin in aging extracellular matrix fibrils is progressively unfolded by cells and elicits an enhanced rigidity response. *Faraday Discuss*. <https://doi.org/10.1038/jid.2014.371>
- Arnal Barbedo, J. G. (2013). *Automatic Object Counting In Neubauer Chambers*. September 2013. <https://doi.org/10.14209/sbrt.2013.34>
- Arora, M. (2013). Cell Culture Media: A Review. *Materials and Methods*, 3. <https://doi.org/10.13070/mm.en.3.175>
- Ashraf, G. M., Greig, N. H., Khan, T. A., Hassan, I., Tabrez, S., Shakil, S., Sheikh, I. A., Zaidi, S. K., Wali, M. A., Jabir, N. R., Firoz, C. K., Naeem, A., Alhazza, I. M., Damanhour, G. A., & Kamal, M. A. (2014). Protein misfolding and aggregation in Alzheimer's disease and Type 2 Diabetes Mellitus HHS Public Access. *CNS Neurol Disord Drug Targets*, 13(7), 1280–1293.

- Atala, A. (2004). Tissue Engineering and Regenerative Medicine: Concepts for Clinical Application. *REJUVENATION RESEARCH*, 7(1), 950–971.  
<https://doi.org/10.1002/9781444303513.ch61>
- Avila Rodríguez, M. I., Rodríguez Barroso, L. G., & Sánchez, M. L. (2017). Collagen: A review on its sources and potential cosmetic applications. *Journal of Cosmetic Dermatology*, 17(1), 20–26. <https://doi.org/10.1111/jocd.12450>
- Baldwin, P., Li, D. J., Auston, D. A., Mir, H. S., Yoon, R. S., & Koval, K. J. (2019). Autograft, Allograft, and Bone Graft Substitutes: Clinical Evidence and Indications for Use in the Setting of Orthopaedic Trauma Surgery. *Journal of Orthopaedic Trauma*, 33(4), 203–213. <https://doi.org/10.1097/BOT.0000000000001420>
- Ball, D. W. (2006). *Field Guide to Spectroscopy* (Vol. FG08). SPIE Press.  
[https://spie.org/publications/fg08\\_p65\\_beers\\_law?SSO=1](https://spie.org/publications/fg08_p65_beers_law?SSO=1)
- Benevides, J. M., Overman, S. A., & Thomas, G. J. (2003). Raman Spectroscopy of Proteins. *Current Protocols in Protein Science*, 17.8.1-17.8.35.  
<https://doi.org/10.1002/0471140864.ps1708s33>
- Bennionn, B. J., & Daggett, V. (2002). Protein conformation and diagnostic tests: The prion protein. *Clinical Chemistry*, 48(12), 2105–2114.
- Biener, J., Wittstock, A., Baumann, T. F., Weissmüller, J., Bäumer, M., & Hamza, A. V. (2009). Surface chemistry in nanoscale materials. *Materials*, 2(4), 2404–2428.  
<https://doi.org/10.3390/ma2042404>
- Boopathi, S., Poma, A. B., & Kolandaivel, P. (2020). Novel 2019 coronavirus structure, mechanism of action, antiviral drug promises and rule out against its treatment. *Journal of Biomolecular Structure and Dynamics*, 10.  
<https://doi.org/10.1080/07391102.2020.1758788>
- Brady, B., Wang, P. H., Steenhoff, V., & Brolo, A. G. (2018). Nanostructuring solar cells using metallic nanoparticles. In *Metal Nanostructures for Photonics* (pp. 197–221). Elsevier. <https://doi.org/10.1016/B978-0-08-102378-5.00009-X>
- Brennan-Fournet, M. E., Huerta, M., Zhang, Y., Malliaras, G., & Owens, R. M. (2015). Detection of fibronectin conformational changes in the extracellular matrix of live cells

- using plasmonic nanoplates. *Journal of Materials Chemistry B*, 3(47), 9140–9147.  
<https://doi.org/10.1039/c5tb02060c>
- Brockman, J. M., Nelson, B. P., & Corn, R. M. (2000). *Surface Plasmon Resonance Imaging Measurements of Ultrathin Organic Films*.
- Bumbrah, G. S., & Sharma, R. M. (2016). Raman spectroscopy – Basic principle, instrumentation and selected applications for the characterization of drugs of abuse. *Egyptian Journal of Forensic Sciences*, 6(3), 209–215.  
<https://doi.org/10.1016/j.ejfs.2015.06.001>
- Bunaciu, A. A., Aboul-Enein, H. Y., & Hoang, V. D. (2015). Raman spectroscopy for protein analysis. *Applied Spectroscopy Reviews*, 50(5), 377–386.  
<https://doi.org/10.1080/05704928.2014.990463>
- Burduşel, A. C., Gherasim, O., Grumezescu, A. M., Mogoantă, L., Ficai, A., & Andronesu, E. (2018). Biomedical applications of silver nanoparticles: An up-to-date overview. *Nanomaterials*, 8(9), 1–25. <https://doi.org/10.3390/nano8090681>
- Burrell, C. J., Howard, C. R., & Murphy, F. A. (2017). Classification of Viruses and Phylogenetic Relationships. In *Fenner and White's Medical Virology* (pp. 15–25). Elsevier. <https://doi.org/10.1016/B978-0-12-375156-0.00002-3>
- Cai, Q., Zhang, L., Li, L., Tan, J., Wu, S., Wang, Y., & Fu, W. (2022). Detection of Chemotherapeutic Drug 6-Mercaptopurine Through Manipulating Localized Surface Plasmon Resonance Absorption of Silver Nanoplates. *NANO*, 16(4).  
<https://doi.org/10.1142/S1793292021500466>
- Cai, Z., Li, F., Rong, M., Lin, L., Yao, Q., Huang, Y., Chen, X., & Wang, X. (2019). Novel Nanomaterials for Biomedical, Environmental and Energy Applications. In *Novel Nanomaterials for Biomedical, Environmental and Energy Applications*. Elsevier Inc. <https://doi.org/10.1016/b978-0-12-814497-8.00001-1>
- Carter, L. J., Garner, L. V., Smoot, J. W., Li, Y., Zhou, Q., Saveson, C. J., Sasso, J. M., Gregg, A. C., Soares, D. J., Beskid, T. R., Jervey, S. R., & Liu, C. (2020). Assay Techniques and Test Development for COVID-19 Diagnosis. *ACS Central Science*, 6(5), 591–605. <https://doi.org/10.1021/ACSCENTSCI.0C00501>

- Cascella, M., Rajnik, M., Cuomo, A., Dulebohn, S. C., & Di Napoli, R. (2022). Features, Evaluation, and Treatment of Coronavirus (COVID-19). *StatPearls*.  
<https://www.ncbi.nlm.nih.gov/books/NBK554776/>
- Castelletti, F., Donadelli, R., Banterla, F., Hildebrandt, F., Zipfel, P. F., Bresin, E., Otto, E., Skerka, C., Renieri, A., Todeschini, M., Caprioli, J., Caruso, M. R., Artuso, R., Remuzzi, G., & Noris, M. (2008). Mutations in FN1 cause glomerulopathy with fibronectin deposits. *Proceedings of the National Academy of Sciences of the United States of America*, *105*(7), 2538–2543. <https://doi.org/10.1073/pnas.0707730105>
- Catoira, M. C., Fusaro, L., Di Francesco, D., Ramella, M., & Boccafoschi, F. (2019). Overview of natural hydrogels for regenerative medicine applications. *Journal of Materials Science: Materials in Medicine*, *30*(10). <https://doi.org/10.1007/s10856-019-6318-7>
- Charles, D. E., Aherne, D., Gara, M., Ledwith, D. M., Gun, Y. K., Kelly, J. M., Blau, W. J., & Brennan-fournet, M. E. (2010). Versatile Solution Phase Triangular Silver Nanoplates for Highly Sensitive Plasmon Resonance Sensing. *ACS Nano*, *4*(1), 55–64.
- Charles, D., Fournet, P., Cunningham, S., Ledwith, D., Kelly, J. M., Blau, W., & Fournet, M. B. (2008). A sensitivity study of the localised surface plasmon resonance of high-definition structured silver nanoparticles in solution. *Plasmonics: Metallic Nanostructures and Their Optical Properties VI*, *7032*(70322), 70322G.  
<https://doi.org/10.1117/12.804259>
- Chen, H., Wang, L., Yeh, J., Wu, X., Cao, Z., Wang, Y. A., Zhang, M., Yang, L., & Mao, H. (2010). Reducing non-specific binding and uptake of nanoparticles and improving cell targeting with an antifouling PEO-b-PyMPS copolymer coating. *Biomaterials*, *31*(20), 5397–5407. <https://doi.org/10.1016/j.biomaterials.2010.03.036>
- Conde-Agudelo, A., Romero, R., & Roberts, J. M. (2014). Tests to predict preeclampsia. In *Chesley's Hypertensive Disorders in Pregnancy, Fourth Edition* (Fourth Edi). Elsevier Inc. <https://doi.org/10.1016/B978-0-12-407866-6.00011-0>
- Cox, K. L., Devanarayan, V., Kriauciunas, A., Manetta, J., Montrose, C., & Sittampalam, S. (2019). Immunoassay Methods. *Assay Guidance Manual*.  
<https://www.ncbi.nlm.nih.gov/books/NBK92434/>

- Darwish, I. A. (2006). Immunoassay Methods and their Applications in Pharmaceutical Analysis: Basic Methodology and Recent Advances. *International Journal of Biomedical Science : IJBS*, 2(3), 217. /pmc/articles/PMC3614608/
- de Almeida, M. L., Saatkamp, C. J., Fernandes, A. B., Pinheiro, A. L. B., & Silveira, L. (2016). Estimating the concentration of urea and creatinine in the human serum of normal and dialysis patients through Raman spectroscopy. *Lasers in Medical Science*, 31(7), 1415–1423. <https://doi.org/10.1007/s10103-016-2003-y>
- Devine, D. M., Hctor, E., Hayes, J. S., Sheehan, E., Christopher, H., Clinic, M., Science, H., & Hospital, M. R. (2019). *Extended release of proteins following encapsulation in hydroxyapatite/chitosan composite scaffolds for bone tissue engineering applications*. 1–24. <https://doi.org/10.1016/j.msec.2017.11.001>.Extended
- Dhillon, J., Kraeutler, M. J., Belk, J. W., Mccarty, E. C., Mcculloch, P. C., & Scillia, A. J. (2022). Similar Clinical Outcomes and Graft Failure Rates : An. *Arthroscopy, Sports Medicine, and Rehabilitation*, 4(4), e1513–e1521. <https://doi.org/10.1016/j.asmr.2022.04.008>
- Ding, M., & Chen, D. (2016). Lanthanide Ions Doped Upconversion Nanomaterials: Synthesis, Surface Engineering, and Application in Drug Delivery. In *Nanoarchitectonics for Smart Delivery and Drug Targeting*. Elsevier Inc. <https://doi.org/10.1016/B978-0-323-47347-7.00009-4>
- Dinis-Oliveira, R. J. (2014). Heterogeneous and homogeneous immunoassays for drug analysis. *Bioanalysis*, 6(21), 2877–2896. <https://doi.org/10.4155/bio.14.208>
- Długosz, M., & Trylska, J. (2011). Diffusion in crowded biological environments: Applications of Brownian dynamics. In *BMC Biophysics* (Vol. 4, Issue 1, p. 3). BioMed Central. <https://doi.org/10.1186/2046-1682-4-3>
- Doria, G., Conde, J., Veigas, B., Giestas, L., Almeida, C., Assunção, M., Rosa, J., & Baptista, P. V. (2012). Noble metal nanoparticles for biosensing applications. *Sensors*, 12(2), 1657–1687. <https://doi.org/10.3390/s120201657>
- Eberhardt, K., Stiebing, C., Matthäus, C., Schmitt, M., & Popp, J. (2015). Advantages and limitations of Raman spectroscopy for molecular diagnostics: An update. *Expert Review of Molecular Diagnostics*, 15(6), 773–787.

<https://doi.org/10.1586/14737159.2015.1036744>

El-Sherbiny, I. M., & Yacoub, M. H. (2013). Hydrogel scaffolds for tissue engineering: Progress and challenges. *Global Cardiology Science & Practice*, 2013(3), 316.

<https://doi.org/10.5339/GCSP.2013.38>

Endo, T., Kerman, K., Nagatani, N., Hiepa, H. M., Kim, D. K., Yonezawa, Y., Nakano, K., & Tamiya, E. (2006). Multiple label-free detection of antigen-antibody reaction using localized surface plasmon resonance-based core-shell structured nanoparticle layer nanochip. *Analytical Chemistry*, 78(18), 6465–6475. <https://doi.org/10.1021/ac0608321>

Escobar-sierra, D. M., Martins, J., & Ossa-, C. P. (2015). *Chitosan / hydroxyapatite scaffolds for tissue engineering manufacturing method effect comparison*. 24–35.

<https://doi.org/10.17533/udea.redin.n75a04>

Etacheri, V., Georgekutty, R., Seery, M. K., & Pillai, S. C. (2010). Single step morphology-controlled synthesis of silver nanoparticles. *Materials Research Society Symposium Proceedings*, 1217, 7–13. <https://doi.org/10.1557/PROC-1217-YO8-40>

Featherstone, S. (2015). In-plant quality control in food canning operations. In *A Complete Course in Canning and Related Processes* (pp. 235–254). Elsevier.

<https://doi.org/10.1016/b978-0-85709-678-4.00010-5>

Feig, M., Yu, I., Wang, P. H., Nawrocki, G., & Sugita, Y. (2017). Crowding in Cellular Environments at an Atomistic Level from Computer Simulations. *Journal of Physical Chemistry B*, 121(34), 8009–8025. <https://doi.org/10.1021/acs.jpcc.7b03570>

Feist, E., & Hiepe, F. (2013). Fibronectin Autoantibodies. In *Autoantibodies: Third Edition* (Third Edit). Elsevier. <https://doi.org/10.1016/B978-0-444-56378-1.00039-3>

Funari, R., Chu, K. Y., & Shen, A. Q. (2020). Detection of antibodies against SARS-CoV-2 spike protein by gold nanospikes in an opto-microfluidic chip. *Biosensors and Bioelectronics*, 169, 112578. <https://doi.org/10.1016/j.bios.2020.112578>

Gadkari, V. V., Harvey, S. R., Raper, A. T., Chu, W. T., Wang, J., Wysocki, V. H., & Suo, Z. (2018). Investigation of sliding DNA clamp dynamics by single-molecule fluorescence, mass spectrometry and structure-based modeling. *Nucleic Acids Research*, 46(6), 3103–3118. <https://doi.org/10.1093/nar/gky125>

- Gee, E. P. S., Ingber, D. E., & Stultz, C. M. (2008). Fibronectin unfolding revisited: Modeling cell traction-mediated unfolding of the tenth type-III repeat. *PLoS ONE*, 3(6), 1–10. <https://doi.org/10.1371/journal.pone.0002373>
- Goh, P. S., Ismail, A. F., & Ng, B. C. (2017). Raman Spectroscopy. *Membrane Characterization*, 31–46. <https://doi.org/10.1016/B978-0-444-63776-5.00002-4>
- Gomes, D. S., Santos, A. M. C., Neves, G. A., & Menezes, R. R. (2019). A brief review on hydroxyapatite production and use in biomedicine. *Ceramica*, 65(374), 282–302. <https://doi.org/10.1590/0366-69132019653742706>
- Gourdon, D., Wang, K., Andresen Eguiluz, R. C., Wu, F., & Seo, B. R. (2015). *Stiffening and unfolding of early deposited-fibronectin increase proangiogenic factor secretion by breast cancer-associated stromal cells contributed new reagents/analytic tools; K HHS Public Access*. 54, 63–71. <https://doi.org/10.1016/j.biomaterials.2015.03.019>
- Gubin, S. P., Koksharov, Y. A., Khomutov, G. B., & Yurkov, G. Y. (2005). Magnetic nanoparticles: Preparation, structure and properties. *Uspekhi Khimii*, 74(6), 539–574. <https://doi.org/10.1070/rc2005v074n06abeh000897>
- Guo, L., Jackman, J. A., Yang, H. H., Chen, P., Cho, N. J., & Kim, D. H. (2015). Strategies for enhancing the sensitivity of plasmonic nanosensors. *Nano Today*, 10(2), 213–239. <https://doi.org/10.1016/j.nantod.2015.02.007>
- Güzel, R., & Gülbahar, E. (2016). Synthesis of Silver Nanoparticles. *Intech*, i, 13. <https://doi.org/http://dx.doi.org/10.5772/intechopen.75363>
- Ha, T., Ting, A. Y., Liang, J., Caldwell, W. B., Deniz, A. A., Chemla, D. S., Schultz, P. G., & Weiss, S. (1999). Single-molecule fluorescence spectroscopy of enzyme conformational dynamics and cleavage mechanism. *Proceedings of the National Academy of Sciences of the United States of America*, 96(3), 893–898. <https://doi.org/10.1073/pnas.96.3.893>
- Haes, A. J., Stuart, D. A., Nie, S., & Van Duyne, R. P. (2004). Using solution-phase nanoparticles, surface-confined nanoparticle arrays and single nanoparticles as biological sensing platforms. In *Journal of Fluorescence* (Vol. 14, Issue 4, pp. 355–367). <https://doi.org/10.1023/B:JOFL.0000031817.35049.1f>
- Hall, W. P., Ngatia, S. N., & Van Duyne, R. P. (2011). LSPR biosensor signal enhancement

- using nanoparticle-antibody conjugates. *Journal of Physical Chemistry C*, 115(5), 1410–1414. [https://doi.org/10.1021/JP106912P/SUPPL\\_FILE/JP106912P\\_SI\\_001.PDF](https://doi.org/10.1021/JP106912P/SUPPL_FILE/JP106912P_SI_001.PDF)
- Hamill, K. J., Kligys, K., Hopkinson, S. B., & Jones, J. C. R. (2009). Laminin deposition in the extracellular matrix : a complex picture emerges. *J Cell Sci*, 122(24), 4409–4417. <https://doi.org/10.1242/jcs.041095>
- Harapan, H., Itoh, N., Yufika, A., Winardi, W., Keam, S., Te, H., Megawati, D., Hayati, Z., Wagner, A. L., & Mudatsir, M. (2020). Coronavirus disease 2019 (COVID-19): A literature review. *Journal of Infection and Public Health*, 13(5), 667–673. <https://doi.org/10.1016/J.JIPH.2020.03.019>
- Hasan, S. (2014). A Review on Nanoparticles : Their Synthesis and Types. *Research Journal of Recent Sciences Res . J . Recent . Sci . Uttar Pradesh ( Lucknow Campus )*, 4(February), 1–3.
- Held, P. (2012). *An Introduction to Fluorescence Resonance Energy Transfer (FRET) Technology and its Application in Bioscience*  $fd * k 2 * J) 1/6 \text{ \AA}$ . [www.biotek.com](http://www.biotek.com)
- Hellewell, A. L., Rosini, S., & Adams, J. C. (2017). A Rapid, Scalable Method for the Isolation, Functional Study, and Analysis of Cell-derived Extracellular Matrix. *Journal of Visualized Experiments : JoVE*, 2017(119), 55051. <https://doi.org/10.3791/55051>
- Henderson, B., Nair, S., Pallas, J., & Williams, M. A. (2011). Fibronectin: A multidomain host adhesin targeted by bacterial fibronectin-binding proteins. *FEMS Microbiology Reviews*, 35(1), 147–200. <https://doi.org/10.1111/j.1574-6976.2010.00243.x>
- Hong, Y., Huh, Y. M., Yoon, D. S., & Yang, J. (2012). Nanobiosensors based on localized surface plasmon resonance for biomarker detection. *Journal of Nanomaterials*, 2012(1). <https://doi.org/10.1155/2012/759830>
- Hörmann, H. (1995). Fibronectin and Its Role in Wound Healing. *Wound Healing and Skin Physiology*, 219–226. [https://doi.org/10.1007/978-3-642-77882-7\\_19](https://doi.org/10.1007/978-3-642-77882-7_19)
- Howard, D., Buttery, L. D., Shakesheff, K. M., & Roberts, S. J. (2008). Tissue engineering: Strategies, stem cells and scaffolds. *Journal of Anatomy*, 213(1), 66–72. <https://doi.org/10.1111/j.1469-7580.2008.00878.x>
- Hwang, P. W., & Horton, J. A. (2019). Variable osteogenic performance of MC3T3-E1



- subclones impacts their utility as models of osteoblast biology. *Scientific Reports*, 9(1), 1–9. <https://doi.org/10.1038/s41598-019-44575-8>
- Iravani, S. (2020). Nano-and biosensors for the detection of SARS-CoV-2: challenges and opportunities. *This Journal Is Cite This: Mater. Adv*, 1, 3092. <https://doi.org/10.1039/d0ma00702a>
- Iravani, S., Korbekandi, H. Mirmohammadi, S. V., & Zolfaghari, B. (2014). Synthesis of silver nanoparticles: chemical, physical and biological methods. *Research in Pharmaceutical Sciences*, 9(6), 385–406.
- Irsen, S. H., Milz, S., Tille, C., Schieker, M., & Seitz, H. (2005). *Hydroxyapatite scaffolds for bone tissue engineering made by 3D printing*. 6, 1121–1124.
- Ito, H., Inoue, H., Hasegawa, K., Hasegawa, Y., Shimizu, T., Kimura, S., Onimaru, M., Ikeda, H., & Kudo, S. ei. (2014). Use of surface-enhanced Raman scattering for detection of cancer-related serum-constituents in gastrointestinal cancer patients. *Nanomedicine: Nanotechnology, Biology, and Medicine*, 10(3), 599–608. <https://doi.org/10.1016/j.nano.2013.09.006>
- Iwamoto, K., Shindo, Y., & Takahashi, K. (2016). Modeling Cellular Noise Underlying Heterogeneous Cell Responses in the Epidermal Growth Factor Signaling Pathway. *PLoS Computational Biology*, 12(11), 1–18. <https://doi.org/10.1371/journal.pcbi.1005222>
- Jayaweera, M., Perera, H., Gunawardana, B., & Manatunge, J. (2020). Transmission of COVID-19 virus by droplets and aerosols: A critical review on the unresolved dichotomy. *Environmental Research*, 188. <https://doi.org/10.1016/J.ENVRES.2020.109819>
- Jia, H., Xu, W., An, J., Li, D., & Zhao, B. (2006). A simple method to synthesize triangular silver nanoparticles by light irradiation. *Spectrochimica Acta - Part A: Molecular and Biomolecular Spectroscopy*, 64(4), 956–960. <https://doi.org/10.1016/j.saa.2005.09.004>
- Jiménez-Gómez, C. P., Cecilia, J. A., Guidotti, M., & Soengas, R. (2020). molecules Chitosan: A Natural Biopolymer with a Wide and Varied Range of Applications. *Molecules*. <https://doi.org/10.3390/molecules25173981>

- Jones, E., Michael, S., & Sittampalam, G. S. (2004). Basics of Assay Equipment and Instrumentation for High Throughput Screening. In *Assay Guidance Manual*. Eli Lilly & Company and the National Center for Advancing Translational Sciences.  
<http://www.ncbi.nlm.nih.gov/pubmed/22553880>
- Jordan, C. C., Kaiser, I., & Moore, V. (2014). *2013 Nanotechnology Patent Literature Review: Graphitic Carbon-Based Nanotechnology And Energy Applications Are On The Rise - Energy and Natural Resources - United States*.  
<https://www.mondaq.com/unitedstates/energy-law/292674/2013-nanotechnology-patent-literature-review-graphitic-carbon-based-nanotechnology-and-energy-applications-are-on-the-rise>
- Kammakakam, I. (2021). Nanomaterials: a review of synthesis methods, properties, recent progress, and challenges. *Materials Advances*, 2, 1821–1871.  
<https://doi.org/10.1039/d0ma00807a>
- Katagiri, T., Yamaguchi, A., Komaki, M., Abe, E., Takahashi, N., Ikeda, T., Rosen, V., Wozney, J. M., Fujisawa-Sehara, A., & Suda, T. (1994). Bone morphogenetic protein-2 converts the differentiation pathway of C2C12 myoblasts into the osteoblast lineage. *Journal of Cell Biology*, 127(6 I), 1755–1766. <https://doi.org/10.1083/jcb.127.6.1755>
- Kelly, J. M., Keegan, G., & Brennan-Fournet, M. E. (2012). Triangular silver nanoparticles: Their preparation, functionalisation and properties. *Acta Physica Polonica A*, 122(2), 337–345. <https://doi.org/10.12693/APhysPolA.122.337>
- Kim, H. H. (2015). Endoscopic Raman Spectroscopy for Molecular Fingerprinting of Gastric Cancer: Principle to Implementation. *BioMed Research International*, 2015.  
<https://doi.org/10.1155/2015/670121>
- Klemis, V., Ghura, H., Federico, G., Wü Rfel, C., Bentmann, A., Gretz, N., Miyazaki, T., Grö Ne, H.-J., & Nakchbandi, I. A. (2017). Circulating fibronectin contributes to mesangial expansion in a murine model of type 1 diabetes. *Kidney International*, 91, 1374–1385.  
<https://doi.org/10.1016/j.kint.2016.12.006>
- Kong, K., Kendall, C., Stone, N., & Notingher, I. (2015). Raman spectroscopy for medical diagnostics - From in-vitro biofluid assays to in-vivo cancer detection. In *Advanced Drug Delivery Reviews* (Vol. 89, pp. 121–134). Elsevier.

<https://doi.org/10.1016/j.addr.2015.03.009>

- Kuhar, N., Sil, S., Verma, T., & Umapathy, S. (2018). Challenges in application of Raman spectroscopy to biology and materials. In *RSC Advances* (Vol. 8, Issue 46, pp. 25888–25908). Royal Society of Chemistry. <https://doi.org/10.1039/c8ra04491k>
- Kular, J. K., Basu, S., & Sharma, R. I. (2014). The extracellular matrix : Structure , composition , age-related differences , tools for analysis and applications for tissue engineering. *Journal of Tissue Engineering*. <https://doi.org/10.1177/2041731414557112>
- Kumar, A., Narayan, R. K., Prasoon, P., Kumari, C., Kaur, G., Kumar, S., Kulandhasamy, M., Sesham, K., Pareek, V., Faiq, M. A., Pandey, S. N., Singh, H. N., Kant, K., Shekhawat, P. S., Raza, K., & Kumar, S. (2021). COVID-19 Mechanisms in the Human Body—What We Know So Far. *Frontiers in Immunology*, *12*. <https://doi.org/10.3389/FIMMU.2021.693938>
- Kurokawa, N., Endo, F., Maeda, T., & Hotta, A. (2017). Electrospinning and surface modification methods for functionalized cell scaffolds. In *Nanostructures for Novel Therapy: Synthesis, Characterization and Applications*. Elsevier Inc. <https://doi.org/10.1016/B978-0-323-46142-9.00008-6>
- Kuttappan, S., Mathew, D., Jo, J. ichiro, Tanaka, R., Menon, D., Ishimoto, T., Nakano, T., Nair, S. V., Nair, M. B., & Tabata, Y. (2018). Dual release of growth factor from nanocomposite fibrous scaffold promotes vascularisation and bone regeneration in rat critical sized calvarial defect. *Acta Biomaterialia*, *78*, 36–47. <https://doi.org/10.1016/j.actbio.2018.07.050>
- Lee, S., Lee, K., Ahn, J., Lee, J., Kim, M., & Yong-Beom, S. (2011). *Highly Sensitive Biosensing Using Arrays of Plasmonic Au Nanodisks Realized by Nanoimprint Lithography*. *2*, 897–904.
- Levengood, S. K. L., & Zhang, M. (2014). Chitosan-based scaffolds for bone tissue engineering. *Journal of Materials Chemistry B*, *2*(21), 3161–3184. <https://doi.org/10.1039/c4tb00027g>
- Li, J. J., Kaplan, D. L., & Zreiqat, H. (2014). Scaffold-based regeneration of skeletal tissues to meet clinical challenges. *Journal of Materials Chemistry B*, *2*(42), 7272–7306. <https://doi.org/10.1039/c4tb01073f>

- Li, T., Bu, G., & Xi, G. (2021). Effects of heat treatment on the antigenicity , antigen epitopes , and structural properties of  $\beta$  -conglycinin. *Food Chemistry*, 346(November 2020), 128962. <https://doi.org/10.1016/j.foodchem.2020.128962>
- Liu, H., Rong, P., Jia, H., Yang, J., Dong, B., Dong, Q., Yang, C., Hu, P., Wang, W., Liu, H., & Liu, D. (2016). A Wash-Free Homogeneous Colorimetric Immunoas-say Method. *Theranostics*, 6(1), 54–64. <https://doi.org/10.7150/thno.13159>
- Liyanage, T., Sangha, A., & Sardar, R. (2017). Achieving biosensing at attomolar concentrations of cardiac troponin T in human biofluids by developing a label-free nanoplasmonic analytical assay. *Analyst*, 142(13), 2442–2450. <https://doi.org/10.1039/c7an00430c>
- Lizardi-Mendoza, J., Argüelles Monal, W. M., & Goycoolea Valencia, F. M. (2016). Chemical Characteristics and Functional Properties of Chitosan. In *Chitosan in the Preservation of Agricultural Commodities*. Elsevier Inc. <https://doi.org/10.1016/B978-0-12-802735-6.00001-X>
- Loiseau, A., Asila, V., Boitel-Aullen, G., Lam, M., Salmain, M., & Boujday, S. (2019). Silver-based plasmonic nanoparticles for and their use in biosensing. *Biosensors*, 9(2). <https://doi.org/10.3390/bios9020078>
- Long, Y.-T., & Jing, C. (2014). Localized surface plasmon resonance based nanobiosensors. In *SpringerBriefs in Molecular Science*. <https://doi.org/10.1007/978-3-642-54795-9>
- Lyddy, R. (2009). Nanotechnology. *Information Resources in Toxicology*, 321–328. <https://doi.org/10.1016/B978-0-12-373593-5.00036-7>
- Maffei, M., Montemiglio, L. C., Vitagliano, G., Fedele, L., Sellathurai, S., Bucci, F., Compagnone, M., Chiarini, V., Exertier, C., Muzi, A., Roscilli, G., Vallone, B., & Marra, E. (2021). The nuts and bolts of SARS-CoV-2 spike receptor-binding domain heterologous expression. *Biomolecules*, 11(12). <https://doi.org/10.3390/biom11121812>
- Malekzad, H., Sahandi Zangabad, P., Mirshekari, H., Karimi, M., & Hamblin, M. R. (2017). Noble metal nanoparticles in biosensors: Recent studies and applications. *Nanotechnology Reviews*, 6(3), 301–329. <https://doi.org/10.1515/ntrev-2016-0014>
- Mantha, S., Pillai, S., Khayambashi, P., Upadhyay, A., & Zhang, Y. (2019). Smart Hydrogels

- in Tissue Engineering and. *Materials*, 12(3323), 33.  
<https://www.ncbi.nlm.nih.gov/pmc/articles/PMC68/>
- Mao, A. S., & Mooney, D. J. (2015). Regenerative medicine: Current therapies and future directions. *Proceedings of the National Academy of Sciences of the United States of America*, 112(47), 14452–14459. <https://doi.org/10.1073/pnas.1508520112>
- Marian, M., & Seghezzi, W. (2013). Novel Biopharmaceuticals: Pharmacokinetics, Pharmacodynamics, and Bioanalytics. *Nonclinical Development of Novel Biologics, Biosimilars, Vaccines and Specialty Biologics*, 97–137. <https://doi.org/10.1016/B978-0-12-394810-6.00004-6>
- Martins Ramos, I. ., Malkin, A., & Lyng, F. M. (2015). Current Advances in the Application of Raman Spectroscopy for Molecular Diagnosis of Cervical Cancer. *BioMed Research International*. <https://doi.org/10.1155/2015/561242>
- Maurer, L. M., Ma, W., & Mosher, D. F. (2015). Dynamic Structure of Plasma Fibronectin. *Crit Rev Biochem Mol Biol*. <https://doi.org/10.1080/10409238.2016.1184224>
- Mauriz, E., Dey, P., & Lechuga, L. M. (2019). Advances in nanoplasmonic biosensors for clinical applications. *Analyst*, 144(24), 7105–7129. <https://doi.org/10.1039/c9an00701f>
- McNamara, K., & Tofail, S. A. M. (2017). Nanoparticles in biomedical applications. *Advances in Physics: X*, 2(1), 54–88. <https://doi.org/10.1080/23746149.2016.1254570>
- Mizutani, T., Kondo, T., Darmanin, S., Tsuda, M., Tanaka, S., Tobiume, M., Asaka, M., & Ohba, Y. (2010). A novel FRET-based biosensor for the measurement of BCR-ABL activity and its response to drugs in living cells. *Clinical Cancer Research*, 16(15), 3964–3975. <https://doi.org/10.1158/1078-0432.CCR-10-0548>
- Mobasser, S., & Firoozi, A. A. (2016). Review of Nanotechnology Applications in Science and Engineering. *Journal of Civil Engineering and Urbanism*, 6(4), 84–93.
- Moitra, P., Alafeef, M., Alafeef, M., Alafeef, M., Dighe, K., Frieman, M. B., Pan, D., Pan, D., & Pan, D. (2020). Selective Naked-Eye Detection of SARS-CoV-2 Mediated by N Gene Targeted Antisense Oligonucleotide Capped Plasmonic Nanoparticles. *ACS Nano*, 14(6), 7617–7627. <https://doi.org/10.1021/acsnano.0c03822>
- Moree, B., Connell, K., Mortensen, R. B., Liu, C. T., Benkovic, S. J., & Salafsky, J. (2015).

Protein Conformational Changes Are Detected and Resolved Site Specifically by Second-Harmonic Generation. *Biophysical Journal*, 109(4), 806–815.

<https://doi.org/10.1016/j.bpj.2015.07.016>

Munehika, K., Smith, J. M., Chen, Y., & Ginger, D. S. (2007). Plasmon line widths of single silver nanoprisms as a function of particle size and plasmon peak position. *Journal of Physical Chemistry C*, 111(51), 18906–18911. <https://doi.org/10.1021/jp076099e>

Naikoo, G. A., Arshad, F., Hassan, I. U., Awan, T., Salim, H., Pedram, M. Z., Ahmed, W., Patel, V., Karakoti, A. S., & Vinu, A. (2022). Nanomaterials-based sensors for the detection of COVID-19: A review. *Bioengineering and Translational Medicine*, 7(3), 1–19. <https://doi.org/10.1002/btm2.10305>

National Institutes of Health. (2020a). FN1 gene. *U.S. National Library of Medicine*, 1–4. <https://ghr.nlm.nih.gov/gene/FN1>

National Institutes of Health. (2020b). FN1 gene. *U.S. National Library of Medicine*, 1–4.

National Institutes of Health. (2020c, March 3). *Novel coronavirus structure reveals targets for vaccines and treatments | National Institutes of Health (NIH)*. <https://www.nih.gov/news-events/nih-research-matters/novel-coronavirus-structure-reveals-targets-vaccines-treatments>

Nayantara, P. K. (2018). Biosynthesis of nanoparticles using eco-friendly factories and their role in plant pathogenicity: a review. *Biotechnology Research and Innovation*, 2(1), 63–73. <https://doi.org/10.1016/j.biori.2018.09.003>

NIH. (2018). *Tissue Engineering and Regenerative Medicine*. <https://www.nibib.nih.gov/science-education/science-topics/tissue-engineering-and-regenerative-medicine>

O'Brien, F. J. (2011). Biomaterials & scaffolds for tissue engineering. *Materials Today*, 14(3), 88–95. [https://doi.org/10.1016/S1369-7021\(11\)70058-X](https://doi.org/10.1016/S1369-7021(11)70058-X)

Ohashi, T., Lemmon, C. A., & Erickson, H. P. (2017). Fibronectin Conformation and Assembly: Analysis of Fibronectin Deletion Mutants and Fibronectin Glomerulopathy (GFND) Mutants. *Biochemistry*, 56(34), 4584–4591. <https://doi.org/10.1021/acs.biochem.7b00589>

- Ostrowska, N., Feig, M., & Trylska, J. (2019). Modeling Crowded Environment in Molecular Simulations. *Frontiers in Molecular Biosciences*, 6, 86.  
<https://doi.org/10.3389/fmolb.2019.00086>
- Pandya, A., Sutariya, P. G., & Menon, S. K. (2013). A non enzymatic glucose biosensor based on an ultrasensitive calix[4]arene functionalized boronic acid gold nanoprobe for sensing in human blood serum. *Analyst*, 138(8), 2483–2490.  
<https://doi.org/10.1039/c3an36833e>
- Peng, Y., & Alexov, E. (2017). Protein Conformational Disease: Visit the Facts at a Glance. *ELS*, 1–7. <https://doi.org/10.1002/9780470015902.A0021868>
- Pentassuglia, S., Agostino, V., & Tommasi, T. (2018). EAB-electroactive biofilm: A biotechnological resource. In *Encyclopedia of Interfacial Chemistry: Surface Science and Electrochemistry* (pp. 110–123). Elsevier. <https://doi.org/10.1016/B978-0-12-409547-2.13461-4>
- PerkinElmer, & Inc. (n.d.). *Eight Limitations of ELISA and How to Overcome Them Using Alternative Technologies*. Retrieved April 6, 2022, from [www.perkinelmer.com](http://www.perkinelmer.com)
- Petryayeva, E., & Krull, U. J. (2011). Localized surface plasmon resonance: Nanostructures, bioassays and biosensing-A review. *Analytica Chimica Acta*, 706(1), 8–24.  
<https://doi.org/10.1016/j.aca.2011.08.020>
- Proctor, R. A. (1987). Fibronectin: a brief overview of its structure, function, and physiology. *Reviews of Infectious Diseases*, 9 Suppl 4(August).
- Qasim, S. B., Husain, S., Huang, Y., Pogorielov, M., Deineka, V., Lyndin, M., Rawlinson, A., & Rehman, I. U. (2017). In-vitro and in-vivo degradation studies of freeze gelated porous chitosan composite scaffolds for tissue engineering applications. *Polymer Degradation and Stability*, 136, 31–38.  
<https://doi.org/10.1016/j.polymdegradstab.2016.11.018>
- Qiu, X., & Hildebrandt, N. (2019). A clinical role for Förster resonance energy transfer in molecular diagnostics of disease. In *Expert Review of Molecular Diagnostics* (Vol. 19, Issue 9, pp. 767–771). Taylor and Francis Ltd.  
<https://doi.org/10.1080/14737159.2019.1649144>

- Rafferty, J. P. (2019). *Beer's law*. <https://www.britannica.com/science/Beers-law>
- Ram, K., Thomas, U., & Ruth, E. (2013). Raman Spectroscopy and Microscopy. In *Reference Module in Materials Science and Materials Engineering* (Vol. 96, Issue 4). Elsevier Ltd. <https://doi.org/doi:10.1016/B978-0-12-803581-8.03091-5>
- Raza, M. A., Kanwal, Z., Rauf, A., Sabri, A. N., Riaz, S., & Naseem, S. (2016). Size- and shape-dependent antibacterial studies of silver nanoparticles synthesized by wet chemical routes. *Nanomaterials*, *6*(4). <https://doi.org/10.3390/nano6040074>
- Riond, B., Wenger-Riggenbach, B., Hofmann-Lehmann, R., & Lutz, H. (2009). Serum protein concentrations from clinically healthy horses determined by agarose gel electrophoresis. *Veterinary Clinical Pathology*, *38*(1), 73–77. <https://doi.org/10.1111/j.1939-165X.2008.00100.x>
- Rizzo, F. (2022). Optical Immunoassays Methods in Protein Analysis: An Overview. *Chemosensors*, *10*(8), 1–24. <https://doi.org/10.3390/chemosensors10080326>
- Rodríguez-Vázquez, M., Vega-Ruiz, B., Ramos-Zúñiga, R., Saldaña-Koppel, D. A., & Quiñones-Olvera, L. F. (2015). Chitosan and Its Potential Use as a Scaffold for Tissue Engineering in Regenerative Medicine. *BioMed Research International*, *2015*. <https://doi.org/10.1155/2015/821279>
- Rohleder, D., Kiefer, W., & Petrich, W. (2004). Quantitative analysis of serum and serum ultrafiltrate by means of Raman spectroscopy. *Analyst*, *129*(10), 906–911. <https://doi.org/10.1039/b408927h>
- Rozario, T., Dzamba, B., Weber, G. F., Davidson, L. A., & DeSimone, D. W. (2010). *The Physical State of Fibronectin Matrix Differentially Regulates Morphogenetic Movements In Vivo*. *46*(4), 564–574. <https://doi.org/10.1016/j.cortex.2009.08.003.Predictive>
- Saade, J., Pacheco, M. T. T., Rodrigues, M. R., & Silveira, L. (2008). Identification of hepatitis C in human blood serum by near-infrared Raman spectroscopy. *Spectroscopy*, *22*(5), 387–395. <https://doi.org/10.3233/SPE-2008-0344>
- Saifullah, S., Ali, I., Kawish, M., El-Shabasy, R. M., Chen, L., & El-Seedi, H. R. (2020). Surface functionalized magnetic nanoparticles for targeted cancer therapy and diagnosis.



- Metal Nanoparticles for Drug Delivery and Diagnostic Applications*, 215–236.  
<https://doi.org/10.1016/B978-0-12-816960-5.00012-4>
- Sandhu, R., Singh, N., & Dhankhar, J. (2018). *Dynamic light scattering ( DLS ) technique , principle , theoretical considerations and applications*. January.
- Schintke, S., & Frau, E. (2020). Modulated 3d cross-correlation dynamic light scattering applications for optical biosensing and time-dependent monitoring of nanoparticle-biofluid interactions. *Applied Sciences (Switzerland)*, 10(24), 1–11.  
<https://doi.org/10.3390/app10248969>
- Sediq, A. S., Van Duijvenvoorde, R. B., Jiskoot, W., & Nejadnik, M. R. (2016). No Touching! Abrasion of Adsorbed Protein Is the Root Cause of Subvisible Particle Formation during Stirring. *Journal of Pharmaceutical Sciences*, 105(2), 519–529.  
<https://doi.org/10.1016/j.xphs.2015.10.003>
- Segtnan, V. H., Hildrum, K. I., & Wold, J. P. (2009). New methods for analysis of factors affecting meat eating quality. In *Improving the Sensory and Nutritional Quality of Fresh Meat*. Woodhead Publishing Limited. <https://doi.org/10.1533/9781845695439.4.519>
- Sekar, R. B., & Periasamy, A. (2003). Fluorescence resonance energy transfer (FRET) microscopy imaging of live cell protein localizations. *Journal of Cell Biology*, 160(5), 629–633. <https://doi.org/10.1083/jcb.200210140>
- Sikka, M. P., & Midha, V. K. (2019). The role of biopolymers and biodegradable polymeric dressings in managing chronic wounds. *Advanced Textiles for Wound Care*, 463–488.  
<https://doi.org/10.1016/B978-0-08-102192-7.00016-3>
- Silla, E., Arnau, A., Tuñón, I., Nakanishi, K., & Wypych, G. (2014). Fundamental principles governing solvents use. *Handbook of Solvents: Second Edition*, 1, 11–72.  
<https://doi.org/10.1016/B978-1-895198-64-5.50004-0>
- Solomon, S. D., Mulfinger, L., Bahadory, M., Jeyarajasingam, A. V., Rutkowsky, S. A., & Boritz, C. (2007). Synthesis and Study of Silver Nanoparticles. *Journal of Chemical Education*, 84(2), 322. <https://doi.org/10.1021/ed084p322>
- Soto, C. (2001). Protein misfolding and disease - Preface. *Federation of European Biochemical Societies*, 356(September), 129–131.

- Speziale, P., Arciola, C. R., & Pietrocola, G. (2019). Fibronectin and Its Role in Human Infective Diseases. *Cells*, 8(12), 1516. <https://doi.org/10.3390/cells8121516>
- Stuart, D. A., Haes, A. J., McFarland, A. D., Nie, S., & Van Duyne, R. P. (2004). Refractive-index-sensitive, plasmon-resonant-scattering, and surface-enhanced Raman-scattering nanoparticles and arrays as biological sensing platforms. *Plasmonics in Biology and Medicine*, 5327(February 2014), 60. <https://doi.org/10.1117/12.554416>
- Sulaiman, S. Bin, Keong, T. K., Cheng, C. H., Saim, A. Bin, & Hj Idrus, R. B. (2013). Tricalcium phosphate/hydroxyapatite (TCP-HA) bone scaffold as potential candidate for the formation of tissue engineered bone. *Indian Journal of Medical Research*, 137(6), 1093–1101. [/pmc/articles/PMC3734714/?report=abstract](https://pubmed.ncbi.nlm.nih.gov/2374714/)
- T. Heyduk. (2002). Measuring protein conformational changes by FRET / LRET Tomasz Heyduk. *Current Opinion in Chemical Biology*, 13, 292–296.
- Tang, G., Zhou, B., Li, F., Wang, W., Liu, Y., Wang, X., Liu, C., & Ye, X. (2020). Advances of Naturally Derived and Synthetic Hydrogels for Intervertebral Disk Regeneration. *Frontiers in Bioengineering and Biotechnology*, 8(June), 1–13. <https://doi.org/10.3389/fbioe.2020.00745>
- Tang, Y., Zeng, X., & Liang, J. (2010). Surface Plasmon Resonance: An Introduction to a Surface Spectroscopy Technique. *J Chem Educ*, 87(7), 742–746. <https://doi.org/10.1021/ed100186y.Surface>
- Teymouri, M., Mollazadeh, S., Mortazavi, H., & Ghale-noie, Z. N. (2021). Recent advances and challenges of RT-PCR tests for the diagnosis of COVID-19. *Pathology - Research and Practice*, January.
- Tooney, N. M., Mosesson, M. W., Amrani, D. L., Hainfeld, J. F., & Wall, J. S. (1983). Solution and surface effects on plasma fibronectin structure. *Journal of Cell Biology*, 97(6), 1686–1692. <https://doi.org/10.1083/jcb.97.6.1686>
- Turnbull, G., Clarke, J., Picard, F., Riches, P., Jia, L., Han, F., Li, B., & Shu, W. (2018). 3D bioactive composite scaffolds for bone tissue engineering. *Bioactive Materials*, 3(3), 278–314. <https://doi.org/10.1016/j.bioactmat.2017.10.001>
- Ummul, H., & Salisbury, H. (2020). *Hydroxyapatite Dental Material*. StatPearls - NCBI

Bookshelf. <https://www.ncbi.nlm.nih.gov/books/NBK513314/?report=printable>

- Unser, S., Bruzas, I., He, J., & Sagle, L. (2015). Localized surface plasmon resonance biosensing: Current challenges and approaches. *Sensors (Switzerland)*, *15*(7), 15684–15716. <https://doi.org/10.3390/s150715684>
- Vashist, S. K., & Luong, J. H. T. (2018). Immunoassays: An Overview. *Handbook of Immunoassay Technologies: Approaches, Performances, and Applications*, 1–18. <https://doi.org/10.1016/B978-0-12-811762-0.00001-3>
- Vasile, E., Rusen, E., Mocanu, A., Patrascu, M., & Calinescu, I. (2012). Polymer colloids and silver nanoparticles hybrid materials. *Colloid and Polymer Science*, *290*(3), 193–201. <https://doi.org/10.1007/s00396-011-2530-9>
- Vinci, G., & Rapa, M. (2019). Noble metal nanoparticles applications: Recent trends in food control. *Bioengineering*, *6*(1). <https://doi.org/10.3390/bioengineering6010010>
- Vu Nu, T. T., Tran, N. H. T., Nam, E., Nguyen, T. T., Yoon, W. J., Cho, S., Kim, J., Chang, K. A., & Ju, H. (2018). Blood-based immunoassay of tau proteins for early diagnosis of Alzheimer's disease using surface plasmon resonance fiber sensors. *RSC Advances*, *8*(14), 7855–7862. <https://doi.org/10.1039/c7ra11637c>
- Walker, C., & Mojares, E. (2018). *Role of Extracellular Matrix in Development and Cancer Progression*. <https://doi.org/10.3390/ijms19103028>
- Wang, D., Christensen, K., Chawla, K., Xiao, G., Krebsbach, P. H., & Franceschi, R. T. (1999). Isolation and characterization of MC3T3-E1 preosteoblast subclones with distinct in vitro and in vivo differentiation/mineralization potential. *Journal of Bone and Mineral Research*, *14*(6), 893–903. <https://doi.org/10.1359/jbmr.1999.14.6.893>
- Wang, E. C., & Wang, A. Z. (2014). NANOPARTICLES AND THEIR APPLICATIONS IN CELL AND MOLECULAR BIOLOGY. *Integrative Biology*, *6*(1). <https://doi.org/10.1039/c3ib40165k>
- Wang, J. P., & Hielscher, A. (2017). Fibronectin: How its aberrant expression in tumors may improve therapeutic targeting. *Journal of Cancer*, *8*(4), 674–682. <https://doi.org/10.7150/jca.16901>
- Wang, K., Shangguan, L., Liu, Y., Jiang, L., Zhang, F., Wei, Y., Zhang, Y., Qi, Z., Wang, K.,

- & Liu, S. (2017). In Situ Detection and Imaging of Telomerase Activity in Cancer Cell Lines via Disassembly of Plasmonic Core–Satellites Nanostructured Probe. *Anal. Chem.*, *89*, 7268. <https://doi.org/10.1021/acs.analchem.7b01882>
- Wijaya, Y. N., Kim, J., Choi, W. M., Park, S. H., & Kim, M. H. (2017). A systematic study of triangular silver nanoplates: One-pot green synthesis, chemical stability, and sensing application. *Nanoscale*, *9*(32), 11705–11712. <https://doi.org/10.1039/c7nr03077k>
- Wiley, B. J., Im, S. H., Li, Z. Y., McLellan, J., Siekkinen, A., & Xia, Y. (2006). Maneuvering the surface plasmon resonance of silver nanostructures through shape-controlled synthesis. *Journal of Physical Chemistry B*, *110*(32), 15666–15675. <https://doi.org/10.1021/jp0608628>
- Willems, K. A., & Van Duyne, R. P. (2007). Localized Surface Plasmon Resonance Spectroscopy and Sensing. *Annual Review of Physical Chemistry*, *58*(1), 267–297. <https://doi.org/10.1146/annurev.physchem.58.032806.104607>
- Yanagishita, M. (1993). *Function of proteoglycans in the extracellular matrix*. *March*, 283–293.
- Yu, X., Hayden, E. Y., Xia, M., Liang, O., Cheah, L., Teplow, D. B., & Xie, Y. H. (2018). Surface enhanced Raman spectroscopy distinguishes amyloid B-protein isoforms and conformational states. *Protein Science*, *27*(8), 1427–1438. <https://doi.org/10.1002/pro.3434>
- Yue, B. (2014). Biology of the extracellular matrix: An overview. *Journal of Glaucoma*, *23*(8), S20–S23. <https://doi.org/10.1097/IJG.000000000000108>
- Zamarreño, C. R., Rivero, P. J., Hernaez, M., Goicoechea, J., Matías, I. R., & Arregui, F. J. (2014). Optical Sensors for Corrosion Monitoring. *Intelligent Coatings for Corrosion Control*, 603–640. <https://doi.org/10.1016/B978-0-12-411467-8.00018-0>
- Zarrintaj, P., Saeb, M. R., Jafari, S. H., & Mozafari, M. (2020). Application of compatibilized polymer blends in biomedical fields. *Compatibilization of Polymer Blends: Micro and Nano Scale Phase Morphologies, Interphase Characterization, and Properties*, 511–537. <https://doi.org/10.1016/B978-0-12-816006-0.00018-9>
- Zhang, Y., Charles, D. E., Ledwith, D. M., Aherne, D., Cunningham, S., Voisin, M., Blau,

W. J., Gun'Ko, Y. K., Kelly, J. M., & Brennan-Fournet, M. E. (2014). Wash-free highly sensitive detection of C-reactive protein using gold derivatised triangular silver nanoplates. *RSC Advances*, 4(55), 29022–29031. <https://doi.org/10.1039/c4ra04958f>

Zhang, Z., Shen, W., Xue, J., Liu, Y., Liu, Y., Yan, P., Liu, J., & Tang, J. (2018). Recent advances in synthetic methods and applications of silver nanostructures. *Nanoscale Research Letters*, 13. <https://doi.org/10.1186/s11671-018-2450-4>

# APPENDICES

## Appendix 1: EPIGEUM online course certificate of completion



## Appendix 2: Abstract for Bioengineering in Ireland Conference 2019, January 2019

Early Stage Researcher (PhD Year 1)	<input type="checkbox"/>	Post-Doctoral Researcher/Senior Researcher/PI	<input type="checkbox"/>
Entry for the Engineers Ireland Biomedical Research Medal	<input type="checkbox"/>	Corresponding author has completed PhD and would like to review Biml abstract submissions	<input type="checkbox"/>

Please place an X in any appropriate categories

### EXTRACELLULAR MATRIX PROTEIN CONFORMATION MONITORING FOR THE OPTIMIZATION OF BIOMIMETIC BONE TISSUE REGENERATION SCAFFOLDS

Rodriguez, L.<sup>1</sup>, Lanzagorta Garcia, E.<sup>1</sup>, Azaman, F.A.<sup>1</sup>, Devine, D.<sup>1</sup>, Fournet, M.B.<sup>1</sup>,  
<sup>1</sup> Materials Research Institute, Athlone Institute of Technology  
email: mfournet@ait.ie

#### INTRODUCTION

Tissue scaffolds, which mimic the native extracellular matrix (ECM) are under intense development for a range of regenerative medical applications. The specific three-dimensional ultrastructure of ECM macromolecules is essential for the provision of structural support and signalling cues for the modulation of diverse host processes including cell migration and cell proliferation.

Here we present the in situ on scaffold detection of conformational transitions of the ubiquitous ECM protein, fibronectin.<sup>1</sup> This critical ECM protein was incorporated into biocompatible and biodegradable chitosan composite bone tissue scaffolds, developed as excellent alternatives to bone grafting techniques. Fibronectin conformations are monitored using plasmonic gold-edge-coated triangular silver nanoplates (AuTSNP) which exhibit some of the highest reported spectral shift responses to surface biomolecular interactions.<sup>1,2</sup> Large spectral shifts distinguish between compact and extended fibronectin conformations in the presence of the chitosan bone regeneration scaffolds.

#### MATERIALS AND METHODS

High MW chitosan, fibronectin and chemicals for AuTSNP synthesis were obtained from Sigma Aldrich. Chitosan scaffolds were prepared using a previously reported crosslinking process.<sup>3</sup> AuTSNP were synthesised using a previously described seed mediated approach.<sup>4</sup> The highly sensitive local surface plasmon resonance (LSPR) of the AuTSNP was used to record the fibronectin conformations.<sup>1</sup> Zeta potential measurements were used to verify the fibronectin conformational status. The conformational profile of fibronectin was investigated at physiological pH with and without the presence of the scaffold.

#### RESULTS

Fibronectin in a compact conformation has a hydrodynamic radius of the order of 23 nm as recorded by zetasizer measurements. In the extended conformation the increases for up to 130 nm for single fibronectin strands, however, can become much larger as networks and fibrils are formed. Figure 1 shows the AuTSNP LSPR signature readings for compact and extended fibronectin conformations.

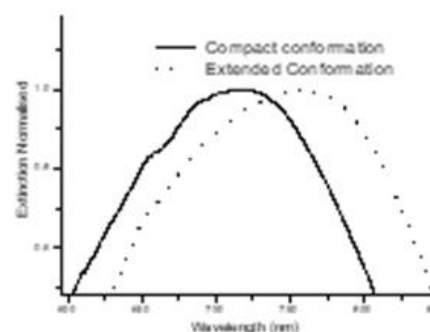


Figure 1 The LSPR signature of compact vs extended fibronectin conformations.

#### DISCUSSION

The overall results demonstrate that fibronectin conformations within chitosan bone regeneration scaffolds can be readily detected using AuTSNP. This highlights the potential to readily monitor ECM macromolecular behaviour for the improvement of tissue regeneration scaffold properties using AuTSNP LSPR.

#### REFERENCES

- Brennan-Fournet, M. E., Huerta, M., Zhang, Y., Malliaras, G. & Owens, R. M. Detection of fibronectin conformational changes in the extracellular matrix of live cells using plasmonic nanoplates. *J. Mater. Chem. B* **3**, 9140–9147 (2015).
- Charles, D. E., Aherne, D., Gara, M., Ledwith, D.M., Gun'ko, Y. K., Kelly, J. M., Blau, W. J., Brennan-Fournet, M. E. Versatile Solution Phase Triangular Silver Nanoplates for Highly Sensitive Plasmon Resonance Sensing. *ACS Nano* **4**, 55–64 (2010).
- Devine, D. M., Hoctor, E., Hayes, J. S., Sheehan, E. & Evans, C. H. Extended release of proteins following encapsulation in hydroxyapatite/chitosan composite scaffolds for bone tissue engineering applications. *Mater. Sci. Eng. C* **84**, 281–289 (2018).
- Aherne, D., Charles, D. E., Brennan-Fournet, M. E., Kelly, J. M. & Gun'ko, Y. K. Etching-Resistant Silver Nanoprisms by Epitaxial Deposition of a Protecting Layer of Gold at the Edges. *Langmuir* **25**, 10165–10173 (2009).

THE SUNDAY TIMES  
GOOD UNIVERSITY GUIDE  
2018  
INSTITUTE OF TECHNOLOGY OF THE YEAR

# AIT Research

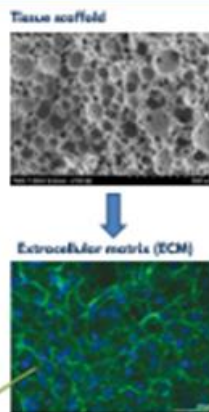


## EXTRACELLULAR MATRIX PROTEIN CONFORMATION MONITORING FOR THE OPTIMIZATION OF BIOMIMETIC BONE TISSUE REGENERATION SCAFFOLDS

Rodriguez Barroso, L.<sup>1</sup>, Lanzagorta Garcia, E.<sup>1</sup>, Azaman, F.A.<sup>1</sup>, Devine, D.,<sup>1</sup> Fournet, M.B.<sup>1</sup>, Lynch, M.<sup>1</sup>  
<sup>1</sup> Materials Research Institute, Athlone Institute of Technology

### Introduction

Tissue scaffolds, which mimic the native extracellular matrix (ECM) are under intense development for regenerative medical applications. The three-dimensional structure of ECM macromolecules is essential for the provision of structural support and signalling cues for the modulation of processes including cell migration and cell proliferation.



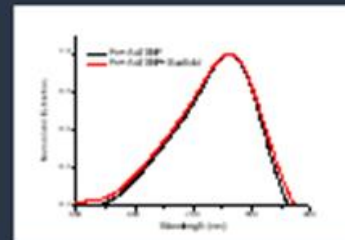
In this work, we present the detection of conformational transitions of fibronectin (Fn), a critical ECM protein. Plasmonic gold-edge-coated triangular silver nanoplates (AuTSNP) were used to spectrally monitor the conformation of fibronectin in the presence of biocompatible chitosan tissue scaffolds.



### Materials & Methods



### Results & discussion

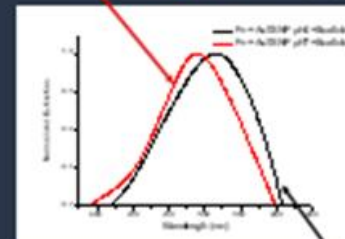


Spectrum of fibronectin-coated nanoplates with/without scaffold

Spectral signature of compact conformation



Compact Fn loaded AuTSNP (pH 7)



Extended Fn loaded AuTSNP (pH 4)



Spectral signature of extended conformation

Overall results demonstrate that fibronectin conformations in the presence chitosan bone regeneration scaffolds can be readily detected using AuTSNP. This highlights the potential to readily monitor ECM macromolecular behaviour for the improvement of tissue regeneration scaffold properties using AuTSNP spectrum.

References:  
 1. Brennan-Fournet, M. E., Huerta, M., Zhang, Y., Mullisras, G. & Owens, R. M. Detection of fibronectin conformational changes in the extracellular matrix of live cells using plasmonic nanoplates. *J. Mater. Chem. B*, 9140-9147 (2015).  
 2. Charles, D. E., Ahern, D., Gara, M., Leubold, D.M., Gun'ko, Y. K., Kelly, J. M., Han, W. J., Brennan-Fournet, M. E. Versatile Solution Phase Triangular Silver Nanoplates for Highly Sensitive Plasmon Resonance Sensing. *ACS Nano* 4, 55-64 (2010).  
 3. Devine, D. M., Hocker, E., Hayes, J. S., Sheehan, E. & Evans, C. H. Extended release of proteins following encapsulation in hydroxyapatite/chitosan composite scaffolds for bone tissue engineering applications. *Mater. Sci. Eng. C* 34, 281-289 (2013).  
 4. Ahern, D., Charles, D. E., Brennan-Fournet, M. E., Kelly, J. M. & Gun'ko, Y. K. Ethylenediamine-Resistant Silver Nanoplates by Epitaxial Deposition of a Protecting Layer of Gold at the Edges. *Langmuir* 25, 10165-10173 (2009).



## Appendix 4: Abstract for Materials Science and Smart Materials Conference 2019 (MSSM 2019)

### EXTRACELLULAR MATRIX PROTEIN CONFORMATION MONITORING IN THE PRESENCE OF BIOMIMETIC BONE TISSUE REGENERATION SCAFFOLDS

Rodriguez Barroso, L.<sup>1</sup>, Lanzagorta Garcia, E.<sup>1</sup>, Azaman, F.A.<sup>1</sup>, Devine, D.,<sup>1</sup> Fournet, M.B.<sup>1</sup>, Lynch M.<sup>1</sup>, Huerta, M.<sup>2</sup>.

<sup>1</sup> Materials Research Institute, Athlone Institute of Technology

<sup>2</sup> Department of Science and Technology, Linköping University

#### INTRODUCTION

Tissue scaffolds mimic the native extracellular matrix (ECM), which makes them attractive for the development for a range of regenerative medicine applications. The three-dimensional structure of the macromolecules present in the ECM is crucial for the provision of structural support to surrounding cells and signalling cues for the modulation of diverse processes including cell migration and proliferation.

In this work we present the detection of conformational transitions and behaviour of the ubiquitous ECM protein, fibronectin<sup>1</sup> in the presence of bone regeneration scaffolds and living cells. This critical ECM protein was attached to gold-edge-coated triangular silver nanoplates (AuTSNP), which exhibit some of the highest reported spectral shift responses to surface biomolecular interactions<sup>1,2</sup>, and was later added to cultured cells. Large spectral shifts distinguish between compact and extended fibronectin conformations in the presence of the chitosan bone regeneration scaffolds.

#### MATERIALS AND METHODS

High MW chitosan, fibronectin and chemicals for AuTSNP synthesis were obtained from Sigma Aldrich. Chitosan scaffolds were prepared using a previously reported crosslinking process.<sup>3</sup> AuTSNP were synthesised using a previously described seed mediated approach.<sup>4</sup> The highly sensitive local surface plasmon resonance (LSPR) of the AuTSNP was used to record the fibronectin conformations.<sup>1</sup> Zeta potential measurements were used to verify the fibronectin conformational status. The conformational profile of fibronectin was investigated in a cellular environment with and without the presence of the scaffold over time from 0 to 48h.

#### RESULTS

Fibronectin in a compact conformation has a hydrodynamic radius of the order of 23 nm as recorded by zetasizer measurements. In the extended conformation the increases for up to 130 nm for single fibronectin strands, however, can become much larger as networks and fibrils are formed over time. Figure 1 shows the AuTSNP LSPR signature readings for compact and extended fibronectin conformations.

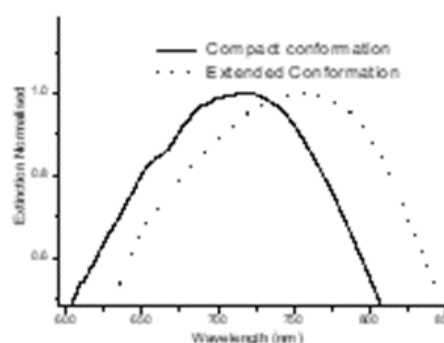


Figure 1 The LSPR signature of compact vs extended fibronectin conformations.

#### DISCUSSION

The overall results demonstrate that fibronectin conformations in the presence of living cells and chitosan bone regeneration scaffolds can be readily detected using AuTSNP. This highlights the potential to readily monitor ECM macromolecular behaviour for the improvement of tissue regeneration scaffold properties using AuTSNP LSPR.

#### REFERENCES

1. Brennan-Fournet, M. E., Huerta, M., Zhang, Y., Malliaras, G. & Owens, R. M. Detection of fibronectin conformational changes in the extracellular matrix of live cells using plasmonic nanoplates. *J. Mater. Chem. B* 3, 9140–9147 (2015).
2. Charles, D. E., Aherne, D., Gara, M., Ledwith, D.M., Gun'ko, Y. K., Kelly, J. M., Blau, W. J., Brennan-Fournet, M. E. Versatile Solution Phase Triangular Silver Nanoplates for Highly Sensitive Plasmon Resonance Sensing. *ACS Nano* 4, 55–64 (2010).
3. Devine, D. M., Hoctor, E., Hayes, J. S., Sheehan, E. & Evans, C. H. Extended release of proteins following encapsulation in hydroxyapatite/chitosan composite scaffolds for bone tissue engineering applications. *Mater. Sci. Eng. C* 84, 281–289 (2018).
4. Aherne, D., Charles, D. E., Brennan-Fournet, M. E., Kelly, J. M. & Gun'ko, Y. K. Etching-Resistant Silver Nanoprisms by Epitaxial Deposition of a Protecting Layer of Gold at the Edges. *Langmuir* 25, 10165–10173 (2009).

### Monitoring of Extracellular Matrix Protein Conformations in the Presence of Biomimetic Bone Tissue Regeneration Scaffolds

Rodriguez Barroso, L.<sup>1a</sup>, Lanzagorta Garcia, E.<sup>1b</sup>, Azaman, F.A.<sup>1c</sup>, Devine, D.M.<sup>1d</sup>, Lynch M.<sup>1e</sup>, Huerta, M.<sup>2f</sup>, Fournet, M.B.<sup>1g</sup>

<sup>1</sup>Materials Research Institute, Athlone Institute of Technology, Athlone, Ireland

<sup>2</sup>Department of Science and Technology, Linköping University, Norrköping, Sweden

<sup>a</sup>l.rodriguez@research.ait.ie, <sup>b</sup>e.lgarcia@research.ait.ie, <sup>c</sup>f.alwani@research.ait.ie, <sup>d</sup>ddevine@ait.ie, <sup>e</sup>marklynch@ait.ie, <sup>f</sup>miriam.huerta@liu.se, <sup>g</sup>mfournet@ait.ie

**Keywords:** Tissue scaffolds, extracellular matrix, fibronectin, triangular silver nanoplates, local surface plasmon resonance.

**Abstract.** Tissue scaffolds can be designed to mimic the native extracellular matrix (ECM), making them attractive for the development for a range of regenerative medicine applications. The macromolecules present in the ECM are critical for the provision of structural support to surrounding cells and signalling cues for the modulation of diverse processes including cell migration, proliferation and healing activation. Here, conformational and transitional behaviour of the ubiquitous ECM protein, fibronectin (Fn), in the presence of bone tissue regeneration scaffolds and living C2C12 myoblast cells is reported. Spectral monitoring of Fn functionalised high plasmonic resonance responsive gold-edge-coated triangular silver nanoplates (AuTSNP) is used to distinguish between compact and extended fibronectin conformations. Large spectral red shifts of ~20 to ~57 nm indicate Fn unfolding and fibril formation on incubation with C2C12 cells. The label-free nature, excellent sensitivity and straightforward application of the AuTSNP within cellular environments presents them as a powerful new tool to signature protein conformational activity in living cells and monitor essential protein activity for the assisted development of improved tissue scaffolds promoting enhanced tissue repair.

#### Introduction

Chitosan is a promising crustacean derivative biomaterial prepared by the deacetylation of chitin and is abundant in nature. Chitosan has excellent biodegradability, biomimetic and biocompatibility properties for tissue engineering applications and the simulation of self-healing matrices and mimetic tissue repair scaffolds [1]. Here chitosan (CS) is combined with the bone ceramic hydroxyapatite (HAp) and photocrosslinked to form an osteoconductive and osteointegrative CS-HAp bone tissue regeneration scaffold as previously reported [2].

Tissue scaffolds mimic the native extracellular matrix (ECM), this critical component controls fundamental cellular processes and provides structural support to surrounding cells. The three-dimensional structure of the macromolecules present in the ECM is essential for the delivery of signalling cues for the modulation of diverse cell behaviours including cell-cell communication and promoting tissue repair [3].

ECM proteins are implicated in cancer and have active participation in tumor progression [3]. In particular, fibronectin (Fn), a critical ECM protein whose functions are governed by its conformational activity, is receiving increasing attention due to its participation in various phases of tumor proliferation. Fn can exhibit a compact soluble formation while circulating within the bloodstream [3]. Under conditions where Fn expression is altered, it can

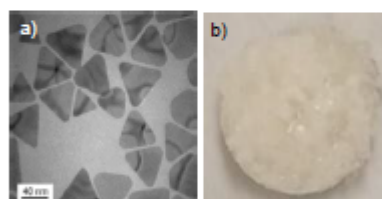


Fig. 1. (a) Transmission electron microscopy (TEM) of AuTSNP, b) CS-HAp bone tissue regeneration scaffold sample,

promote tumor cell invasion where upregulation and binding to cell-adhesion molecules and integrins, causes an activation of signaling pathways that promote tumorigenesis, metastasis and therapy resistance [3, 4]. Structurally Fn can experience conformational transitions induced by changes in the pH or temperature. Under physiological conditions (pH 7-7.4), Fn presents a folded compact shape, while at lower pH (pH 2.8-4) it extends to enable fibril formation [5].

The potential for versatile in-situ real-time monitoring of protein activity and conformational behaviour is possible using high sensitivity localized surface plasmon resonance (LSPR) Triangular Silver Nanoplates (TSNPs) [6]. LSPR is an optical phenomenon where light interacting with nanoparticle surface electrons, observed as an extinction spectrum, exhibits measurable spectral shifts in response to surface interactions. These shifts are induced by local material and molecular interactions which alter the refractive index in the immediate vicinity of the nanoparticles [6]. This feature allows the TSNP to be used as a sensitive and straightforward tool to detect both the presence and conformation of proteins, and has previously been reported for real-time monitoring of conformational changes in Fn in the presence of live cells [7].

In this work we present the detection of conformational transitions and fibril formation activity of Fn in the presence of CS-HAp bone tissue regeneration scaffolds and C2C12 myoblast cells. Fn functionalised on to gold-edge-coated triangular silver nanoplates (AuTSNP), which exhibit some of the highest reported spectral shift responses to surface biomolecular interactions, are used to record in situ real time progression of the Fn behaviour [7].

### Materials and Methods

High MW chitosan, fibronectin and chemicals for AuTSNP synthesis were obtained from Sigma Aldrich. C2C12 myoblast cell line was obtained from the European Collection of Authenticated Cell Cultures (ECACC). Extinction measurements were carried out using a UV-vis spectrometer (Synergy HT BioTek microplate reader). Scaffold sterilization was carried out using pulsed UV (Samtech Pulsed UV system).

#### Bone Tissue Regeneration Scaffold preparation

Chitosan- hydroxyapatite scaffolds (CS-HAp) were prepared using a previously reported novel one-step photocrosslinking reaction under the presence of UV light [2].

#### Gold-edge coated triangular silver nanoplates (AuTSNP) preparation

AuTSNP were synthesised using a previously described seed mediated approach [6]. TSNP growth was carried out by mixing 350  $\mu\text{L}$  of seed solution with ascorbic acid (AA) (75  $\mu\text{L}$ , 10mM), 4 mL of water and adding  $\text{AgNO}_3$  (3 mL, 0.5 mM) at a rate of 1 mL  $\text{min}^{-1}$ . After synthesis, TSC (500  $\mu\text{L}$ , 25 mM) was added to the solution. Gold coating for 1 mL of TSNP solution was carried out by adding and mixing Gold (III) chloride trihydrate (20  $\mu\text{L}$ , 0.5 mM) and AA (18.9  $\mu\text{L}$ , 10 mM).

#### Protein conformational changes monitoring

Before monitoring Fn conformational changes in the presence of C2C12 myoblast cells, LSPR sensing of fibronectin activity was carried out at two different pH values (pH 7 and pH 4) to monitor and record conformational transitions of the protein in the presence of bone tissue regeneration scaffolds. After that, nanoplates were incubated with the C2C12 myoblast cell line and bone tissue regeneration scaffolds and monitored over 32 hours using UV-Vis spectrometry. Before carrying out the assays, nanoplates were coated with polyethylene glycol (PEG-Np) to provide a protective layer and minimise the direct contact between fibronectin and the nanoplates surface minimising the influence in the protein conformational behaviour [7]. PEG-Np and Fn PEG-Np, were incubated with the cells to monitor the conformational behaviour and interactions in the cellular and scaffold environments and observe any changes in cell morphology.

### Cell culture

Cells were cultured with phenol red-free supplemented DMEM (Dulbecco's Modified Eagle Medium, 10% fetal bovine serum, 5% penicillin-streptomycin, 5% L-glutamine) in a humidified atmosphere of 5% CO<sub>2</sub> at 37 °C. Cells were plated at an initial density of 34 x 10<sup>4</sup> cells per mL in a 96 well plate and incubated for 24 h until confluence was reached. 600 μL of PEG-Np were preincubated with 20 μL of 1 mg/mL Fn. Before adding the nanoplates to the cells, media was changed to fresh media. Nanoplates and fibronectin-functionalised nanoplates were incubated with the cells in a PEG-Np - DMEM 1:1 ratio.

### Results and Discussion

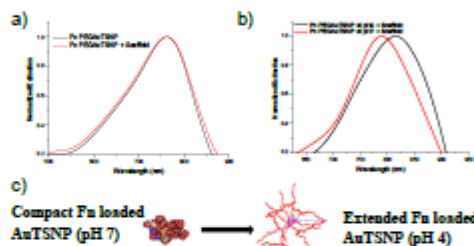


Fig. 2. a) UV-vis spectra of Fn functionalised PEG-Np with and without the presence of CS-HAp bone tissue regeneration scaffold. b) Spectral signatures of extended (black) and contracted (red) conformations of Fn at pH 4 and pH 7 respectively. c) Representation of Fn functionalised PEG-Np in compact and extended conformations.

associated with minimal interactions between the CS-HAp scaffold and the Fn functionalised PEG-Np. Upon pH adjustment from 7 to 4, the LSPR spectrum for Fn functionalised PEG-Np in the presence of the CS-HAp scaffold is observed to red shift by 27 nm, indicating the unfolding of the protein and its increased density in the vicinity of the AuTSNP (Fig. 2b) [7]. These large LSPR spectral differences distinguish between compact and extended Fn conformations due to induced refractive index changes local to the surface of the Au-TSNP. A red shift in the AuTSNP LSPR therefore provides a signature for Fn conformational transitioning from more compact to extended formats (Fig. 2c).

In order to observe Fn protein conformational transitions in the presence of CS-HAp bone tissue regeneration scaffolds and myoblast cells, Fn functionalised AuTSNP were incubated with C2C12 myoblast cells, CS-HAp scaffolds and monitored over time. Normal C2C12 myoblast morphology is shown for all treatments indicating that the AuTSNP have no observable detrimental effect on the cells (Fig 3).

In its contracted conformation, Fn has a hydrodynamic radius of the order of 23 nm which is exhibited when the pH is adjusted to 7. In the extended conformation at pH 4, the radius increases up to 130 nm for single Fn strands, however, it can become much larger as networks and fibrils are formed over time [7]. The LSPR extinction spectrum for Fn functionalised PEG-Np with and without the presence of CS-HAp bone tissue regeneration scaffolds is very similar indicating the strong attachment and insulating effect of the Fn on the AuTSNP surface from CS-HAp scaffold interactions. When no variation in pH is induced the LSPR spectrum shows no significant change with the LSPR<sub>max</sub> remaining constant, as shown in Fig. 2a. The minor broadening in the spectrum can be

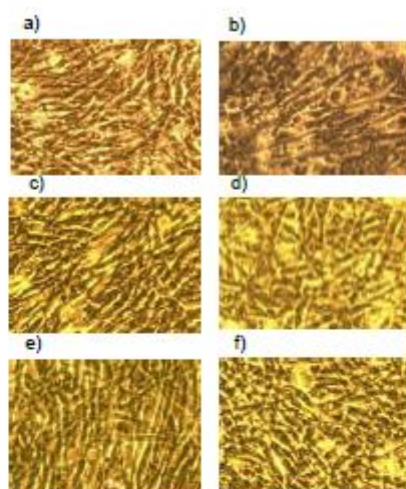


Fig. 3. Images of C2C12 cells taken after 32h of incubation with a) Fn, b) Fn and scaffold, c) Fn PEGNP, d) Fn PEGNP and scaffold, e) PEGNP, f) PEGNP and scaffold.

Fn PEG-NP in the presence of C2C12 myoblasts without the presence of the CS-HAP scaffolds, exhibit shifts of approximately  $\sim 20$  nm between 0h and 8h of incubation, while longer shifts of approximately  $\sim 57$  and  $\sim 50$  nm were measured from 24 h, as shown in figure 4 a). This can be associated with the expected increased unfolding and extension activity and the progressive fibrillar organization of the Fn within the cellular environment [8]. This is in keeping with reported evolution of Fn fibril formation at time points between 24h and 48h [9].

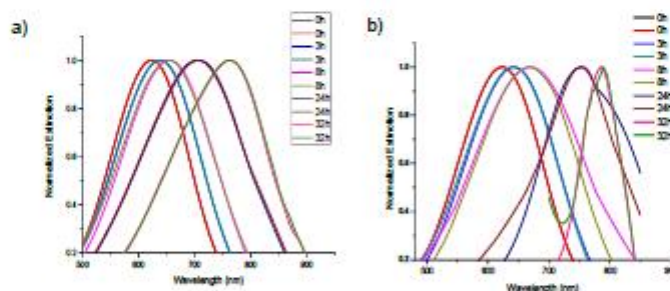


Fig. 4. LSPR spectra of a) Fn functionalised PEG-Np incubated with C2C12 over 32 hours, b) Fn PEG-Np incubated with C2C12 and tissue scaffolds over 32 hours.

The on-scaffold cellular incubated Fn-PEG-NP exhibited a similar behaviour with strong red shifts recorded overtime (Fig. 4b). These results correlate with the most recent models on Fn conformational activity within the cellular environment demonstrating the potential of the functionalised AuTSNP to detect dynamic protein conformational behaviour in living cells. Furthermore, this capacity to readily monitor critical on-scaffold protein behaviour has the potential to provide an essential tool for the development of advanced ECM mimetic tissue scaffolds for regenerative medicine applications.

### Conclusion

High sensitive LSPR Fn functionalised AuTSNP were used to monitor the conformational transitions of the ubiquitous ECM protein, Fn, in the presence of C2C12 myoblast cells. The conformational profile of Fn was investigated in a cellular environment with and without the presence of CS-HAp bone tissue regeneration scaffolds over time from 0 to 32h. As Fn unfolds from a compact conformation to form fibrils in which Fn displays a highly extended conformation, LSPR spectra exhibit large red shift shifts of ~20 nm generated over 32 hours. These results correlate directly with the most recent models on Fn conformational activity within the cellular environment, demonstrating the potential of the AuTSNP to provide critical detailed information on dynamic protein conformational response and behaviour. This highlights the capacity of the AuTSNP LSPR technique for straightforward, versatile non-labelling measurements of protein conformational dynamics in the high noise cellular environment and potential application in the development of advanced tissue scaffolds with improved regenerative and repair performance.

### References

- [1] Abdel-Fattah, W. I. et al. (2007) 'Synthesis, characterization of chitosans and fabrication of sintered chitosan microsphere matrices for bone tissue engineering', *Acta Biomaterialia*, 3(4), pp. 503–514. doi: 10.1016/j.actbio.2006.12.004.
- [2] Devine, D. M., Hoctor, E., Hayes, J. S., Sheehan, E. & Evans, C. H. (2018) Extended release of proteins following encapsulation in hydroxyapatite/chitosan composite scaffolds for bone tissue engineering applications. *Mater. Sci. Eng. C* 84, 281–289.
- [3] Wang, J., & Hielscher, A. (2017). Fibronectin: How Its Aberrant Expression in Tumors May Improve Therapeutic Targeting. *Journal Of Cancer*, 8(4), 674-682. doi: 10.7150/jca.16901
- [4] Pankov, R., & Yamada, K. (2002). Fibronectin at a glance. *Journal Of Cell Science*, 115(20), 3861-3863. doi: 10.1242/jcs.00059
- [5] Tooney, N. M., Mosesson, M. W., Amrani, D. L., Hainfeld, J. F., & Wall, J. S. (1983). Solution and surface effects on plasma fibronectin structure. *The Journal of cell biology*, 97(6), 1686–1692. doi:10.1083/jcb.97.6.1686
- [6] Zhang, Y., Charles, D. E., Ledwith, D. M., Aherne D., Cunningham, S., Voisin, M., Blau, W. J., Gun'ko, Y. K., Kelly, J. M. & Brennan-Fournet, M. E. (2014) Wash-free highly sensitive detection of C-reactive protein using gold derivatized triangular silver nanoplates. *Royal Society of Chemistry*, 4, 29022-29031. Doi: 10.1039/c4ra04958f
- [7] Brennan-Fournet, M. E., Huerta, M., Zhang, Y., Malliaras, G. & Owens, R. M. (2015) Detection of fibronectin conformational changes in the extracellular matrix of live cells using plasmonic nanoplates. *J. Mater. Chem. B* 3, 9140–9147.
- [8] Rozario, T., Dzamba, B., Weber, G. F., Davidson, L. A., & DeSimone, D. W. (2009). The physical state of fibronectin matrix differentially regulates morphogenetic movements in vivo. *Developmental biology*, 327(2), 386–398. doi:10.1016/j.ydbio.2008.12.025
- [9] Antia, M., Baneyx, G., Kubow, K. and Vogel, V. (2008). Fibronectin in aging extracellular matrix fibrils is progressively unfolded by cells and elicits an enhanced rigidity response. *Faraday Discussions*, 139, p.229.

## Appendix 6: MSSM 2019 Certificate of participation



THE SUNDAY TIMES  
GOOD UNIVERSITY GUIDE  
2018  
INSTITUTE OF TECHNOLOGY OF THE YEAR

# AIT Research



## MONITORING OF EXTRACELLULAR MATRIX PROTEIN CONFORMATIONS IN THE PRESENCE OF BIOMIMETIC BONE TISSUE REGENERATION SCAFFOLDS

Rodriguez Barroso, L.<sup>1</sup>, Lanzagorta Garcia, E.<sup>1</sup>, Azaman, F.A.<sup>1</sup>, Devine, D.M.<sup>1</sup>, Lynch M.<sup>1</sup>, Huerta, M.<sup>2</sup>, Fournet, M.B.<sup>1</sup>

<sup>1</sup> Materials Research Institute, Athlone Institute of Technology, Athlone, Ireland  
<sup>2</sup> Department of Science and Technology, Linköping University, Norrköping, Sweden

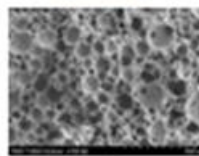
### Introduction

Tissue scaffolds, which mimic the native extracellular matrix (ECM) are under intense development for regenerative medical applications. The three-dimensional structure of ECM macromolecules is essential for the provision of structural support and signalling cues for the modulation of processes including cell migration and cell proliferation. ECM proteins are implicated in cancer and have active participation in tumour progression. In particular, fibronectin (Fn), a critical ECM protein whose functions are governed by its conformational activity, is receiving increasing attention due to its participation in various phases of tumour proliferation.

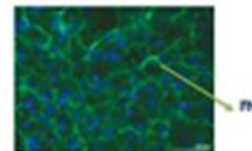
In this work, conformational and transitional behaviour of Fn in the presence of bone tissue regeneration scaffolds and living C2C12 myoblast cells is reported. Spectral monitoring of Fn functionalised high plasmonic resonance responsive gold-edge-coated triangular silver nanoparticles (AuTSNP) is used to distinguish between compact and extended fibronectin conformations.



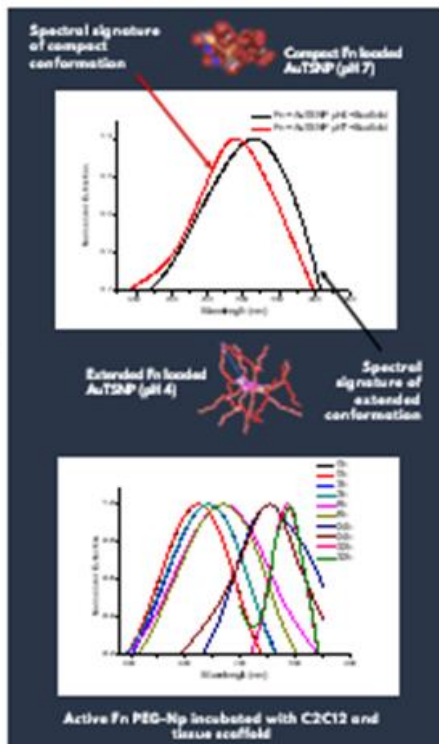
Tissue scaffold



Extracellular matrix (ECM)



### Results & discussion



### Materials & Methods



High sensitive LSPR Fn functionalised AuTSNP were used to monitor the conformational transitions of Fn in the presence of C2C12 myoblast cells over time from 0 to 32h. As Fn unfolds from a compact conformation to form fibrils in which Fn displays a highly extended conformation, LSPR spectra exhibit large red shifts. These results correlate with the most recent models on Fn conformational activity within the cellular environment, demonstrating the potential of the AuTSNP to provide critical detailed information on dynamic protein conformational response and behaviour.

References:  
 1. Brennan-Fournet, M. E., Huerta, M., Zhang, Y., Mellinas, G. & Owens, R. M. Detection of fibronectin conformational changes in the extracellular matrix of live cells using plasmonic nanoparticles. *J. Mater. Chem.* **23**, 9160-9167 (2013).  
 2. Charles, D. E., Aherne, D., Gora, M., Lech, S., D.M. Gue'ra, Y. K. Kelly, J. M. Blou, M. J. Brennan-Fournet, M. E. Versatile Solution Phase Triangular Silver Nanoplates for Highly Sensitive Plasmonic Sensing. *ACS Nano* **4**, 55-64 (2010).  
 3. Devine, D. M., Hackett, E., Hayes, J. S., Sheehan, E. & Evans, C. H. Extended release of proteins following encapsulation in hydroxyapatite/chitosan composite scaffolds for bone tissue engineering applications. *Mater. Sci. Eng. C* **84**, 281-289 (2018).  
 4. Ahirra, D., Charles, D. E., Brennan-Fournet, M. E., Kelly, J. M. & Gue'ra, Y. K. Etching-Resistant Silver Nanoplates by Epitaxial Deposition of a Protecting Layer of Gold at the Edges. *Langmuir* **23**, 10165-10173 (2009).



## Appendix 8: Abstract for Bioengineering in Ireland Conference 2020, January 2020

Early Stage Researcher (PhD Year 1)	<input checked="" type="checkbox"/>	Post-Doctoral Researcher/Senior Researcher/PI	<input type="checkbox"/>
Entry for the Engineers Ireland Biomedical Research Medal	<input type="checkbox"/>	Corresponding author has completed PhD and would like to review Biml abstract submissions	<input type="checkbox"/>

Please place an X in any appropriate categories

### DEVELOPMENT OF A VERSATILE MONITORING TECHNIQUE FOR REAL-TIME PROTEIN ACTIVITY TRACKING WITHIN CELLULAR AND BIOMIMETIC SCAFFOLD SYSTEMS

Rodriguez Barroso, L.<sup>1</sup>, Lanzagorta Garcia, E.<sup>1</sup>, Azaman, F.A.<sup>1</sup>, Devine, D.M.<sup>1</sup>, Lynch M.<sup>1</sup>, Huerta, M.<sup>2</sup> Fournet, M.B<sup>1</sup>

<sup>1</sup> Materials Research Institute, Athlone Institute of Technology, Athlone, Ireland

<sup>2</sup> Department of Science and Technology, Linköping University, Norrköping, Sweden  
email: mfournet@ait.ie

#### INTRODUCTION

Crowded cellular environments with complex and intricate molecular interactions underpin biological processes. High biological noise is intrinsic within these biological systems, and this poses critical challenges to the in situ detection and measurement of biomolecular and protein activities important to advancing approaches to disease and injury treatment. Currently the techniques available to characterize protein behaviours in living biological systems are highly elaborate and are generally greatly hindered by the high background noise<sup>2</sup>.

Here we present a versatile and straight forward technique for monitoring Fibronectin, a critical extracellular matrix (ECM) protein and its interactions within cells, based on a novel nano-bio-technology method. High sensitive gold edge coated triangular silver nanostructures (AuTSNP), which are highly responsive to molecular interactions on their surfaces, are used to probe protein behaviours within complex cellular and tissue regeneration environments.

#### MATERIALS AND METHODS

High MW chitosan, fibronectin and chemicals for AuTSNP synthesis were obtained from Sigma Aldrich. Chitosan scaffolds were prepared using a previously reported crosslinking process.<sup>3</sup> AuTSNP were synthesised using a previously described seed mediated approach.<sup>4</sup> The highly sensitive local surface plasmon resonance (LSPR) of the AuTSNP was used to record the fibronectin conformations.<sup>1</sup> Fn functionalised PEG-AuTSNP were incubated with C2C12 myoblast cells and chitosan scaffolds, and monitored over 32 hours.

#### RESULTS

LSPR measurements showed significant red shifts associated with the expected increased unfolding and extension activity and the progressive fibrillary organization of the active Fn within the cellular environment. Figure 1 shows the AuTSNP LSPR readings for fibronectin upon incubation with C2C12 myoblasts and scaffold.

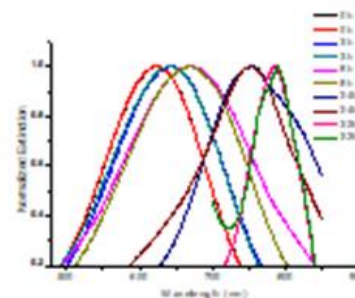


**Figure 1** LSPR spectra of active Fn PEG-AuTSNP incubated with C2C12 myoblasts and Cs-HAP regeneration scaffolds.

#### DISCUSSION

The conformational profile of Fn was investigated in a cellular environment with and without the presence of CS-HAP bone tissue regeneration scaffolds over time from 0 to 32h. The results correlate directly with the most recent models on Fn conformational activity within the cellular environment, demonstrating the potential of the AuTSNP to provide critical detailed information on dynamic protein conformational response and behaviour

#### REFERENCES

- Brennan-Fournet, M. E., Huerta, M., Zhang, Y., Malliaras, G., & Owens, R. M. (2015). Detection of fibronectin conformational changes in the extracellular matrix of live cells using plasmonic nanoplates. *Journal of Materials Chemistry B*, 3(47), 9140-9147.
- Eberhardt, K., Stiebing, C., Matthäus, C., Schmitt, M., & Popp, J. (2015). Advantages and limitations of Raman spectroscopy for molecular diagnostics: An update. *Expert Review of Molecular Diagnostics*, 15(6), 773787.
- Devine, D. M., Hoctor, E., Hayes, J. S., Sheehan, E., & Evans, C. H. Extended release of proteins following encapsulation in hydroxyapatite/chitosan composite scaffolds for bone tissue engineering applications. *Mater. Sci. Eng. C* **84**, 281-289 (2018).
- Aherne, D., Charles, D. E., Brennan-Fournet, M. E., Kelly, J. M. & Gun'ko, Y. K. Etching-Resistant Silver Nanoprisms by Epitaxial Deposition of a Protecting Layer of Gold at the Edges. *Langmuir* **25**, 10165-10173 (2009).

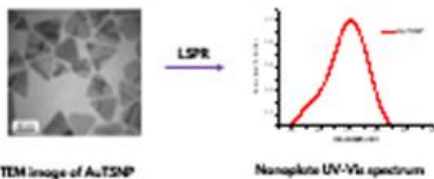
**DEVELOPMENT OF A VERSATILE MONITORING TECHNIQUE FOR REAL-TIME PROTEIN ACTIVITY TRACKING WITHIN CELLULAR ENVIRONMENTS AND BIOMIMETIC TISSUE ENGINEERING SCAFFOLD SYSTEMS**

Rodriguez Barroso, L.<sup>1</sup>, Lanzagorta Garcia, E.<sup>1</sup>, Azaman, F.A.<sup>1</sup>, Devine, D.M.<sup>1</sup>, Lynch M.<sup>1</sup>, Huerta, M.<sup>2</sup>, Fournet, M.B<sup>1</sup>

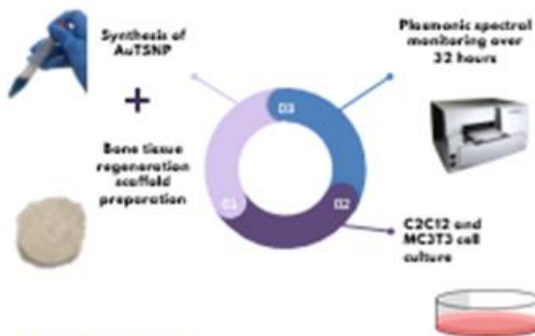
<sup>1</sup> Materials Research Institute, Athlone Institute of Technology, Athlone, Ireland  
<sup>2</sup> Department of Science and Technology, Linköping University, Norrköping, Sweden

**Introduction**

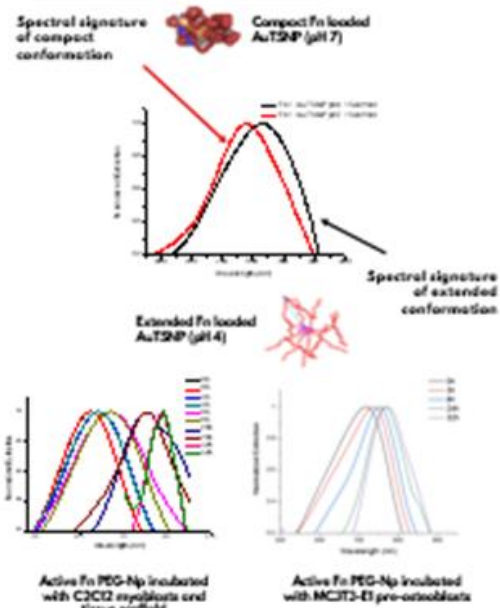
Crowded cellular environments with complex and intricate molecular interactions underpin biological processes. High biological noise is intrinsic within these biological systems, and this poses critical challenges to the in situ detection and measurement of biomolecular and protein activities important to advancing approaches to disease and injury treatment. Currently the techniques available to characterise protein behaviours in living biological systems are highly elaborate and are generally greatly hindered by the high background noise of the cellular environments. Here we present a versatile and straight forward technique for monitoring proteins and protein interactions within cells, based on a novel nano-bio-technology method based on nanoparticles Local Surface Plasmon Resonance (LSPR). High sensitive gold edge coated triangular silver nanostructures (AuTSNP), which exhibit a highly sensitive spectral response to the molecular interactions on their surfaces, are used to probe protein behaviours within complex cellular and tissue regeneration environments. In this work, monitoring of the dynamic behaviour of a critical extracellular protein, Fibronectin (Fn) in its active form, within the presence of bone tissue regeneration scaffolds and living cells (C2C12 myoblasts, MC3T3-E1 pre-osteoblasts) is presented. The excellent sensitivity and straight forward application within cellular environments, demonstrates AuTSNP as powerful new tools to signature protein conformational transitions and monitor essential protein activity.



**Materials & Methods**



**Results & discussion**



High sensitive LSPR Fn functionalised AuTSNP were used to monitor the conformational transitions of Fn in the presence of C2C12 myoblast cells and bone tissue regeneration scaffolds over time from 0 to 32h. As Fn unfolds from a compact conformation to form fibrils in which Fn displays a highly extended conformation, LSPR spectra exhibit large red shifts. A similar behaviour is observed when fibronectin functionalised AuTSNP are incubated with MC3T3-E1 pre-osteoblasts and monitored over the same time. These results correlate with the most recent models on Fn conformational activity within the cellular environment, demonstrating the potential of the AuTSNP to provide critical detailed information on dynamic protein conformational response and behaviour.

**References**

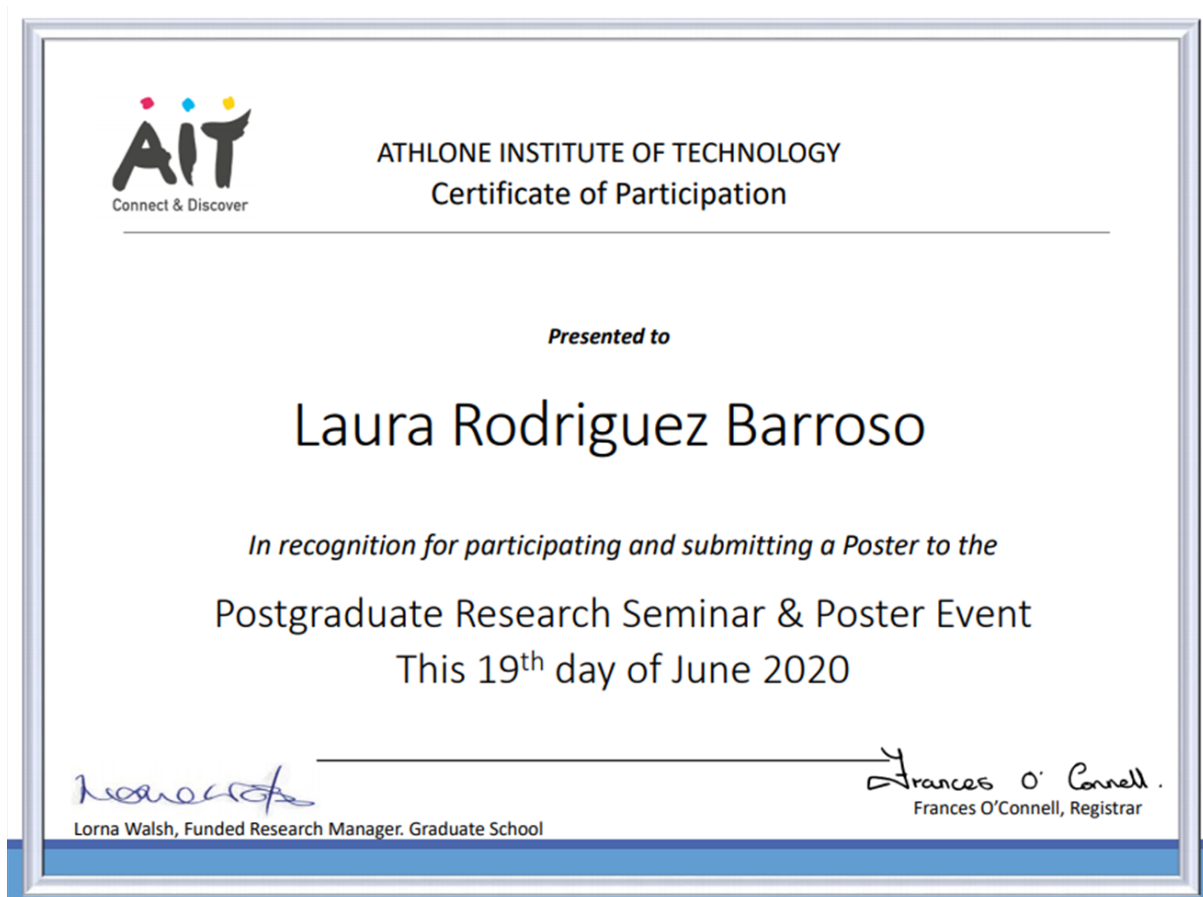
1. Brennan-Fournet, M. S., Huerta, M., Zhang, Y., Mallam, G. & Devine, E. M. Detection of fibronectin conformational changes in the extracellular matrix of live cells using plasmonic nanoparticles. *J Mater Chem C*, 3(19), 5190-5197 (2015).
2. Charles, D. S., Alvarez, D. S., Azaman, F. A., Garcia, F. A., Kelly, J. M., Lynch, M. J., Brennan-Fournet, M. S. Versatile Solution Phase Triangular Silver Nanoplates for Highly Sensitive Plasmonic Resonance Imaging. *ACS Nano* 4, 55-64 (2010).
3. Devine, D. M., Huerta, M., Hayes, J. S., Brennan, G. & Brown, C. H. Extended release of proteins following encapsulation in hydroxyapatite/collagen composite scaffolds for bone tissue engineering applications. *Mater Sci Eng C* 28, 287-297 (2010).
4. Alvarez, D., Charles, D. S., Brennan-Fournet, M. S., Kelly, J. M. & Garcia, Y. K. Sinking-Suspended Silver Nanoplates by Epitaxial Deposition of a Protecting Layer of Gold at the Substrate. *Langmuir* 24, 12763-12771 (2008).



AIT Research



**Appendix 10: Postgraduate Research Seminar and Poster Event certificate of participation**



**Appendix 11: Shannon Region Postgraduate Research Conference certificate of participation**



**CERTIFICATE OF PARTICIPATION** 

---

SRPRC RECOGNISES THAT

**LAURA GABRIELA RODRIGUEZ BARROSO**

---

Attended the 1st Shannon Region Postgraduate  
Research Conference, between 18th and 19th May  
2021, VIRTUAL.

---

THE SRPRC COMMITTEE 2021  
19TH MAY 2021

# Appendix 12: PosterFest 2022, Technological University of the Shannon: Midlands Midwest



## Functionality of Gold-Edge-Coated Triangular Silver Nanoparticles in Monitoring Extracellular Matrix Protein Conformations in C2C12/MC3T3-E1 Culture in the Presence of Biomimetic Bone Tissue Regeneration Scaffolds

Laura G. Rodriguez Barroso,<sup>a</sup> Farah Alwani Azaman<sup>a</sup>, Robert Pogue<sup>a,b</sup>, Declan Devine<sup>a</sup> and Margaret Brennan Fournet<sup>a</sup>

a. Technological University of the Shannon, Dublin Rd, N37 HD68, Athlone, Co. Westmeath, Ireland.  
 b. Universidade Católica de Brasília, Campus Asa Norte. SGAN módulo B 916 Avenida W5 – Asa Norte, 70790-160-DF, Brasília, Brazil.

### Introduction

In the cellular environment high noise levels can both mediate and interfere with cellular functions.

The extracellular matrix (ECM) regulates protein dynamics and trajectories, which underpin critical biological processes involved in the development of human disorders and healing processes.

FRET and Raman Spectroscopy are conventional techniques for the study of proteins, however, they are elaborate, and their signals are hindered by the high noise levels of cellular environments.

Noble metal nanoparticles are known to have remarkable optical properties and have been researched for the development of highly sensitive nanobiosensors to study molecules and their interactions in the extracellular matrix.

Gold edge-coated triangular silver nanoparticles (AuTNSP) were validated as a promising new tool to point protein conformational transitions in cultured cells, and to monitor protein activity in the presence of a biomimetic chitosan-based scaffold, since it mimics the ECM as a natural scaffold.

Scaffolds of different formulations were characterised to obtain the strongest construct, with regard to the strength of the linkage formation under photocrosslinking procedures.

### Results

Chitosan-Hydroxyapatite biomimetic scaffold

**C2C12 +/- scaffold**

**MC3T3 +/- scaffold**

### Methodology

AuTNSP optimization and preparation

Chitosan scaffold preparation and crosslinking characterisation

C2C12, MC3T3 cell culture

Monitoring of Fn in cell culture

Monitoring of Fn in cells + chitosan-based scaffold

### Conclusion

Functionalised AuTNSPs performance as Fibronectin (Fn) biosensors in the presence of ECM-mimicking bone regeneration scaffolds was demonstrated. The specificity of the Fn monitoring was confirmed through spectral monitoring denatured and active protein where it was successfully demonstrated that gold edge-coated triangular silver nanoparticles are powerful tools for non-labelling measurements for biomolecule dynamics in high background noise environments such as MC3T3 and C2C12 cell lines. The remarkable sensitivity of AuTNSPs enables their capability to interact with and sense tissue molecular signalling and hence can provide extraordinary possibilities for the development and progression of regenerative medicine.

### References

[List of references]







**Appendix 13: Nanotech France 2022 Conference, certificate of participation. Paris, France, 15-17 June 2022**



## Article

# Monitoring In Vitro Extracellular Matrix Protein Conformations in the Presence of Biomimetic Bone-Regeneration Scaffolds Using Functionalized Gold-Edge-Coated Triangular Silver Nanoparticles

Laura G. Rodriguez Barroso <sup>1</sup>, Farah Alwani Azaman <sup>1</sup>, Robert Pogue <sup>1,2</sup>, Declan Devine <sup>1</sup> and Margaret Brennan Fournet <sup>1,\*</sup>

<sup>1</sup> Technological University of the Shannon: Midlands Midwest, Dublin Rd., N37 HD68 Athlone, Co. Westmeath, Ireland

<sup>2</sup> Universidade Católica de Brasília, Campus Asa Norte, SGAN Módulo B 916 Avenida W5—Asa Norte, Brasília 70790-160-DF, Brazil

\* Correspondence: [mfournet@tsh.ie](mailto:mfournet@tsh.ie)

**Abstract** In the cellular environment, high noise levels, such as fluctuations in biochemical reactions, protein variability, molecular diffusion, cell-to-cell contact, and pH, can both mediate and interfere with cellular functions. In this work, gold edge-coated triangular silver nanoparticles (AuTNSNP) were validated as a promising new tool to indicate protein conformational transitions in cultured cells and to monitor essential protein activity in the presence of an optimized bone biomimetic chitosan-based scaffold whose rational design mimics the ECM as a natural scaffold. A chitosan-based scaffold formulation with hydroxyapatite (CS/HAp) was selected due to its promising features for orthopedic applications, including combined high mechanical strength biocompatibility and biodegradability. Functionalized AuTNSNP-based tests with the model ECM protein, fibronectin (Fn), illustrate that the protein interactions can be clearly sensed over time through the local surface plasmon resonance (LSPR) technique. This demonstrates that AuTNSNP are a powerful tool to detect protein conformational activity in the presence of biomimetic bone tissue regeneration scaffolds within a cellular environment that comprises a diversity of molecular cues.

**Keywords:** triangular silver nanoparticles; fibronectin; LSPR; extracellular matrix; regeneration scaffold



**Citation:** Rodriguez Barroso, L.G.; Azaman, F.A.; Pogue, R.; Devine, D.; Fournet, M.B. Monitoring In Vitro Extracellular Matrix Protein Conformations in the Presence of Biomimetic Bone-Regeneration Scaffolds Using Functionalized Gold-Edge-Coated Triangular Silver Nanoparticles. *Nanomaterials* **2023**, *13*, 57. <https://doi.org/10.3390/nano13010057>

Academic Editor: Csaba Balazsi

Received: 7 December 2022

Revised: 20 December 2022

Accepted: 22 December 2022

Published: 23 December 2022



Copyright: © 2022 by the authors. Licensee MDPI, Basel, Switzerland. This article is an open access article distributed under the terms and conditions of the Creative Commons Attribution (CC BY) license (<https://creativecommons.org/licenses/by/4.0/>).

## 1. Introduction

The crowded extracellular matrix (ECM) controls protein dynamics and trajectories, which underpin important biological processes that can activate response chains for the development of numerous human disorders as well as healing processes. Fluorescence Resonance Energy Transfer (FRET) and Raman Spectroscopy are conventional techniques used to characterize and analyze these protein activities and interactions; however, they are elaborated, and their signals are hindered or obstructed by the high background noise of physiological environments. As an alternative, noble metal nanoparticles are known to have remarkable optical properties and have been intensely researched for the development of highly sensitive nano biosensors to investigate a range of molecules and detect their interactions in the extracellular matrix. Proteins are the most abundant macromolecules in all organisms, with defined amino acid geometries and structures. Three-dimensional protein structures are diverse, ranging from fibrous to globular, and are integral to protein function [1,2]. These structures may possess moving parts where mechanical actions are correlated with biochemical reactions [3]. This correlation between protein conformation and function is being widely analyzed to progress our understanding

of biological processes ranging from proteinopathy (protein conformational disorders) development to healing processes [4].

Several techniques exist for the detection of conformational changes and structural variations in proteins, though each has associated limitations or requires compromise for their implementation. These techniques include spectroscopic methods such as Raman spectroscopy, fluorescent methods such as fluorescence resonance energy transfer (FRET), and nuclear magnetic resonance (NMR) [5]. While sensitive when used for protein analysis, they are however remarkably complex, requiring specialized equipment, and their signals are generally greatly hindered by the high background noise of the cellular environment. This complex environment contains water molecules, ions, and metabolites, as well as macromolecules, including proteins, carbohydrates, nucleic acids, and lipids [6]. This represents a challenge when measurements are performed under cellular conditions and required for advanced real-time detection in applications such as personalized medicine [7]. In this context, noble metal nanoparticles present exceptional optical properties which are highly localized at the nanoscale and exhibit important features for the development of highly sensitive nano biosensors to study a variety of molecules and their interactions [8]. Several nanostructures with high refractive index sensitivities have been reported, such as triangular silver nanoparticles (TSNP), silver nanoprisms, nanorice, among others [9]. The strong localization of the detection exhibited by high refractive index sensitive nanostructure provides a critical advantage when operating within high noise environments. For biosensing applications, the local surface plasmon resonance (LSPR) of the nanostructures governs their optical spectrum, which can respond to interactions at the nanostructures' surface. In this optical phenomenon, light wavelengths which are resonant with the surface electrons result in an extinction spectrum with distinctive LSPR bands [10]. The LSPR position depends on the nanostructures' shape, size, uniformity, and composition as well as the refractive index of its environment [11]. The latter feature can be exploited for biosensing as variation in the localized refractive index due to analyte interactions or conformational changes can result in LSPR peak alterations. Nanostructure LSPR has been used for several biological applications, including monitoring of protein interactions, detection of toxins, and monitoring of biomarkers, including glucose, peptides, and microRNAs [12]. Among these diverse nanostructures, TSNPs exhibit some of the strongest LSPR responsivities [13].

The extracellular matrix (ECM) is known to play an important role in regulating cell function, health, repair, and growth through a diversity of physical, chemical, and biological cues [14]. Since tissue engineering research evolved during the early 1990s, a range of 3D porous scaffolds has been developed, including biomimetic scaffolds, which have the ability to mimic the architecture of natural ECM. This is a promising technology in the advancement of tissue repair in areas including orthopedics, dermatology, and dental treatment [15]. Since tissue engineering aims to restore the tissue and organ functionality that may be lost due to injury, aging, or diseases [16], this field is indeed an advanced alternative to traditional surgical approaches of autologous and allogeneic treatment, which involve increased risks of complications such as lack of donors and a high risk of donor-site morbidity. Therefore, extensive work has been ongoing in creating scaffold formulations that have the capability to mimic the natural extracellular matrix of the body by using biodegradable materials such as chitosan [17]. An important approach involves biomimetic scaffolds suffusion with suitable growth factors to aid the process of tissue repair, such as bone tissue regeneration. The incorporated growth factors are designed to be released in a gradual manner, providing a fully functional effect on the site [18]. As such, it is important to be able to monitor the bioactivity of such growth factor through its induction of conformational changes in the cellular environment.

In the current work, an optimized formulation of high LSPR responsive gold-edge-coated triangular silver nanoparticles (AuTSNP) [19] was utilized for label-free monitoring of conformations of the ECM fibronectin (Fn) protein component in both C2C12 myoblast culture and MC3T3 pre-osteoblasts, in the presence of an optimized bioactive



biomimetic bone regeneration scaffold as a model for the ECM. This LSPR methodology is illustrated in Figure 1.

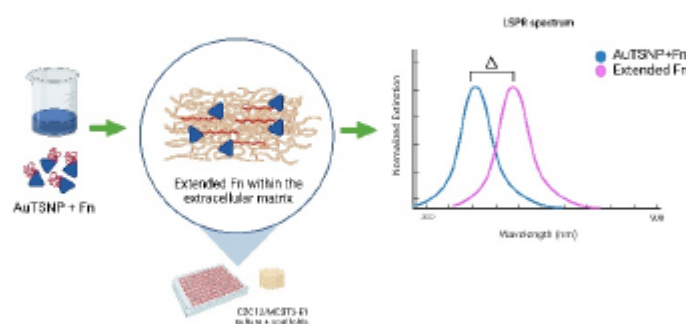


**Figure 1.** LSPR methodology for Fn extension monitoring overtime within cells ECM. Created with Biorender.com.

## 2. Materials and Methods

High molecular weight chitosan, hydroxyapatite, tricalcium phosphate, acetic acid, reagents for AuTSNP synthesis, and fibronectin were obtained from Sigma-Aldrich. Poly (ethylene glycol) dimethyl methacrylate 600 (PEGDMA600) was obtained from Polysciences Inc. (Polysciences Europe GmbH, Germany), and Benzophenone, 99% was purchased from Alfa Aesar (ThermoFisher (Kandel) GmbH). The C2C12 myoblast cell line was purchased from the European Collection of Authenticated Cell Cultures (ECACC). MC3T3-E1 pre-osteoblast cell line (CRL-2593) was obtained from American Type Culture Collection (ATCC). Extinction measurements were performed using an Ultraviolet-visible (UV-vis) spectrometer (Synergy HT BioTek microplate reader, Winooski, VT, USA). Scaffold sterilization was performed using a pulsed UV chamber (Santech Pulsed UV system, Ltd., Glasgow, Scotland).

### 2.1. Fabrication of Chitosan-Based Scaffolds

Chitosan (CS) scaffold composites were prepared by means of a one-step photocrosslinking method under a UV lamp as described previously [20,21]. Chitosan was first dissolved in 1% acetic acid to make 12% (*w/v*) chitosan paste. Following this, 0.1% (*w/v*) benzophenone photoinitiator and poly (ethylene glycol) dimethyl methacrylate 600 (PEGDMA600) were also added to the mixture to initiate the photocrosslinking process under UV light. Hydroxyapatite (HAp) bioceramic was incorporated into the mixture, making 1:1 CS/HAp scaffolds. The composite paste was transferred into silicone molds of 5 mm diameter and placed in a UV chamber (Dr. Gröbel UV-Elektronik GmbH) with 20 UV lamps to cure for 10 min, with flipping mid-curing.

### 2.2. Scaffold Characterization

The linkage and structural properties of CS/HAp scaffolds were examined by using attenuated total reflectance Fourier-transform infrared (FTIR) spectroscopy on a Perkin-Elmer Spectrum One FTIR spectrometer fitted with a universal ATR sampling accessory. All tests were run by using a spectral range of 4000 to 650  $\text{cm}^{-1}$ . Four scans per sample cycle were utilized with a resolution of 0.5  $\text{cm}^{-1}$  at room temperature. The samples were dried in a vacuum oven at 37 °C and 70 mbar prior to the tests to avoid shadowing the significant signature peaks of the materials by the broad water peaks. Following the tests, all spectra obtained were analyzed to observe the linkages formed within all the formulations.

### 2.3. Gold-Edge Coated Triangular Silver Nanoplates (AuTSNP) Preparation

Triangular silver nanoplates (TSNP) were prepared through a seed-silver catalyzed reduction of silver nitrate by sodium borohydride. The preparation of the seeds involved a one-pot synthesis in 4.5 mL of Sigma water followed by the addition of trisodium citrate (TSC) (500  $\mu$ L, 25 mM), poly (4-styrene sulfonate sodium salt) (PSSS) (250  $\mu$ L, 500 mg/L), sodium borohydride ( $\text{NaBH}_4$ ) (300  $\mu$ L, 10 mM), and finally the addition of silver nitrate ( $\text{AgNO}_3$ ) (5 mL, 0.5 mM). The latter was added via a pump at a rate of 2 mL  $\text{min}^{-1}$ . Upon seeds synthesis, TSNP production was performed by mixing 75  $\mu$ L of ascorbic acid (10 mM) with 350  $\mu$ L of seed solution, 4 mL of water and 3 mL of  $\text{AgNO}_3$  (0.5 mM) added via a pump at a rate of 1 mL  $\text{min}^{-1}$ . After TSNP growth, 500  $\mu$ L of TSC (25 mM) was added to the solution as a stabilizer.

TSNP were protected against etching through the deposition of a thin layer of gold on the edge of the nanoplates. This was achieved by mixing 20  $\mu$ L of Gold (III) chloride trihydrate ( $\text{HAuCl}_4$ ) (0.5 mM) and 18.9  $\mu$ L of ascorbic acid (10 mM) with 1 mL of TSNP solution. Further protection of the nanoplates for the protein monitoring experiments within cell culture was carried out by adding a coat of PEG 20,000 on the nanoparticle's surface to minimize contact between the functionalized protein and the particles to avoid influence on the protein's performance.

### 2.4. Cell Culture

For the initial experiments, the C2C12 myoblast cell line was grown in phenol red-free DMEM (Dulbecco's Modified Eagle Medium) completed with 10% fetal bovine serum (FBS), 5% penicillin–streptomycin, and 5% L-glutamine in a humidified atmosphere (5%  $\text{CO}_2$  at 37  $^\circ\text{C}$ ). C2C12 cells were plated in a 96-well plate at an initial density of  $5 \times 10^4$  cells per well and incubated until confluent for 24 h. Smaller diameter CS-HAP scaffolds (0.5 cm) were placed in the wells before adding the cells. PEG-Np (600  $\mu$ L) were preincubated with 20  $\mu$ L of fibronectin (1 mg/mL) in its active and denatured forms. Fibronectin denaturation was carried out by heating the protein in a water bath at 95  $^\circ\text{C}$  for 15 min. Before adding the nanoplate treatments to the cells after 24 h of incubation, the growth media was changed to fresh media. The cultured cells were incubated with the nanoplates and fibronectin-functionalized nanoplates in a PEG-Np-DMEM 1:1.167 ratio. The experiments with MC3T3-E1 pre-osteoblast cells were performed in a similar manner. Cells were cultured in phenol red-free Alpha-MEM (Minimum Essential Medium) containing 10% FBS, 5% penicillin–streptomycin and, 5% L-glutamine under an atmosphere of 5%  $\text{CO}_2$  at 37  $^\circ\text{C}$ . A density of  $38 \times 10^4$  cells per well was plated in a 24-well plate and incubated until confluent for 24 h. CS-HAP scaffolds were placed in transwell inserts after seeding the cells and placed in the wells for incubation. PEG-Np (1.2 mL) were preincubated with 40  $\mu$ L of fibronectin (1 mg/mL) in its active and denatured forms. Prior to the addition of the nanoplates to the cells, the culture media was changed to fresh media. Cells were incubated with the nanoplates and fibronectin-functionalized nanoplates in a PEG-Np-DMEM 1:1.167 ratio.

### 2.5. Protein Monitoring

Upon incubation of the functionalized nanoplates with the cells, protein monitoring was performed using UV-Vis spectrometry with a Biotek Synergy HT microplate reader. UV measurements were taken at five different time points over 32 h (0 h, 3 h, 8 h, 24 h, 32 h) to observe shifts in the LSPR recordings indicating the Fn extension and fibril formation over time. The microplate reader was set for absorbance measurements from 300 to 900 nm wavelengths in 1 nm steps. CS/HAP scaffolds were removed from the wells before UV measurements.

### 3. Results and Discussion

#### 3.1. Biomimetic Bone Regeneration Scaffold

A CS/HAp scaffold formulation with good biocompatible and osteoconductive properties [20,21] was selected to mimic the ECM. Its high performance in supporting the proliferation and attachment of alveolar bone-derived mesenchymal stem cells (ABMSCs) has been demonstrated. Increased osteogenic activity as indicated by increased alkaline phosphatase assay and osteogenic gene expression for the CS/HAp-treated ABMSCs has been observed compared to CS alone [22,23]. HAp presents as a versatile material for wide applications, including the fabrication of implants in ophthalmology and drug delivery devices as well as in mimicking vascularization [24].

The CS/HAp scaffolds (Figure 2b) were analyzed using FTIR to identify and confirm the incorporation of calcium phosphate materials within the scaffolds. Chitosan was characterized by peaks corresponding to N-H stretching at 1558–1642  $\text{cm}^{-1}$  and asymmetrical C-H stretch of  $-\text{CH}_2$  at 2869–2921  $\text{cm}^{-1}$  (Figure 2a) [21]. The main components of hydroxyapatite include the phosphate group ( $\text{PO}_4^{3-}$ ), hydroxyl group (OH), and carbonate group ( $\text{CO}_3^{2-}$ ). The FTIR spectrum exhibited a phosphate band observed at 1020  $\text{cm}^{-1}$ , which was due to  $\text{PO}_4$  tetrahedra internal vibrations, normally seen at 1200–900  $\text{cm}^{-1}$  [25]. The presence of the bioceramic within the scaffolds was also confirmed by orthophosphate bands visible at 1998  $\text{cm}^{-1}$ , 1030–1033  $\text{cm}^{-1}$  (phosphate bending vibration), 960  $\text{cm}^{-1}$  (phosphate stretching vibration), 620 and 560  $\text{cm}^{-1}$  [26]. In addition,  $\text{CO}_3^{2-}$  groups from the scaffolds were identified at 1411–1657  $\text{cm}^{-1}$ .

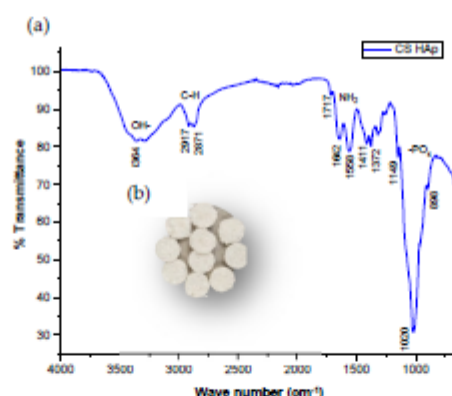


**Figure 2.** (a) FTIR spectrum shows the phosphate and carbonate characteristics of the bioceramics incorporated in the formulations of the scaffolds fabricated (b) CS/HAp scaffolds fabricated from a photocrosslinking reaction in a UV chamber.

#### 3.2. Fn Monitoring in C2C12 Myoblast Cells

The validation of AuTSNP as powerful biosensors for the detection of proteins and other biomolecular components in these high background noise environments is outlined. Fn behavior was monitored in the presence of cells alone, the ECM alone, and cells in the presence of the CS/HAp scaffold.

C2C12 cells were incubated and treated with functionalized AuTSNP, namely Polyethylene glycol (PEG) coated AuTSNP, denoted PEG-Np, active Fn coated PEG-Np, denoted active Fn-PEG-Np, and denatured Fn-PEG-Np as controls. Fn behavior in its active and denatured forms was analyzed over time through LSPR measurements at five different time points. PEG-Np alone was used as a further control for the impact on cellular morphology and non-specific binding [19]. Denatured Fn was used to validate the spectral red shifts recorded over time corresponding to the active Fn unfolding conformation within the ECM.

As shown in Figure 3, between the 0 h and 8 h time points, a shift of  $-40$  nm for the active Fn was observed, while longer shifts were recorded at the 24 h and 32 h time points with shifts up to  $-80$  nm. Although the denatured protein showed a similar profile, shifts as short as 6 nm showed beyond the 24 h time point, which indicates the limited shifting of an inactive protein due to decreased extension activity (Table 1). Long spectral shifts for the active protein can be correlated with the Fn unfolding behavior within the extracellular matrix mediated by cells through integrin binding, which was reported as the indication of matrix aging and maturation [27,28].

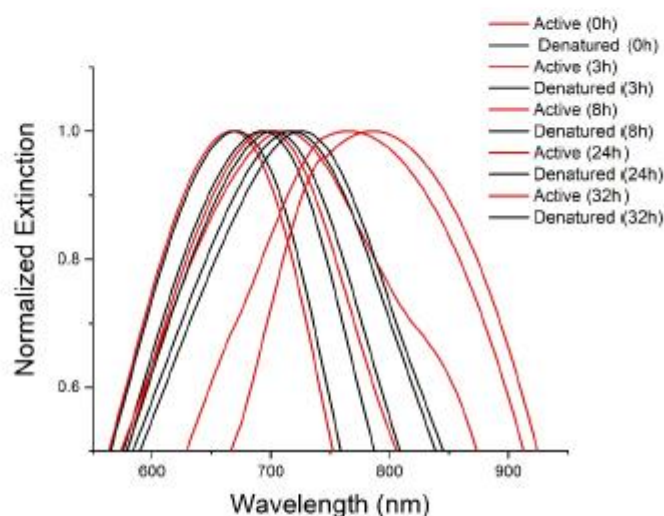


**Figure 3.** LSPR spectra of active (blue) and denatured (black) Fn PEG-NP in C2C12 cell culture from 0 h to 32 h.

**Table 1.** C2C12 cell culture wavelength shift table for active and denatured Fn PEG-NP.

Time	Wavelength	
	Active	Denatured
0 h	667	670
3 h	697	693
8 h	711	702
24 h	766	718
32 h	786	726

When in presence of a CS-HAp scaffold, active Fn showed similar red-shifting performance (Figure 4a) with shifts as long as 80 nm between the 8 h and 32 h time points (Table 2). The morphology of C2C12 cells was observed to be normal with a high percentage of confluence, which indicated that the NPs had no observable negative impact on the cell culture regardless of the treatment up to 32 h (Figure 4b). This result is in keeping with findings in the literature, which reports that C2C12 cells exposed to low concentrations of silver nanoparticles show no negative effect on morphology or cytotoxicity between 0.25 and 2  $\mu\text{g}/\text{mL}$  [29].

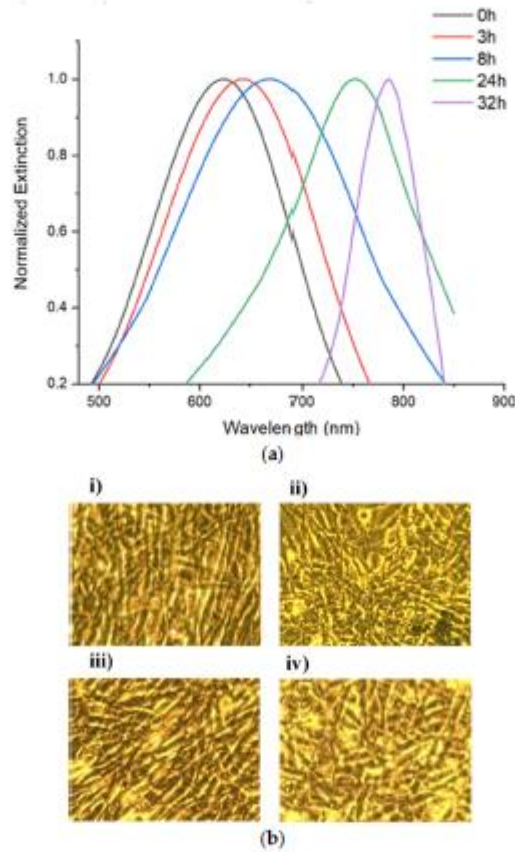


**Figure 4.** (a) UV-vis spectra of Fn-PEG-Np incubated with C2C12 cells (20X magnification) in the presence of CS-HAP tissue regeneration scaffolds. (b) Images of C2C12 myoblast cells taken after 32 h of incubation with (i) PEG-Np, (ii) Denatured Fn-PEG-NP, (iii) Active Fn-PEG-NP, (iv) Fn-PEG-NP and scaffold.

**Table 2.** C2C12 cell culture: wavelength shift table for Fn-PEG-NP in the presence of CS-HAP tissue regeneration scaffolds.

Sample	Peak Wavelength (nm)
0 h	623
3 h	643
8 h	669
24 h	753
32 h	785

### 3.3. Fn Monitoring in MC3T3 Pre-Osteoblast Cells

Fn behavior was then studied in the presence of MC3T3-E1 pre-osteoblasts to observe any contrasting interactions within a different cellular environment. In these experiments, the same controls were used but with the addition of BSA-PEG-Np as a control for nanoparticle degradation due to cellular conditions and non-specific binding interactions [19].

Similar performance of the protein on and off-scaffold was observed over time with longer red shifts for the active protein in comparison to the denatured Fn. Shifts up to 103 nm can be observed by the end of 32 h for the active protein, while the inactive protein shows shorter shifts of 78 nm (Figure 5a).

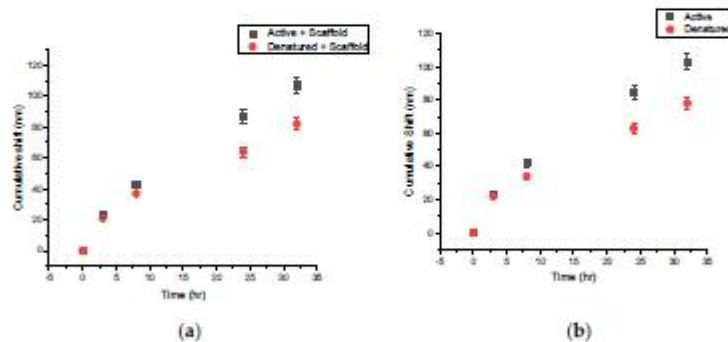


**Figure 5.** Cumulative shifts for active and denatured Fn PEG-NP within MC3T3-E1 cell culture with (a) and without (b) CS-HAp bone regeneration scaffolds.

It was previously reported that the development of the Fn matrix within the ECM develops after 4 h once Fn is added to the cell culture, and the most unfolded matrix is measured at the 24 h time point [27]. This correlates to the longer shifts being recorded after the 3 h time point, with the longest shifts overall occurring at 24 h (Figure 5b).

Similar to previous experiments, Fn monitoring in the presence of chitosan-based scaffolds showed comparable results where longer shifts for the active Fn could be observed in comparison to shorter shifts from the denatured protein (107 nm and 82 nm respectively). Pre-osteoblast morphology and confluence can still be observed after 32 h of culture, demonstrating the cellular compatibility of the scaffold in the presence of MC3T3 cells and no observable negative effect of PEG-NP on the cells (Figure 6), as also demonstrated by Hashimoto, et al. (2013), where water-dispersible silver nanoparticles were co-cultured with the MC3T3 cell line with no cytotoxic effects observed [30].

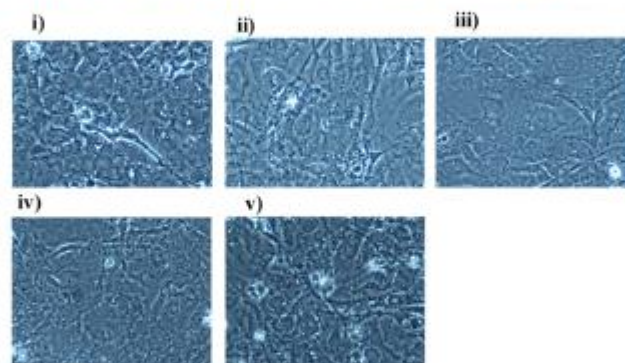


**Figure 6.** Images of MC3T3-E1 cells (20X magnification) taken after 32 h of incubation with (i) Active Fn-PEG-Np, (ii) Denatured Fn-PEG-Np, (iii) Active Fn-PEG-Np and scaffold, (iv) Denatured Fn-PEG-Np and scaffold, (v) BSA-PEG-NP.

Our results showed a similar performance to the work of Y. Zhang, et al. (2014), where TSNP were used for the detection of C-reactive protein (hs-CRP) at different concentrations, with a red-shifting profile observed as a result of the increment in the refractive index surrounding the nanoparticles as the concentration of hs-CRP increases in the samples [9]. In the case of fibronectin, red shifts were observed over time as the protein extended and interacted within the extracellular matrix of the cells, causing an increase in Fn strands that interacted with the nanoparticle surface.

For the past few years, metallic nanoparticles have been used in the biomedical field for a range of applications, such as the detection of specific antibodies and other proteins, among others. Gold nanoparticles have mostly been the gold standard for these applications due to their functional properties and straightforward synthesis; nonetheless, triangular silver nanoparticles have been reported to possess some of the highest sensitivities among noble metals and promising plasmonic properties due to their sharp corners, making them excellent alternatives for accurate biosensing applications [13,31].

#### 4. Conclusions

In this work, we have validated the functionality of AuTSNPs to perform as biosensors in the presence of high-noise cellular environments, with and without the presence of ECM-mimicking bone regeneration scaffolds. The specificity of the Fn monitoring was confirmed through the implemented denatured and active protein approaches, where it was successfully demonstrated that gold edge-coated triangular silver nanoparticles are powerful tools for straightforward, versatile non-labeling measurements for biomolecule dynamics in high background noise environments such as MC3T3 and C2C12 cell lines. Results showed a highly similar shifting profile in all experiments regardless of the cultured cell line and the presence of scaffolds. This remarkable sensitivity in the presence of both cell lines and scaffold demonstrated the clear capability of the functionalized AuTSNPs in interacting and sensing tissue molecular signaling and therefore has the potential to provide extraordinary possibilities for the development and progression of regenerative medicine. Furthermore, it can provide fast and accurate detection of biomolecules of clinical importance within point-of-care clinical settings, which will lead to a better course of treatments for rising-disease challenges.

**Author Contributions:** Conceptualization, L.G.R.B. and M.B.F.; methodology, L.G.R.B. and F.A.A.; formal analysis, L.G.R.B. and F.A.A.; investigation, L.G.R.B. and F.A.A.; resources, D.D.; writing—original draft preparation, L.G.R.B. and F.A.A.; writing—review and editing, L.G.R.B., F.A.A. and R.P.; supervision, M.B.F.; project administration, M.B.F. and D.D.; funding acquisition, M.B.F. and D.D. All authors have read and agreed to the published version of the manuscript.

**Funding:** Funding for this work was provided by the Technological University of The Shannon through the President Seed Fund, the COVID support by the Higher Education Authority (HEA), and Higher Education, Research, Innovation, and Science (D/FHERIS). RP was supported by funding from the Fundação de Amparo à Pesquisa do Distrito Federal (FAP-DF), by the Universidade Católica de Brasília, Brazil, and by the Technological University of the Shannon: Midlands Midwest.

**Institutional Review Board Statement:** Not applicable.

**Informed Consent Statement:** Not applicable.

**Data Availability Statement:** Not applicable.

**Conflicts of Interest:** The authors declare no conflict of interest.

#### References

1. Pollock, V. Proteins. *Xpharm Compr. Pharmacol. Ref.* **2007**, *1–11*. [[CrossRef](#)]
2. Nachimuthu, S.; Ponnusamy, R. Introduction to proteomics. In *Concepts and Techniques in Genomics and Proteomics*; Woodhead Publishing Limited: Sawston, UK, 2007; Volume 367, pp. 147–158.
3. Alberts, B.; Johnson, A.; Lewis, J.; Raff, M.; Roberts, K.; Walter, P. Protein Function. In *Molecular Biology of the Cell*, 4th ed.; Garland Science: New York, NY, USA, 2002; pp. 1–19.

4. Moree, B.; Connell, K.; Mortensen, R.B.; Liu, C.T.; Benkovic, S.J.; Salafsky, J. Protein Conformational Changes Are Detected and Resolved Site Specifically by Second-Harmonic Generation. *Biophys. J.* **2015**, *109*, 806–815. [CrossRef] [PubMed]
5. Charles, D.E.; Aherne, D.; Gara, M.; Ledwith, D.M.; Gun, Y.K.; Kelly, J.M.; Blau, W.J.; Brennan-Fournet, M.E. Silver Nanoplates for Highly Sensitive Plasmon Resonance Sensing. *ACS Nano* **2010**, *4*, 55–64. [CrossRef] [PubMed]
6. Ostrowska, N.; Feig, M.; Trylska, J. Modeling Crowded Environment in Molecular Simulations. *Front. Mol. Biosci.* **2019**, *6*, 86. [CrossRef]
7. Feig, M.; Yu, L.; Wang, P.H.; Nawrocki, G.; Sugita, Y. Crowding in Cellular Environments at an Atomistic Level from Computer Simulations. *J. Phys. Chem. B* **2017**, *121*, 8009–8025. [CrossRef]
8. Long, Y.-T.; Jing, C. *Localized Surface Plasmon Resonance Based Nanobiosensors*; Springer: Berlin/Heidelberg, Germany, 2014; ISBN 978-3-642-54794-2.
9. Zhang, Y.; Charles, D.E.; Ledwith, D.M.; Aherne, D.; Cunningham, S.; Voisin, M.; Blau, W.J.; Gun'Ko, Y.K.; Kelly, J.M.; Brennan-Fournet, M.E. Wash-free highly sensitive detection of C-reactive protein using gold derivatised triangular silver nanoplates. *RSC Adv.* **2014**, *4*, 29022–29031. [CrossRef]
10. Willets, K.A.; Van Duyne, R.P. Localized surface plasmon resonance spectroscopy and sensing. *Annu. Rev. Phys. Chem.* **2007**, *58*, 267–297. [CrossRef]
11. Loiseau, A.; Asila, V.; Boitel-Aulen, G.; Lam, M.; Salmair, M.; Boujday, S. Silver-based plasmonic nanoparticles for and their use in biosensing. *Biosensors* **2019**, *9*, 78. [CrossRef]
12. Mauriz, E.; Dey, P.; Lechuga, L.M. Advances in nanoplasmonic biosensors for clinical applications. *Analyst* **2019**, *144*, 7105–7129. [CrossRef]
13. Petryayeva, E.; Krull, U.J. Localized surface plasmon resonance: Nanostructures, bioassays and biosensing—A review. *Anal. Chim. Acta* **2011**, *706*, 8–24. [CrossRef]
14. Svystonyuk, D.A.; Mewhort, H.E.M.; Fedak, P.W.M. Using Acellular Bioactive Extracellular Matrix Scaffolds to Enhance Endogenous Cardiac Repair. *Front. Cardiovasc. Med.* **2018**, *5*, 35. [CrossRef]
15. Kim, Y.G.; Shin, H.; Lim, D.W. Biomimetic scaffolds for tissue engineering. *Adv. Funct. Mater.* **2012**, *22*, 2446–2468. [CrossRef]
16. Dorati, R.; De Trizio, A.; Modena, Y.; Conti, B.; Benazzo, F.; Gastaldi, G.; Genta, I. Biodegradable scaffolds for bone regeneration combined with drug-delivery systems in osteomyelitis therapy. *Pharmaceuticals* **2017**, *10*, 96. [CrossRef]
17. Amariei, G.; Kokol, V.; Boltes, K.; Letón, P.; Rosal, R. Incorporation of antimicrobial peptides on electrospun nanofibres for biomedical applications. *RSC Adv.* **2018**, *8*, 28013–28023. [CrossRef]
18. Zhang, F.; King, M.W. Biodegradable Polymers as the Pivotal Player in the Design of Tissue Engineering Scaffolds. *Adv. Healthc. Mater.* **2020**, *9*, 1901358. [CrossRef]
19. Brennan-Fournet, M.E.; Huerta, M.; Zhang, Y.; Malliaras, G.; Owens, R.M. Detection of fibronectin conformational changes in the extracellular matrix of live cells using plasmonic nanoplates. *J. Mater. Chem. B* **2015**, *3*, 9140–9147. [CrossRef]
20. Devine, D.M.; Hoctor, E.; Hayes, J.S.; Sheehan, E.; Christopher, H. Extended release of proteins following encapsulation in hydroxyapatite/chitosan composite scaffolds for bone tissue engineering applications. *Mater. Sci. Engineering: C Mater. Biol. Appl.* **2019**, *84*, 1–24. [CrossRef]
21. Azaman, F.A.; Zhou, K.; Blanes-Martinez, M.D.M.; Brennan Fournet, M.; Devine, D.M. Bioresorbable Chitosan-Based Bone Regeneration Scaffold Using Various Bioceramics and the Alteration of Photoinitiator Concentration in an Extended UV Photocrosslinking Reaction. *Gels* **2022**, *8*, 696. [CrossRef]
22. Kim, B.S.; Kim, J.S.; Chung, Y.S.; Sin, Y.W.; Ryu, K.H.; Lee, J.; You, H.K. Growth and osteogenic differentiation of alveolar human bone marrow-derived mesenchymal stem cells on chitosan/hydroxyapatite composite fabric. *J. Biomed. Mater. Res. Part A* **2013**, *101 A*, 1550–1558. [CrossRef]
23. Kargozar, S.; Mozafari, M.; Hamzehlou, S.; Milan, P.B. Bone Tissue Engineering Using Human Cells: A Comprehensive Review on Recent Trends, Current Prospects, and Recommendations. *Appl. Sci.* **2019**, *9*, 174. [CrossRef]
24. Costa-Pinto, A.R.; Lemos, A.L.; Tavará, F.K.; Pintado, M. Chitosan and hydroxyapatite based biomaterials to circumvent periprosthetic joint infections. *Materials* **2021**, *14*, 804. [CrossRef] [PubMed]
25. Fern, H.W.; Salimi, M.N. Hydroxyapatite nanoparticles produced by direct precipitation method: Optimization and characterization studies. *AIP Conf. Proc.* **2021**, *2339*, 020215. [CrossRef]
26. Maachou, H.; Bal, K.E.; Bal, Y.; Chagnes, A.; Cote, G.; Alliouche, D. Characterization and in vitro bioactivity of chitosan/hydroxyapatite composite membrane prepared by freeze-gelation method. *Trends Biomater. Artif. Organs* **2008**, *22*, 15–24. [CrossRef]
27. Antia, M.; Baneyx, G.; Kubow, K.E.; Abstract, V.V. Fibronectin in aging extracellular matrix fibrils is progressively unfolded by cells and elicits an enhanced rigidity response. *NIH Public Access* **2008**, *139*, 229–420. [CrossRef]
28. Singh, P.; Carraher, C.; Schwarzbauer, J.E. Assembly of fibronectin extracellular matrix. *Annu. Rev. Cell Dev. Biol.* **2010**, *26*, 397–419. [CrossRef]
29. Bhatia, D.; Mittal, A.; Malik, D.K. Antimicrobial potential and in vitro cytotoxicity study of polyvinyl pyrrolidone-stabilised silver nanoparticles synthesised from *Lysinibacillus boronitolerans*. *IET Nanobiotechnol.* **2021**, *15*, 427–440. [CrossRef]







30. Hashimoto, M.; Yoshima, H.; Yonezawa, T.; Kawai, K.; Narushima, T.; Kaga, M.; Endo, K. Micromorphological cellular responses of MC3T3-E1 and RAW 264.7 after exposure to water-dispersible silver nanoparticles stabilized by metal-carbon  $\sigma$ -bonds. *Dent. Mater. J.* **2013**, *32*, 725–733. [[CrossRef](#)]
31. Hu, X.; Zhang, Y.; Ding, T.; Liu, J.; Zhao, H. Multifunctional Gold Nanoparticles: A Novel Nanomaterial for Various Medical Applications and Biological Activities. *Front. Biog. Biotechnol.* **2020**, *8*, 990. [[CrossRef](#)]

**Disclaimer/Publisher's Note:** The statements, opinions and data contained in all publications are solely those of the individual author(s) and contributor(s) and not of MDPI and/or the editor(s). MDPI and/or the editor(s) disclaim responsibility for any injury to people or property resulting from any ideas, methods, instructions or products referred to in the content.

Article

# Triangular Silver Nanoparticles Synthesis: Investigating Potential Application in Materials and Biosensing

Laura G. Rodriguez Barroso<sup>1</sup>, Eduardo Lanzagorta Garcia<sup>1</sup> , Marija Mojicevic<sup>1,\*</sup> , Miriam Huerta<sup>2</sup> , Robert Pogue<sup>3</sup>, Declan M. Devine<sup>1</sup>  and Margaret Brennan-Fournet<sup>1</sup>

<sup>1</sup> PRISM Research Institute, Technological University of the Shannon: Midlands Midwest, Dublin Rd., N37 HD68 Athlone, Ireland; laura.rodriguez@tus.ie (L.G.R.B.); e.lgarcia@research.tus.ie (E.L.G.); declan.devine@tus.ie (D.M.D.); margaret.brennanfournet@tus.ie (M.B.-F.)

<sup>2</sup> Physics Institute, Universidad Autónoma de San Luis Potosí, Av. Parque Chapultepec 1570, San Luis Potosí 78295, Mexico; miriam.huerta@f.uaslp.mx

<sup>3</sup> Campus Asa Norte, Universidade Católica de Brasília, SGAN Módulo B 916 Avenida W5—Asa Norte, Brasília 70790-160, Brazil; redward@p.ucb.br

\* Correspondence: marija.mojicevic@tus.ie

**Abstract:** Triangular silver nanoplates (TSNPs) exhibit unique optical and antimicrobial properties due to their shape, sharp edges, and vertices. In this study, TSNPs were incorporated into biopolymer blends (bacterial cellulose (BC) with polylactic acid (PLA), polycaprolactone (PCL), and polyhydroxybutyrate (PHB)). Antimicrobial activity of materials was tested against *Escherichia coli* ATCC 95922 and *Staphylococcus aureus* ATCC 25923 ( $10^6$  CFU/mL). After incubation (24 h at 37 °C, 100 rpm), optical density was measured at 630 nm. In order to assess biosensing applications, specifically fibronectin (Fn) behavior, TSNPs were protected with gold (AuTSNP) and analyzed via sucrose sensitivity test and monitored by localized surface plasmon resonance (LSPR). Additionally, AuTSNPs were coated with polyethylene glycol (PEGAuTSNP). Fibronectin functionalization of PEGAuTSNPs and pH-conformation was monitored (FnPEGAuTSNP). Eventually, adequate Fn and anti-Fn antibody concentrations were determined. BC/PHB/TSNPs showed antimicrobial activity against *E. coli* and *S. aureus* with 80 and 95% of growth inhibition, respectively. The sucrose sensitivity test indicated that the LSPR<sub>λmax</sub> of the spectra is directly proportional to the sucrose concentration. LSPR<sub>λmax</sub> of Fn-PEGAuTSNPs at pH 7 and pH 4 were measured at 633 and 643 nm, respectively. A total of 5 μg of Fn was determined to be adequate concentration, while 0.212 mg/mL of anti-Fn antibody indicated system saturation.

**Keywords:** nanoparticles; silver; triangular silver nanoplates; biosensing; antimicrobial; biopolymers; fibronectin



Citation: Rodriguez Barroso, L.G.; Lanzagorta Garcia, E.; Mojicevic, M.; Huerta, M.; Pogue, R.; Devine, D.M.; Brennan-Fournet, M. Triangular Silver Nanoparticles Synthesis: Investigating Potential Application in Materials and Biosensing. *Appl. Sci.* 2023, 13, 8100. <https://doi.org/10.3390/app13148100>

Academic Editor: Alexander V. Syuy and Gleb I. Yselikov

Received: 13 June 2023

Revised: 5 July 2023

Accepted: 10 July 2023

Published: 11 July 2023



Copyright © 2023 by the authors. Licensee MDPI, Basel, Switzerland. This article is an open access article distributed under the terms and conditions of the Creative Commons Attribution (CC BY) license (<https://creativecommons.org/licenses/by/4.0/>).

## 1. Introduction

The potential applications and synthesis procedures of nanoscale materials were extensively investigated [1–3]. Humans began using metallic nanoparticles (NPs) in ancient times, though were not fully aware of their nature. The earliest examples of NPs in a practical application date back to Mesopotamian and Egyptian cultures when they used metals in the fabrication of glass. Through history, this technique was used and improved, mainly for decorative purposes, allowing glass staining in a variety of colors due to the plasmonic properties of the NPs [4]. While gold nanoparticles were extensively utilized for several decades, the application of silver nanomaterials with similar potential is considerably restricted due to certain seemingly unfavorable characteristics, such as their susceptibility to be quickly oxidized in the presence of halide ions [5].

Silver (Ag) is one of the most attractive metals for the synthesis of nanoparticles because of the wide range of applications derived from its properties. Attributes such as its malleability, conductivity, ductility, resilience, rareness, and antimicrobial properties

made it valuable and convenient for several everyday life purposes through ancient and modern times. The most common applications of Ag include optoelectronics [6], water disinfection [7], diagnostics [8], anti-cancer therapeutics [9], biomedical technologies [10], drug-gene delivery [11], energy science [12], and clinical anti-bacterial purposes, etc. [13,14]. The increasing list of practical uses found for Ag and its NPs present it as highly valuable for current and future technologies and applications. In recent years, there was significant attention focused on enhancing the controlled synthesis methods for triangular silver nanoplates (TSNPs), primarily due to the widespread utilization of these nanoplates in diverse fields, such as surface-enhanced Raman scattering (SERS) detection and the production of antifungal nanocomposites [15]. Due to their shape, sharp edges, and vertices, TSNPs are proven to exhibit distinctive optical and antibacterial properties [16,17]. In comparison to other nanoparticles, TSNPs garnered significant interest due to their ability to tune SPR bands over a wide range by controlling the aspect ratio of the particles [18]. Moreover, the enhanced antimicrobial activity of TSNPs in comparison to spherical nanoparticles is proven to be a consequence of their unique morphology, allowing easier attachment and penetration into the cell membrane and provoking bacterial death [19]. After bacterial membrane damage, the mechanism proposed for antimicrobial action is connected to the formation of reactive oxygen (ROS) and free radical species in high levels inside of the bacteria, inducing their death [20]. Additionally, colloidal stability of NP was proven to play a significant role in antimicrobial action. Controlled growth and ambient media used are critical points for TSNP antimicrobial activity [21].

Silver nanoparticles (AgNP) amalgamated materials are currently used in a range of different applications, including improving electrical and thermal conductivity, water treatment, antimicrobial medical materials, and sensing materials for diagnosis, among others [22]. In the specific case of TSNPs, there are only a limited number of reports of their incorporation into other materials for different applications, and the exploration of the antimicrobial activity of said materials is even more limited. Dispersion of triangular silver nanoprisms in an aqueous acrylamide matrix was reported. The dispersion showed highly tuneable optical properties, and was used as a carrier liquid for a fluorescent dye in the fabrication process of poly(acrylamide) microparticles [23]. Additionally, dispersion of triangular silver nanoplates in a polyvinylidene fluoride matrix for the improvement of electrical conductivity was reported by [24]. Zhang et al. (2013) fabricated a composite of a TSNPs and chitosan, which significantly enhanced the sensitivity as a surface plasmon resonance (SPR) biosensor [25]. Dithiocarbamate-stabilized TSNP were used to obtain nanocomposites with polythiophene-derived nanoparticles, in order to obtain a stable system that could be used for applications in catalysis, biosensing, electronics, and optics [26]. The synthesis of solid silver/polyvinylpyrrolidone/polyacrylonitrile nanocomposite films with triangular silver nanoprisms was also reported, taking advantage of their optical absorption spectra to increase the efficiency of photothermal conversion in the polymer matrix, expecting this material to be used in applications such as absorbing materials for solar collectors [27]. Djafari et al. (2019) compared the antimicrobial activity of TSNPs with different polymeric coatings (such as silica, PVP, or mercaptohexadecanoic acid), and found that the surface charge of the selected polymeric coating has an effect on the antimicrobial efficacy of TSNPs towards Gram-positive or Gram-negative strains [28]. Similarly, Vo et al. (2019) studied the feasibility of a gelatin-chitosan coating on the synthesis of TSNPs and evaluated their antimicrobial activity, which was higher than other AgNP morphologies [29]. A chemical method for synthesis of TSNPs and posterior ex situ incorporation into polyvinyl alcohol (PVA) was also reported. Potential applications of this method include dichroic materials and antimicrobial materials, but the antibacterial effects were not evaluated during this study [30]. As the applications for TSNPs can be diverse, their incorporation into polymers for purposes such as improvement of electrical conductivity, thermal conductivity, and biosensing were explored, but there is still a lack of research about their integration into plastics for antimicrobial purposes.

With regard to application in diagnostics, noble metal nanoparticles such as Ag and Au particles exhibit localized surface plasmon resonance (LSPR) in the visible region of the electromagnetic spectrum, making them attractive for sensing applications, as changes can even be detected with the naked eye in some cases, making detection faster, easier, and inexpensive [31]. LSPR is an optical phenomenon that uses the sensitivity of these plasmons' frequency to change the local refractive index at the nanoparticle surface, emerging as a highly sensitive label-free biosensing technique [31]. This presents the LSPR technique as a powerful tool for optical biosensing applications in a range of areas, including biology, biochemistry, and medical sciences, with the potential to be used as portable devices for diagnosis and easy-to-use point-of-care (POC) device platforms [32,33]. In biosensing applications, the nanoparticles' LSPR is used to detect changes in the position of the LSPR bands where the position depends on the nanoparticles' shape, size, uniformity, composition, dielectric environment, local refractive index, and separation distance of NPs [34–37]. To date, several silver nanostructures with high refractive index sensitivities were reported, such as nanorice, nanobipyramids, nanorings, triangular silver nanoplates (TSNPs), and edge gold-coated silver nanoprisms [38]. Among these diverse nanostructures, TSNPs exhibit attractive tunable plasmonic properties due to their sharp corners, and their optical profile displays the strongest and sharpest peaks among all metals [36]. AgNPs are particularly attractive because among all metals, silver possesses the greater scattering cross-section, which means a higher probability of interaction between radiation and the target [39]. Consequently, AgNPs show the most intense plasmonic interaction with incident light, compared to other metallic NPs [40]. Due to their properties, AgNPs are recognized as efficient optical sensors for pesticide residues detection [41]. Moreover, the nanostructure of silver nanoparticles decorated on gold nanoparticles was reported as a sensitive medium for localized surface LSPR biosensing applications [42].

TSNPs are already being used as biosensors in research. For instance, Zhang et al. (2014) used a cytidine 5'-diphosphocholine-coated TSNP and AuTSNP (gold-coated TSNP) for detection of C-reactive protein, an inflammatory marker [38]. Brennan-Fournet et al. (2015) successfully detected conformational changes in fibronectin, a protein related to tumor growth and cell survival, using AuTSNPs [43]. Rodriguez Barroso et al. (2023) monitored fibronectin behavior overtime within different complex cellular environments [44]. Vinayagam et al. (2018) built a nanoprobe by conjugating single-strand DNA to the TSNP surface, for specific detection of dengue virus [45]. Cai et al. (2017) proposed a TSNP-AuNP nanoconjugate that allows detection of glucose due to LSPR changes caused by TSNP etching [46]. Fang et al. (2017) also applied TSNP etching color changes in the design of a colorimetric method for the detection of dopamine, which possesses a high affinity to Ag and formed a protective coating against chlorine [47]. A similar approach for the detection of mercury (Hg(II)) was reported, taking advantage of Ag/Hg amalgam formation to protect the TSNP from the effects of chlorine [48]. A slightly contrasting method reported by Furlatov et al. (2017), measured the reduction in TSNP color intensity after the addition of Hg(II) alone, attributing such changes to both oxidation by  $Hg^{+2}$  ions and amalgam formation [49].

The inconsistent findings regarding the antibacterial and biosensing applications of TSNPs can be attributed to the absence of convenient fabrication methods for producing well-defined anisotropic particles with distinct morphologies, as well as the variations in fabrication approaches employed across different studies. In this study, following up on our previous work, we aimed to prove that our TSNP preparation method can be used for successful incorporation into biopolymer blends (bacterial cellulose (BC) with polylactic acid (PLA), polycaprolactone (PCL), and polyhydroxybutyrate (PHB)), showing high potential for a broad spectrum of applications. Additionally, we investigated potential applications of these nanoplates in biosensing, specifically fibronectin (Fn) conformational behavior within dynamic environments and the detection of this protein with its antibody conjugate, Anti-Fn.

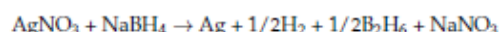
## 2. Materials and Methods

### 2.1. Materials

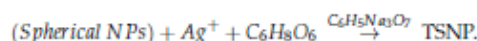
HPLC-grade ultrapure water (34877-2.5L), sodium citrate tribasic (C8532-100G) [TSC], poly(sodium 4-styrenesulfate) (434574-5G) [PSSS], sodium borohydride (213462-25G) [NaBH<sub>4</sub>], silver nitrate (204390-10G) [AgNO<sub>3</sub>], L-ascorbic acid (A92902-25G) [AA] and O-[2-(3-mercaptopropionylamino)ethyl]-O'-methylpolyethylene glycol (11124-1G-F) [SH-PEG], gold (III) chloride trihydrate (520918-1G) [HAuCl<sub>4</sub>], disodium phosphate buffer (30414-500G) ≥99.9–101%, sodium phosphate monobasic monohydrate (71507-1KG), fibronectin bovine plasma [1 mg/mL] (F4759-1G), polyethylene glycol 20000 (8.17018), sucrose (84097-1KG), and anti-Fn antibody (AV41490-100UL) were obtained from Sigma-Aldrich. The FRX pump from Syrris was used for the addition of AgNO<sub>3</sub> in the original method and LP-BT100-1F Peristaltic Dispensing Pump with YZII15 pump head and Tygon LMT-55 Tubing (SC0375T) from Drifton (Hvidovre, Denmark) was used for the scaled-up method. Polycaprolactone (PCL) CAPA 6250 was obtained from Perstorp. Ingeo™ polylactic acid biopolymer PLA 4044D was obtained from NatureWorks LLC. PHB (P226) was obtained from Biomer.

### 2.2. Synthesis of TSNP

The TSNP solution method was adapted from a previously reported seed-mediated approach [50], consisting of a step for seed production and a subsequent step for TSNP growth. Briefly, 5 mL of TSC (2.5 mM), 0.25 mL of PSSS (500 mg/L), and 0.3 mL of NaBH<sub>4</sub> (10 mM) were mixed, followed by the addition of 5 mL of AgNO<sub>3</sub> (0.5 mM) at a rate of 2 mL/min on constant stirring for the formation of the seed solution. For the TSNP growth, 4 mL of distilled water, 0.075 mL of AA (10 mM), and 0.35 mL of seed solution were mixed, followed by the addition of 3 mL of AgNO<sub>3</sub> (0.5 mM) at a rate of 1 mL/min with constant stirring. Finally, 0.5 mL of TSC (25 mM) was added, for a TSNP solution with a final Ag concentration of 21.34 ppm. The chemical reaction occurs as follows [51]:



Afterwards, in the growth step, the spherical Ag seeds can react with new Ag<sup>+</sup> ions in the presence of ascorbic acid and citrate ions, forming the TSNP. The chemical reaction can be explained as follows [52]:



TSC was added at the end of the synthesis to stabilize the nanoplates.

Increased concentration of NPs is desired to aid treatment for the intended TSNP-polymer processing. A reduction of 20% of water for the synthesis was successfully achieved without negatively affecting the results. Different volumes ranging between 0.2 and 0.7 mL were used until 0.35 mL eventually became the standard. Consequently, the adapted method consists of mixing 4 mL of water, 0.075 mL of AA (10 mM), and 0.35 mL of seed solution (25.56 ppm of Ag), followed by the addition of 3 mL of AgNO<sub>3</sub> (0.5 mM) at a rate of 1 mL/min. Finally, 0.5 mL of TSC (25 mM) are added when the reaction is finished, resulting in a final Ag concentration of 21.34 ppm and a volume of 8 mL. Noticeably, upon adding AgNO<sub>3</sub>, the color starts changing from yellow to shades of orange, then shades of red, then purple, and finally takes on a dark blue color, as demonstrated in Figure 1.

### Scale-Up of TSNP Production

Unlike the original method where a smaller pump was used, the LP-BT100-1F Peristaltic Dispensing Pump with a YZII15 pump head and Tygon LMT-55 Tubing (SC0375T), provided by Drifton, were used for the addition of AgNO<sub>3</sub>. The production of TSNP solution was scaled up to a final volume of 300 mL. To achieve this without affecting the synthesis reaction and the final properties of the TSNP, all the volumes and the rate

for addition of  $\text{AgNO}_3$  were increased proportionally for both the seed solution and the TSNP growth reaction. Thus, to prepare 20 mL of seeds: 8.53 mL of water, 0.95 mL of TSC (25 mM), 0.47 mL of PSSS (500 mg/mL), and 0.57 mL of  $\text{NaHB}_4$  (10 mM) are mixed, followed by the addition of 9.48 mL of  $\text{AgNO}_3$  (0.5 mM) at a rate of 3.79 mL/min. After 4 h, the seeds can be used in the second step of the reaction, mixing 150 mL of water, 2.81 mL of AA (10 mM), and 13.12 mL of seed solution (25.56 ppm), followed by the addition of 112.5 mL of  $\text{AgNO}_3$  (0.5 mM) at the rate of 37.5 mL/min, then 18.75 mL of TSC (25 mM) was added after reaction was finished.



**Figure 1.** Seed solution (left) and TSNP solution (right).

A method of water evaporation was used to further increase the concentration of TSNP in the produced solution. A total of 300 mL of the TSNP solution were kept inside the oven at 40 °C for 8 days, until approximately 50% of the water volume was evaporated. UV-Vis spectrum of the solution was recorded before and after heat treatment to monitor the stability of the geometry and optical properties of the TSNP through LSPR. Estimated concentration of the solution after evaporation was 42.64 ppm of atomic silver.

### 2.3. BC/PHB Blends Preparation

PHB powder, PCL pellets, and PLA pellets were, respectively, dissolved in chloroform to make solutions containing 40 g/L of each polymer. BC production was achieved using *Komagataibacter medelinensis* ID13488 as described in Garcia et al. (2022) [53].

Stripes of 1 × 10 cm of BC were cut and each sample was immersed in 30 mL of polymer solution inside 50 mL Falcon tubes. Tubes containing the samples were incubated overnight at 30 °C and 120 rpm in a horizontal position. After incubation, the films were removed from the solution and left inside the waste fume hood for at least 4 h to allow complete evaporation of the chloroform. The films were immersed in 20 mL of distilled water and autoclaved (121 °C, 15 min) prior to the test of antimicrobial activity.

The obtained BC blends were cut in 1 × 2 cm pieces and each piece was fully immersed into 5 mL of TSNP solution with the highest concentration obtained after the water evaporation method (42.64 µL/mL) and incubated overnight at 30 °C with agitation on a horizontal platform (100 rpm). Afterwards, films were removed from the solution and dried overnight at 60 °C. To estimate the amount of TSNP absorbed from the solution into the BC materials, the UV-VIS spectrum reading of the solution was measured before and after the immersion and incubation, and the difference in the absorbance at the peak of the spectrum, between the initial and final solution, was observed. A calibration curve with dilutions of the TSNP solution was used to obtain an estimation of the resulting concentration based on absorbance.

Scanning electron microscopy (SEM) images were obtained using Mira XMU SEM (Tescan™, Brno, Czech Republic) in back scattered electron mode for surface analysis. The accelerating voltage used was 9 kV. Prior to analysis, tested samples were placed on an aluminum stub and sputtered with a thin layer of gold using the Baltec SCD 005 for 110 at 0.1 mbar vacuum.

#### Evaluation of Antimicrobial Activity

The antimicrobial activity of all derived materials was evaluated against *E. coli* ATCC 95922 and *S. aureus* ATCC 25923 in Luria-Bertani (LB) broth (10 g/L tryptone, 10 g/L NaCl, and 5 g/L yeast extract, pH 7.2). Overnight cultures of the bacteria were diluted to a concentration of  $10^8$  CFU/mL to be used as pre-culture. Dried BC films (10 mg of each specimen) were immersed in fresh LB broth and inoculated with 1% (*v/v*) from pre-culture, for a final concentration of  $10^6$  CFU/mL of bacteria. Untreated materials were used as negative control. After incubation for 24 h at 37 °C and 100 rpm, BC films were removed from the cultures and optical density (OD) of the cultivated broth was measured at 630 nm using a Biotek Synergy HT microplate reader (Biotek Instruments GmbH, Bad Friedrichshall, Germany). Growth percentage was calculated using the following equation (Equation (1)).

$$\text{Growth Percentage} = \left( \frac{\text{Absorbance of tested sample}}{\text{Absorbance of positive control}} \right) \times 100 \quad (1)$$

### 2.4. Evaluation of TSNP Application in Biosensing and Diagnostics

#### 2.4.1. TSNP Gold Coating

Nanoplate protection against etching by chloride ions present in physiological environments was achieved by covering the edges of the nanoplates with gold to keep their plasmonic resonance properties. Gold edge coating of the TSNP was carried out following the method reported by [44], consisting of the use of 20  $\mu$ L of 0.5 mM HAuCl<sub>4</sub> salt and 18.9  $\mu$ L of 10 mM ascorbic acid per 1 mL of TSNP solution. In this method, there is a reduction in AuCl<sub>4</sub> and inhibition of Ag oxidation at the surface of the TSNP, resulting in the deposition of a thin layer of gold in the edges of the TSNP due to galvanic replacement.

#### 2.4.2. AuTSNP Sucrose Sensitivity Test

Assessment of the AuTSNPs performance as nanobiosensors was analyzed through a sensitivity test (sucrose test) adapted from [54] by changing the refractive index of the nanoplates' local environment. A range of AuTSNP volumes were suspended in a 1:1 ratio to different concentrations of sucrose solutions (10%, 20%, 30%, 40%, and 50% (*w/v*) in ultrapure water), increasing the refractive index as the sucrose concentration rises. UV-Vis spectrum measurements of each sample were recorded to observe changes in the LSPR spectra.

#### 2.4.3. Polyethylene Glycol Coating of AuTSNP

To secure nanoplate extra protection against the physiological environment for biosensing assays, AuTSNPs were coated with polyethylene glycol (PEG). One of the most researched polymers for coating or stabilizing nanoparticles is polyethylene glycol. Public health agencies granted approval for the use of this biocompatible, neutral, and hydrophilic polymer in biomedical and pharmaceutical applications [37]. The AuTSNP solution was centrifuged at 16,000 rpm at 4 °C for 40 min and the clear supernatant was discarded. The blue pellet of the nanoplates was resuspended with a 0.01% solution of PEG 20,000 at a 1:1 AuTSNP-PEG ratio.

#### 2.4.4. Fibronectin Functionalization of PEGAuTSNP and pH-Conformation Monitoring

AuTSNPs were used to monitor fibronectin (Fn) conformational changes induced under different pH conditions. As described by [43], Fn has a compact, folded conformation under physiological buffer conditions (pH 7.4), but is extended at a more acidic pH. Disodium phosphate buffer (pH 4) and phosphate buffer (pH 7) were prepared to induce Fn conformational transitions. Phosphate buffer NaH<sub>2</sub>PO<sub>4</sub>, 0.2 M at pH 4.16 was prepared by dissolving 3.12 g of NaH<sub>2</sub>PO<sub>4</sub> in 100 mL of NaCl 0.2 M. To prepare the buffer at pH 7.23, 40.5 mL Na<sub>2</sub>HPO<sub>4</sub> 0.2 M, 9.5 mL NaH<sub>2</sub>PO<sub>4</sub> 0.2 M, and 50 mL of ultrapure water were mixed. Both buffers were diluted to 0.01 M before use.

PEG-coated AuTSNPs were functionalized with Fn by incubating 25  $\mu\text{g}$  of Fn (1 mg/mL) with 50  $\mu\text{L}$  of PEGAuTSNPs. Upon functionalization, 37.5  $\mu\text{L}$  of Fn-PEGAuTSNPs were incubated with 200  $\mu\text{L}$  of phosphate buffer pH 7.2 and pH 4.1, respectively. UV-Vis measurements were performed to record the protein structural changes.

#### 2.4.5. Determination of Adequate Fn Concentration

To ensure successful coating of the nanoplates: 1  $\mu\text{g}$ , 5  $\mu\text{g}$ , 8  $\mu\text{g}$ , 10  $\mu\text{g}$ , and 15  $\mu\text{g}$  of Fn (antigen Ag) were added to different 1 mL aliquots of PEGAuTSNPs and analyzed in a 96-well plate to observe the minimum volume required to observe a difference in the LSPR spectrum, and 1  $\mu\text{g}$  of anti-Fn antibody (Ab) was added to each of the scanned samples after the first reading and analyzed again to observe shift differences upon antibody-antigen binding.

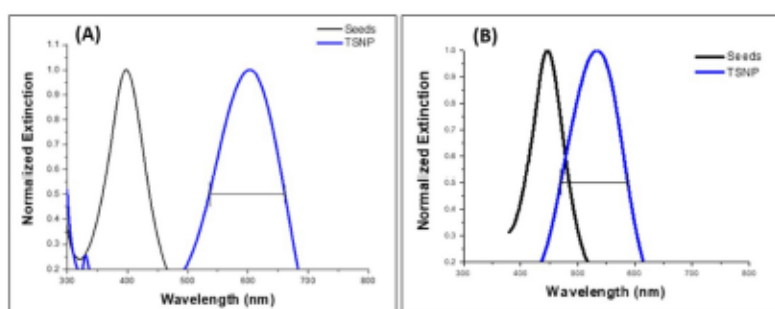
#### 2.4.6. Determination of Adequate Anti-Fn Antibody Concentration

Varied concentrations of antibody were added to a sample of Fn-PEGAuTSNPs to determine the limit of detection (LOD) of the Ag-Ab system. A total of 5  $\mu\text{g}$  of Fn was incubated with 1 mL of PEGAuTSNP. A sample of 99  $\mu\text{L}$  of Fn-PEGAuTSNPs was placed in a well of a 96-well plate and 1  $\mu\text{g}$  of anti-Fn antibody was added and analyzed in the microplate reader. Subsequently, 2  $\mu\text{g}$ , 4  $\mu\text{g}$ , 6  $\mu\text{g}$ , 8  $\mu\text{g}$ , 10  $\mu\text{g}$ , 12  $\mu\text{g}$ , and 14  $\mu\text{g}$  of anti-Fn antibody were added to the well and readings were performed between each concentration. The experiment was performed in the same well to avoid variations and preserve uniformity.

### 3. Results

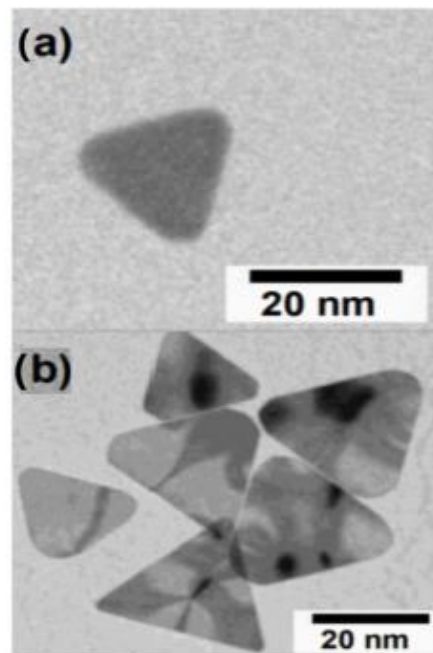
#### 3.1. Synthesis of TSNP

Figure 2 shows the normalized UV-Vis spectrum of the seeds and the TSNP prepared using 200  $\mu\text{L}$  of seeds, and afterwards with the modified method (with 350  $\mu\text{L}$  seeds) for increased concentration. TSC and PSSS were used as stabilizers for the seed production, and both were reported to aid the formation of the nanoplates. It is postulated that citrate ions and PSSS (being a charged polymer), bind to the surface of the face of the particles, promoting growth of the NPs in a triangular plate shape [5,50]. When the TSNP synthesis procedure was modified, the amount of silver in the nanoplate solution increased to 21.962 ppm, which led to a narrower LSPR spectrum of  $\sim 115$  FWHM showing homogeneity of the TSNP with edge lengths around 20–25 nm [38,50] (Figure 2). The triangular morphology of the TSNP prepared through this method was evaluated using TEM on a previous study performed by our team (Figure 3), where the same synthesis method for the TSNP was used [55].



**Figure 2.** (A): UV-Vis spectrum of Ag seeds and TSNPs (200  $\mu\text{L}$  seeds), (B): UV-Vis spectrum of Ag seeds and TSNPs prepared with the optimized method (350  $\mu\text{L}$  seeds).





**Figure 3.** Transmission electron microscopy (TEM) images of (a) single TSNP and (b) multiple TSNP. Adapted from a previous study [55].

### 3.2. Scale-Up TSNP Production and Increase in Concentration via Thermal Evaporation

Figure 4 shows the normalized UV-Vis spectrum for the scaled-up TSNP solution. LSPR peak wavelength is 584 and FWHM of 112 nm (635–523 nm). Although there is a small blue shift in the peak and a small reduction in FWHM compared to the results obtained from smaller volumes, these differences are not expected to represent a reduction in antimicrobial activity or in the stability of the nanoparticles, hence, the scale up method is considered functional. Figure 5 shows the resulting UV-Vis spectrum of TSNPs (21.34 ppm) before evaporation, with an LSPR peak wavelength of 621 nm. After incubation, peak wavelength presented a small blue shift to 617 nm and the concentration was estimated to be approximately 43 ppm. FWHM also exhibited a change from 153 nm (707–554 nm) of the original solution to 178 nm (722–544 nm). Considering the prolonged time inside the oven, differences between both spectra were not significant and were not considered an issue, as increasing the concentration is the principal objective of this method.

### 3.3. Integration of TSNP in Biopolymers for Enhanced Antimicrobial Activity

#### 3.3.1. Preparation of BC Blends with the Addition of TSNP

Following previous examples of integrating TSNPs into polymeric matrices for antimicrobial purposes [53,55], blends of BC with PHB, PLA, and PCL were prepared. After drying the BC/PHB blends, the amount of polymer incorporated into the BC was determined by weighing the dry BC and the films after immersion in the polymer solution. For PHB, approximately 15% of the final weight was accounted for by the incorporated polymer. In the case of PCL, this value was approximately 45%, while for PLA, it was approximately 50%. The BC blends initially showed a milky and white color, but they turned dark blue after immersion in the TSNP solution, corroborating the incorporation of TSNPs into the materials. The amount of TSNPs absorbed by each film was calculated by

measuring the maximum absorbance point on the spectrum of the TSNP solution before and after the immersion and incubation of the BC materials. After contrasting the obtained absorbance values with a calibration curve for the concentration of TSNPs, the amounts absorbed by the materials were estimated as the difference between the initial amount in the solution vs. the final amount after incubation. The average weight of incorporated TSNPs was estimated to be approximately 200  $\mu\text{g}$  for BC/PHB, 153  $\mu\text{g}$  for BC/PCL, and 116  $\mu\text{g}$  for BC/PLA, on each of the  $1 \times 2$  cm pieces, respectively. Figure 6 shows that the BC/PHB samples exhibited the most homogeneous blue coloration throughout the film and they incorporated the largest amount of TSNPs compared to the blends with PLA and PCL. Figure 7 shows the distribution of TSNP clusters on the surface of BC through SEM images.

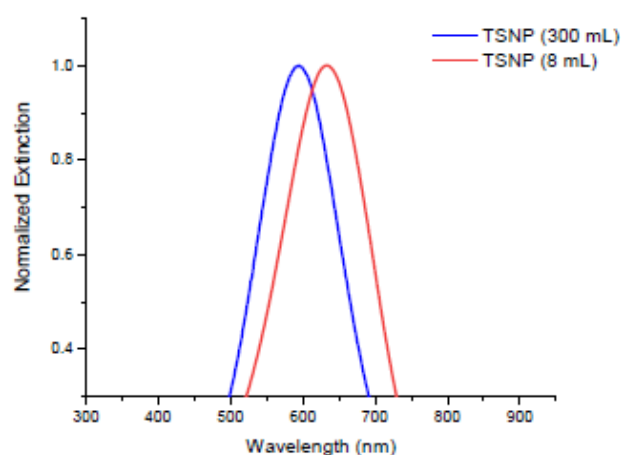


Figure 4. UV-Vis spectrum of scaled-up TSNPs (300 mL) compared to original synthesis method (8 mL).

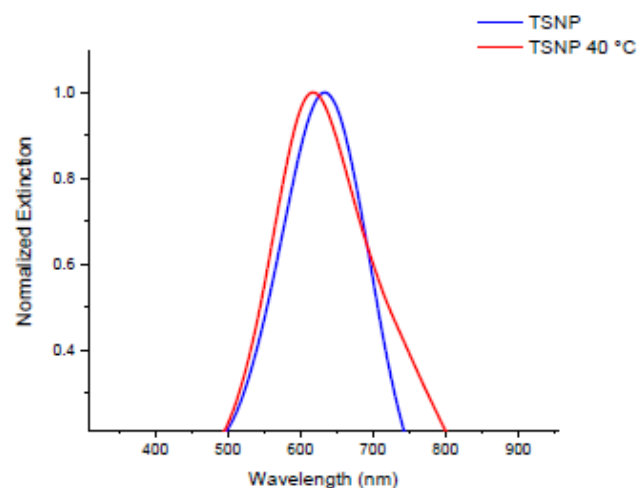
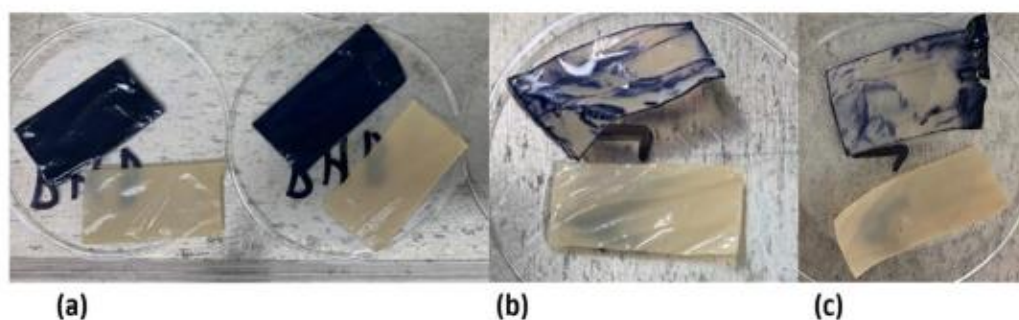
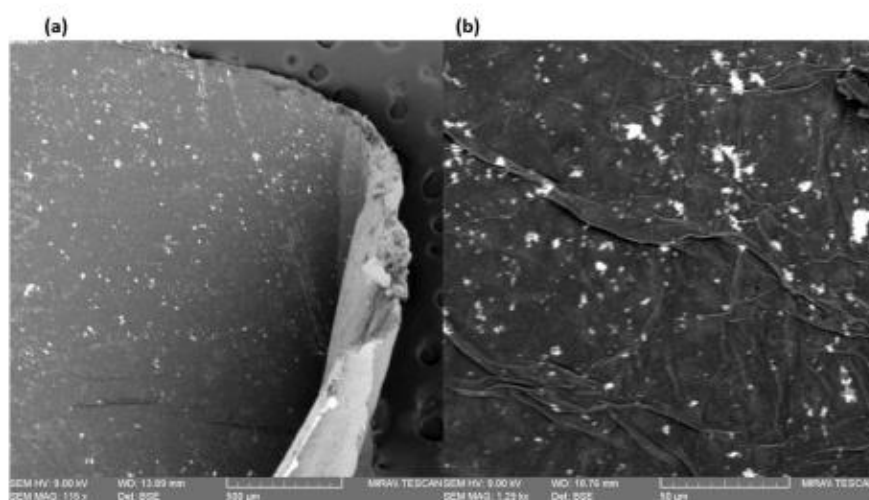


Figure 5. UV-Vis spectra of TSNPs before and after evaporation at 40 °C.



**Figure 6.** Bare BC blends (white) and BC/TSNP blends (dark blue). (a) BC/PHB blends, (b) BC/PLA blends, and (c) BC/PCL blends.



**Figure 7.** SEM micrographs of BC/TSNP films, showing distribution of TSNP clusters (white spots) at (a) 115 $\times$  magnification and (b) 1.29 k $\times$  magnification.

### 3.3.2. Antimicrobial Activity of BC Blends

The antimicrobial evaluation of the prepared BC blends was performed by incubating the samples in inoculated broth, with *E. coli* and *S. aureus* as respective representatives of Gram-negative and Gram-positive strains. The results for PCL, PLA, and PHB blends incorporated with TSNPs can be observed in Figure 8. As it can be observed, the PCL and PLA blends showed no significant antimicrobial activity against either of the tested strains, even with the incorporation of TSNPs. Contrary to the results exhibited by the PLA and PCL blends, the blend made with PHB showed significant antimicrobial activity against both, *E. coli* and *S. aureus* strains after the incorporation of TSNPs. This is likely due to the highly homogeneous absorption of TSNPs that was observed in the BC/PHB blends, allowing for a visibly higher antimicrobial response compared to the other blends, which absorbed a smaller amount of TSNPs.

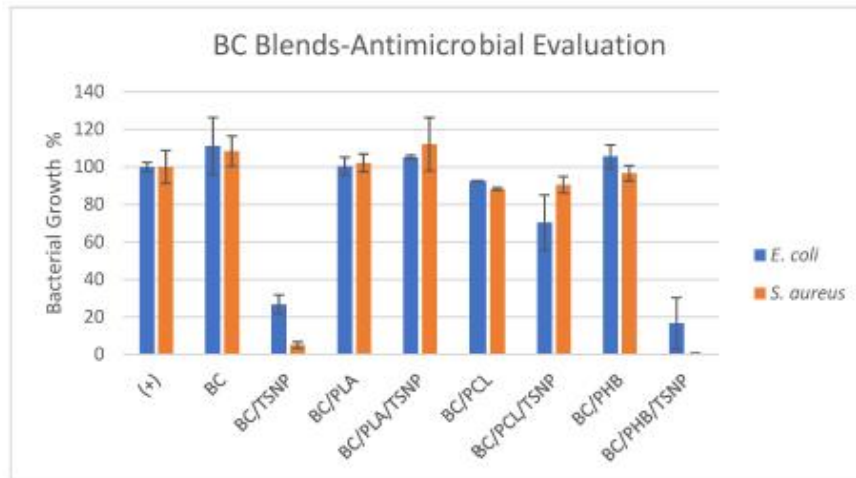


**Figure 8.** Results of antimicrobial evaluations for blends of BC with PLA, PCL, and PHB, incorporated with TSNPs, as well as bare materials used as control.

### 3.4. Evaluation of TSNP Application in Biosensing and Diagnostics

#### 3.4.1. TSNP Gold Coating and Protection Check

The adapted method by Zhang et al. (2014) [38] was used in this study for coating of the TSNP, and the efficacy of the gold layer protection was evaluated with NaCl. Results show a TSNP LSPR<sub>λmax</sub> recorded at 579 nm, and after gold coating, the LSPR showed a red shift measured at 599 nm (Figure 9). Upon exposure to NaCl 20 mM, no blue shift in the LSPR peak was observed.

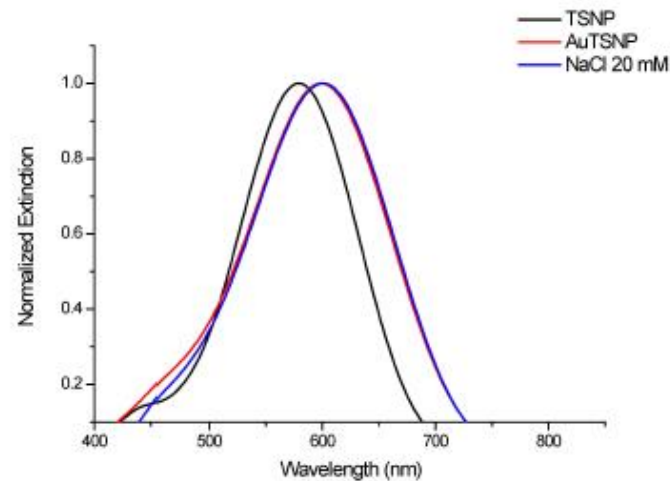


**Figure 9.** UV-Vis spectrum of TSNPs, AuTSNPs, and AuTSNPs exposed to NaCl 20 mM (protection check).

### 3.4.2. Sensitivity Test

The sensitivity test changes the refractive index of the medium in which the AuTSNPs are suspended, and can provide a measure of the nanoplates sensitivity without interfering with their stability. AuTSNP solution was added to increasing concentrations of sucrose solutions to evaluate the potential of the nanoplates for their use in sensing applications when there is a variation in the nanoplates' surrounding medium. Results (Figure 10) are in agreement with the reported outcomes by Charles et al., where the  $LSPR_{\lambda_{max}}$  of the spectra increases linearly as the sucrose concentration increases [54,56].

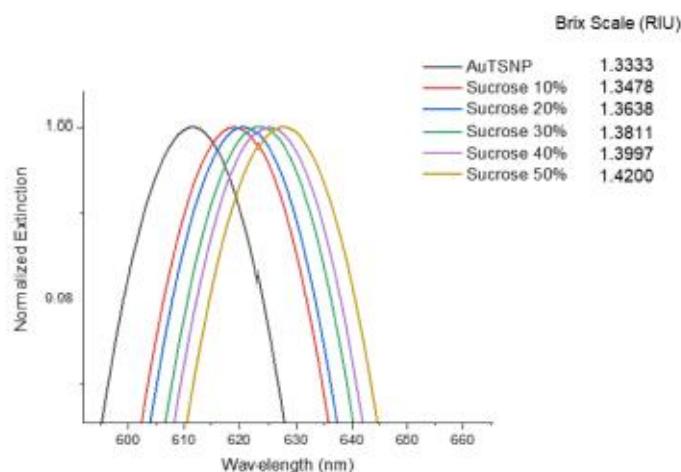


**Figure 10.** UV-Vis spectra of AuTSNPs suspended in a range of water-sucrose solutions.

### 3.4.3. Functionalization of Fn-PEGAuTSNPs and pH Monitoring

Prior to pH adjustment assays, AuTSNPs were coated with polyethylene glycol (PEGAuTSNP) to minimize contact between the Fn and the nanoplates' surface to avoid potential impact in the protein conformational behavior. Conformational changes in the protein were monitored by suspending the Fn-PEGAuTSNP in two phosphate buffers at pH 7.2 and pH 4.1, respectively. In Figure 11, the  $LSPR_{\lambda_{max}}$  of Fn-PEGAuTSNPs at pH 7 was measured at 633 nm; upon pH adjustment from pH 7 to pH 4, the  $LSPR_{\lambda_{max}}$  was measured to be 643 nm.

### 3.4.4. Determination of Adequate Fn Concentration

Several concentrations of Fn were added to aliquots of PEGAuTSNPs to determine the minimum amount of the protein to successfully cover the nanoplates and observe differences in the spectrum. One  $\mu\text{g}$  of anti-Fn was added afterwards to analyze binding. As reflected in Figure 12, changes in the spectra were observed with low concentrations of Fn. Results show that when higher concentrations of the protein were added to PEGAuTSNPs, longer red shifts were recorded as expected (Figure 12a). For all added concentrations of Fn, a red shift in the  $\lambda_{max}$  was observed upon addition of anti-Fn antibody (Figure 12b). In Figure 12c, expanded results show that shorter red shifts are recorded in higher Fn concentration samples once the anti-Fn antibody is added. This could be attributed to the anti-Fn binding to the excess of free unattached Fn within the nanoplate solution.

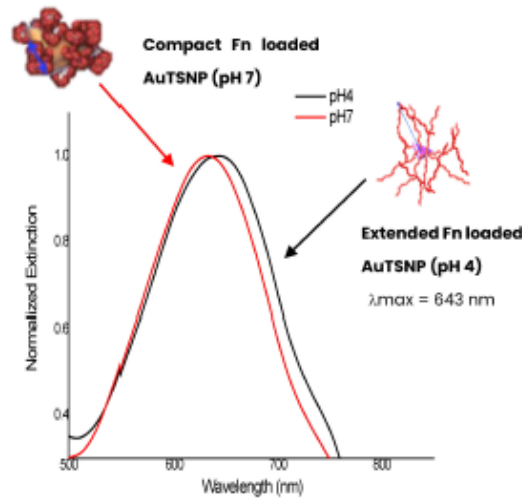


Figure 11. LSPR spectra of Fn-PEGAuTSNPs upon pH adjustment.

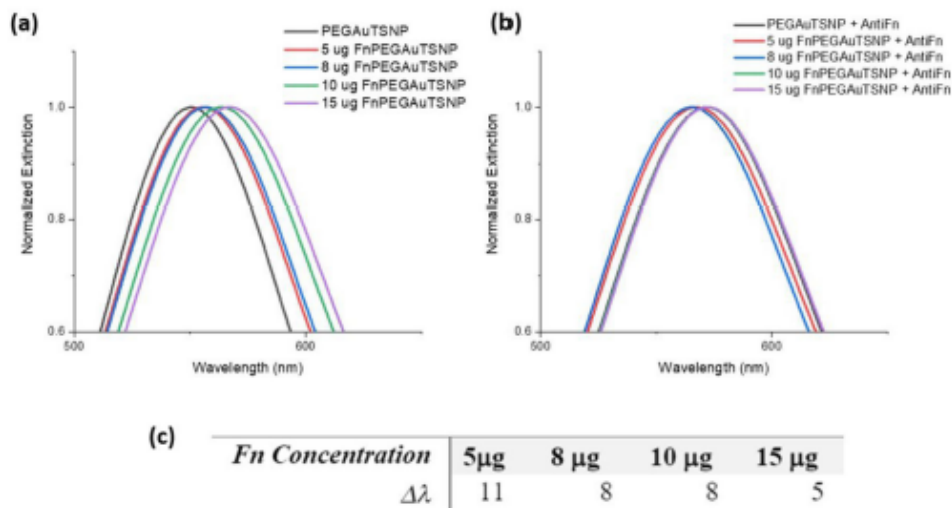
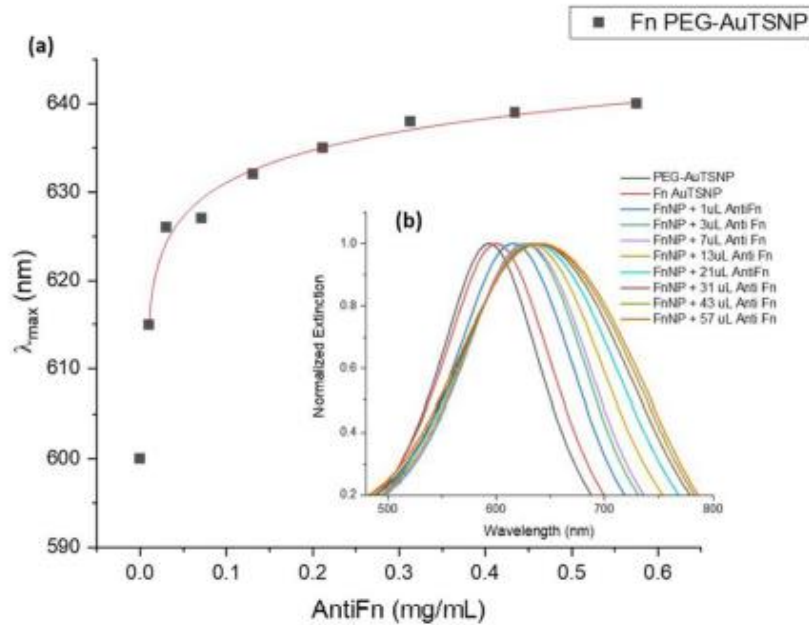


Figure 12. LSPR spectra of FnPEGAuTSNP samples (a) before and (b) after addition of anti-Fn antibody with (c) shift differences in  $\lambda_{\text{max}}$  upon addition of anti-Fn.

3.4.5. Determination of Adequate Anti-Fn Antibody Concentration

The limit of detection of the Ag-Ab system was determined by exposing a sample of Fn-PEGAuTSNPs to increasing concentrations of anti-Fn antibody. As observed in Figure 11b, there is evident red shifting as the concentration of anti-Fn increases, which indicates intensifying binding of the antibody to the Fn functionalized nanoplates. There is detection of Fn-anti-Fn binding with antibody concentrations as low as 0.01 mg/mL, and shorter redshifts are recorded for the highest concentrations of antibody, indicating system saturation from 0.212 mg/mL of the anti-Fn antibody (Figure 13a).



**Figure 13.** (a) LSPR peak shift as a function of anti-Fn antibody concentration for Fn-PEGAuTSNPs (b) LSPR spectra of Fn-PEGAuTSNPs upon addition of increasing concentrations of anti-Fn.

#### 4. Discussion

It was established that different morphologies of AgNPs present different properties to one another. They can be synthesized in a range of shapes, including spheres, rods, wires, triangles, and cubes, each possessing unique characteristics. Spheres possess excellent stability and dispersibility, while in the case of TSNPs and other nanostructures with sharp geometries, it was observed that the tips can provide a greater electric field enhancement, allowing optical properties to be more easily tuned and controlled [17]. Furthermore, the same sharp edges and corners present in TSNPs make them more susceptible to oxidation, resulting in a higher rate of Ag<sup>+</sup> ions released compared to spherical NPs, resulting in a higher antimicrobial activity [16]. In the solution form, color variations provide a visual means to differentiate and identify the specific shapes of silver nanoparticles: spheres are exhibiting yellow color while in the form of triangles the solution acquires a distinct blue (Figure 1).

In the original protocol of [50] the concentration of silver is 16.692 ppm in the TSNP solution, where results show broad localized surface plasmon resonances (LSPR) of more than 130 nm full width at half maximum (FWHM) (Figure 2). The broad FWHM of the TSNP spectrum can be attributed to the inhomogeneity of sizes and nanoparticle shapes in the solution. This can reduce the nanoplate sensitivity, which is a critical property in TSNPs when used in nanosensing applications [56]. The triangular morphology of the TSNP prepared through this method was evaluated using TEM on a previous study performed by our team (Figure 3), where the same synthesis method for the TSNP was used [55]. The TEM images, the color, and the spectra readings of our TSNP solution come in accordance to other studies that used similar seed-mediated methods to synthesize TSNPs [5,50,54]. An increase in the produced volume and in the amount of silver in the nanoplate solution was achieved, and the resulting LSPR spectrum demonstrated that a reduced water amount does not have an impact on the LSPR behavior of the TSNP (Figures 4 and 5). It was

reported that high sensitivity of the TSNP LSPR is due to the high proportion of triangular geometries and the platelet structure of the nanoparticles. Furthermore, compared to single silver nanoparticles, the sensitivity is increased in highly organized silver nanoparticle aggregates (in solution) [56].

Silver nanoplates emerged as a remarkable tool in the development of antimicrobial materials, offering unique properties that make it a valuable asset in the fight against microbial infections. Through the incorporation of silver into diverse materials, such as coatings, textiles, and medical devices, significant advancements were made in the field of antibacterial therapeutics [57]. Taking into consideration previously mentioned properties and the lack of research on TSNPs for antimicrobial applications in polymeric materials, studies were performed to evaluate their suitability as antimicrobial agents for polymers and biopolymers. The TSNP synthesis method used in this study resulted in a highly concentrated TSNP solution, which is desirable in order to include the TSNPs into polymer processing. Using this method, the amount of water required to be removed was decreased, while the number of nanoplates available for the process was increased. Incorporation of TSNPs in biopolymer blends with a lower percentage of incorporated polymer (PHB) resulted in higher absorption of the aqueous TSNP solution by the hydrophilic BC matrix compared to the PLA and PCL blends that incorporated a higher percentage of polymer on the BC. Previous studies also evaluated the integration of TSNPs into BC supplemented with curcumin [53], as well as their integration into pure PCL and PLA using a solvent casting method, resulting in improved properties of BC and biocompatible materials [55]. BC/PHB blends with TSNPs (Figure 6a) showed significant decrease in microbial growth for both tested bacterial strains; this is attributed to the higher amount of absorbed TSNPs compared to the PCL and PLA blends (Figure 8). These results come in accordance with previous work on the incorporation of AgNPs into polymeric materials, where a higher antimicrobial response is exhibited on the materials that are able to maintain a higher rate of silver and Ag<sup>+</sup> ions release [58]. Contrary to the previously reported study for evaluation of the antimicrobial activity of TSNPs incorporated into polymeric materials through solvent casting [55], the BC/PHB blend exhibited a higher antimicrobial response towards the Gram-negative strain under the examined conditions.

Proteins are known to easily bind to gold and silver nanoparticles spontaneously. It occurs through ionic or hydrophobic interactions [59]. Nanoparticles may be pre-functionalized with specific proteins, which will determine which new protein will attach to the newly formed NP-protein system [60]. According to Aherne et al., line widths of the LSPR are reduced as the nanoplate volume increases, which improves sensitivity of the nanoplates. Furthermore, a blue shift in the LSPR can be observed (from 600 to 530 nm) upon silver seed volume adjustment, resulting in a size reduction of the nanoplates [50]. This can be advantageous for the use of TSNPs in biosensing, since it allows for a higher range in which shifts in the spectrum can be easily detected within the UV-Vis range (Figures 4 and 5). Unprotected TSNPs can be highly susceptible to degradation or etching by catalytic oxidation in the presence of chlorine or other reactive ions. This can lead to alterations of the geometry and structure of the TSNP, normally resulting in a substantial blue shift in their spectrum and impairing their LSPR properties [38]. Different coatings can be used to protect the TSNP structure; nonetheless, most coatings will also affect the plasmonic response of the nanoparticles. A method used by [38] proved to successfully coat TSNP edges with a layer of gold, providing the nanoparticles with protection from etching while allowing them to maintain their plasmonic response and refractive index sensitivity. Results of this study are in accordance to the results reported by the [38] deposition of a thin layer of gold in the triangular nanoplate edges at low Ag:Au ratios, successfully protecting the nanoplates without causing any structural damages associated with galvanic replacement (Figure 9). Moreover, no major changes in the nanoplates' optical properties occurred besides an enhancement of its optical sensitivity. The LSPR spectrum at pH 4 was redshifted by 10 nm upon Fn extension due to a higher refractive index surrounding the nanoplates. The presence of the compact protein strand on top of the nanoparticle



surface occupies a larger surface area; however, it does not bulge from the surface more than an elongated Fn strand, which can explain the shift in the spectrum. As presented in Figure 10, sucrose sensitivity assay confirmed that  $LSPR_{\lambda_{max}}$  of the spectra directly correlates to sucrose concentration [54,56]. In order to minimize any potential impact on the protein's conformational behavior, AuTSNPs were coated with PEG in order to avoid any direct interaction between the nanoplates' surface and the protein, thus reducing the likelihood of any influence on its conformation. Conformational changes of the protein were monitored by suspending the Fn-PEGAuTSNP in two phosphate buffers at pH 7.2 and pH 4.1 since Fn is known to change its structure upon pH variations (Figure 11). Fn has an uncoiled conformation when in acidic or high salt conditions, whereas within low salt conditions it shows a "coiled compact" conformation [61]. In previous studies where Fn conformational changes are analyzed within different pH environments, Fn is reported to have a hydrodynamic radius of 23 nm when compacted, and when it extends the radius increases up to 130 nm for single Fn strands [43,44]. Fn can form much larger strands as networks and fibrils can develop and be mediated within the extracellular matrix (ECM) [62].

When it comes to determination of adequate concentration of Fn, as reflected in Figure 12, changes in the spectra were observed with low concentrations of Fn. On the other hand, Fn-anti-Fn binding with antibody concentrations as low as 0.01 mg/mL were detected, and shorter redshifts are recorded for the highest concentrations of antibody, indicating system saturation from 0.212 mg/mL of the anti-Fn antibody (Figure 13). This correlates with the studies by Zhang et al. (2014) where cytidine 50-diphosphocholine (PC)-coated AuTSNPs detect C-reactive protein (CRP) in concentrations as low as 0.0033 mg/L, showing the remarkable features of the AuTSNPs and their wide-ranging limits of detection [38]. Detection limits for several other nanobiosensors were reported with ranging limits between 0.8 and 40 ng/mL for gold nanoparticles and 12 pM for Cu nanoclusters, among others [63].

This demonstrates the ability of AuTSNPs for their use as versatile and efficient platforms for immunoassays, opening up exciting possibilities for cutting-edge diagnostic applications. Functionalization of these AuTSNPs with specific antibodies or antigens could facilitate the detection and quantification of analytes. The integration of AuTSNPs into immunoassay platforms has the potential to transform disease diagnosis and biomedical research, providing a powerful tool for rapid detection of diseases with high sensitivity.

## 5. Conclusions

In conclusion, different morphologies of silver nanoparticles exhibit unique properties. Spherical AgNPs are stable and dispersible, while triangular silver nanoplates with sharp edges enhanced electric field enhancement and antimicrobial activity. The synthesis method used in this study resulted in a highly concentrated TSNP solution, which is desirable for incorporating TSNPs into polymer processing. TSNPs incorporated into biopolymer blends, particularly BC/PHB blends, showed significant antimicrobial activity against bacterial strains compared to blends with other polymers such as PCL and PLA. The higher absorption of TSNPs by the hydrophilic BC matrix contributed to this antimicrobial response. Adjusting the silver seed volume reduces nanoplate size, improving sensitivity for biosensing applications. Coating the edges of TSNPs with a layer of gold protected the nanoparticles from degradation without impairing their plasmonic response and refractive index sensitivity. The functionalization of AuTSNPs with specific antibodies or antigens enables their use as versatile platforms for immunological assays, facilitating the rapid and sensitive detection of diseases. Future work will include investigation of the proposed detection system's selectivity fare in the presence of physiological elements.

Overall, the unique properties and versatility of silver nanoplates, particularly TSNPs, make them valuable assets in various fields, including antimicrobial materials, nanosensing, and biomedical research. Further exploration and utilization of these nanoparticles hold

great potential for advancements in antibacterial therapeutics, disease diagnosis, and biomedical applications.

**Author Contributions:** L.G.R.B. conceptualization, methodology, investigation, writing—original draft preparation; E.L.G. conceptualization, methodology, investigation, writing—original draft preparation; M.M. conceptualization, writing—original draft preparation, writing—review and editing, supervision; M.H. methodology, writing—original draft preparation, supervision; R.P. methodology, writing—original draft preparation, supervision; D.M.D. methodology, supervision; M.B.-F. conceptualization, methodology, supervision, and funding acquisition. All authors have read and agreed to the published version of the manuscript.

**Funding:** This research was supported by the Technological University of The Shannon through the President Seed Fund, the Government of Ireland International Education Scholarship 2018/2019, the European Union's Horizon 2020 Research and Innovation program [grant number: 870292 (BioCEP)]; European Union's Horizon Europe EIC Pathfinder program [grant number: 101046758 (EcoPlastiC)].

**Institutional Review Board Statement:** Not applicable.

**Informed Consent Statement:** Not applicable.

**Data Availability Statement:** <https://zenodo.org/> (accessed on 5 May 2023).

**Conflicts of Interest:** The authors declare no conflict of interest.

## References

1. Tanasa, E.; Zaharia, C.; Radu, I.C.; Surdu, V.A.; Vasile, B.S.; Damian, C.M.; Andronescu, E. Novel Nanocomposites Based on Functionalized Magnetic Nanoparticles and Polyacrylamide: Preparation and Complex Characterization. *Nanomaterials* **2019**, *9*, 1384. [CrossRef]
2. Andronescu, E.; Predoi, D.; Neacsu, I.A.; Paduraru, A.V.; Musuc, A.M.; Trusca, R.; Oprea, O.; Tanasa, E.; Vasile, O.R.; Nicoara, A.L.; et al. Photoluminescent Hydroxylapatite: Eu<sup>3+</sup> Doping Effect on Biological Behaviour. *Nanomaterials* **2019**, *9*, 1187. [CrossRef] [PubMed]
3. Lee, K.W.; Kim, Y.H.; Du, W.X.; Kim, J.Y. Stretchable and Low-Haze Ag-Nanowire-Network 2-D Films Embedded into a Cross-Linked Polydimethylsiloxane Elastomer. *Nanomaterials* **2019**, *9*, 576. [CrossRef]
4. Jeevanandam, J.; Barhoum, A.; Chan, Y.S.; Dufresne, A.; Danquah, M.K. Review on Nanoparticles and Nanostructured Materials: History, Sources, Toxicity and Regulations. *Balistan J. Nanotechnol.* **2018**, *9*, 1050–1074. [CrossRef] [PubMed]
5. Kelly, J.M.; Keegan, G.; Brennan-Fournet, M.E. Triangular Silver Nanoparticles: Their Preparation, Functionalisation and Properties. *Acta Phys. Pol. A* **2012**, *122*, 337–345. [CrossRef]
6. Zhang, C.; Huang, Q.; Cui, Q.; Ji, C.; Zhang, Z.; Chen, X.; George, T.; Zhao, S.; Guo, L.J. High-Performance Large-Scale Flexible Optoelectronics Using Ultrathin Silver Films with Tunable Properties. *ACS Appl. Mater. Interfaces* **2019**, *11*, 27216–27225. [CrossRef]
7. Bhardwaj, A.K.; Sundaram, S.; Yadav, K.K.; Srivastav, A.L. An Overview of Silver Nano-Particles as Promising Materials for Water Disinfection. *Environ. Technol. Innov.* **2021**, *23*, 101721. [CrossRef]
8. Takáč, P.; Michalková, R.; Čížmáriková, M.; Bedlovičová, Z.; Balážová, I.; Takáčová, G. The Role of Silver Nanoparticles in the Diagnosis and Treatment of Cancer: Are There Any Perspectives for the Future? *Life* **2023**, *13*, 466. [CrossRef]
9. Gomes, H.L.O.; Martins, C.S.M.; Prior, J.A.V. Silver Nanoparticles as Carriers of Anticancer Drugs for Efficient Target Treatment of Cancer Cells. *Nanomaterials* **2021**, *11*, 964. [CrossRef]
10. Shanmuganathan, R.; Karuppusamy, I.; Saravanan, M.; Muthukumar, H.; Ponnuchamy, K.; Ramkumar, V.S.; Pugazhendhi, A. Synthesis of Silver Nanoparticles and Their Biomedical Applications—A Comprehensive Review. *Curr. Pharm. Des.* **2019**, *25*, 2650–2660. [CrossRef]
11. Gopinath, P.; Gogoi, S.K.; Chattopadhyay, A.; Ghosh, S.S. Implications of Silver Nanoparticle Induced Cell Apoptosis for in Vitro Gene Therapy. *Nanotechnology* **2008**, *19*, 075104. [CrossRef]
12. Suter, S.; Haussener, S. Optimizing Mesostructured Silver Catalysts for Selective Carbon Dioxide Conversion into Fuels. *Energy Environ. Sci.* **2019**, *12*, 1668–1678. [CrossRef]
13. Lee, S.H.; Jun, B.H. Silver Nanoparticles: Synthesis and Application for Nanomedicine. *Int. J. Mol. Sci.* **2019**, *20*, 865. [CrossRef]
14. Güzel, R.; Erdal, G. *Synthesis of Silver Nanoparticles*; IntechOpen: London, UK, 2016; Chapter 1; Volume 13. [CrossRef]
15. Le, V.T.; Bach, L.G.; Pham, T.T.; Le, N.T.T.; Ngoc, U.T.P.; Tran, D.H.N.; Nguyen, D.H. Synthesis and Antifungal Activity of Chitosan-Silver Nanocomposite Synergize Fungicide against *Phytophthora Capsici*. *J. Macromol. Sci. Part A Pure Appl. Chem.* **2019**, *56*, 522–528. [CrossRef]
16. Lu, W.; Yao, K.; Wang, J.; Yuan, J. Ionic Liquids-Water Interfacial Preparation of Triangular Ag Nanoplates and Their Shape-Dependent Antibacterial Activity. *J. Colloid Interface Sci.* **2015**, *437*, 35–41. [CrossRef]

17. Kelly, K.L.; Coronado, E.; Zhao, L.L.; Shatz, G.C. The Optical Properties of Metal Nanoparticles: The Influence of Size, Shape, and Dielectric Environment. *J. Phys. Chem. B* **2003**, *107*, 668–677. [CrossRef]
18. Pastoriza-Santos, I.; Liz-Marzán, L.M. Colloidal Silver Nanoplates: State of the Art and Future Challenges. *J. Mater. Chem.* **2008**, *18*, 1724–1737. [CrossRef]
19. Qing, Y.; Cheng, L.; Li, R.; Liu, G.; Zhang, Y.; Tang, X.; Wang, J.; Liu, H.; Qin, Y. Potential Antibacterial Mechanism of Silver Nanoparticles and the Optimization of Orthopedic Implants by Advanced Modification Technologies. *Int. J. Nanomed.* **2018**, *13*, 3311–3327. [CrossRef]
20. Siritongsuk, P.; Hongsing, N.; Thammawithan, S.; Daduang, S.; Klaynongsruang, S.; Tuanyok, A.; Patramanon, R. Two-Phase Bactericidal Mechanism of Silver Nanoparticles against *Burkholderia Pseudomallei*. *PLoS ONE* **2016**, *11*, e0168098. [CrossRef]
21. Pal, S.; Tak, Y.K.; Song, J.M. Does the Antibacterial Activity of Silver Nanoparticles Depend on the Shape of the Nanoparticle? A Study of the Gram-Negative Bacterium *Escherichia Coli*. *Appl. Environ. Microbiol.* **2007**, *73*, 1712–1720. [CrossRef]
22. Abbas, M.; Naeem, N.; Iftikhar, H.; Latif, U. *Synthesis, Characterization and Antimicrobial Properties of Silver Nanocomposites*; IntechOpen: London, UK, 2018; Volume 1, Chapter 4; p. 13. [CrossRef]
23. Knauer, A.; Csáki, A.; Fritzsche, W.; Serra, C.A.; Leclerc, N.; Michael Köhler, J. Micro Continuous Flow-through Synthesis of Triangular Silver Nanoprisms and Their Incorporation in Complexly Composed Polymer Microparticles. *Chem. Eng. J.* **2013**, *227*, 191–197. [CrossRef]
24. Audoit, J.; Laffont-dantras, L.; Lonjon, A.; Dantras, E.; Audoit, J.; Laffont-dantras, L.; Lonjon, A.; Dantras, E.; Percolative, C.L. Percolative Silver Nanoplates/PVDF Nanocomposites: Bulk and Surface Electrical Conduction. *Polymer* **2016**, *78*, 104–110. [CrossRef]
25. Zhang, J.; Sun, Y.; Zhang, H.; Xu, B.; Zhang, H.; Song, D. Preparation and Application of Triangular Silver Nanoplates/Chitosan Composite in Surface Plasmon Resonance Biosensing. *Anal. Chim. Acta* **2013**, *769*, 114–120. [CrossRef] [PubMed]
26. Reynoso-García, P.J.; Gúizado-Rodríguez, M.; Barba, V.; Ramos-Ortiz, G.; Martínez-Gutiérrez, H. Stabilization of Silver Nanoparticles with a Dithiocarbamate Ligand and Formation of Nanocomposites by Combination with Polythiophene Derivative Nanoparticles. *Adv. Condens. Matter Phys.* **2018**, *2018*, 4376051. [CrossRef]
27. Kudryashov, M.; Logunov, A.; Gogova, D.; Mashin, A.; De Filpo, G. Ag/PVP/PAN Nanocomposites with Triangular Nanoprisms of Silver Synthesized by UV-Induced Polymerization: Morphology Manipulation and Optical Properties Tuning. *Opt. Mater.* **2020**, *101*, 109746. [CrossRef]
28. Djafari, J.; Fernández-Lodeiro, C.; Fernández-Lodeiro, A.; Silva, V.; Poeta, P.; Igñejas, G.; Lodeiro, C.; Capelo, J.L.; Fernández-Lodeiro, J. Exploring the Control in Antibacterial Activity of Silver Triangular Nanoplates by Surface Coating Modulation. *Front. Chem.* **2019**, *6*, 677. [CrossRef]
29. Vo, Q.K.; Phung, D.D.; Nguyen, Q.N.V.; Thi, H.H.; Thi, N.H.N.; Thi, P.P.N.; Bach, L.G.; Tan, L. Van Controlled Synthesis of Triangular Silver Nanoplates by Gelatin-Chitosan Mixture and the Influence of Their Shape on Antibacterial Activity. *Processes* **2019**, *7*, 873. [CrossRef]
30. Velgosova, O.; Mačák, L.; Lisnichuk, M.; Vojtko, M. Synthesis and Analysis of Polymorphic Silver Nanoparticles and Their Incorporation into the Polymer Matrix. *Polymers* **2022**, *14*, 2666. [CrossRef]
31. Unser, S.; Bruzas, I.; He, J.; Sagle, L. Localized Surface Plasmon Resonance Biosensing: Current Challenges and Approaches. *Sensors* **2015**, *15*, 15684–15716. [CrossRef]
32. Mauriz, E.; Dey, P.; Lechuga, L.M. Advances in Nanoplasmonic Biosensors for Clinical Applications. *Analyst* **2019**, *144*, 7105–7129. [CrossRef]
33. Tang, Y.; Zeng, X.; Liang, J. Surface Plasmon Resonance: An Introduction to a Surface Spectroscopy Technique. *J. Chem. Educ.* **2010**, *87*, 742–746. [CrossRef]
34. Aherne, D.; Charles, D.E.; Brennan-Fournet, M.E.; Kelly, J.M.; Gun'ko, Y.K. Etching-Resistant Silver Nanoprisms by Epitaxial Deposition of a Protecting Layer of Gold at the Edges. *Langmuir* **2009**, *25*, 10165–10173. [CrossRef]
35. Willets, K.A.; Van Duyne, R.P. Localized Surface Plasmon Resonance Spectroscopy and Sensing. *Annu. Rev. Phys. Chem.* **2007**, *58*, 267–297. [CrossRef]
36. Petryayeva, E.; Krull, U.J. Localized Surface Plasmon Resonance: Nanostructures, Bioassays and Biosensing—A Review. *Anal. Chim. Acta* **2011**, *706*, 8–24. [CrossRef]
37. Loiseau, A.; Asila, V.; Boitel-Aullen, G.; Lam, M.; Salmain, M.; Boujday, S. Silver-Based Plasmonic Nanoparticles for and Their Use in Biosensing. *Biosensors* **2019**, *9*, 78. [CrossRef]
38. Zhang, Y.; Charles, D.E.; Ledwith, D.M.; Aherne, D.; Cunningham, S.; Voisin, M.; Blau, W.J.; Gun'ko, Y.K.; Kelly, J.M.; Brennan-Fournet, M.E. Wash-Free Highly Sensitive Detection of C-Reactive Protein Using Gold Derivatized Triangular Silver Nanoplates. *RSC Adv.* **2014**, *4*, 29022–29031. [CrossRef]
39. Michael Kotlarchyk Scattering Theory. In *Encyclopedia of Spectroscopy and Spectrometry*; Academic Press: Cambridge, MA, USA, 1999; pp. 2074–2084.
40. Wu, C.; Zhou, X.; Wei, J. Localized Surface Plasmon Resonance of Silver Nanotriangles Synthesized by a Versatile Solution Reaction. *Nanoscale Res. Lett.* **2015**, *10*, 354. [CrossRef]
41. Zhang, C.; Qiu, M.; Wang, J.; Liu, Y. Recent Advances in Nanoparticle-Based Optical Sensors for Detection of Pesticide Residues in Soil. *Biosensors* **2023**, *13*, 415. [CrossRef]

42. Liu, L.; Liang, X.; Qiu, G.; Guo, C.; Chan, Y.K.; Wu, C.-M.L. Self-Assembly Silver Nanoparticles Decorated on Gold Nanoislands for Label-Free Localized Surface Plasmon Resonance Biosensing. *Adv. Mater. Interfaces* **2022**, *9*, 2200339. [CrossRef]
43. Brennan-Fournet, M.E.; Huerta, M.; Zhang, Y.; Malliaras, G.; Owens, R.M. Detection of Fibronectin Conformational Changes in the Extracellular Matrix of Live Cells Using Plasmonic Nanoplates. *J. Mater. Chem. B* **2015**, *3*, 9140–9147. [CrossRef]
44. Rodríguez Barroso, L.G.; Azaman, F.A.; Pogue, R.; Devine, D.; Fournet, M.B. Monitoring In Vitro Extracellular Matrix Protein Conformations in the Presence of Biomimetic Bone-Regeneration Scaffolds Using Functionalized Gold-Edge-Coated Triangular Silver Nanoparticles. *Nanomaterials* **2023**, *13*, 57. [CrossRef] [PubMed]
45. Vinayagam, S.; Rajaiah, P.; Mukherjee, A.; Natarajan, C. DNA-Triangular Silver Nanoparticles Nanoprobe for the Detection of Dengue Virus Distinguishing Serotype. *Spectrochim. Acta Part A Mol. Biomol. Spectrosc.* **2018**, *202*, 346–351. [CrossRef] [PubMed]
46. Cai, T.; Gao, Y.; Yan, J.; Wu, Y.; Di, J. Visual Detection of Glucose Using Triangular Silver Nanoplates and Gold Nanoparticles. *RSC Adv.* **2017**, *7*, 29122–29128. [CrossRef]
47. Fang, X.; Ren, H.; Zhao, H.; Li, Z. Ultrasensitive Visual and Colorimetric Determination of Dopamine Based on the Prevention of Etching of Silver Nanoprisms by Chloride. *Microchim. Acta* **2017**, *184*, 415–421. [CrossRef]
48. Li, L.; Zhang, L.; Zhao, Y.; Chen, Z. Colorimetric Detection of Hg(II) by Measurement of the Color Alterations from the “before” and “after” RGB Images of Etched Triangular Silver Nanoplates. *Microchim. Acta* **2018**, *185*, 235. [CrossRef]
49. Furletov, A.A.; Apyari, V.V.; Garshev, A.V.; Dmitrienko, S.G.; Zolotov, Y.A. Triangular Silver Nanoplates as a Spectrophotometric Reagent for the Determination of Mercury(II). *J. Anal. Chem.* **2017**, *72*, 1203–1207. [CrossRef]
50. Aherne, D.; Ledwith, D.M.; Gara, M.; Kelly, J.M. Optical Properties and Growth Aspects of Silver Nanoprisms Produced by a Highly Reproducible and Rapid Synthesis at Room Temperature. *Adv. Funct. Mater.* **2008**, *18*, 2005–2016. [CrossRef]
51. Solomon, S.D.; Bahadory, M.; Jeyarajasingam, A.V.; Rutkowsky, S.A.; Boritz, C.; Mulfinger, L. Synthesis and Study of Silver Nanoparticles. *J. Chem. Educ.* **2007**, *84*, 322–325.
52. Etacheri, V.; Georgekutty, R.; Seery, M.K.; Pillai, S.C. Single Step Morphology-Controlled Synthesis of Silver Nanoparticles. *Mater. Res. Soc. Symp. Proc.* **2010**, *1217*, 7–13. [CrossRef]
53. Garcia, E.L.; Mojicevic, M.; Milivojevic, D.; Aleksic, I.; Vojnovic, S.; Stevanovic, M.; Murray, J.; Attallah, O.A.; Devine, D.; Fournet, M.B. Enhanced Antimicrobial Activity of Biocompatible Bacterial Cellulose Films via Dual Synergistic Action of Curcumin and Triangular Silver Nanoplates. *Int. J. Mol. Sci.* **2022**, *23*, 12198. [CrossRef]
54. Charles, D.E.; Aherne, D.; Gara, M.; Ledwith, D.M.; Gun, Y.K.; Kelly, J.M.; Blau, W.J.; Brennan-fournet, M.E. Versatile Solution Phase Triangular Silver Nanoplates for Highly Sensitive Plasmon Resonance Sensing. *ACS Nano* **2010**, *4*, 55–64. [CrossRef] [PubMed]
55. Garcia, E.L.; Attallah, O.A.; Mojicevic, M.; Devine, D.M.; Fournet, M.B. Antimicrobial Active Bioplastics Using Triangular Silver Nanoplate Integrated Polycaprolactone and Polylactic Acid Films. *Materials* **2021**, *14*, 1132. [CrossRef] [PubMed]
56. Charles, D.; Fournet, P.; Cunningham, S.; Ledwith, D.; Kelly, J.M.; Blau, W.; Fournet, M.B. A Sensitivity Study of the Localised Surface Plasmon Resonance of High-Definition Structured Silver Nanoparticles in Solution. *Plasmon. Met. Nanostruct. Their Opt. Prop. VI* **2008**, *7032*, 70322G. [CrossRef]
57. Bruna, T.; Maldonado-Bravo, F.; Jara, P.; Caro, N. Silver Nanoparticles and Their Antibacterial Applications. *Int. J. Mol. Sci.* **2021**, *22*, 7202. [CrossRef]
58. Lyutakov, O.; Goncharova, I.; Rimpelova, S.; Kolarova, K.; Svanda, J.; Svorcik, V. Silver Release and Antimicrobial Properties of PMMA Films Doped with Silver Ions, Nano-Particles and Complexes. *Mater. Sci. Eng. C* **2015**, *49*, 534–540. [CrossRef] [PubMed]
59. Szymanski, M.S.; Porter, R.A. Preparation and Quality Control of Silver Nanoparticle-Antibody Conjugate for Use in Electrochemical Immunoassays. *J. Immunol. Methods* **2013**, *387*, 262–269. [CrossRef]
60. Saptarshi, S.R.; Duschl, A.; Lopata, A.L. Interaction of Nanoparticles with Proteins: Relation to Bio-Reactivity of the Nanoparticle. *J. Nanobiotechnol.* **2013**, *11*, 26. [CrossRef]
61. Maurer, L.M.; Ma, W.; Mosher, D.F. Dynamic Structure of Plasma Fibronectin. *Crit. Rev. Biochem. Mol. Biol.* **2016**, *51*, 213–227. [CrossRef]
62. Tooney, N.M.; Mosesson, M.W.; Amrani, D.L.; Hainfeld, J.F.; Wall, J.S. Solution and Surface Effects on Plasma Fibronectin Structure. *J. Cell Biol.* **1983**, *97*, 1686–1692. [CrossRef]
63. Karabulut, G.; Ülgen, N.B.; Karakuş, S. Nanostructures in Biosensors Development and Applications. In *Biosignal Processing*; IntechOpen: London, UK, 2022; ISBN 978-1-80355-562-1.

**Disclaimer/Publisher's Note:** The statements, opinions and data contained in all publications are solely those of the individual author(s) and contributor(s) and not of MDPI and/or the editor(s). MDPI and/or the editor(s) disclaim responsibility for any injury to people or property resulting from any ideas, methods, instructions or products referred to in the content.



Article

## Triangular Silver Nanoplates as a Bioanalytical Tool: Potential COVID-19 Detection

Laura G. Rodriguez Barroso<sup>1</sup>, Eduardo Lanzagorta Garcia<sup>1</sup>, Marija Mojicevic<sup>1,\*</sup>, Buket Alkan Tas<sup>1</sup>, Miriam Huerta<sup>2</sup>, Robert Pogue<sup>3</sup>, Declan M. Devine<sup>1</sup> and Margaret Brennan-Fournet<sup>1</sup>

- <sup>1</sup> PRISM Research Institute, Technological University of the Shannon: Midlands Midwest, Dublin Rd, N37 HD68 Athlone, Ireland; laura.rodriguez@tus.ie (L.G.R.B.); e.lgarcia@research.tus.ie (E.L.G.); buket.tas@tus.ie (B.A.T.); declan.devine@tus.ie (D.M.D.); margaret.brennanfournet@tus.ie (M.B.-F.)
  - <sup>2</sup> Physics Institute, Universidad Autónoma de San Luis Potosí, Av. Parque Chapultepec 1570, San Luis Potosí 78295, Mexico; miriam.huerta@f.uaslp.mx
  - <sup>3</sup> Campus Asa Norte, Universidade Católica de Brasília, SGAN Módulo B 916 Avenida W5, Brasília 70790-160, Brazil; redward@p.ucb.br
- \* Correspondence: marija.mojicevic@tus.ie

**Abstract:** Nanotechnology offers new possibilities in molecular diagnostics, with nanoparticles gaining attention as biosensor upgrades. This study evaluates gold-coated silver nanoplates coated with PEG for enhanced protection, aiming to detect Spike protein with higher sensitivity, and emphasizes the importance of considering complex environments and appropriate controls for specific binding and accurate analysis. The sensitivity of antibody-coated PEGAuTSNPs as tools for immunoassays is demonstrated through fibronectin (Fn)- anti-fibronectin binding within an isolated extracellular matrix as a complex and native environment of Fn. Moreover, the optimal functionalization volume of Spike protein was determined (4 µg/mL of PEGAuTSNP). Anti-Spike was added to confirm binding, while the TJP1 protein was used as a negative control. The same experiment was used in the presence of horse serum to simulate a complex environment. According to Localized Surface Plasmon Resonance analysis and Dynamic Light Scattering size measurements, anti-Spike exhibited a stronger affinity for the nanoplates, causing TJP1 to be replaced by the antibody on the nanoplates' surface. Future research will involve exploring alternative complex environments, filtering larger molecules, and the optimization of immunoassay performance.

**Keywords:** TSNP; nanoplates; fibronectin; immunoassay; COVID-19; spike; immunodetection



Citation: Rodríguez Barroso, L.G.; Lanzagorta García, E.; Mojicevic, M.; Alkan Tas, B.; Huerta, M.; Pogue, R.; Devine, D.M.; Brennan-Fournet, M. Triangular Silver Nanoplates as a Bioanalytical Tool: Potential COVID-19 Detection. *Int. J. Mol. Sci.* **2023**, *24*, 11974. <https://doi.org/10.3390/ijms241511974>

Academic Editor: Irina Zaretskovskaya

Received: 30 June 2023

Revised: 21 July 2023

Accepted: 24 July 2023

Published: 26 July 2023



Copyright © 2023 by the authors. Licensee MDPI, Basel, Switzerland. This article is an open access article distributed under the terms and conditions of the Creative Commons Attribution (CC BY) license (<https://creativecommons.org/licenses/by/4.0/>).

### 1. Introduction

Immunoassays (IAs) have been used for decades for various bioanalytical applications, ranging from clinical diagnostics and pharmaceutical analyses to environmental and food monitoring and testing. The early-stage and precise detection of analytes has been recognized as a crucial factor in these applications [1]. Successful monitoring, disease prevention and overall care for public health rely on the effectiveness of biomarkers regarding food and clinical samples. IAs are based on the quantitation of an analyte through the reaction of an antigen (Ag) and an antibody (Ab) [2,3]. They are selective and sensitive; however, labeling agents are commonly used to increase sensitivity and catalyze the reaction [4]. Moreover, these methods involve laborious protocols and, in some cases, take several days to complete a reaction [5]. Similar limitations are present in enzyme-linked immunosorbent assays (ELISAs), one of the commonly used IA procedures based on the catalytic potential and specificity of enzymes to detect antigen-antibody reactions. Additionally, the application of enzymes is usually accompanied by low stability and non-specificity, together with large amounts of the required sample to perform the test [6,7]. Antibodies, a family of related glycoproteins, are being extensively used as the biorecognition element in various immunoassays, while their utilization in the field of biosensors offers potential for



the development of new bioanalytical tools. IAs' selectivity and high sensitivity toward analytes ensure specific interactions, resulting in highly effective and reliable test results [8].

The currently available techniques for protein characterization that are able to detect conformations and structural changes in proteins require expensive instrumentation and extensive data analysis, and their signals are obstructed by cellular noise when applied in complex biological environments [9]. The necessity for the development of enzyme-free analytical assays has arisen in order to overcome ELISA assays' limitations [10]. Thus, the accurate and rapid detection of newly emerging diseases is crucial to prevent transmission and allow rapid treatment for affected individuals. For instance, the COVID-19 pandemic has had a significant impact in the world, resulting in the loss of millions of lives. It has emerged as one of the most consequential global health crises since the influenza pandemic [11], leading to the development and commercialization of a significant number of ELISAs that allow the detection of antibodies binding to structural proteins [12,13]. However, the emergence of nanotechnology has created new possibilities when it comes to molecular diagnostics.

The utilization of nanoparticles has become an attractive option for upgrading biosensors; because of their small size, a greater surface to volume ratio is provided, accompanied with their inherent physicochemical properties and decreased sensitivity to external factors [14]. Noble metal nanoparticles are known to have remarkable optical, catalytic, electronic and magnetic properties and have been intensely researched for the development of highly sensitive nano-biosensors to investigate a range of molecules and detect specific biomarkers [15,16]. Recent research has presented metallic nanoparticles as a promising tool for the detection of COVID-19, establishing new research pathways for the development of a range of techniques in assisting the prompt response to rising disease challenges. To date, evidence indicates that SARS-CoV-2 targets various organs, including the kidneys, heart, and lungs, leading to the eventual failure of multiple organ systems; hence, the necessity of developing accurate systems for its detection is crucial [17]. Silver nanoparticles have been used to improve glucose and hydrogen peroxide biosensors [18,19]. Moreover, they have been utilized for the dramatic enhancement of electrochemical IAs by coupling nanoparticles with enzyme catalytic effects [20]. It was reported that silver nanoparticles used as electrochemical labels have significantly improved IAs for the detection of tick-borne encephalitis virus Ab [21]. Specifically, triangular silver nanoparticles (TSNPs) have appealing tunable plasmonic characteristics and have been used for biosensing applications. Furthermore, their optical profile has been reported to show the strongest and sharpest peaks among other metals [22]. Moreover, gold-edge-coated triangular silver nanoparticles (AuTSNPs) with enhanced sensitivity have proven to be powerful new tools to monitor protein activity. This versatile method has the potential to provide the accurate and rapid detection of viral proteins and lead to better treatments for emerging infections and global outbreaks [23].

In this study, the high sensitivity of AuTSNPs as a tool for immunoassays is demonstrated through an analysis of Ab-Ag binding within an isolated extracellular matrix (ECM) as a complex environment, where anti-fibronectin (Fn) functionalized nanoplates bind to the corresponding antigen in its native environment. Moreover, the development of a potential platform for SARS-CoV-2 Spike protein detection is presented. This technique holds promise for adaptation and application in future outbreaks.

## 2. Results

### 2.1. Detection of Native Fn Using Anti-Fn Antibody-Functionalized PEGAuTSNP

The sensitivity of Fn antibody-functionalized nanoparticles to detect their corresponding antigen within its native environment was tested. Anti-Fn-PEGAuTSNPs were exposed to different concentrations of cell-extracted extracellular matrix (ECM) as a complex and native environment for Fn. As presented in Figure 1 and Table 1, according to Localized Surface Plasmon Resonance analysis (LSPR), PEGAuTSNPs'  $\lambda_{max}$  was recorded at 638 nm, and upon functionalization with anti-Fn, a shift of 65 nm was observed, indicating the

successful coating of the nanoplates with the antibody. Following this, the functionalized nanoplates were exposed to different concentrations of cell-isolated ECM and analyzed, showing a shifting profile, different than expected, with longer shifts recorded for the less concentrated ECM samples.

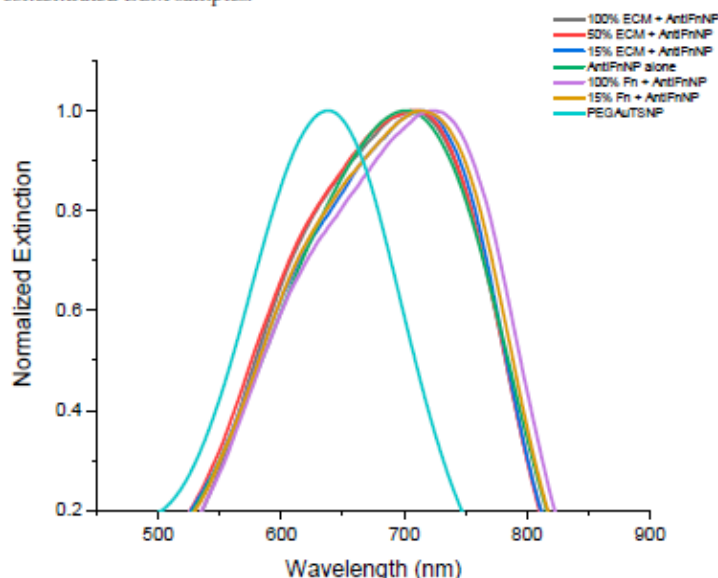


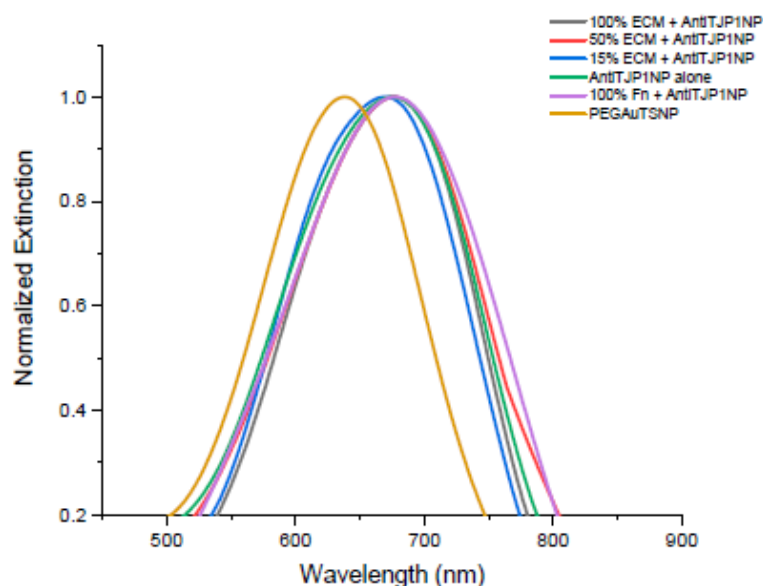
Figure 1. LSPR spectra of anti-Fn-native Fn binding experiment

Table 1.  $\lambda_{max}$  of anti-Fn-PEGAuTSNP within different concentrations of ECM.

Treatment	$\lambda_{max}$
PEGAuTSNP	638 nm
Anti-Fn-PEGAuTSNP	703 nm
100% ECM + Anti-Fn-PEGAuTSNP	707 nm
50% ECM + Anti-Fn-PEGAuTSNP	711 nm
15% ECM + Anti-Fn-PEGAuTSNP	715 nm
100% Fn + Anti-Fn-PEGAuTSNP	723 nm
15% Fn + Anti-Fn-PEGAuTSNP	714 nm

For all concentrations of ECM, the shift recorded was positive, from 4 nm to 12 nm shifts indicating the binding of anti-Fn-PEGAuTSNP to native Fn. This was validated with the addition of 100% and 15% purified Fn (non-native) as positive controls, where expected redshifts of 20 nm and 11 nm, respectively, were recorded (Figure 1). Further testing was carried out with the use of anti-TJP1-PEGAuTSNP as a negative control for binding, since this human tight junction protein 1 (TJP1)-targeted antibody should not show specificity to Fn. As shown in Figure 2 and Table 2, a shift of 37 nm was recorded for PEGAuTSNPs upon the addition of anti-TJP1, indicating the functionalization of the nanoparticles with the antibody. When the nanoparticles were exposed to the different concentrations of ECM extract, limited shifts between 1 and 2 nm were observed. Similar behavior was observed when the TJP1 antibody-functionalized nanoplates were exposed to purified Fn with a 3 nm shift compared to ~20 nm shifts when Fn was exposed to anti-Fn-PEGAuTSNPs.





**Figure 2.** LSPR spectra of anti-TJP1-Anti-Fn binding experiment.

**Table 2.**  $\lambda_{max}$  of anti-TJP1-PEGAuTSNPs within different concentrations of ECM.

Treatment	$\lambda_{max}$
PEGAuTSNP	638 nm
Anti-TJP1-PEGAuTSNP	675 nm
100% ECM + Anti-TJP1-PEGAuTSNP	677 nm
50% ECM + Anti-TJP1-PEGAuTSNP	677 nm
15% ECM + Anti-TJP1-PEGAuTSNP	671 nm
100% Fn + Anti-TJP1-PEGAuTSNP	678 nm

### 2.2. Spike Protein Optimal Functionalization Volume Determination

To determine the amount of Spike protein required to successfully cover the nanoplates' surfaces, a range of protein concentrations were added to 1 mL of PEGAuTSNP samples and analyzed. One  $\mu\text{g}$  of the Spike's corresponding antibody was added afterwards to analyze changes in the LSPR recordings. As shown in Table 3, the recorded  $\lambda_{max}$  for the Spike-functionalized PEGAuTSNPs was higher as the amount of Spike protein increased. Nonetheless, when between 5  $\mu\text{g}$  and 10  $\mu\text{g}$  concentrations of Spike were used to functionalize the nanoplates, the recorded  $\lambda_{max}$  started to decrease and stabilized around 632 nm, presumably indicating saturation of the nanoparticles' surface. This was tested by adding 1  $\mu\text{g}$  of the anti-Spike antibody, where a short increase in the  $\lambda_{max}$  was predicted as a result of the further coverage of uncoated sections of the nanoplates and the binding of the Ab-Ag complex. Upon exposure to the antibody, the results demonstrated higher  $\lambda_{max}$  recordings for all samples as expected; however, the  $\lambda_{max}$  for the samples with higher protein levels (between 5 and 10  $\mu\text{g}$ ) showed decreasing values, similar to the recordings prior to anti-Spike addition.

**Table 3.**  $\lambda_{\max}$  recordings before and after the addition of anti-Spike.

Spike volume	1 $\mu\text{g}$	3 $\mu\text{g}$	5 $\mu\text{g}$	7 $\mu\text{g}$	10 $\mu\text{g}$
$\lambda_{\max}$ before anti-Spike (nm)	603	647	641	632	632
$\lambda_{\max}$ after anti-Spike (nm)	615	651	647	639	638
$\Delta\lambda$ (nm)	12	4	6	7	6

The results suggested that the protein concentration that successfully covers the nanoplates surface before the saturation point is between 3  $\mu\text{g}$  and 5  $\mu\text{g}$ . Considering this, a concentration of 4  $\mu\text{g}/\text{mL}$  of PEGAuTSNPs was used for further testing.

### 2.3. Spike-PEGAuTSNP Detection Limit Determination

Spike-functionalized PEGAuTSNPs were used with different amounts of anti-Spike. As shown in Figure 3a, expected redshifts were recorded for increasing concentrations of anti-Spike, which suggests the intensifying binding of the antibody to the Spike-functionalized nanoplates. The binding of the Spike–anti-Spike complex could be detected in a linear range of anti-Spike concentration between 0.01 and 0.1 mg/mL (Figure 3b). Moreover, shorter redshifts were observed for the highest concentrations of antibody, indicating Ab-Ag system saturation from 0.13 mg/mL of anti-Spike.

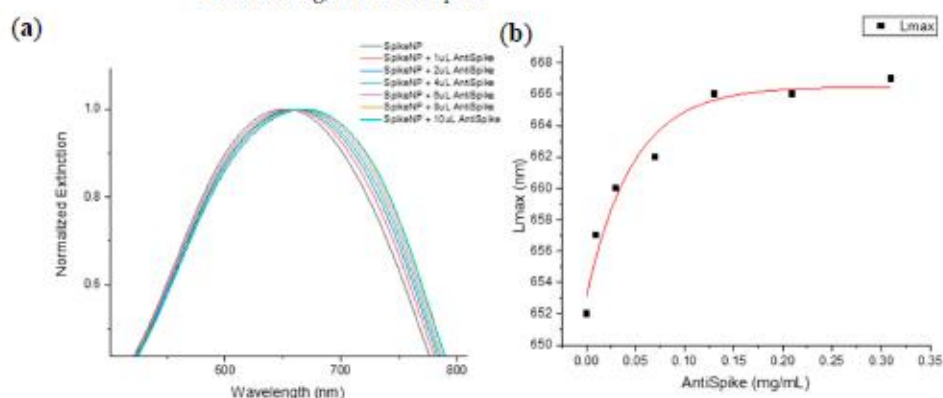


**Figure 3.** (a) LSPR spectra of Spike PEG-AuTSNP with increasing amounts of anti-Spike; (b) LSPR peak shift as a function of anti-Spike concentration for Spike PEG-AuTSNPs.

### 2.4. Specificity Analysis of the Spike–Anti-Spike System

The specificity of the Spike–anti-Spike system was tested with the previously established concentrations of Spike-PEGAuTSNPs and anti-Spike as per detection curves (Figure 3). The TJP1 protein was used as a negative control for binding since the anti-Spike antibody is specific to Spike protein according to the manufacturer’s information [24]. The amount of used TJP1 was equivalent to the Spike concentration to secure proper control conditions. As shown in Figure 4, the LSPR for bare PEGAuTSNPs was recorded at 575 nm, and redshifts of 65 nm (to 639 nm) and 25 nm (to 600 nm) were observed upon functionalization with Spike and TJP1 proteins, respectively. According to Table 4, a shift of 7 nm for the Spike PEGAuTSNPs was measured after exposure to its corresponding antibody, while a shift of only 1 nm was detected for the TJP1-PEGAuTSNPs.

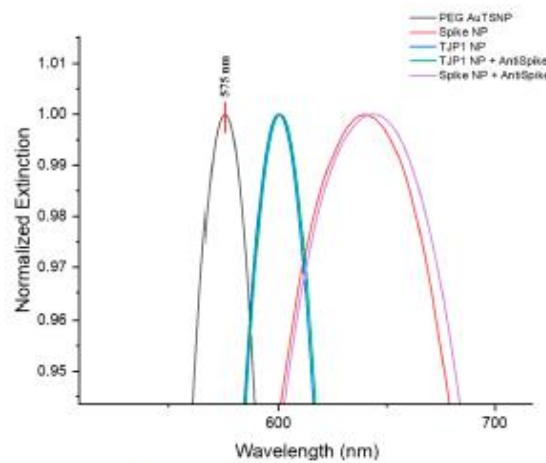


**Figure 4.** LSPR spectral shifts of PEGAuTSNPs, Spike-functionalized PEGAuTSNPs, TJP1-functionalized PEGAuTSNPs before and after exposure to anti-Spike.

**Table 4.**  $\lambda_{max}$  for Spike-PEGAuTSNPs and TJP1-PEGAuTSNPs before and after the addition of anti-Spike.

	$\lambda_{max}$ Spike-PEGAuTSNP (nm)	$\lambda_{max}$ TJP1-PEGAuTSNP (nm)
Before anti-Spike	639	600
After anti-Spike	646	601
$\Delta\lambda$	7	1

**2.5. Spike Protein Detection-Platform Testing within a Complex System**

The binding of Spike to anti-Spike was analyzed in the presence of horse serum (HS), simulating a complex environment to study the nanoparticles’ sensitivity. TJP1 was used as a control for binding. As shown in Table 5, the  $\lambda_{max}$  for the Spike-functionalized PEGAuTSNPs was initially recorded at 590 nm. As predicted, upon binding of the antibody to the Spike, a shift of 13 nm was detected. There was similar behavior in the cases where the Spike-PEGAuTSNPs were in the presence of three different concentrations of HS (100%, 50% and 10%), where positive shifts of 8 nm, 7 nm and 2 nm were recorded, respectively. When TJP1-PEGAuTSNPs (initial  $\lambda_{max}$  of 596 nm) were exposed to anti-Spike, a minimal shift (1 nm) was recorded, similar to previous experiments. Nonetheless, shifts of 8 nm, 3nm and 2 nm were recorded for TJP1-NP upon the addition of anti-Spike in the presence of HS.

**Table 5.**  $\lambda_{max}$  for Spike-PEGAuTSNP and TJP1-PEGAuTSNP treatments within HS before and after exposure to anti-Spike.

	Spike NP	HS 100% + Spike	HS 50% + Spike	HS 10% + Spike	TJP1 NP	HS 100% + TJP1 NP	HS 50% + TJP1 NP	HS 10% + TJP1 NP
$\lambda_{max}$ before anti-Spike (nm)	590	609	612	607	596	612	617	604
$\lambda_{max}$ after anti-Spike (nm)	603	617	619	609	597	620	620	606
$\Delta\lambda$ (nm)	13	8	7	2	1	8	3	2

Additional experiments were carried out, analyzing only TJP1 in order to confirm the previous results and further investigate the behavior patterns of the protein when

exposed to anti-Spike in the presence of serum. PEGAuTSNPs'  $\lambda_{\max}$  was recorded at 589 nm, and shifts of 15 nm and 8 nm were recorded upon functionalization with Spike and TJP1, respectively. Similar to previous tests, there was a weaker attachment of TJP1 onto the nanoplates. According to Table 6, registered  $\lambda_{\max}$  values appear to be higher upon exposure to anti-Spike in all treatments, comparable to the previous experiment.

**Table 6.**  $\lambda_{\max}$  for TJP1-PEGAuTSNP treatments within HS before and after exposure to anti-Spike.

	PEG AuTSNP	Spike NP	TJP1 NP	HS 100% + TJP1 NP	HS 50% + TJP1 NP	HS 10% + TJP1 NP
$\lambda_{\max}$ before anti-Spike (nm)	589	604	597	628	627	618
$\lambda_{\max}$ after anti-Spike (nm)	614	619	614	633	632	620
$\Delta\lambda$	25	15	17	5	5	2

Moreover, shifts of 5 nm and 2 nm were recorded for TJP1-NP upon the addition of anti-Spike in the presence of HS in concentrations of 100%, 50% and 10%. As mentioned earlier, the binding of anti-Spike to the TJP1 protein was not expected; however, there appears to be interaction between anti-Spike and the TJP1 nanoplates. For this reason, further analysis was necessary to gain a better understanding of the possible causes of binding; thus, dynamic light scattering (DLS) measurements were carried out for all treatments following the addition of antibodies.

#### 2.6. Dynamic Light Scattering (DLS) Size Measurements

Table S1 shows the DLS size measurements for all treatments before and after exposure to anti-Spike. In most cases, it can be observed that there was an increase in the average size of the particles after the apparent binding of the antibody. According to Figure 5, DLS showed a size measurement of 395.9 nm for TJP1-PEGAuTSNPs, which only corresponds to an 8 nm shift in the LSPR spectrum, as stated in Table 6 (from 589 nm to 597 nm). Upon anti-Spike addition, there was a reduction in size to 53.53 nm; however, there was an LSPR recording of a 17 nm shift, which could be attributed to the replacement of TJP1 by anti-Spike on the PEGAuTSNPs' surfaces.

#### 2.7. Spike–Anti-Spike Binding PEGAuTSNP-Based Immunoassay within Horse Serum

For the system within horse serum, a more detailed analysis of the results revealed that upon the addition of anti-Spike, there was an increase in size only for a small population of particles. In the case of 100% HS (HS100) with TJP1 nanoplates (Figure 6a), an average size of 142.1 nm was recorded with a Polydispersity Index (PI) of 0.33; after the sample interacted with the antibody, there was an increase in size to an average of 172.5 nm and PI of 0.78.

When the results are compared to TJP1 NP + anti-Spike (red plot, 53.53 nm in size), resemblance can be observed with the HS100 + TJP1 NP plot (blue), where a size of 39.28 nm was recorded. When the system is analyzed as a whole, namely HS100 + TJP1 NP + anti-Spike, a peak of 163.1 nm (blue plot) can be related to the 165.8 nm peak from the green-colored plot, suggesting the TJP1-coated nanoparticles did not bind to anti-Spike and kept their size; nonetheless, a fourth peak in the green plot above the 1000 nm region could be attributed to the anti-Spike binding and networking with components from the HS.

Fifty percent diluted horse serum (HS50) behaved in a similar manner, where an increase in the average size was observed with the presence of anti-Spike in the sample. The 50% HS with TJP1 nanoplates sample (Figure 6b) with an average size of 211.2 nm and a PI of 0.4 showed an increase to a size of 755 nm and PI of 0.69 as a consequence of higher polydispersity. Similar to HS100, relation can be observed between the plots, where TJP1 NP + anti-Spike (red plot) and HS50 + TJP1 NP (blue plot) can be identified within the HS50 + TJP1 NP + anti-Spike sample (green plot), where it can be observed that a fraction of the HS50 + TJP1 nanoplates interacted with the antibody, resulting in a higher intensity peak of 470.7 nm.

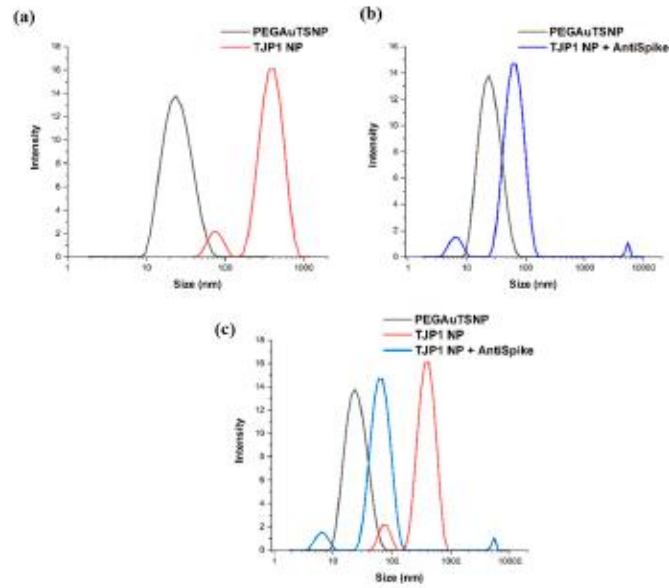


**Figure 5.** DLS size measurements of (a) PEGAuTSNPs and TJP1-PEGAuTSNPs, (b) TJP1-PEGAuTSNPs + anti-Spike, (c) superimposed graphs of (a,b).

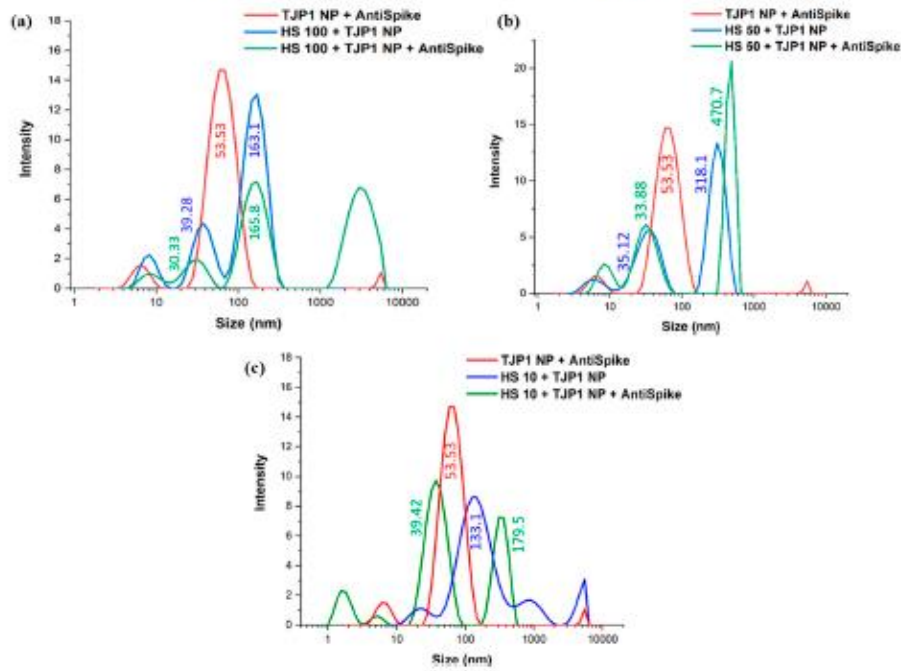


**Figure 6.** DLS measurements for TJP1-NP + anti-Spike and TJP1-NP within (a) 100%, (b) 50% and (c) 10% HS before and after addition of anti-Spike.

In line with the previous HS concentrations, TJP1 NP + anti-Spike and HS10 + TJP1 NP can be identified within the most diluted sample (Figure 6c). Similar to the other HS samples, the plot suggests the TJP1-coated nanoplates did not bind to anti-Spike, but the antibody created networks with serum contents, resulting in a peak in the highest region among all samples (179.5 nm). Moreover, it can be observed that, comparable with the above results, the size of the HS10 + TJP1 NP sample was 133.1 nm (blue plot), and upon anti-Spike addition, a fraction of the sample reduced in size to 39.42 nm (green), validating the hypothesis that the antibody breaks the TJP1 network, causing the size reduction.

### 3. Discussion

Fibronectin (Fn), a critical ECM protein whose functions are governed by its conformational activity, is receiving increasing attention due to its participation in various phases of tumor proliferation and other complications of medical importance such as Fn glomerulopathy [25–27]. In this study, the suitability of PEGAuTSNPs for use as platforms for IAs was successfully demonstrated. The effective protein volumes to functionalize the nanoparticles and avoid potential non-specific binding were determined. Ab-Ag binding was detected within a complex environment where native Fn from the extracellular matrix was successfully detected by using anti-Fn antibody-coated nanoplates.

Spike-PEGAuTSNPs' detection limit was determined as a linear range of anti-Spike concentration between 0.01 and 0.1 mg/mL. In a comparative study of [28], detection limit ranges of rapid antigen tests were recorded between 9.8 and 78.6 ng/mL. This opens an area of opportunity to improve the proposed technique detection limits.

The results of the functionalization of PEGAuTSNPs'  $\lambda_{max}$  with anti-Fn (a shift of 65 nm) indicated the successful coating of the nanoplates with the antibody. However, when the functionalized nanoplates were exposed to different concentrations of cell-isolated ECM and analyzed, they showed a shifting profile, different than expected, with longer shifts recorded for the less concentrated ECM samples. One of the reasons could be attributed to the clumping of ECM proteins as a result of the cell scraping performed in the isolation protocol, impeding Fn binding sites to be sufficiently exposed to bind to its corresponding antibody; once the sample is diluted, the proteins disaggregate and Fn is exposed. According to Sediq et al., one of the reasons for protein aggregation is the induced mechanical stress during the friction of two solid surfaces, which, in this case, were the cell scraper and the flask containing the cell culture [29]. In future testing, ECM samples can be briefly homogenized to make the proteins scatter and aid in binding site recognition for the antigen of interest. Our results also implied that the TJP1 antibody did not recognize any epitope from MC3T3-E1 ECM proteins [30].

When it comes to the determination of optimal volumes for Spike protein functionalization, the results indicated the binding of the antibody only to the Spike protein available on the now fully functionalized nanoplates surface. The latter can be confirmed through the analysis of the  $\Delta\lambda$ , where it can be observed that between the concentrations of 5  $\mu\text{g}$  and 10  $\mu\text{g}$  of Spike in PEGAuTSNPs, the shift difference is constantly between 6 nm and 7 nm, indicating the maximum possible binding of the anti-Spike to Spike was reached. After the Spike-anti-Spike system specificity analysis, a reduced shift of the TJP1 nanoplates (25 nm) compared to the Spike nanoplates (65 nm) was observed, suggesting weak attachment of the TJP1 protein to the PEGAuTSNPs' surfaces. This can also be inferred when evident binding between the antibody and its Spike counterpart (7 nm) was observed, but there was unexpected interaction between anti-Spike and TJP1, where there was almost no shifting (1 nm). This behavior could indicate no recognition of the antibody, which would be expected, or a stronger affinity of the anti-Spike for the nanoplates, causing a replacement on the nanoplates' surface.

The binding of Spike to anti-Spike was analyzed in the presence of HS to simulate a complex environment. As mentioned in the Results section, after TJP1-PEGAuTSNPs were exposed to anti-Spike, a minimal shift was recorded, similar to previous experiments; however, shifts of 8 nm, 3 nm and 2 nm were recorded for TJP1-NP upon addition of

anti-Spike in the presence of 100%, 50% and 10% HS, respectively. These unanticipated positive shifts in relation to TJP1 could be associated with the non-specific binding of the HS components to the added anti-Spike. According to [31], HS is a non-standardized component of blood with varying concentrations of several proteins, albumins and globulins, among other components; this could interrupt, obstruct or, in this case, interfere with the predicted experiment behavior.

These results were further analyzed with DLS measurements, where several nanoparticle populations of varying sizes were identified in the samples, explaining the outcomes of the experiment. DLS size measurements showed the increase in the average size of the particles after the apparent binding of the antibody in most cases; nonetheless, three peaks could be observed in all samples containing HS even before exposure to anti-Spike, possibly indicating the coexistence of nanoparticles of different sizes within the same sample or agglomeration of HS proteins [32]. A similar phenomenon was observed in the study of Schintke and Frau (2020), where the interaction between nanoparticles and mouse serum sample showed poor signal stability in DLS measurements as the unfiltered serum sample contained large agglomerates that affected the particle size, causing several peaks [33]. The use of TJP1 as a control showed interesting performance within HS samples, and thus, it could be concluded that protein–protein networks were formed which were then broken up by the added anti-Spike antibody due to its stronger affinity to the nanoplates.

As mentioned before, anti-Spike seemed to show stronger affinity for the nanoplates, causing TJP1 to be replaced by the antibody on the nanoplates' surface (Figure 7). DLS measurements for TJP1-PEGAuTSNPs could be attributed to TJP1 causing networking by itself. Since networking is not a close reaction to the PEGAuTSNP surface, it does not reflect in a large shift (8 nm) [25]. Nonetheless, upon anti-Spike addition, there was a reduction in size, possibly indicating the breakage of the TJP1 network on the nanoplates. The anti-Spike antibody seemed to show a stronger affinity for the nanoplates, causing the TJP1 protein to be replaced by the antibody on the nanoplates' surface, reflected in a redshift. Nonetheless, the formed TJP1 network may be broken up, causing less protein molecules on the surface of the nanoplate, resulting in a DLS size reduction [25].

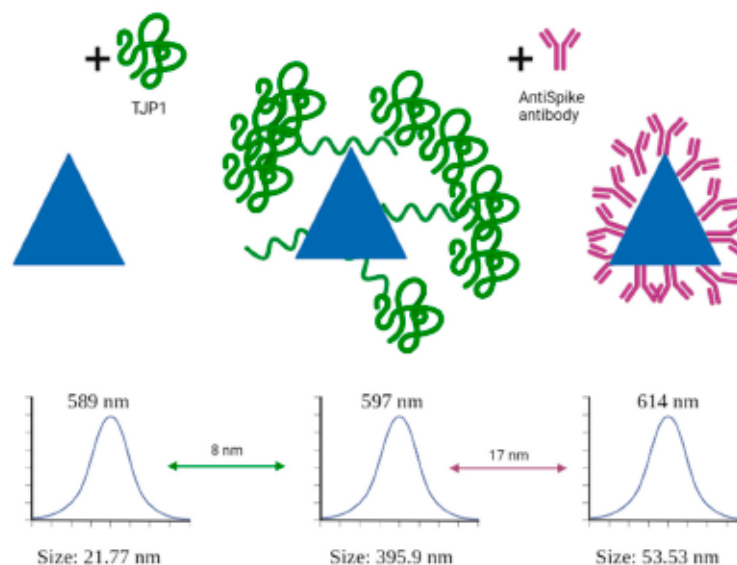


**Figure 7.** Illustration of protein replacement due to stronger attachment of anti-Spike to PEGAuTSNPs.

In future research, alternative complex environments and controls to validate the results will be assessed, and additional steps such as the filtering of bigger molecules within the samples to minimize non-specific binding and polydispersity will be taken.

#### 4. Materials and Methods

##### 4.1. Materials

Fibronectin bovine plasma (1 mg/mL) (F4759-1G), Horse Serum donor herd (H1270-500ML) and anti-FN antibody (1 mg/mL) (AV41490-100UL) were obtained from Sigma Aldrich (St. Louis, MO, USA). The MC3T3-E1 pre-osteoblast cell line (CRL-2593) was obtained from ATCC, and Gibco Alpha Minimum Essential Medium (41061029), Invitrogen SARS-CoV-2 Spike Protein (RBD) Polyclonal Antibody (PA5-114451, 0.5–1 mg/mL) and Invitrogen SARS-CoV-2 Nucleocapsid/Spike Protein (RBD) Recombinant Protein (RP87706, 1 mg/mL) were obtained from Thermo Fisher (Waltham, MA, USA). Human TJP1 recombinant protein (APrEST83050, 0.5–1 mg/mL) and human-specific anti-TJP1 antibody (HPA001636, 0.5–1 mg/mL) were obtained from Atlas Antibodies (Stockholm, Sweden).

##### 4.2. Anti-Fn-PEGAuTSNP Preparation

PEGAuTSNPs were synthesized through a seed-mediated approach where silver nitrate was reduced by sodium borohydride [9]. Subsequently, 1 mL of freshly synthesized nanoplates was incubated with 20 µg of anti-Fn antibody, with the concentration before nanoplate saturation being as described by Rodriguez Barroso et al. (2023).

##### 4.3. Extracellular Matrix Isolation Protocol

Extracellular matrix (ECM) isolation from cell culture was performed based on the protocol developed by [34] to study the interaction between native Fn from live cells and anti-Fn antibody. MC3T3-E1 pre-osteoblast cells were cultured and plated in a 6 well-plate at high density and placed in the incubator for 24 h until they were 95% confluent. Ammonium Hydroxide (NH<sub>4</sub>OH, 20 mM) was prepared with de-ionized water in an extractor hood. The culture plate was removed from the incubator, and the culture medium was removed from each well with a micropipette. Wells were gently rinsed with 1 mL of PBS without Ca<sup>2+</sup>/Mg<sup>2+</sup>, and the liquid containing PBS and remaining media were removed from the wells. Subsequently, 300 µL of 20 mM NH<sub>4</sub>OH was added to each well and rocked for a few seconds before washing each well with 1 mL of distilled water. The ammonium-hydroxide-solubilized material containing water, ammonium hydroxide and lysed cells was immediately removed with a micropipette. After that, the 6-well plate was tilted at an angle, and remaining ECM was collected from the bottom of the well by using a cell scrapper and placed in Eppendorf tubes.

##### 4.4. Detection of Native Fibronectin with Anti-Fn-PEGAuTSNP

Three concentrations of MC3T3-E1 cells-isolated ECM (100%, 50% and 15%) were prepared with distilled water. ECM samples were further exposed to a concentration of 0.21 mg/mL of anti-Fn-PEGAuTSNPs (functionalized NPs before saturation point, as stated by Rodriguez Barroso et al. 2023) in a 1:1.5 ECM/anti-Fn-PEGAuTSNP ratio and placed on a 96-well plate to analyze interactions between native Fn and the antibody. Purified Fn samples in concentrations of 100% and 15% were used as positive controls for the binding of anti-Fn with Fn (1:1.5 Fn: Anti-Fn-PEGAuTSNP ratio). The 96-well plate was analyzed in the microplate reader. Results were compared to a second experiment where human-specific TJP1 antibody was used as a negative control for binding with the ECM isolated from cells. In order to detect changes in LSPR and  $\lambda_{max}$ , absorbance spectra measurements were performed in a microplate reader adjusted from wavelengths 300–900 nm in 1 nm increments.



#### 4.5. Spike Protein Optimal Functionalization Volume Determination

PEGAuTSNPs were prepared as previously stated, and different amounts of spike protein were added to the nanoplates. Then, 1 mL of PEGAuTSNPs was placed in five Eppendorf tubes (5 mL total) and 1 µg, 3 µg, 5 µg, 7 µg and 10 µg of Spike protein were added to each tube. A sample of 100 µL was taken from each tube and placed on a 96-well plate. The plate was analyzed in an Ultraviolet-visible (UV-vis) spectrometer (Synergy HT BioTek microplate reader, Winooski, VT, USA) reader. After the first reading, 1 µg of anti-Spike antibody was added to each well, and the plate was analyzed again to observe changes in the LSPR. UV-Vis spectra measurements were adjusted from wavelengths 300–900 nm in 1 nm increments.

#### 4.6. Nanoplate-Based Immunoassay with Changing Concentrations of Anti-Spike Antibody

After the suitable concentration of spike PEGAuTSNPs was determined, 4 µL spike/mL PEGAuTSNPs were used with different amounts of anti-Spike to determine the nanoparticle saturation point. A sample of 100 µL of Spike PEG-AuTSNPs was placed on a 96-well plate and analyzed in the plate reader. After that, 1 µg of anti-Spike was added to the well and the plate was analyzed again in a microplate reader with adjusted wavelengths from 300–900 nm in 1 nm increments. Following that, 2 µg, 4 µg, 6 µg, 8 µg and 10 µg were added to the same well, and the plate was analyzed between every addition. The final sum of anti-Spike in the well at the end of the experiment was 31 µg. Experiments were performed in the same well to avoid variations in the readings and to keep uniformity.

#### 4.7. Spike–Anti-Spike Binding PEGAuTSNP-Based Immunoassay

Spike-PEGAuTSNPs were exposed to anti-Spike to test the nanoplate-based immunoassay system. Then, 100 µL of Spike-PEGAuTSNPs in a 4 µg Spike/mL PEGAuTSNP concentration and 100 µL of TJP1-PEGAuTSNPs (5 µg TJP1/mL PEGAuTSNP) were placed in a 96-well plate and analyzed on the plate reader. After the first reading, 4 µg of anti-Spike was added to both wells and the plate was analyzed again. The microplate reader was adjusted from wavelengths 300–900 nm in 1 nm increments for absorbance measurements.

#### 4.8. Spike–Anti-Spike Binding PEGAuTSNP-Based Immunoassay within Horse Serum

The binding of the Spike–anti-Spike complex within horse serum as a high-noise environment was monitored using PEGAuTSNPs. Spike-PEGAuTSNPs were prepared with 4 µg of Spike in 1 mL of PEGAuTSNPs, and TJP1-PEGAuTSNPs were prepared in a similar concentration of 5 µg of TJP1 per 1 mL of PEGAuTSNPs. The latter was used as a negative control for binding with the Spike antibody. Three different concentrations of horse serum (100%, 50% and 10%) were prepared with distilled water to observe differences in the LSPR as a result of the high concentration of proteins within the serum. Samples were placed in a 96-well plate in a ratio of 1:1.67 horse serum/functionalized PEGAuTSNPs. The plate was analyzed in the plate reader. After the first analysis, 4 µg of anti-Spike was added to all wells, and the plate was analyzed again.

#### 4.9. Dynamic Light Scattering (DLS) Size Measurements

Dynamic Light Scattering (DLS) is extensively used in research for the study of proteins, colloidal particles, and nanoparticles [33]. It studies the diffusion of molecules in solution through the diffusion coefficient and hydrodynamic radius, which are dependent on the analyzed molecules' size and shape [35]. In this study, Zetasizer Pro (Malvern Panalytical Ltd., Malvern, UK) with DTS0012 polystyrene disposable cuvettes was used to determine the particle size of the samples.

All samples from Section 4.7 were diluted with ultrapure water in a 1:10 dilution. Then, 1 mL of the newly diluted sample was placed in the disposable cuvette and the cuvette lid was placed on top. Size measurements were repeated 3 times per sample at 25 °C, and the results were analyzed in ZS XPLORER software (<https://www.malvernpanalytical.com/jp/support/product-support/software/zetasizer-ultra-pro-zs-xplorer-software-update-v1-0>, accessed on 29 June 2023).

## 5. Conclusions

This study successfully demonstrated the potential of PEGAuTSNPs as platforms for immunoassays, showcasing the effective protein volumes for functionalization and successful detection of native Fn using AntiFn antibody-coated nanoplates. When exposed to cell-isolated ECM samples, unexpected shifting profiles were observed, potentially attributed to protein clumping caused by the ECM-isolation protocol. Future testing could involve brief homogenization of ECM samples to aid in binding site recognition. On the other hand, successful binding of AntiSpike antibody to Spike protein on the fully functionalized nanoplates was demonstrated upon Spike protein optimal functionalization volume determination. Moreover, weak attachment of the control protein, TJP1, to the nanoplates was observed. The detection limit of the Spike-PEGAuTSNP ranged between 0.01–0.1 mg/mL, while the detection limits reported for rapid antigen tests range between 9.8–78.6 ng/mL. This opens an area of opportunity to improve the detection limits of the Spike-PEGAuTSNP system. In the presence of complex environments such as HS, unanticipated positive shifts in TJP1 nanoplates were recorded, possibly due to non-specific binding of HS components. DLS measurements revealed the coexistence of nanoparticle populations of varying sizes and protein-protein networks formation within horse serum samples. Future research should explore alternative complex environments, implement appropriate controls, and consider filtering larger molecules to minimize non-specific binding and polydispersity. Overall, this study provides valuable insights into the behavior of immunoassay platforms and highlights areas for further investigation and refinement.

**Supplementary Materials:** The supporting information can be downloaded at: <https://www.mdpi.com/article/10.3390/ijms241511974/s1>.

**Author Contributions:** Conceptualization, L.G.R.B., M.H., M.B.-F. and M.M.; methodology, L.G.R.B., E.L.G. and R.P.; validation, L.G.R.B., E.L.G. and M.H.; formal analysis, L.G.R.B., M.H. and M.B.-F.; investigation, L.G.R.B., E.L.G., R.P. and M.M.; data curation, L.G.R.B., E.L.G., B.A.T. and M.M.; writing—original draft preparation, L.G.R.B., B.A.T. and M.M.; writing—review and editing, L.G.R.B., E.L.G., B.A.T., M.M., M.H., R.P. and M.B.-F.; visualization, L.G.R.B., E.L.G. and M.M.; supervision, M.M., M.B.-F. and D.M.D.; project administration, M.H. and M.B.-F.; funding acquisition, M.B.-F. All authors have read and agreed to the published version of the manuscript.

**Funding:** Funding for this work was provided by the Technological University of The Shannon through the President Seed Fund and European Union's Horizon 2020 Research and Innovation program [grant number: 870292 (BioCEP)].

**Institutional Review Board Statement:** Not applicable.

**Informed Consent Statement:** Not applicable.

**Data Availability Statement:** [zenodo.org](https://zenodo.org), accessed on 15 June 2023.

**Conflicts of Interest:** The authors declare no conflict of interest.

## References

1. Vashist, S.K.; Luong, J.H.T. *Immunoassays: An Overview*; Elsevier Inc.: Amsterdam, The Netherlands, 2018; ISBN 9780128117620.
2. Darwish, I.A. Immunoassay Methods and Their Applications in Pharmaceutical Analysis: Basic Methodology and Recent Advances. *Int. J. Biomed. Sci.* **2006**, *2*, 217.
3. Mousavi, S.M.; Hashemi, S.A.; Kalashgrani, M.Y.; Gholami, A.; Omidifar, N.; Babapoor, A.; Vijayakameswara Rao, N.; Chiang, W.H. Recent Advances in Plasma-Engineered Polymers for Biomarker-Based Viral Detection and Highly Multiplexed Analysis. *Biosensors* **2022**, *12*, 286. [[CrossRef](#)] [[PubMed](#)]
4. Ahmed, S.; Ning, J.; Peng, D.; Chen, T.; Ahmad, I.; Ali, A.; Lei, Z.; Abu bakr Shabbir, M.; Cheng, G.; Yuan, Z. Current Advances in Immunoassays for the Detection of Antibiotics Residues: A Review. *Food Agric. Immunol.* **2020**, *31*, 268–290. [[CrossRef](#)]
5. Cox, K.L.; Devanarayan, V.; Kriauciunas, A.; Manetta, J.; Montrose, C.; Sittampalam, S. Immunoassay Methods. In *Assay Guidance Manual*; Eli Lilly & Company and the National Center for Advancing Translational Sciences: Bethesda, MD, USA, 2019.
6. Gan, S.D.; Patel, K.R. Enzyme Immunoassay and Enzyme-Linked Immunosorbent Assay. *J. Investig. Dermatol.* **2013**, *133*, e12. [[CrossRef](#)]

7. Lajtha, A.; Baker, G.; Dunn, S.; Holt, A. *Handbook of Neurochemistry and Molecular Neurobiology: Practical Neurochemistry Methods*; Springer Science: New York, NY, USA, 2007; ISBN 978-0-387-30359-8.
8. Farka, Z.; Juřík, T.; Kovář, D.; Trnková, L.; Skládal, P. Nanoparticle-Based Immunochemical Biosensors and Assays: Recent Advances and Challenges. *Chem. Rev.* **2017**, *117*, 9973–10042. [[CrossRef](#)] [[PubMed](#)]
9. Rodríguez Barroso, L.G.; Azaman, F.A.; Pogue, R.; Devine, D.; Fournet, M.B. Monitoring In Vitro Extracellular Matrix Protein Conformations in the Presence of Biomimetic Bone-Regeneration Scaffolds Using Functionalized Gold-Edge-Coated Triangular Silver Nanoparticles. *Nanomaterials* **2023**, *13*, 57. [[CrossRef](#)]
10. Mercadal, P.A.; Fraire, J.C.; Motrich, R.D.; Coronado, E.A. Enzyme-Free Immunoassay Using Silver Nanoparticles for Detection of Gliadin at Ultralow Concentrations. *ACS Omega* **2018**, *3*, 2340–2350. [[CrossRef](#)]
11. Mallah, S.I.; Ghorab, O.K.; Al-Salmi, S.; Abdellatif, O.S.; Tharmaratnam, T.; Iskandar, M.A.; Sefen, J.A.N.; Sidhu, P.; Atallah, B.; El-Labadi, R.; et al. COVID-19: Breaking down a Global Health Crisis. *Ann. Clin. Microbiol. Antimicrob.* **2021**, *20*, 1–36. [[CrossRef](#)]
12. Casella, M.; Rajnik, M.; Cuomo, A.; Dulebohn, S.C.; Di Napoli, R. *Features, Evaluation, and Treatment of Coronavirus (COVID-19)*; StatPearls: Treasure Island, FL, USA, 2022.
13. Valdivia, A.; Torres, I.; Latorre, V.; Francés-Gómez, C.; Albert, E.; Gozalbo-Rovira, R.; Alcaraz, M.J.; Buesa, J.; Rodríguez-Díaz, J.; Geller, R.; et al. Inference of SARS-CoV-2 Spike-Binding Neutralizing Antibody Titers in Sera from Hospitalized COVID-19 Patients by Using Commercial Enzyme and Chemiluminescent Immunoassays. *Eur. J. Clin. Microbiol. Infect. Dis.* **2021**, *40*, 485–494. [[CrossRef](#)]
14. Yatsunyk, L.A.; Mendoza, O.; Mergny, J.-L. “Nano-Oddities”: Unusual Nucleic Acid Assemblies for DNA-Based Nanostructures and Nanodevices. *Acc. Chem. Res.* **2014**, *47*, 1836–1844. [[CrossRef](#)]
15. Zhang, Y.; Charles, D.E.; Ledwith, D.M.; Aherne, D.; Cunningham, S.; Voisin, M.; Blau, W.J.; Gun’ko, Y.K.; Kelly, J.M.; Brennan-Fournet, M.E. Wash-Free Highly Sensitive Detection of C-Reactive Protein Using Gold Derivatized Triangular Silver Nanoplates. *RSC Adv.* **2014**, *4*, 29022–29031. [[CrossRef](#)]
16. Jia, H.; Xu, W.; An, J.; Li, D.; Zhao, B. A Simple Method to Synthesize Triangular Silver Nanoparticles by Light Irradiation. *Spectrochim. Acta Part A Mol. Biomol. Spectrosc.* **2006**, *64*, 956–960. [[CrossRef](#)] [[PubMed](#)]
17. Askari, H.; Sanadgol, N.; Azarmezah, A.; Tajbaksh, A.; Rafiei, H.; Safarpour, A.R.; Gheibihayat, S.M.; Raeis-Abdollahi, E.; Savardashtaki, A.; Ghanbariasad, A.; et al. Kidney Diseases and COVID-19 Infection: Causes and Effect, Supportive Therapeutics and Nutritional Perspectives. *Heliyon* **2021**, *7*, e06008. [[CrossRef](#)]
18. Ren, X.; Meng, X.; Chen, D.; Tang, F.; Jiao, J. Using Silver Nanoparticle to Enhance Current Response of Biosensor. *Biosens. Bioelectron.* **2005**, *21*, 433–437. [[CrossRef](#)] [[PubMed](#)]
19. Rad, A.S.; Mirabi, A.; Binaian, E.; Tayebi, H. A Review on Glucose and Hydrogen Peroxide Biosensor Based on Modified Electrode Included Silver Nanoparticles. *Int. J. Electrochem. Sci.* **2011**, *6*, 3671–3683. [[CrossRef](#)]
20. Chen, Z.P.; Peng, Z.F.; Luo, Y.; Qu, B.; Jiang, J.H.; Zhang, X.B.; Shen, G.L.; Yu, R.Q. Successively Amplified Electrochemical Immunoassay Based on Biocatalytic Deposition of Silver Nanoparticles and Silver Enhancement. *Biosens. Bioelectron.* **2007**, *23*, 485–491. [[CrossRef](#)]
21. Khristunova, E.; Barek, J.; Kratochvíl, B.; Korotkova, E.; Dorozhko, E.; Vyskocil, V. Electrochemical Immunoassay for the Detection of Antibodies to Tick-Borne Encephalitis Virus by Using Various Types of Bioconjugates Based on Silver Nanoparticles. *Bioelectrochemistry* **2020**, *135*, 107576. [[CrossRef](#)]
22. Rodríguez Barroso, L.G.; Garcia, E.L.; Mojicevic, M.; Huerta, M.; Pogue, R.; Devine, D.M.; Brennan-fournet, M. Triangular Silver Nanoparticles Synthesis: Investigating Potential Application in Materials and Biosensing. *Appl. Sci.* **2023**, *13*, 8100. [[CrossRef](#)]
23. Choi, H.K.; Lee, M.J.; Lee, S.N.; Kim, T.H.; Oh, B.K. Noble Metal Nanomaterial-Based Biosensors for Electrochemical and Optical Detection of Viruses Causing Respiratory Illnesses. *Front. Chem.* **2021**, *9*, 672739. [[CrossRef](#)]
24. Macdonald, P.J.; Ruan, Q.; Grieshaber, J.L.; Swift, K.M.; Taylor, R.E.; Prostko, J.C.; Tetin, S.Y. Affinity of Anti-Spike Antibodies in SARS-CoV-2 Patient Plasma and Its Effect on COVID-19 Antibody Assays. *eBioMedicine* **2022**, *75*, 103796. [[CrossRef](#)]
25. Brennan-Fournet, M.E.; Huerta, M.; Zhang, Y.; Malliaras, G.; Owens, R.M. Detection of Fibronectin Conformational Changes in the Extracellular Matrix of Live Cells Using Plasmonic Nanoplates. *J. Mater. Chem. B* **2015**, *3*, 9140–9147. [[CrossRef](#)] [[PubMed](#)]
26. Castelletti, E.; Donadelli, R.; Banterla, F.; Hildebrandt, F.; Zipfel, P.F.; Bresin, E.; Otto, E.; Skerka, C.; Renieri, A.; Todeschini, M.; et al. Mutations in FN1 Cause Glomerulopathy with Fibronectin Deposits. *Proc. Natl. Acad. Sci. USA* **2008**, *105*, 2538–2543. [[CrossRef](#)] [[PubMed](#)]
27. Wang, J.P.; Hielscher, A. Fibronectin: How Its Aberrant Expression in Tumors May Improve Therapeutic Targeting. *J. Cancer* **2017**, *8*, 674–682. [[CrossRef](#)] [[PubMed](#)]
28. Dobrynin, D.; Polischuk, I.; Pokroy, B. A Comparison Study of the Detection Limit of Omicron SARS-CoV-2 Nucleocapsid by Various Rapid Antigen Tests. *Biosensors* **2022**, *12*, 1083. [[CrossRef](#)] [[PubMed](#)]
29. Sediq, A.S.; Van Duijvenvoorde, R.B.; Jiskoot, W.; Nejadnik, M.R. No Touching! Abrasion of Adsorbed Protein Is the Root Cause of Subvisible Particle Formation during Stirring. *J. Pharm. Sci.* **2016**, *105*, 519–529. [[CrossRef](#)] [[PubMed](#)]
30. McIntyre, B.A.S.; Alev, C.; Mechaie, R.; Salci, K.R.; Lee, J.B.; Fiebig-Comyn, A.; Guezguez, B.; Wu, Y.; Sheng, G.; Bhatia, M. Expansive Generation of Functional Airway Epithelium From Human Embryonic Stem Cells. *Stem Cells Transl. Med.* **2014**, *3*, 7–17. [[CrossRef](#)]

31. Riond, B.; Wenger-Riggenbach, B.; Hofmann-Lehmann, R.; Lutz, H. Serum Protein Concentrations from Clinically Healthy Horses Determined by Agarose Gel Electrophoresis. *Vet. Clin. Pathol.* **2009**, *38*, 73–77. [[CrossRef](#)]
32. Vasile, E.; Rusen, E.; Mocanu, A.; Patrascu, M.; Calinescu, I. Polymer Colloids and Silver Nanoparticles Hybrid Materials. *Colloid Polym. Sci.* **2012**, *290*, 193–201. [[CrossRef](#)]
33. Schintke, S.; Frau, E. Modulated 3d Cross-Correlation Dynamic Light Scattering Applications for Optical Biosensing and Time-Dependent Monitoring of Nanoparticle-Biofluid Interactions. *Appl. Sci.* **2020**, *10*, 8969. [[CrossRef](#)]
34. Hellewell, A.L.; Rosini, S.; Adams, J.C. A Rapid, Scalable Method for the Isolation, Functional Study, and Analysis of Cell-Derived Extracellular Matrix. *J. Vis. Exp.* **2017**, *2017*, 55051. [[CrossRef](#)]
35. Stetefeld, J.; Mckenna, S.A.; Patel, T.R. Dynamic Light Scattering: A Practical Guide and Applications in Biomedical Sciences. *Biophys. Rev.* **2016**, *8*, 409–427. [[CrossRef](#)] [[PubMed](#)]

**Disclaimer/Publisher's Note:** The statements, opinions and data contained in all publications are solely those of the individual author(s) and contributor(s) and not of MDPI and/or the editor(s). MDPI and/or the editor(s) disclaim responsibility for any injury to people or property resulting from any ideas, methods, instructions or products referred to in the content.